CONTENTS

Section Page

1 SUMMARY 1 **1/B4**
2 INTRODUCTION 2 **1/B5**
2.1 Background 2 **1/B5**
2.2 Scope 8 **1/B11**
3 DIGITAL IMAGE PROCESSING OF EARTH OBSERVATION SENSOR DATA 10 **1/B13**
3.1 General Overview 10 **1/B13**
3.2 MSS and TM Functional Description 11 **1/B14**
3.2.1 Data Reformatting 15 **1/C4**
3.2.2 Radiometric Calibration 23 **1/C12**
3.2.3 Radiometric Correction 42 **1/E3**
3.2.4 Geometric Correction/Temporal Registration 43 **1/E4**
3.2.5 Resampling for Scanner Sensors 88 **2/A12**
3.3 Return Beam Vidicon (RBV) 99 **2/B11**
3.3.1 RBV Functional Overview 100 **2/B12**
3.3.2 Radiometric Calibration and Correction 104 **2/C3**
3.3.3 Geometric Correction 110 **2/C9**
3.3.4 Resampling for RBV 119 **2/D4**
3.4 Heat Capacity Mapper Mission (HCMM) 120 **2/D5**
3.4.1 Heat Capacity Mapper (HCM) Functional Description 121 **2/D6**
3.4.2 HCM Phase I Processing 123 **2/D8**
3.4.3 Radiometric Calibration Processing. . . 124 **2/D9**
3.4.4 Radiometric Correction 128 **2/D13**
3.4.5 Geometric Correction 133 **2/E4**

Section Page

3.4.6 Resampling for HCM 140 2/E11
3.5 Analysis of Geometric Correction/Temporal Registration Errors 141 2/E12
3.5.1 Landsat-D TM and MSS Error Analysis . . 143 2/E14
3.5.2 Input and Internal Errors 145 2/F3
3.6 Classification 158 2/G5
3.6.1 Introduction 158 2/G5
3.6.2 LACIE Overview 163 2/G10
3.6.3 Classification Approaches 167 3/A3
3.6.4 Baseline Classification Process 171 3/A7
3.6.5 On-Board Classification Configuration Analysis 176 3/A13
4 CONCLUSIONS AND RECOMMENDATIONS 209 3/E2
Appendix A TM AND MSS DATA REFORMATTING STUDY 213 3/E6
Appendix B ERROR ANALYSIS 233 3/G5
Appendix C EFFECT OF DATA STRIPING ON CLASSIFICATION ACCURACY 249 4/A10
Appendix D EFFECT OF LANDSAT ORBITAL CHARACTERISTICS ON ON-BOARD CLASSIFICATION 278 4/E1

Item 830-H-14

NAS1.26:3134

JAN 23 1980

COMPLETED

ORIGINAL

NASA Contractor Report 3134

On-Board Multispectral Classification Study

D. Ewalt

CONTRACT NAS1-15119
DECEMBER 1979

MICROFILMED FROM
BEST AVAILABLE COPY

NASA

307

NASA Contractor Report 3134

On-Board Multispectral Classification Study

D. Ewalt
International Business Machines, Inc.
Gaithersburg, Maryland

Prepared for
Langley Research Center
under Contract NAS1-15119

National Aeronautics
and Space Administration

Scientific and Technical
Information Branch

1979

CONTENTS

Section Page

1 SUMMARY 1
2 INTRODUCTION 2
2.1 Background 2
2.2 Scope 8
3 DIGITAL IMAGE PROCESSING OF EARTH OBSERVATION SENSOR DATA 10
3.1 General Overview 10
3.2 MSS and TM Functional Description 11
3.2.1 Data Reformatting 15
3.2.2 Radiometric Calibration 23
3.2.3 Radiometric Correction 42
3.2.4 Geometric Correction/Temporal Registration 43
3.2.5 Resampling for Scanner Sensors 88
3.3 Return Beam Vidicon (RBV) 99
3.3.1 RBV Functional Overview 100
3.3.2 Radiometric Calibration and Correction 104
3.3.3 Geometric Correction 110
3.3.4 Resampling for RBV 119
3.4 Heat Capacity Mapper Mission (HCMM) 120
3.4.1 Heat Capacity Mapper (HCM) Functional Description 121
3.4.2 HCM Phase I Processing 123
3.4.3 Radiometric Calibration Processing. . . 124
3.4.4 Radiometric Correction 128
3.4.5 Geometric Correction 133

Section		Page
3.4.6	Resampling for HCM	140
3.5	Analysis of Geometric Correction/Temporal Registration Errors	141
3.5.1	Landsat-D TM and MSS Error Analysis . .	143
3.5.2	Input and Internal Errors	145
3.6	Classification	158
3.6.1	Introduction	158
3.6.2	LACIE Overview	163
3.6.3	Classification Approaches	167
3.6.4	Baseline Classification Process	171
3.6.5	On-Board Classification Configuration Analysis	176
4	CONCLUSIONS AND RECOMMENDATIONS	209
Appendix A	TM AND MSS DATA REFORMATTING STUDY	213
Appendix B	ERROR ANALYSIS	233
Appendix C	EFFECT OF DATA STRIPING ON CLASSIFICATION ACCURACY	249
Appendix D	EFFECT OF LANDSAT ORBITAL CHARACTERISTICS ON ON-BOARD CLASSIFICATION	278

ILLUSTRATIONS

Figure		Page
1	Landsat Data Acquisition/Processing/Dissemination System	10
2	TM and MSS Data Processing Functional Flow	12
3	MSS Scanning Arrangement	15
4	MSS Data Formats	16
5	MSS Light Pipe Array and Detector Sampling Sequence	18
6	MSS-Multiplexed Data Format, 150-Word Minor Frame	18
7	Ground Scan Pattern for a Single MSS Detector	19
8	Detector Array Geometry	20
9	Thematic Mapper Multiplexed Data Format-102-Word Minor Frame	21
10	Scanner Ground Patterns	22
11	In-Flight Radiometric Calibration	24
12	Calibration Apparatus	25
13	MSS In-Flight Calibration Data for Landsats-1, -2, and -C	25
14	Nominal MSS Calibration Wedge Output	26
15	MSS-D Calibration Wedge Output	29
16	Curve Fitting of Averaged Data	31
17	Gain and Bias Determination	32
18	Window Sizes Used in Destriping Experiments	34
19	Local Averaging Method	36
20	How Histogram Equalization Works	37
21	Striping Detection Equations	39
22	Radiometric Calibration Data Flow For TM Visible Bands	40
23	Destriping Equations	41

Figure Page

24 Search Area Definition 46
25 Control Point Location 48
26 CLA Correlation Processing 49
27 Interpolation of Correlation Surface 49
28 Registration Verification 50
29 CPLBS Control Point Processing Overview 52
30 Scanning Sensor (TM & MSS) Geometric Distortions 57
31 Error Modeling Steps 58
32 Geometric Error Model Coefficient Processing 59
33 Earth-Centered Coordinates of Spacecraft Nadir 67
34 Rotation Matrixes 67
35 Earth-Centered to Tangent-Space Transformations 67
36 Effects of Attitude and Position (Ephemeris) Errors 68
37 Equivalance of Attitude and Position Errors 68
38 Image Error Effects of Attitude and Altitude Errors 68
39 Modeling Approach for Attitude/Altitude Estimates 75
40 Space-to-Space Mapping 77
41 Iterative Technique for LCC Space-to-Space Mapping 79
42 Space-to-Space Mapping Functions 79
43 Universal Transverse Mercator Projection 81
44 Polar Stereographic Projection 82
45 Space Oblique Mercator Projection 83
46 Lambert Conformal Conic Projection 85
47 Output Space Grid Point Locations 86
48 Input Space Grid Point Locations 87

Figure		Page
49	Locating Output Points in Output Space	88
50	Nearest Neighbor Assignment	90
51	Resampling Model for Cubic Convolution	91
52	Cubic Convolution Resampling Scheme	92
53	Cubic Convolution Interpolation	93
54	Initial Position of Output Column at Different Points	95
55	Output Columns Process at Different Rates	95
56	Horizontal Resampling	97
57	Vertical Resampling	98
58	One RBV Scene Consists of Four Subframes	101
59	Input and Output Data Arrays	102
60	RBV Functional Processing Overview	103
61	Preprocessing of Hovis Sphere Data	105
62	Zoning the Image	105
63	Horizontally Zoning the RBV Image	107
64	Calibration Lamp Image Processing	108
65	Radiometric Correction Coefficient Application	109
66	Geometric Correction	111
67	Shape and Size of Reseau Within the Search Area	112
68	Typical Set of Row or Column Sums	113
69	Geometric Error Modeling	118
70	Alternative Attitude Determination Procedure	118
71	Functional Diagram of HCMM Data Processing System	122
72	HCMM Functional Flow	123
73	Radiometric Calibration Inputs	125
74	Channel 1 Radiometric Calibration (Sheet 1 of 2)	126
75	Channel 2 Radiometric Calibration (Sheet 1 of 4)	129

Figure Page

76 Radiometric Correction Process 133
77 Space-to-Space Mapping Coordinate Frames 136
78 Tangent Cylinder Coordinates 137
79 HOM Coordinates 139
80 Overview of Geometric Correction Process 141
81 MSS Precision Processing: Error Analysis of Geometric Correction 144
82 TM and MSS Precision Processing: Geometric Correction 146
83 Grid at Which Image Errors Are Computed 147
84 Maximum Error (Meters) Over 90 Percent Grid vs. Number of GCPs 151
85 RBV Precision Processing-Error Analysis of Geometric Correction 153
86 RBV Precision Processing-Geometric Correction 155
87 Typical Spectral Signatures for Wheat 161
88 Variation of Spectral Response for Various Biological Materials 162
89 LACIE Overview 164
90 Processing Functions for Multispectral Classification 172
91 Configuration 1a--Function Data Flow 181
92 Configuration 1b--Functional Data Flow 186
93 Configuration 2--Functional Data Flow 188
94 Configuration 3a--Functional Data Flow 193
95 Configuration 4--Functional Data Flow 196
96 Configuration 4b--Functional Data Flow 199
97 Configuration 5--Functional Data Flow 201
98 Configuration 6--Functional Data Flow 204
99 Configuration 7--Functional Data Flow 205

Figure Page

100 Configuration 8--Functional Data Flow 206

101 TM Sensor Data Flow 214

102 MSS Sensor Data Flow 216

103 Landsat-1, -2 and -C Light Pipe Array and Detector Sampling Sequence 217

104 Detector Sampling Sequence and Spatial Relationship 219

105 Comparison of MSS and TM Ground Coverage Successive Signs 220

106 MSS Multiplexed Data Format, 150-Word Minor Frame 221

107 Thematic Mapper Multiplexed Data Format - 102-Word Minor Frame 222

108 MSS Data Flow (Sheet 1 of 2) 224

109 MSS Sensor Output Format 226

110 MSS BIL Reformatted Output 227

111 MSS BIP Input to Classification 228

112 MSS Data Flow for Sensor Radiometrically Corrected Data 229

113 MSS Sensor Output Format 229

114 TM Data Flow (Sheet 1 of 2) 231

115 Error Grid Points 238

116 Ground Coverage Pattern 281

117 Typical Landsat-D Ground Trace and GMT 281

118 In-Track Picture Scheduling 282

119 Imagery Along-Track Overlap/Sidelap at Equator 282

120 Landsat Sidelapping Coverage 284

121 Ground Coverage Pattern 284

122 Daily Ground Trace (Daylight Passes Only) for Landsats-1, -2, and -C 286

Figure Page

123 Imagery Sidelap at the Equator 287

124 Landsat Sidelapping Coverage 287

125 TDRSS/GSTDN Visibility Limits 289

126 TDRSS Coverage Zones 289

TABLES

Table		Page
1	Scanner Characteristics	3
2	Comparison of Landsat-C/RBV with Landsat-1 and -2/RBV	3
3	Characteristics of Landsat Family	7
4	Destriping Algorithms Considered	34
5	Mean and Standard Deviation Equalization Equations	35
6	Summary of Destriping Test Results	39
7	TM Error Sources	56
8	MSS Error Sources	56
9	Attitude/Altitude Error Modeling Approaches Comparison	69
10	Comparison of Landsat-C/RBV with Landsat-1 and-2/RBV	99
11	Input Errors, Meters (1 Sigma)	143
12	Unmodeled Errors (Meters)	148
13	Internal Error Sources Checked	148
14	GCP Location Error (Meters)	149
15	Interpolation and Resampling Error (Meters)	149
16	Predicted Total Image Error, Pixels	151
17	Input Errors (Meters) (1 Sigma)	152
18	Internal Error Sources	156
19	GCP Location Errors (Meters)	157
20	Predicted Total Image Error, Pixels	157
21	Similarity Functions and Statistical Implications	169
22	Processing Times for Various Similarity Functions	169
23	Sensor Parameters of the Landsat-C	174
24	Processing Requirements	174

Table Page

25 Processing Functions Computed On-Board or at Ground 175
26 On-Board Configuration Comparisons 177
27 Numerical Values for Light Pipe Array and Detector Sampling Sequence 218
28 Coordinates of Error Grid Points 239
29 Maximum Error Over 90 Percent Grid 242
30 Error Source Values for the Simulation 243
31 Proportion Estimates Obtained From Classification of the Three Images 253
32 Proportion Estimates for Image NASACAL Under Two Threshold Settings 253
33 Average (Over Six Sensors) Gain a_k and b_k 257
34 Channel Means As Computed in ERMAN II and from Equation 40 257
35 Landsat Series Orbit Parameters 279
36 Coverage Redundancy Due to Imagery Sidelap 283
37 Coverage Redundancy Due to Imagery Sidelap 287

GLOSSARY OF SYMBOLS

G_0 = the longitude of the nadir in radians

H_0 = nominal spacecraft altitude in meters

$H_M(t)$ = measured altitude as a function of time

I_S = the nominal number of samples per input line

K_{EC} = the earth-curvature and panoramic-projection constant

K_{IL} = the nominal across-scan intersample distance in meters

K_{IS} = the nominal along-scan intersample distance in meters

K_{SS} = scan-skew constant

K_0, K_1, K_2, K_3, K_4 = parameters of the along-scan mirror model (for MSS, $K_4=0$)

LAT = the geodetic latitude of the approximate format center

LC_0 = the geocentric latitude of the nadir in radians

LG_0 = the geodetic latitude of the nadir in radians

L_{nadir} = the line coordinate of the spacecraft nadir

LONG = the longitude of the approximate format center

L_0, L_1, L_2, L_3 = parameters of the across-scan mirror model for Thematic Mapper

N = the number of detectors in one band

R_0 = radius of the earth at the nadir

S = the sample coordinate of a point in input space

T = the time associated with a point in tangent space

T_{ER} = time at which a point in the input space was imaged

T_M = time for an active mirror sweep

T_S = time between mirror sweeps

V_{RA} = the velocity (in the along-track direction) of a point on the earth due to earth rotation

V_{RAn} = V_{RA} for the Flight Segment nadir

V_{RC} = the velocity (in the across-track direction) of a point on the earth due to earth rotation

V_{RCn} = V_{RC} for the Flight Segment nadir

W_s = nominal swath width in meters

X_E, Y_E, Z_E = the earth-centered coordinates of a GCP

X_{FC}, Y_{FC} = tangent space coordinates of the approximate input format center

XNFC, YNFC = output image coordinates of the WRS format center in pixels

X_T, Y_T, Z_T = tangent space coordinates of a control point

X_O, Y_O, Z_O = earth-centered coordinates of nadir

β = the spacecraft heading associated with the nadir in radians

β_{mm} = maximum mirror angle in radians

$\Delta H(t)$ = altitude error model

$\Delta H_E(t)$ = error in measured altitude errors as a function of time

$\frac{\Delta V}{V}$ = the normalized spacecraft velocity error

δ_{AT} = along-track ephemeris error

δ_{CT} = cross-track ephemeris error

$\theta(t)$ = pitch model

$\theta_E(t)$ = pitch measurement error as a function of time

$\theta_M(t)$ = measured pitch as a function of time

$\phi(t)$ = roll model

$\phi_E(t)$ = roll measurement error as a function of time

$\phi_M(t)$ = measured roll as a functional time

$\psi(t)$ = yaw model

$\psi_E(t)$ = yaw measurement error as a function of time

$\psi_M(t)$ = measured yaw as a function of time

Section 1

SUMMARY

This study sought to establish the factors relating to on-board multispectral classification. The study was conducted in two parts. Part 1 reviews the functions implemented in ground-based image processing systems for current earth observation sensors. The sensors reviewed were the Multispectral Scanner (MSS), Thematic Mapper (TM), Return Beam Vidicon (RBV), and Heat Capacity Mapper (HCM). The functions required to produce imagery from each of these sensors are described in detail as implemented by the Master Data Processor (MDP). The MDP represents the first production system built for image processing. The MDP is installed and operating at the Goddard Space Flight Center (GSFC) in Greenbelt, Md.

Part 2 of this study reviews the concept of classification and conceptually extends the ground-based image processing functions, discussed in Part 1, to an on-board system capable of multispectral classification. Eight separate on-board configurations, with varying amounts of ground-spacecraft interaction, were evaluated. As a result of this evaluation, it is recommended that additional studies be undertaken to define the ground-space interface necessary for accomplishing on-board classification. Until this interface is better defined, classification can be best performed on the ground. The conditioning and selection of the image data to be classified can, however, be accommodated by the on-board system.

As a result of this study, it is recommended that a criteria be developed for extracting sample segments of interest and that these data be further screened to select only those with an acceptable amount of cloud cover (less than 50 percent). This would reduce the amount of downlinked data and provide a faster turnaround time.

Section 2

INTRODUCTION

This report investigated the factors relating to on-board multispectral classification. A concise summary of the principal data characteristics, significant error sources, and end-to-end information flow for contemporary sensor programs, such as Multispectral Scanner (MSS), Thematic Mapper (TM), Return Beam Vidicon (RBV), and Heat Capacity Mapper (HCM), will be assessed as an integrated system to support ground-based, image-driven processes such as classification and to satisfy user requirements. Conceptual extensions of these functions to the spacecraft will be formulated as a planning aid to NASA. Thus, the study will extend the ground-based image data handling requirements of current earth observation systems to on-board implementations. Tables 1 and 2 summarize the scanning and RBV sensor characteristics.

2.1 BACKGROUND

The Landsat satellite series is a research series of spaceborne remote sensors whose purpose is to test the feasibility of remote sensing and assess the economic benefits derived from remote sensing. In July 1972, NASA launched the first Earth Resources Technology Satellite (ERTS-1), since renamed Landsat-1, and a second satellite Landsat-2 was launched in January 1975. Landsat-1 and -2 carried two kinds of sensors to detect and record sunlight reflected from the earth's surface in specific spectral bands: the Return Beam Vidicon (RBV) and the Multispectral Scanner (MSS). The RBV camera system consists of three independent television cameras, each sensing a different spectral band in the range of 0.43 to 0.83 μm, while viewing the same 185 by 185 km ground area. The RBV uses conventional lenses and shutters and vidicon for image scanning and storing prior to transmission of the image data to ground stations.

The Multispectral Scanner consists of an oscillation mirror and an optical system that reflects and directs scene radiance into a solid-state detector array. The oscillating mirror continually scans a 185-km swath in a direction perpendicular to the spacecraft orbital track, while spacecraft motion pro-

Table 1. Scanner Characteristics

	MSS	TM	HCM
Function	Landsat-C	Landsat-D	
Instantaneous Field of View	0.086	0.0426	0.83
Mirror Scan Rate (Hz)	13.62	7.12	14
Scan Lines/Oscillation	6	16	1
Field of View (Scene) (Km)	185	185	700
Spectral Band Range (m)	4 0.5-0.6	0.45-0.5	Thermal IR. 10.5-12.5
	5 0.6-0.7	0.52-0.6	Visible 0.5-1.1
	6 0.7-0.8	0.63-0.68	
	7 0.8-1.1	0.76-0.90	
	8 10.4-12.6	1.55-1.75	
		10.4-12.5	
Sampling Interval (sec)	9.95	9.75	9.2
Sample Word Length, Input/Output (Bits)	6/7	8/8	8/8
Samples per Line	2340	6167	1500
Lines per Band	2340	6167	1500
Scan Period (msec)	73.42	140.49	71.43
Samples/Res. Element	1.4	1	1
Active Scan (msec)	33	59.7	32.6
Information/Band (Bits)	$.46 \times 10^8$	$.3 \times 10^9$	18×10^6 1/
Information/Sc (bits)	2.3×10^8 2/	1.9×10^9	36×10^6 1/
Number of Detectors	26	100	2
Spatial Resolution (m)	79	30	500

1/ Daytime only

2/ Full bands

Table 2. Comparison of Landsat-C/RBV with Landsat-1 and -2/RBV

Item	Landsat 1 and 2	Landsat-C
Number of Cameras	Three	Two
Ground Coverage/Frame	185x185 km	183x98 km
Ground Coverage/Camera	185x185 km	98x98 km (nom)
Spectral Coverage	Camera 1: 475-575 mu Camera 2: 580-680 mu Camera 3: 690-830 mu	Each Camera 505-750 mu
Readout	Staggered for 2 Cameras	Staggered for 2 Cameras
Nominal Exposure Time	12 ms	5.6 ms
Cycle Time	25 sec	12.5 sec
Video Bandwidth	3.2 MHz	3.2 MHz
Realtime (Total)	3.5 sec	3.5

vides the along-track sweep. Six scan lines are simultaneously swept in each spectral band with one mirror oscillation. The detectors subtend an instantaneous field of view (IFOV) on the ground 79 meters on a side; their outputs are in digital form for transmission to ground stations. Four spectral bands are covered: 0.5 to 0.6, 0.6 to 0.7, 0.7 to 0.8, and 0.8 to 1.1 μm.

A third satellite, Landsat-C, was launched March 1978. Landsat-C carries a five-band MSS, a two-camera high-resolution RBV system, and uses an improved digital ground system, the Master Data Processor (MDP). The fifth MSS band is in the far infrared covering 0.4 to 12.6 μm and has a 240-meter resolution compared to 80 meters for the other bands. The RBV system for Landsat-C contains two identical cameras that operate in the spectral band 0.50 to 0.75 μm, with a factor of two improvement in ground resolution (40 meters). The two cameras are aligned to view adjacent nominal 98 km square ground scenes with a 14 km overlap, yielding a 183 x 98 km scene pair. Two successive scene pairs will nominally overlap each MSS frame.

A number of cost benefits have already accrued from Landsats-1, -2, and-C in such diverse applications as:

a. Mapping agricultural land use

b. Monitoring worldwide food productivity

c. Monitoring rangeland

d. Surveying forest resources

e. Managing critical watersheds

f. Detecting land use changes

g. Oil/mineral explorations.

The success of the Landsat series has generated a desire for even better spatial and spectral resolution leading to Landsat-D.

Landsat-D is scheduled for a March 1981 launch. This spacecraft will be based on NASA's new Multimission Modular Spacecraft (MMS) and will carry a Thematic Mapper (TM), and a Multispectral Scanner (MSS).

The MSS will be the same sensor as that carried on Landsat-C. The TM represents an evolutionary improvement of the MSS and provides several significant capabilities. The spatial resolution on the ground has been reduced to 30 meters (compared to 80 meters for the MSS) allowing radiances to be measured for areas (pixels) less than one-sixth the size of the MSS. The TM will incorporate six spectral bands (with the capability for a seventh) sensitive to wavelengths in the 0.45 to 1.75 μm (not including the 10.4 to 12.5 μm thermal band). The TM consists of an oscillating mirror and optical system (similar to MSS), with improved radiometric sensitivity. The sensitivity has been improved by reducing the signal-to-noise characteristic of the solid-state detector array and increasing the levels of digital quantization. Sixteen scan lines are simultaneously swept in each spectral band with one mirror oscillation. The detectors subtend an instantaneous field of view on the ground, 30m on a side, with their outputs in digital form for transmission to ground stations.

Heat Capacity Mapper Mission (HCMM) is the first of a series of low-cost, modular-design spacecraft built for the Applications Explorer Missions (AEM). This mission was designed to allow scientists to determine the feasibility of using day-night thermal infrared remote sensor-derived data for:

a. Discrimination of various rock types and possibly locating mineral resources

b. Measuring and monitoring surface soil moisture changes

c. Measuring plant canopy temperatures at frequent intervals to determine transpiration of water and plant stress

d. Measuring urban heat islands

e. Mapping surface temperature changes on land and water bodies

f. Deriving information from snow fields for water runoff prediction.

HCMM data will be correlated with data received from other satellites, especially Landsat, and with ground observations, to provide a better insight into detecting temporal temperature variations of the earth's surface. The AEM-A (HCMM) was successfully launched April 25, 1978 and is currently providing valuable information.

The orbit for the HCMM will permit the measurement of near maximum and minimum surface temperatures occurring during the diurnal cycle which is about 11:30 p.m. and 2:30 a.m. in the middle northern latitudes. From the nominal orbit altitude of 620 km (385 mi.), the spatial resolution of the visible and thermal infrared radiometer channels will be approximately 500 by 500 meters. The ground swath of data coverage along the track will be 700 km wide.

The nearly polar sun synchronous HCMM orbit will cover every area of the earth's surface between 85 degrees north latitude and 85 degrees south at least once during the day and once during the night within a 16-day interval. Both day and night passes over selected areas within 12 hours will repeat at 5- or 16-day intervals, depending on the latitudes of the areas. The areas between 20 degrees and 32 degrees latitude (north and south) will receive only 36-hour day/night coverage.

Table 3 summarizes the characteristics of the Landsat family and HCMM.

Table 3. Characteristics of Landsat Family

	Landsat-1 and -2	Landsat-C	Landsat-D	HCMM
Number of bands	4	5	6 or 7	2
Resolution, m	80 (MSS) 80 (RBV)	80 (MSS) 40 (RBV)	30 (TM) 80 (MSS)	500
Data availability	NA	NA	2-4 days	NA
Global coverage, days				
One satellite	18	18	16	5-16*
Two satellites	9	9	8	NA
Pointing accuracy, deg	0.7	0.7	0.01	±1(P,R),±2(Y)
RMS pointing rate, deg/sec	0.002	0.002	(10^{-6})	.01
Design life, years	1	1	3	1

*Depends on latitude

The sensors currently aboard spacecraft for earth resources survey permit large portions of the earth to be sensed rapidly. These multispectral scanners have fine spectral and spatial resolution with typical average data rates from 10 to 100 megabits/sec. Clearly, there is a need for processing scanner data aboard a spacecraft as a means of reducing the peak and average loads of data to be transmitted to the ground; the data storage requirements on the ground; and also the number, size, and cost of processing systems on the ground.

Most of this past effort in the field of earth resources data processing has been research oriented. Earth resources imagery has been provided by NASA to a number of researchers who have processed the data in various ways to determine what, if any, useful information could be extracted from the given images. These experiments have demonstrated that useful information can indeed be extracted from the multispectral scanner imagery of the earth's surface, but only as an after-the-fact analysis. The present minimum time from the acquisition of data in the United States, of the United States, to the delivery of that data to an investigator is about 3 weeks. The same minimum time, where the data is to be purchased from the EROS Data Center in Sioux Falls rather than be shipped to the investigator by NASA, is on the order of 2 months. This turnaround time has had a serious impact on the experimental program in NASA, especially agricultural investigations where the desirable time from acquisition to delivery to the analyst is 24 hours.

Due to the much higher sensor data rates and need for faster data turnaround, it is anticipated that during the 1980-1990 decade earth resources spacecraft will be designed and flown for specific purposes, i.e., to monitor severe weather systems, to monitor water pollution, to survey and monitor world food production, etc. In these applications it may be more cost-effective to process the data on-board the spacecraft and transmit the data products directly to the users rather than transmit the raw data to a ground processing station for generating the data products and then distributing the data products to the users via another spacecraft system.

This report reviews the current ground processing approach implemented by NASA for generating user desired data products. The functions now implemented at the ground and required for conditioning image data such that the data can be accurately classified is assessed relative to an on-board processing system. On-board processing configurations are presented and compared.

2.2 SCOPE

Subsection 3.1 is a general overview of Landsat image processing currently performed by NASA. Subsection 3.2 outlines the functional data flow for the TM and MSS scanning sensors as implemented by an MDP-like processing configuration for Landsat-D. Subsections 3.3 and 3.4 describe the functional data flow for the RBV and HCM sensors as implemented by the MDP. Subsection 3.5 is an analysis of the expected geometric correction/temporal registration errors for the TM, MSS, and RBV sensors. Subsection 3.6 outlines the problems associated with classifying image data and presents and analyzes eight on-board processing configurations, each implementing classification with varying degrees of complexity and accuracy. Section 4 presents the conclusions and recommendations of the study. Appendixes A through D document supporting studies used to analyze the eight on-board configurations of subsection 3.6.

The author acknowledges the contribution of Mr. Jerome Shipman of IBM for the preparation of Appendixes B and C. In addition, Charlene Jones contributed to Appendix B by developing the APL simulation of the error analysis. Special thanks go to Mr. Ralph Bernstein, Mr. Dal Ferneyhough, Jr., Mr. Kim Seward, and Mr. George Brechling of IBM-Gaithersburg FSD as well as Mr. Stan Wheeler of IBM-Houston FSD for their helpful suggestions and productive discussions.

This contract was monitored by Dr. Harry F. Benz of NASA-Langley. The author wishes to thank him as well as Mr. William M. Howle and Mr. Charles Husson, also of NASA-Langley, for their guidance and support during this contract.

Section 3

DIGITAL IMAGE PROCESSING OF EARTH OBSERVATION SENSOR DATA

3.1 GENERAL OVERVIEW

A proper understanding of the Landsat image processing functions currently performed by NASA is necessary background information for properly assessing those functions capable of on-board implementation. Figure 1 illustrates the current Landsat data acquisition/processing/dissemination system. The ground receiving site equipment accepts the wideband video data from the Landsat spacecraft, decodes, formats, and records it onto wideband video tapes (WBVT) for transmission to Goddard Space Flight Center (GSFC) at Greenbelt, Maryland.

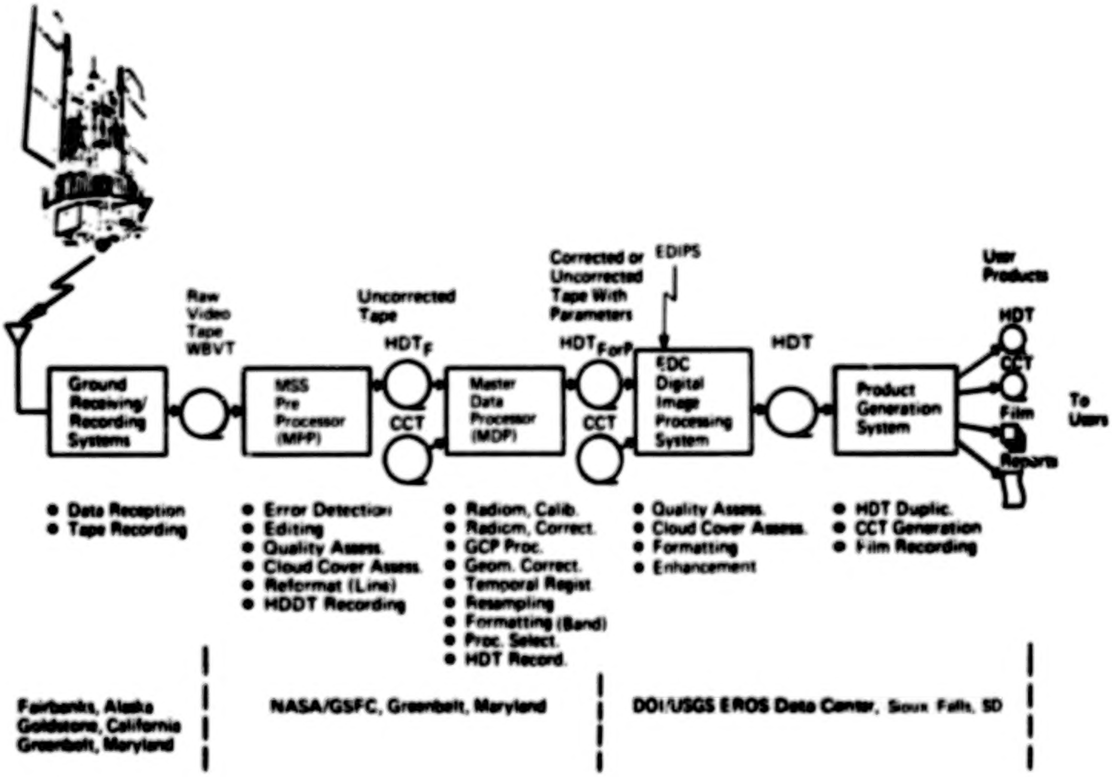
Raw Video Tape WBVT
Uncorrected Tape
Corrected or Uncorrected Tape With Parameters
EDIPS
User Products
Ground Receiving/ Recording Systems
HDT_F
CCT
MSS Pre Processor (MPP)
Master Data Processor (MDP)
HDT_ForP
CCT
EDC Digital Image Processing System
HDT
Product Generation System
HDT
CCT
Film
Reports
To Users
● Data Reception
● Tape Recording
● Error Detection
● Editing
● Quality Assess.
● Cloud Cover Assess.
● Reformat (Line)
● HDDT Recording
● Radiom. Calib.
● Radiom. Correct.
● GCP Proc.
● Geom. Correct.
● Temporal Regist.
● Resampling
● Formatting (Band)
● Proc. Select.
● HDT Record.
● Quality Assess.
● Cloud Cover Assess.
● Formatting
● Enhancement
● HDT Duplic.
● CCT Generation
● Film Recording
Fairbanks, Alaska
Goldstone, California
Greenbelt, Maryland
NASA/GSFC, Greenbelt, Maryland
DOI/USGS EROS Data Center, Sioux Falls, SD

Figure 1. Landsat Data Acquisition/Processing/Dissemination System.

The wideband video data is processed within the Image Processing Facility (IPF) at Goddard. The IPF uses two subsystems for processing MSS data: MSS Preprocessor (MPP), and Master Data Processor (MDP). The MPP performs a quality screening and assessment of the MSS WBVT. Other functions performed include: a display of any selected band of MSS data to perform cloud cover assessment, reformatting of the sensor data from band-interleaved-by-pixel (BIP) to band-interleaved-by-line (BIL), and recording of selected scenes on high-density tape (HDT_F). Radiometric calibration data are also extracted and recorded on the HDT_F but not applied to the data. The MDP radiometrically and geometrically corrects Landsat image data and generates two types of HDTs: the fully corrected (radiometrically and geometrically) high-density digital tapes (HDT_P); and a standard uncorrected high-density tape (HDT_A) with radiometric corrections applied and geometric error coefficients added to the header but not applied to the data. Ancillary data necessary for correcting the image data will be input on computer compatible tape (CCTs).

The MDP output data tapes will be supplied to the EROS Data Center (EDC) at Sioux Falls, South Dakota, for product dissemination to various users. The primary functions of the EDC are data storage, reproduction, dissemination, and user assistance and training. User products include HDT, CCT, film, and reports.

The remainder of this section will describe in more detail functions as implemented within the MDP. The MSS, Return Beam Vidicon (RBV), and Heat Capacity Mapper (HCM) are currently implemented by the MDP. The Thematic Mapper (TM) will not be implemented by the MDP; however, the processing of TM data will be described relative to the procedures currently used for processing MSS data.

3.2 MSS AND TM FUNCTIONAL DESCRIPTION

Figure 2 illustrates the data processing functional flow for the TM and MSS sensors as envisioned for Landsat-D. The functions to be described are currently being implemented by the MDP for the MSS.

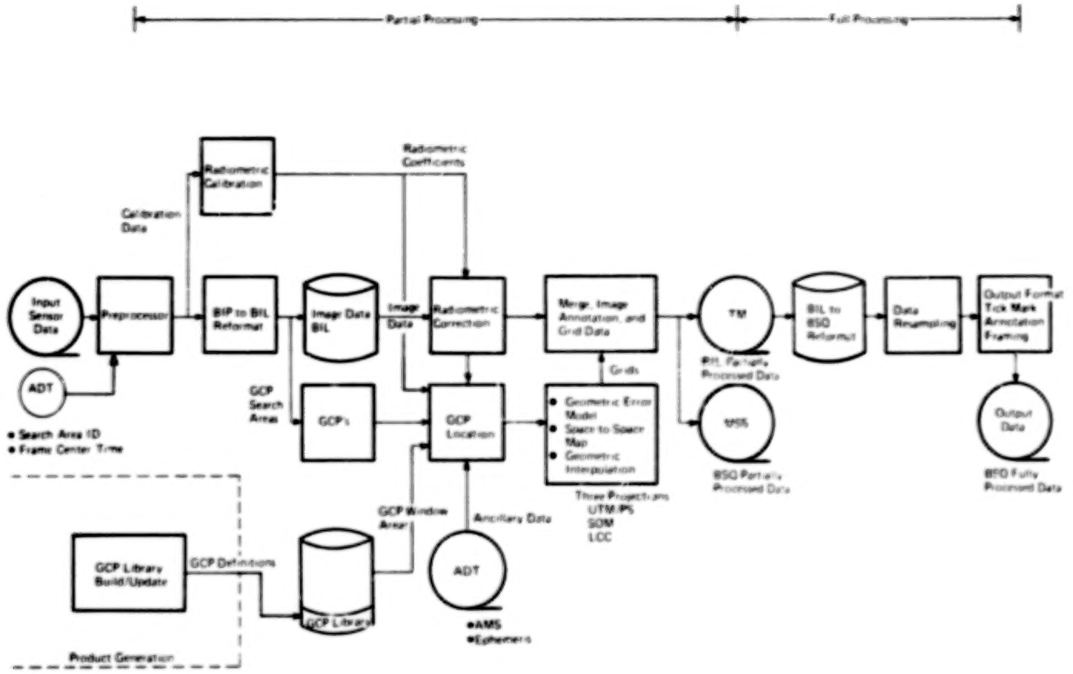
Partial Processing
Full Processing
Input Sensor Data
Preprocessor
ADT
• Search Area ID
• Frame Center Time
Calibration Data
Radiometric Calibration
Radiometric Coefficients
BIP to BIL Reformat
Image Data BIL
Image Data
Radiometric Correction
GCP Search Areas
GCP's
GCP Location
GCP Window Areas
Ancillary Data
ADT
•AMS
•Ephemeris
GCP Library Build/Update
GCP Definitions
GCP Library
Product Generation
Merge, Image Annotation, and Grid Data
Grids
• Geometric Error Model
• Space to Space Map
• Geometric Interpolation
Three Projections
UTM/PS
SOM
LCC
TM
BIL Partially Processed Data
MSS
BSQ Partially Processed Data
BIL to BSQ Reformat
Data Resampling
Output Format Tick Mark Annotation Framing
Output Data
BSQ Fully Processed Data

Figure 2. TM and MSS Data Processing Functional Flow.

Functions unique to the TM will be described relative to implementation by the MDP.

Whereas the sensor data from Landsats-1, -2, and -C were processed by two separate subsystems, the MPP and the MDP, the processing of Landsat-D sensor data will combine these two subsystems into one.

As shown in Figure 2, sensor data is read from HDT, reformatted (BIP to BIL for TM; BIP to BSQ for MSS), and stored on disk. As the data is being reformatted, selected data segments are extracted by the preprocessor for cloud cover evaluation and data quality assessment. Because this information must be appended at the front of a scene (prior to the image data), the disk storage provides a time latency to allow the computation of this appended information.

MICROFILMED FROM
BEST AVAILABLE COPY

Ancillary data necessary for radiometrically and geometrically correcting the image data includes the following:

a. Tracking station ephemeris and spacecraft performance data at specified time intervals contained on the Ancillary Data Tape (ADT).

b. Calibration, quality, line length, and spacecraft time (scan line identification) data contained on the image data tape.

c. Geodetic and relative control point data from a Control Point Library.

d. World Reference System (WRS) frame parameters including output projection parameters, and related tick marks.

Radiometric calibration data is extracted from the incoming data, stored, and processed to generate the coefficients required for radiometric correction of the image data. Ground Control Point (GCP) search areas (subimage areas known to contain GCPs) are extracted from the reformatted image data and stored. These search areas are then correlated with the GCP window area (digital images of the GCP) taken from the GCP library (stored on disk) built from previous coverage of the ground area in question. Prior to the correlation, the search area image data will be radiometrically corrected and adjusted for high-frequency effects (line length and earth rotation). Note that the process of locating search areas within the image data (GCP processing) cannot begin until radiometric coefficients are available.

The computed GCP locations and ancillary data from the ADT are inputs to the Geometric Error Modeling (GEM). The GEM (using Ground Control

Point locations) provides the attitude and altitude coefficients to map the image data from input space to output space. Space-to-Space Mapping uses the accurate input-to-output space transformation from GEM in conjunction with an implicit output-to-input space transformation (dependent on the map projection) to produce an accurate, explicit transformation of output space to input space. The Geometric Interpolation takes the matrix grid of points from Space-to-Space Mapping and interpolates between them to provide inputs for resampling. These grid points will be computed on a scene-by-scene basis, necessitating at least a one-scene delay between input from the processor and output to tape.

The resampling grids, assessment of scene cloud cover, and scene quality will be output to tape prior to the radiometrically corrected image data. After ancillary data to tape is written, the reformatted image data is read from disk, radiometrically corrected using the computed ratiometric calibration coefficients, and written to tape. This merged ancillary and image data represents the partially processed output. Scenes are read from the HDT containing the partially processed image data, reformatted from BIL to BSQ, and stored on disk. A minimum of one scene will be output to disk prior to resampling. The image data is then read from disk and resampled. The resampled image data is merged with the tick mark and annotation data and written to an HDT as the fully processed output.

Each of the functions shown in Figure 2 (excluding preprocessing functions) will be described in greater detail in the following sections.

3.2.1 Data Reformatting

As the scanning sensor orbits the earth, it scans the ground in swaths perpendicular to the direction of the spacecraft track as shown in Figure 3 for the MSS. The scan rate is determined from the velocity of the subsatellite ground point, IFOV size, and number of ground lines imaged each scan of the scanning mechanism. From this scan rate, the width of the swath scanned in the cross-track direction, IFOV size, and scanner efficiency--the "dwell time" of each IFOV is determined. The dwell time represents the maximum permissible time between successive samples of the sensors.

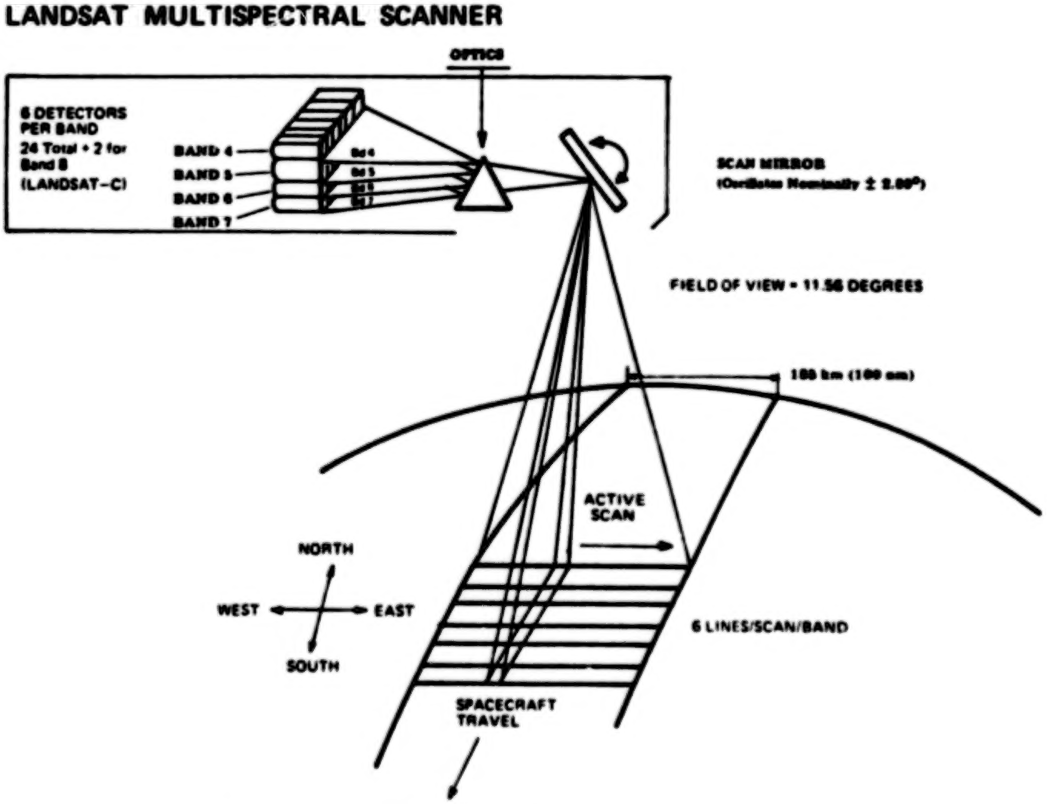
LANDSAT MULTISPECTRAL SCANNER
OPTICS
6 DETECTORS PER BAND
24 Total + 2 for Band 8 (LANDSAT-C)
BAND 4
BAND 5
BAND 6
BAND 7
Bd 4
Bd 5
Bd 6
Bd 7
SCAN MIRROR (Oscillates Nominally ± 2.89°)
FIELD OF VIEW = 11.56 DEGREES
185 km (100 nm)
ACTIVE SCAN
NORTH
WEST
EAST
SOUTH
6 LINES/SCAN/BAND
SPACECRAFT TRAVEL

Figure 3. MSS Scanning Arrangement.

Each sample must be sampled once per dwell time (more if any over-sampling is required), and the resulting data formatted for ground transmission along with synchronization, telemetry, and any required overhead information. These data are downlinked to the ground and recorded on high-density tape (HDT) at a bit rate determined by the previous parameters.

These data are read into the ground processing system at a rate compatible with the available processing time. This rate will be considerably less than the realtime rate. Keep in mind that for onboard processing the data must be either processed or stored at the rate the sensor is creating data.

The downlink data are in a band-interleaved-by-pixel (BIP) format as sampled on board the spacecraft. Depending upon the output product, the data is reformatted to either band-interleaved-by-line (BIL) format or the band sequential (BSQ) format. Examples of these formats for the MSS are shown in Figure 4.

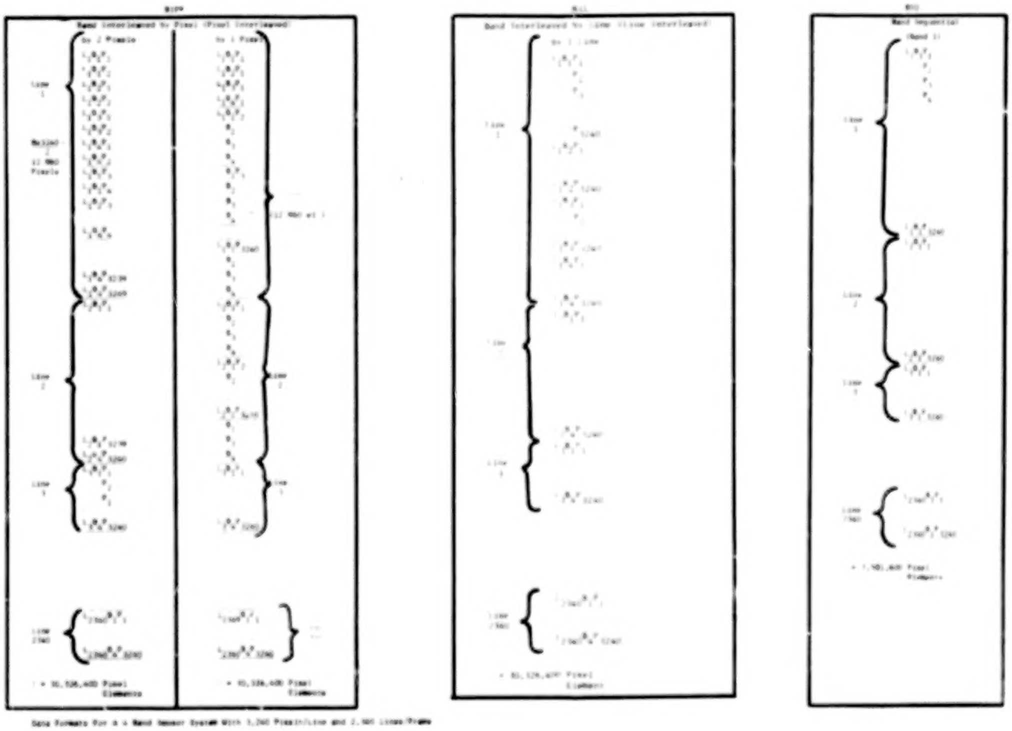
Band Interleaved by Pixel (Pixel Interleaved)
Band Interleaved by Line (Line Interleaved)
Band Sequential
(Band 1)

Figure 4. MSS Data Formats.

MICROFILMED FROM
BEST AVAILABLE COPY

Currently, the input image data to the MDP for MSS processing consists of either unprocessed image data in a BIL format or partially processed image data (pixels radiometrically corrected only) in a BSQ format. The BIP to BIL reformatting is accomplished in the MSS preprocessor (MPP). Output image data from the MDP (partially processed and fully processed) are in BSQ format.

The processing system for Landsat-D will combine the current preprocessor and MDP functions. The reformatting function is, therefore, dependent upon the sampling sequence utilized for the two scanning sensors-TM and MSS. The following two subsections will describe the processes involved in reformatting (BIP to BIL) the TM and MSS sensors.

3.2.1.1 MSS Data Reformatting

Image data from the MSS sensor is sampled as shown in Figure 5. The reflected energy for the four visible bands is incident on six detectors per band (A through F), while in band 8 (not shown), the emitted energy is incident on two detectors. As shown, the physical dimensions of the light pipe array represent a spatial misregistration between bands that must be accounted for during the processing of the data by the MDP. Within a spectral band, there is also a time delay between the outputs of detector A and F due to sequentially sampling the detectors. This is also accounted for by the MDP. These 26 channels are input to a multiplexer which samples, A/D converts, and multiplexes these data in a serial digital stream together with sync, time code, and internal calibration data. The MSS multiplexer data format is shown in Figure 6. These data are formatted into minor frames as shown with the minor frame sync and sensors 25 and 26 sequentially sampled and mixed into the 25th channel. Each minor frame consists of 150 bytes (25 samples x 6 pixels/sample x 1 byte/pixel)

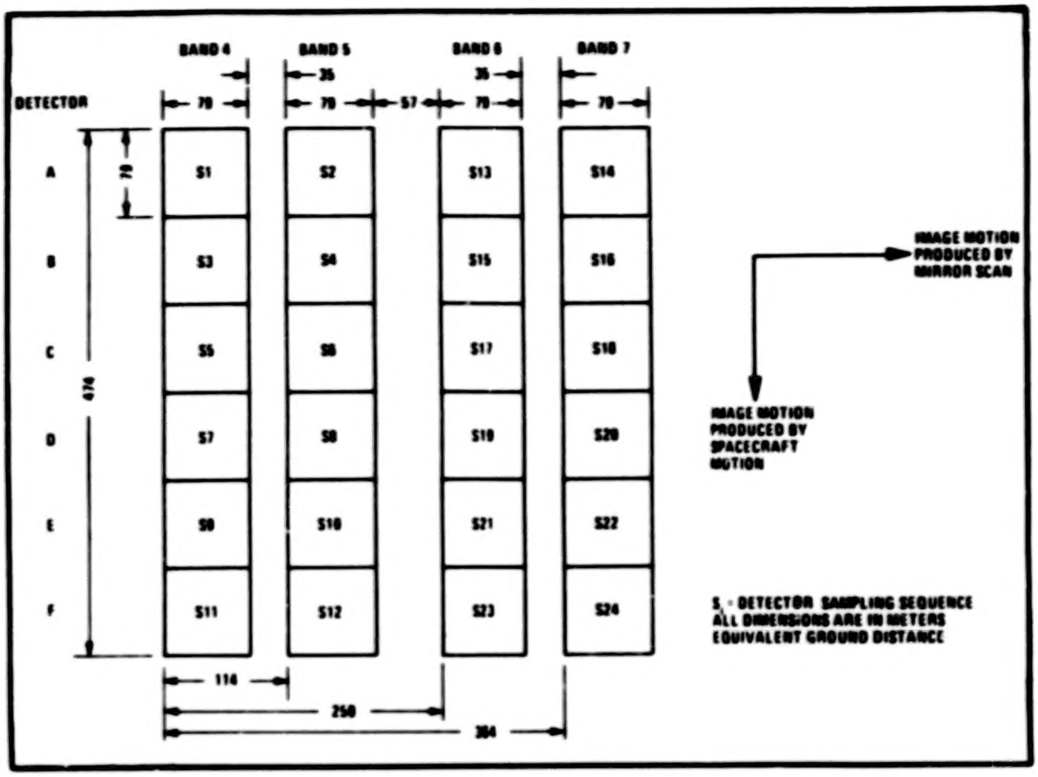
BAND 4
BAND 5
BAND 6
BAND 7
35
35
DETECTOR
79
79
57
79
79
A
B
C
D
E
F
79
474
S1
S2
S13
S14
S3
S4
S15
S16
S5
S6
S17
S18
S7
S8
S19
S20
S9
S10
S21
S22
S11
S12
S23
S24
IMAGE MOTION PRODUCED BY MIRROR SCAN
IMAGE MOTION PRODUCED BY SPACECRAFT MOTION
S = DETECTOR SAMPLING SEQUENCE
ALL DIMENSIONS ARE IN METERS EQUIVALENT GROUND DISTANCE
114
250
384

Figure 5. MSS Light Pipe Array and Detector Sampling Sequence.

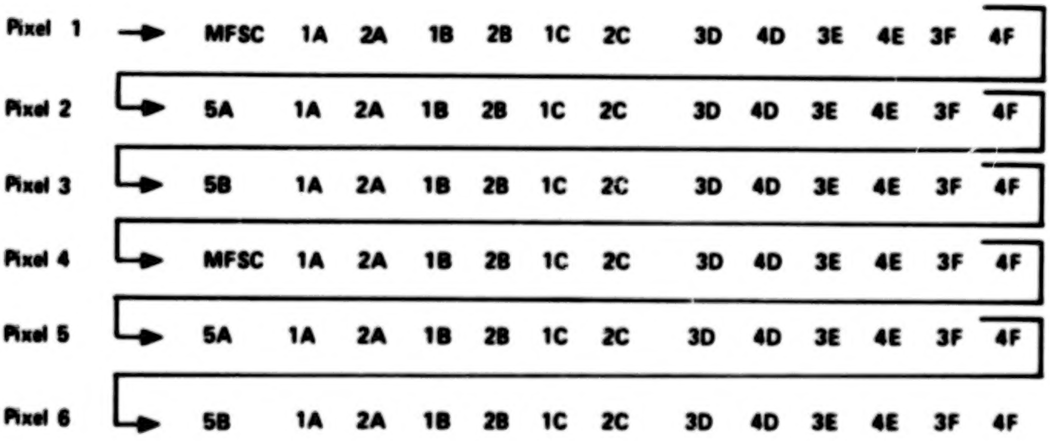

Pixel 1	MFSC	1A	2A	1B	2B	1C	2C	3D	4D	3E	4E	3F	4F
Pixel 2	5A	1A	2A	1B	2B	1C	2C	3D	4D	3E	4E	3F	4F
Pixel 3	5B	1A	2A	1B	2B	1C	2C	3D	4D	3E	4E	3F	4F
Pixel 4	MFSC	1A	2A	1B	2B	1C	2C	3D	4D	3E	4E	3F	4F
Pixel 5	5A	1A	2A	1B	2B	1C	2C	3D	4D	3E	4E	3F	4F
Pixel 6	5B	1A	2A	1B	2B	1C	2C	3D	4D	3E	4E	3F	4F

NOTE: Sensors Within A Band Are Designated A to F

Figure 6. MSS-Multiplexed Data Format, 150-Word Minor Frame.

One sweep of the MSS sensor produces 6 lines x 4 bands x 3300 pixels/line/band x 1 spacecraft byte (visible bands) plus 2 lines x 1 band x 1100 pixels/line/band x 1 spacecraft byte or 81.4K bytes. The MSS sensor is unidirectional, as shown in Figure 7, with image data generated only for the West to East scan. During the mirror retrace period (the East to West scan), calibration data is collected.

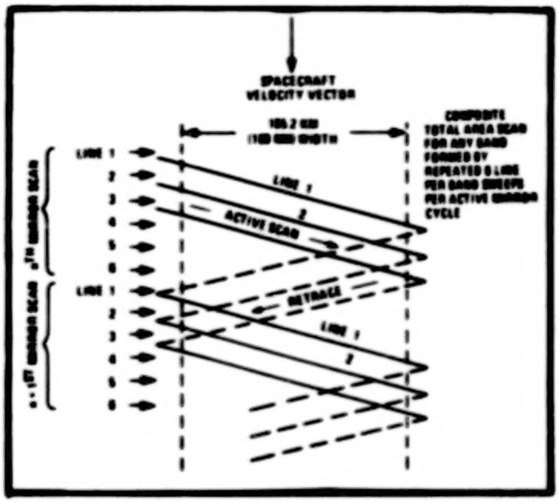
SPACECRAFT VELOCITY VECTOR
185.2 KM (100 NM) SWATH
COMPOSITE TOTAL AREA SCAN FOR ANY BAND FORMED BY REPEATED 6 LINE PER BAND SWEEPS PER ACTIVE MIRROR CYCLE
nTH MIRROR SCAN
n + 1ST MIRROR SCAN
LINE 1
2
3
4
5
6
LINE 1
2
3
4
5
6
LINE 1
2
ACTIVE SCAN
RETRACE
LINE 1
2

Figure 7. Ground Scan Pattern for a Single MSS Detector.

The complete sweep can be buffered and then output in BIL format by reading from the buffer every 25th byte. This allows the image data to be output in pixel order yet band-interleaved-by-line. If the data is required in BSQ format, each sweep will be written to disk such that sequential lines for a given band will be contiguous on disk.

3.2.1.2 TM Data Reformatting

Whereas the MSS data is sequentially sampled, the TM sensor simultaneously samples all odd detectors and then all even detectors thereby eliminating the time delay occurring with sequential sampling. As shown in Figure 8, the odd and even detectors for a band are separated physically by an amount equivalent to 2.5 pixels. The sampling of the odd and even detectors is separated in time by an amount equivalent to 0.5 pixel. This results in a two-pixel equivalent shift between the

MICROFILMED FROM
BEST AVAILABLE COPY

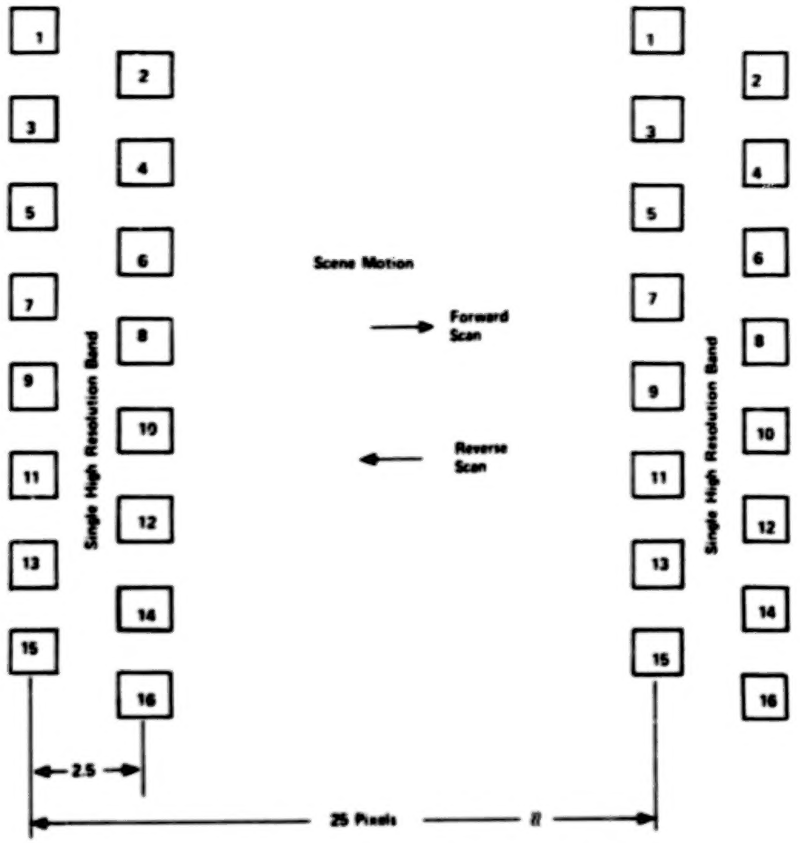
1
2
3
4
5
6
7
8
9
10
11
12
13
14
15
16
Scene Motion
Forward Scan
Reverse Scan
Single High Resolution Band
2.5
25 Pixels
8

Figure 8. Detector Array Geometry.

odd and even detectors accountable during data processing. A spatial misregistration again occurs between bands equivalent to 25 pixels, also accounted for during data processing. Figure 9 illustrates the TM multiplexed data format. The reflected energy for 6 visible bands is incident on 16 detectors per band, while in band 6 (IR), the emitted energy is incident on 1 detector. These 97 channels are input to a multiplexer which samples, A/D converts, and multiplexes these data in a serial bit stream together with sync, telemetry, and internal calibration data. Each minor frame of image data consists of 102 bytes-96 visible band samples, 1 IR band sample, 1 telemetry, and 4 sync.

One sweep of the TM sensor produces 16 lines x 6 bands x 6240 pixels/line/band x 1 byte/pixel plus 4 lines x 1 band x 1560 pixel/line/

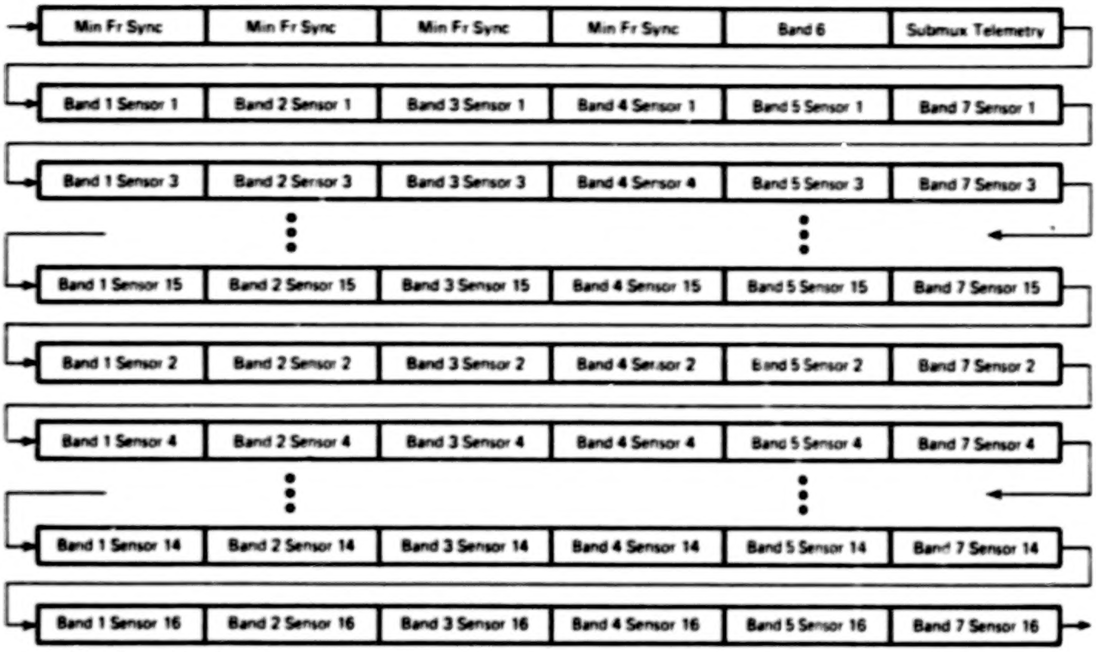
Min Fr Sync
Min Fr Sync
Min Fr Sync
Min Fr Sync
Band 6
Submux Telemetry
Band 1 Sensor 1
Band 2 Sensor 1
Band 3 Sensor 1
Band 4 Sensor 1
Band 5 Sensor 1
Band 7 Sensor 1
Band 1 Sensor 3
Band 2 Sensor 3
Band 3 Sensor 3
Band 4 Sensor 4
Band 5 Sensor 3
Band 7 Sensor 3
Band 1 Sensor 15
Band 2 Sensor 15
Band 3 Sensor 15
Band 4 Sensor 15
Band 5 Sensor 15
Band 7 Sensor 15
Band 1 Sensor 2
Band 2 Sensor 2
Band 3 Sensor 2
Band 4 Sensor 2
Band 5 Sensor 2
Band 7 Sensor 2
Band 1 Sensor 4
Band 2 Sensor 4
Band 3 Sensor 4
Band 4 Sensor 4
Band 5 Sensor 4
Band 7 Sensor 4
Band 1 Sensor 14
Band 2 Sensor 14
Band 3 Sensor 14
Band 4 Sensor 14
Band 5 Sensor 14
Band 7 Sensor 14
Band 1 Sensor 16
Band 2 Sensor 16
Band 3 Sensor 16
Band 4 Sensor 16
Band 5 Sensor 16
Band 7 Sensor 16

1 Minor Frame ≈ 54.3 μsec (D)
≈ 9.7 μsec (T)

Figure 9. Thematic Mapper Multiplexed Data Format-102-Word Minor Frame.

band x 1 byte/pixel or 600K bytes of data. This represents a large amount of buffer storage prior to any reformatting. The TM sensor is bidirectional, as shown in Figure 10, allowing data to be taken on both the forward and reverse portions of the scan cycle. However, when data is acquired during both the forward and reverse scans of an oscillating scan mirror, scan swaths which are contiguous at the nadir will underlap and overlap at mirror reversal due to spacecraft motion along the ground track. This underlap and overlap can be removed by the addition of another mirror system resulting in the corrected scan pattern, shown at the bottom of Figure 10, with parallel, contiguous, scan lines. Note, however, that the order of the pixels have been reversed during the reverse portion of the scan. These pixels must be reordered at some point during the processing such that, following reformatting, all pixels are in proper sequence.

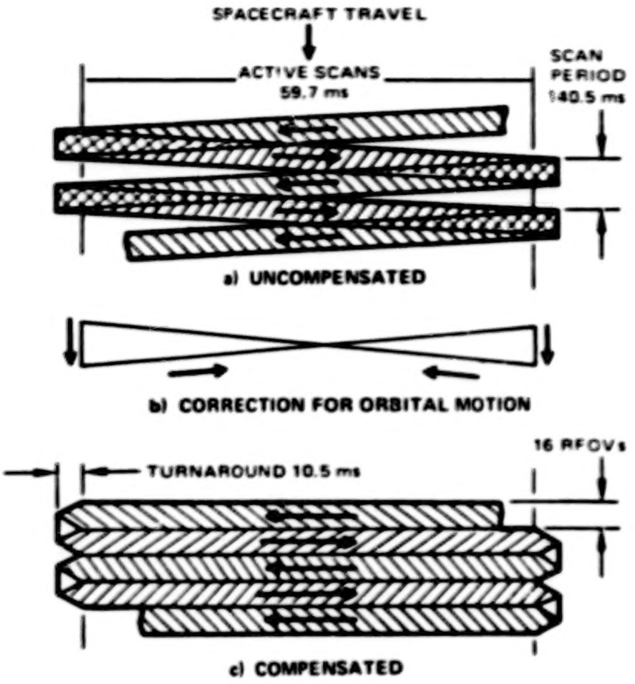
SPACECRAFT TRAVEL
ACTIVE SCANS
59.7 ms
SCAN
PERIOD
140.5 ms
a) UNCOMPENSATED
b) CORRECTION FOR ORBITAL MOTION
16 RFOVs
TURNAROUND 10.5 ms
c) COMPENSATED

Figure 10. Scanner Ground Patterns.

As previously mentioned, one complete sweep of TM data requires 600K bytes of buffer storage. Reducing the size of the buffer can be accomplished by reformatting partial lines for output to disk. The partial lines are assembled on disk to form the full lines. The choice of buffer size prior to the reformatting must be based on a balance between maintaining a high transfer rate of formatted data to disk while minimizing the buffer storage.

The image data is repeatable such that after accessing every 102 bytes of data, the sensor will output the next contiguous pixel from the same line and same band. Accessing every 102nd byte of data from the image buffer will place all pixels in a line in ascending order.

If the image data did not have to be reformatted, but could be processed in the BIP sensor format, the buffers required to hold data prior to reformatting could be reduced in size, and the sensor data could be processed in realtime. Appendix A reviews, in detail, the storage requirements necessary to reformat data from BIP to BIL for radiometric correction and then from BIL to BIP for classification.

3.2.2 Radiometric Calibration

The function of radiometric data calibration is to compute coefficients necessary to adjust the intensity data of each detector. This adjustment is designed to remove both detector-to-detector response differences and time variations of any particular detector's response. It is defined by specifying gain and bias coefficients for each detector in each band; these coefficients are subsequently employed in radiometric correction processing.

Radiometric calibration for the TM and MSS scanning sensors occurs in four phases:

a. A prelaunch calibration of the detectors and the in-flight calibration system

b. Intensive postlaunch observations

c. In-flight periodic detector calibration

d. Sun calibration.

Prior to launch, test calibration sources are carefully calibrated against primary radiance standards. The test calibration sources are then used to determine the response curve (gain and bias) for each detector. This information is used to measure the performance of the in-flight calibration system (radiance levels and detector shading factors).

The data base of temperature-dependent calibration coefficients, resulting from this prelaunch testing, initializes the radiometric correction process. Immediately after launch which extends for 3 weeks, the detectors are monitored closely to determine any apparent changes in output from prelaunch performance. Once the postlaunch performance of the sensor system has stabilized, the in-flight calibration system is used to generate one or two calibration values for each detector at periodic intervals. This in-flight radiometric calibration process is shown in Figure 11. The calibration data must be subjected to heavy smoothing in the hypothesis testing to reduce the random noise components. Both the sensor temperature and channel gains and biases are smoothed. Only when a definite trend is noted along with a significant change from data base values will any changes be made to the data base recorded gain and bias terms.

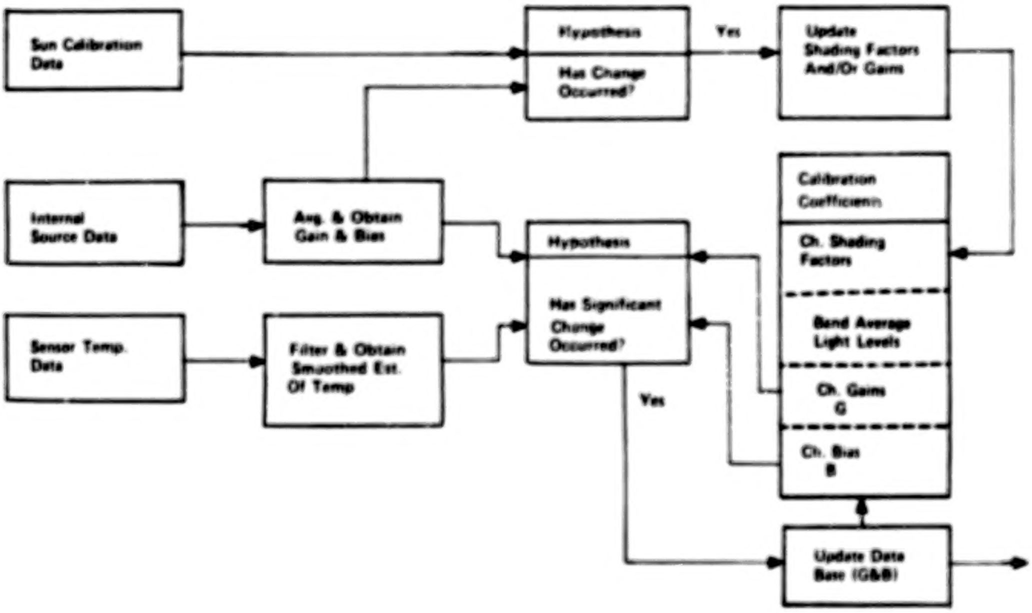

Sun Calibration Data
Hypothesis
Has Change Occurred?
Yes
Update Shading Factors And/Or Gains
Internal Source Data
Avg. & Obtain Gain & Bias
Calibration Coefficients
Hypothesis
Has Significant Change Occurred?
Ch. Shading Factors
Band Average Light Levels
Sensor Temp. Data
Filter & Obtain Smoothed Est. Of Temp
Ch. Gains G
Yes
Ch. Bias B
Update Data Base (G&B)

Figure 11. In-Flight Radiometric Calibration.

At periodic intervals after launch, solar observations are used to measure the performance of the in-flight calibration system. If the observations indicate that a change in the internal light source has occurred, the radiometric coefficients are adjusted appropriately.

3.2.2.1 MSS Radiometric Calibration For Landsats-1,-2, and -C

During every mirror retrace period, the radiance from the earth scene is blanked out by a mechanical shutter. The individual sensors in bands 4 through 7 (visible bands) are exposed every other mirror retrace to a rotating variable density wedge optical filter illuminated by an on-board calibration lamp as shown in Figure 12. Band 8 detectors (IR Band) are exposed to temperature references during alternate mirror retraces when bands 4 through 7 are not being calibrated. The resulting calibration data wedge is introduced into the video data stream. The nominal shape of this wedge is shown in Figure 13.

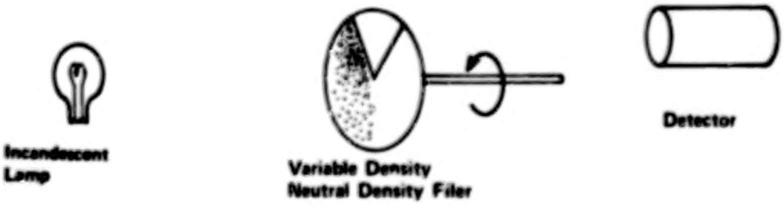

Figure 12. Calibration Apparatus.

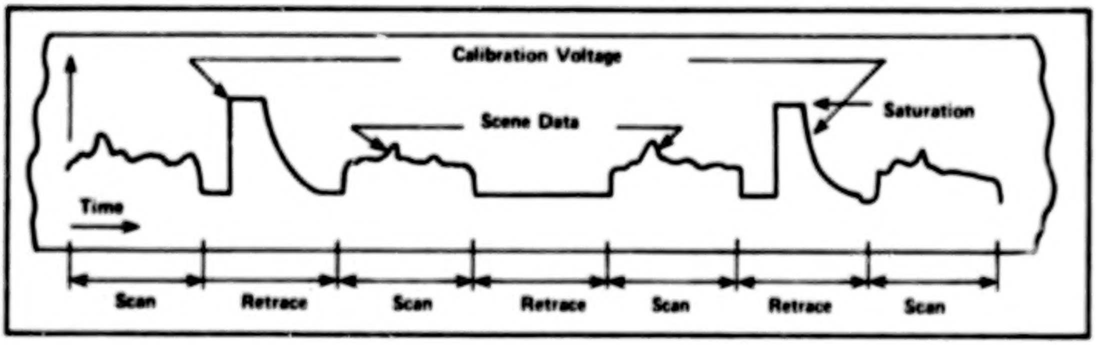

Figure 13. MSS In-Flight Calibration Data for Landsats-1,-2 and -C.

From preflight calibration tests, during which the MSS detectors were used as transfer devices between a standard radiance source and the MSS internal calibration lamp, the radiance at selected calibration word counts and the maximum radiance to be assigned to each spectral band were determined. During flight, a threshold value is detected on the increasing portion of the calibration wedge. Then six calibration values, shown in Figure 14, located a fixed number of words past the threshold value are determined. These six values, from each detector, are fit with a six-point regression analysis according to equations (1) and (2) where the V_i are the calibration values and C_i, D_i are regression co-coefficients.

$$a = \sum_{i=1}^{6} C_i V_i \qquad \text{(bias coefficient)} \qquad (1)$$

$$b = \sum_{i=1}^{6} D_i V_i \qquad \text{(gain coefficient)} \qquad (2)$$

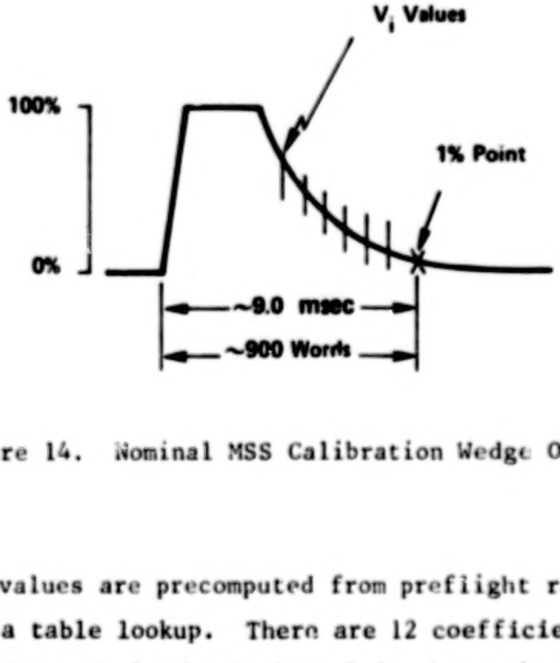

Figure 14. Nominal MSS Calibration Wedge Output.

The C_i and D_i values are precomputed from preflight radiance values and stored in a table lookup. There are 12 coefficients (C_i, D_i, i=1,---6) per detector for bands 4 to 7 for low gain mode or 24 sets (4 x 6) of coefficients per detector. Bands 4 and 5 have an additional set of C's and D's for high gain mode or 12 additional sets (2 x 6) of 12 coefficients.

Due to the presence of noise on received calibration data, the "a" and "b" values are smoothed by equations (3) and (4)

$$b_s(n) = b_s(n-1) + W(n) \cdot b(n) - b_s(n-1) \qquad (3)$$

$$a_s(n) = a_s(n-1) + W(n) \cdot a(n) - a_s(n-1) \qquad (4)$$

where n = sequential number of scanlines/swath

$b(n)$, $a(n)$ = latest value of b and a

$b_s(n-1)$, $a_s(n-1)$ = previous smoothed values of b and a

$b_s(n)$, $a_s(n)$ = new smoothed values of b and a

$W(n) = \frac{1}{n+1}$ for n = 0 to 15

$W(n) = \frac{1}{16}$ for $n > 16$

This filtering is maintained for an entire image swath, i.e., n is not reset to 1 at the beginning of each scene.

The gain and bias coefficients are computed in equations (5) and (6)

$$G = \frac{V_{max}}{M\ b_s} \qquad (5)$$

$$B = \frac{-V_{max}\ a_s}{M\ b_s} - A \qquad (6)$$

where V_{max} = maximum pixel value (127 for bands 4, 5, and 6, 63 for band 7)

M & A = value for each band, for each detector by scene from the ADT. These values are used for the input image frame data.

Thus equation (7) becomes $I_c = GI + B$ (7)

where I_c is a radiometrically corrected pixel output.

Bands 4 and 5 can be operated in either of two modes: low gain and high gain. They can be switched, by ground command to the spacecraft, from one mode to the other independently (e.g., band 4 could be low gain while band 5 is high gain). Bands 6, 7, and 8 can operate in one gain mode only. The gain mode of bands 4 and 5 is made available on the ADT.

Thus far, it has been assumed that the internal MSS calibration lamp emits constant radiance for the life of the spacecraft. In reality, lamp radiance is likely to exhibit a long-term drift. Provision has been made to monitor calibration lamp versus sun radiance on a once per orbit basis. In this technique, an image of the sun is recorded and the resulting detector output observed. Any overall drift in detector outputs may be attributed to changes in internal calibration lamp radiance. The drift can be accommodated by altering a scale factor.

Let K_s represent the updated sun coefficient. K_s is calculated by comparing the most recent sun calibrated voltage with the initial sun calibrated voltage. K_s is given by equation (8)

$$K_s^{\;m} = \frac{(V_c)^{I}\mathrm{sun}}{(V_c)^{m}\mathrm{sun}} \tag{8}$$

where $(V_c)^I\mathrm{sun}$ = initial value of calibrated sun voltage at launch

$(V_c)^M\mathrm{sun}$ = value of calibrated sun voltage for the M^{th} sun calibrated run

The corrected detector output is given by equation (9)

$$I_c^{\;1} = K_s I_c = K_s\ (GI + B) \tag{9}$$

On Landsat-1, reliable sun calibration data could not be obtained because the sun imaging optics were apparently fogged by contaminants released from nearby spacecraft components. The problem was rectified on Landsat-2. Sun calibration data is in operation use for Landsat-C. For Landsat-1 and -2, K_s equals 1.

Experience with the MSS on Landsats-1, -2, and -C has shown that the major difficulty in establishing correct calibration factors prior to launch results from inaccuracies in ground test equipment. This experience on MSS has resulted in several iterations of improvement that will be applied to the MSS and TM sensors for Landsat-D.

3.2.2.2 MSS Radiometric Calibration for Landsat-D

As with the original MSS, the MSS for Landsat-D contains an internal calibration system and sun calibration system for detecting changes in radiometric performance. The MSS-D uses redundant incandescent lamps (MSS original, 1 lamp) and a neutral density grey wedge (MSS original, a variable neutral density grey wedge) to produce a continuous spectrum of light levels for calibration of the visible bands (bands 1 through 4). The IR band (band 5) thermal detectors are calibrated using the shutter ambient temperature and a hot reference black body.

The shape of the grey wedge intensity profile is shown in Figure 15. A threshold crossing of grey level 32 is the time base from which all 64

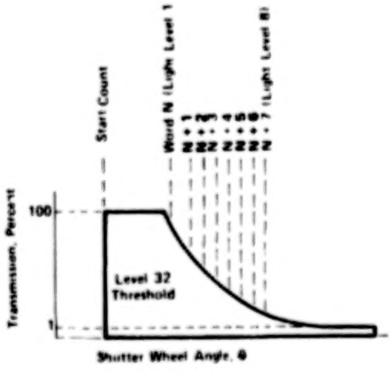

Figure 15. MSS-D Calibration Wedge Output.

MICROFILMED FROM
BEST AVAILABLE COPY

grey levels in the wedge are measured. Typically, 8 or more levels are used for least square fitting the gain slopes in updating the prelaunch gains and biases. The MSS original utilized a six-point regression analysis to update the prelaunch gains and biases.

The remaining portion of the radiometric calibration processing (data smoothing and sun calibration) remains the same as that previously described for the MSS original.

3.2.2.3 TM Radiometric Calibration

The TM internal calibration system uses three incandescent lamps singly and in combinations to produce seven less than full-scale levels in the visible bands (bands 1 through 5). These seven levels, plus the dark current zero level provide the means for measuring gain slopes and biases for each channel. The IR band (band 6) receives two temperature references from the internal calibration system. One is a hot reference black body, and the other is an ambient temperature black body patch on the shutter. These two temperatures are precisely measured and telemetered so that gain slopes and biases can be calculated for each of the four thermal channels.

During system acceptance testing, all seven calibrated internal light levels will be used to establish optimized least squares fit of the gain slopes and biases. After initial checkout in orbit, at most two levels will be needed to update gains repetitively during any single orbit. The need for bias updating should be all but eliminated based on MSS experience which indicated that silicon detectors are extremely stable and linear over years and over expected operating temperatures. The proposed scheme for TM radiometric correction will be to use the postlaunched-checked, acceptance test-derived set of gain and bias correction factors and to adjust these as necessary by hypothesis test, using calibration data from the internal sources and telemetered focal plane temperature data. The overall gain slopes and biases, and internal source light levels and shading factors (variation of light between channels in one band) will be corrected with decreasing frequency after launch as updating of the baseline set of correction factors is found to be unnecessary. The following will describe the procedure for TM radiometric calibration.

The expected shape of the TM calibration wedge output is shown below.

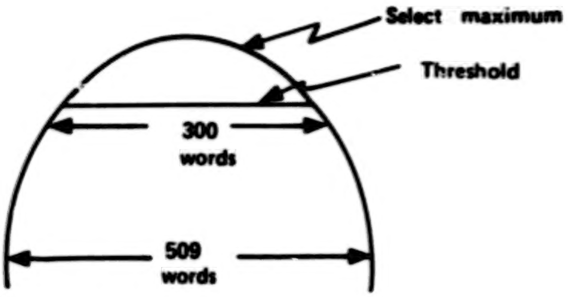

The calibration data will be thresholded and approximately 300 bytes of the 509 bytes of calibration data extracted and stored. A reduced set of calibration values (typically 50) are extracted and stored for each detector (100) and filter (2). Each of the 50 extracted values will be recursively averaged over several sweeps (typically 24) with the running averages returned to storage. These averages are least-squares fitted to a curve having the functional form of detector output vs. filter space input. The curve reduces to a fixed level straight line (Figure 16) for a discrete (nonvariable) filter. Two values are obtained representative of light-level inputs near the high end of the scale. The light levels are $0.85n_{max}$ and $0.95n_{max}$ of the maximum radiance.

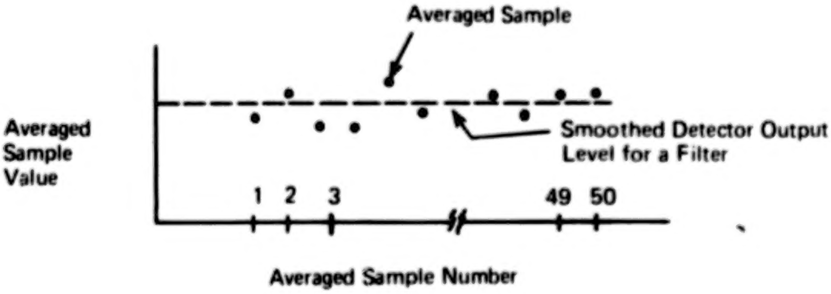

Figure 16. Curve Fitting of Averaged Data.

These two values are plotted vs. nominal detector response to radiance level input. The result is a linear relation which determines gain and bias coefficients for the detector (Figure 17).

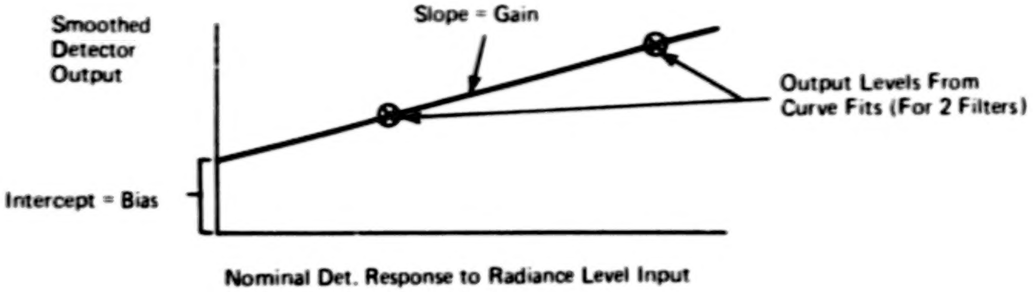
Smoothed Detector Output
Slope = Gain
Output Levels From Curve Fits (For 2 Filters)
Intercept = Bias
Nominal Det. Response to Radiance Level Input

Figure 17. Gain and Bias Determination.

The accuracy of signal calibration depends primarily on the accuracy and precision of the initially determined detector gains and biases. The accuracy of these estimates depends on the accuracy of the initial instrument calibration, the stability of the on-board calibration system, and the ability of the sun calibration to correct for any changes in the on-board calibration system.

The sun calibration process will update the average band radiance levels of the on-board lamp and the relative channel-to-channel shading factors. These values go into determining the calibration lamp radiance level for a given channel (detector).

The sun calibration provides a means of updating the bias estimate or more correctly of verifying that no change has occurred. The gain estimate based on a temperature model can also be updated. This serves two purposes: it provides the data for initial precision required for the remainder of the orbit, and it verifies no significant system change has occurred.

Band 6 signal calibration is accomplished using a table lookup procedure. The telemetered black body and shutter arms temperatures are compared with prestored tables determined during instrument calibration. The tabular values establish the gain and bias values for Band 6.

The calibration process is an evolutionary one, beginning with a minimum of information. As time proceeds, more knowledge of the exact behavior of the temperature model is obtained so that model coefficients are accurately known. The model alone (plus telemetered temperature) can be used for calibration. It is expected that after two or three months of operation, the sun calibration can be limited to once-a-day or even less.

3.2.2.4 Destriping

If all detectors in a given spectral band do not exhibit the same response characteristics, an undesirable phenomenon known as striping will appear in the digital image. In photographic products produced from digital data, striping can be a severe surface flaw and a hindrance to photo interpretation. Striping could be detrimental to multispectral classification applications, if spectral signatures of the digital data are artificially altered by the striping effect. Initial experiments conducted to determine the effect of striping on classification accuracy have been inconclusive (see Appendix B).

The ground-based radiometric calibration process used on the Landsat-1 and-2 MSS data has not removed all of the detector-induced striping. Residual striping has been particularly evident in the first (0.5 to 0.6 micron wavelength) MSS band.

As mentioned in subsection 3.2.2.1, the current method for MSS radiometric calibration is thought to be inadequate and indeed could be the cause of the image striping noted in Landsat-1 and-2. If the calibration data is properly applied, IBM feels the striping will be eliminated for the Landsat-D scanning sensors. The stable response characteristics of the TM, improved prelaunch calibration techniques for the on-board calibration system, and implementation of more efficient calibration algorithms are reasons for this optimism.

If further information proves this optimism to be unwarranted, an automatic scene-dependent destriping algorithm can be implemented. This scene-dependent procedure requires two algorithms: one to detect automatically the presence of striping, and a second to remove the striping from the data.

IBM has investigated several data-dependent techniques for destriping (Table 4). Each of these uses one or more statistical parameters that are derived from the image data. The region of the image data that is used to calculate the statistical parameters is called a window. The windows considered during the investigation, as shown in Figure 18, were rectangular areas of several sizes and shapes. All algorithms tested attempt to equalize some statistical function of the data within some window.

Table 4. Destriping Algorithms Considered.

Frame Mean and Standard Deviation Equalization
Frame Mean and Standard Deviation Equalization to 1 Detector
Sweep Mean and Standard Deviation Equalization
Sweep Histogram Equalization
Local Mean and Standard Deviation Equalization
Local Averaging

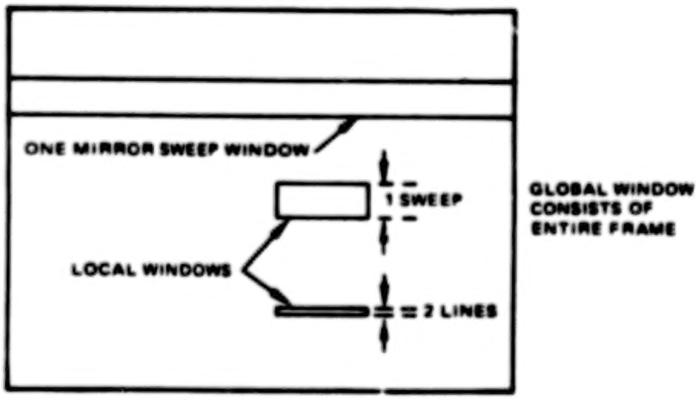

Figure 18. Window Sizes Used in Destriping Experiments.

The first algorithm that was studied consists of equalizing the mean (M) and standard deviation (σ) of each detector's data over a window that is defined to be one entire frame. This equalization can be accomplished by a linear function whose coefficients are shown in Table 5. For each detector, only the sum of the pixel values and the sum of the squared pixel values are required. The result is a global function (for each detector) whose coefficients are constant during one frame of data. After destriping, the data from each detector has mean and standard deviation equal to that of the entire frame before destriping.

Table 5. Mean and Standard Deviation Equalization Equations.

$$V_{i,d} = \text{value of } i \text{ th pixel from detector } d$$

$$P_d = \sum_{i=1}^{N} V_{i,d} \qquad P = \sum_{d=1}^{D} P_d$$

$$Q_d = \sum_{i=1}^{N} V_{i,d}^2 \qquad Q = \sum_{d=1}^{D} Q_d$$

$$M_d = \frac{P_d}{N} = \text{mean} \qquad M = \frac{P}{DN}$$

$$\sigma_d = \sqrt{\frac{Q_d}{N} - M_d^2} = \text{standard deviation} \qquad \sigma = \sqrt{\frac{Q}{DN} - M^2}$$

$$G_d = \frac{\sigma}{\sigma_d} = \text{gain}$$

$$B_d = M - G_d M_d = \text{bias}$$

$$O = G_d V + B_d = \text{corrected pixel value}$$

The second algorithm is quite similar to the previous technique. It also uses frame mean and standard deviation equalization. Only one reference detector's data are corrected using the calibration wedge data before destriping. The remaining detector's data are then corrected so that they have the same mean and standard deviation as that of the reference detector. This is the approach currently used by the Canada Centre for Remote Sensing.

The third algorithm also uses equalization of each detector's mean and standard deviation. It differs from the first algorithm in that the window over which it operates is much smaller. The window consists of all data from one sweep of the scan mirror. This technique results in a new set of linear functions (one for each detector, as in Table 5) for each mirror sweep.

The fourth algorithm is also a mean and standard deviation equalization technique. However, the window involved is much more local in this method. It is a small, rectangular segment of one mirror sweep. As the window is "moved" across the mirror sweep, the mean and standard deviation for each detector's pixels within the window are calculated. These are called local means and standard deviations, and they are assigned to the center pixel of each line segment in each window. For each pixel (except those near the left or right edges of the image), the equations in Table 5 give a correction function.

The fifth algorithm uses the three steps shown in Figure 19. The image intensity data for the entire frame is first expanded linearly

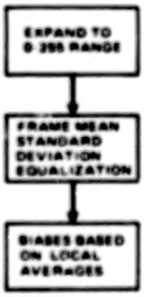

Figure 19. Local Averaging Method.

to fill the interval (0,255). Then frame mean and standard deviation equalization is performed. Finally, a local averaging process is used to attempt to remove residual detector biases. This technique uses a small, two-line window, as shown in Figure 18. The image is processed in one-mirror sweep segments. The first line, from detector one, is left unchanged. Each of the remaining lines in that sweep is processed to be similar to the corrected line above it. A local average of the pixels with a small window around each pixel is computed. This computation is done for the line being processed and for the already processed line immediately above it. The difference between the averages of the reference line neighborhood and the neighborhood of the line being processed is added to the intensity value of the current pixel to get the corrected intensity. This is the approach presently used by the EROS Data Center.

The sixth algorithm uses a one-mirror sweep window as a basis for histogram equalization. One detector is chosen as a reference detector and is not changed by this destriping process. Each line from the other detectors is altered to have a histogram that is similar to the line of the reference detector from the same mirror sweep. This is illustrated in Figure 20 including the equation of the transformation.

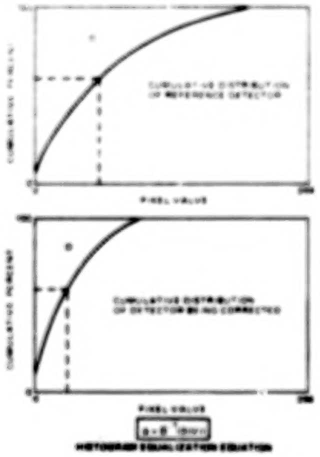

Figure 20. How Histogram Equalization Works.

MICROFILMED FROM
BEST AVAILABLE COPY

3.2.2.4.1 Destriping Algorithm Test Results

A series of destriping tests were conducted by IBM using Landsat-2 MSS data as input. Uncalibrated input data were chosen for the destriping experiments to allow maximum control over the processing performed on the data.

This input data was first radiometrically corrected using the NASA decompression tables and the NASA linear regression coefficients. Gain and bias values were computed for each pair of mirror sweeps from the calibration wedges and the linear regression coefficients. The averages of all these gain and bias values were used as a global gain and bias radiometric correction function. Data corrected with this global function was used as the input data for the radiometric correction experiments.

The results of the tests are summarized in Table 6. The "Power Spectrum" column contains ratios computed from the equations of Figure 21. A high value of the ratio indicates the presence of a six-line repeating pattern. Comparison of the ratios and photographic recordings of the results (not included in this report) shows that algorithms that reduce striping within a sweep do not necessarily produce the best overall images.

FMASDE was selected for implementation, because it produces the highest quality results of the algorithms tested and has the lowest implementation cost. FMASDE did not totally eliminate visible striping from the test data set, although it performed better than any of the other approaches. To investigate this further, FMASDE was applied to the raw, uncalibrated data. Virtually all the striping was removed. This shows clearly that the difficulty in removing striping from calibrated data is linked to the current calibration process and reinforces the expectation that objectionable detector-to-detector differences will not be present in properly calibrated data.

Table 6. Summary of Destriping Test Results.

Algorithm	Power Spectrum	Picture Quality Comments	Implementation Cost
Raw data	0.1274×10^{12}	Severely striped	–
NASA style calibration	0.3287×10^{8}	Considerably improved, moderately striped	–
Frame mean and standard deviation equalization	0.1795×10^{8}	Further improvement, slightly striped	Low
Frame mean and standard deviation equalization to I detector	0.6552×10^{9}	Further improvement, slightly striped	Low
Sweep mean and standard deviation equalization	0.7418×10^{4}	Striping worsened, clearly unacceptable	Medium
Local mean and standard deviation equalization	0.6569×10^{4}	Obvious local distortions, clearly unacceptable	High
Sweep histogram equalization	0.1079×10^{8}	Striping worsened, clearly unacceptable	High
Local averaging	0.5455×10^{2}	Further improvement, slightly striped, some local distortions evident	High

$V_{i,n}$ = value of ith pixel from line n

$$d(n) = \sum_{i=1}^{K} V_{i,n}$$

N = number of detectors

$$\hat{d}(n) = \sum_{i>0} d(n + 16iN)$$

$$D(\omega) = \sum \hat{d}(n) e^{-2\pi i \frac{\omega}{16N}}$$

$$P(\omega) = |D(\omega)|^2, \omega = 0, 1, \ldots, 8N$$

$$M = \frac{1}{7.5\,(N-2)} \sum_{\substack{\omega = 17 \\ \omega \not\equiv 16}}^{8N} P(\omega)$$

$$V(\omega) = P(\omega) - M$$

$$\sigma_c^2 = \frac{1}{7.5\,(N-2)} \sum_{\substack{\omega = 17 \\ \omega \not\equiv 16}}^{8N} V(\omega)^2$$

$$\sigma_s^2 = \frac{1}{0.5\,(N-2)} \sum_{\substack{\omega = 32 \\ \omega \equiv 16}}^{8N} V(\omega)^2$$

$$\frac{\sigma_s^2}{\sigma_c^2} > T \Rightarrow \text{Striping}$$

Figure 21. Striping Detection Equations.

After the radiometric correction coefficients have been computed as described in subsection 3.2.2.1 but before they have been applied to the image data, the coefficients are used to modify the sums of the pixels in each scan line. The modified sums are then digitally analyzed to determine whether striping will be present in the corrected data. If the analysis indicates that the data will not be striped, the computed radiometric correction coefficients are applied to the data. Otherwise, the destriping algorithm is used to modify the computed coefficients before they are applied to the data. The data flow for the TM visible bands implementing this approach is shown in Figure 22.

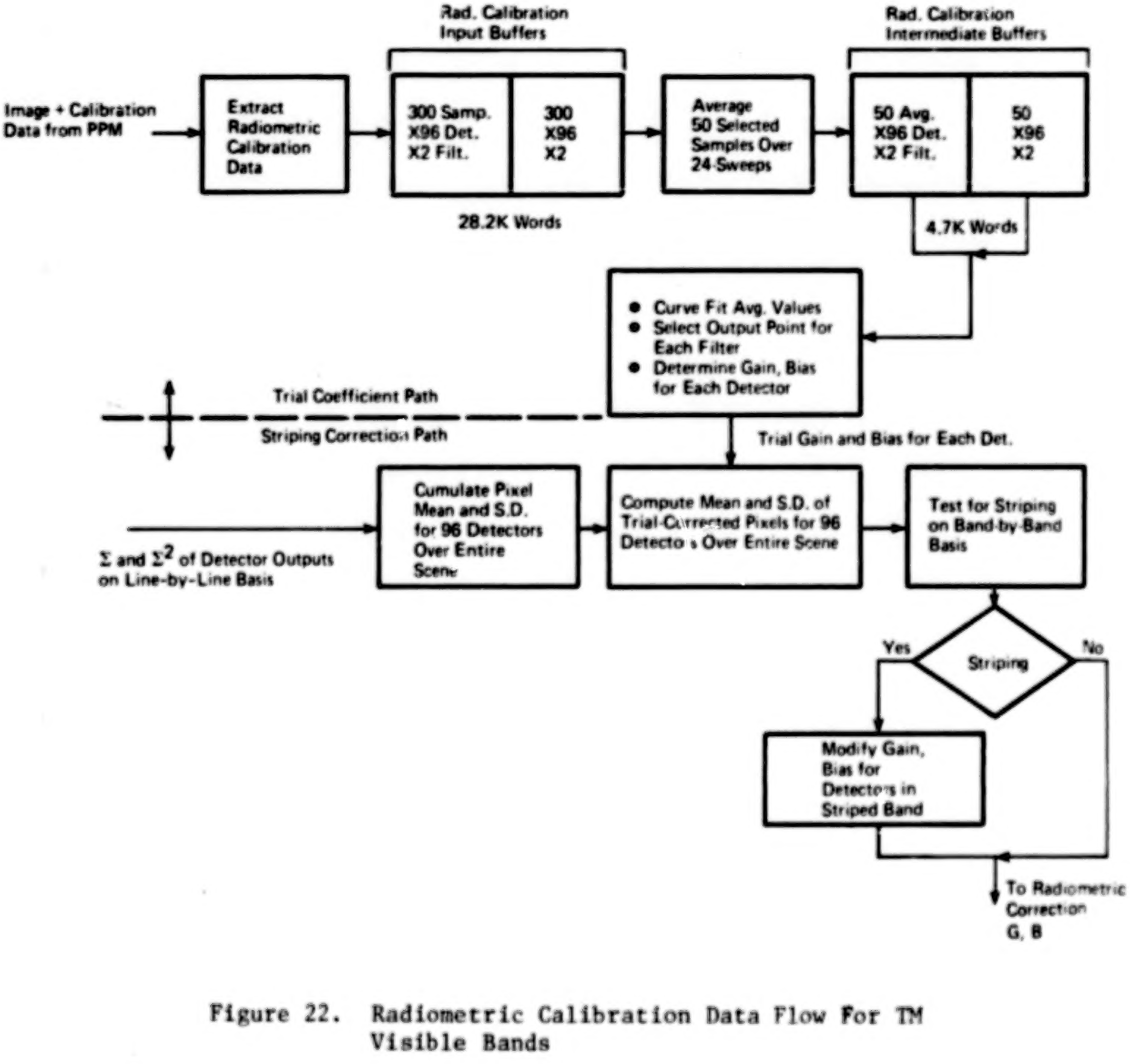
Rad. Calibration Input Buffers
Rad. Calibration Intermediate Buffers
Image + Calibration Data from PPM
Extract Radiometric Calibration Data
300 Samp. X96 Det. X2 Filt.
300 X96 X2
Average 50 Selected Samples Over 24 Sweeps
50 Avg. X96 Det. X2 Filt.
50 X96 X2
28.2K Words
4.7K Words
Curve Fit Avg. Values
Select Output Point for Each Filter
Determine Gain, Bias for Each Detector
Trial Coefficient Path
Striping Correction Path
Trial Gain and Bias for Each Det.
Σ and Σ² of Detector Outputs on Line-by-Line Basis
Cumulate Pixel Mean and S.D. for 96 Detectors Over Entire Scene
Compute Mean and S.D. of Trial-Corrected Pixels for 96 Detectors Over Entire Scene
Test for Striping on Band-by-Band Basis
Yes
Striping
No
Modify Gain, Bias for Detectors in Striped Band
To Radiometric Correction G, B

Figure 22. Radiometric Calibration Data Flow For TM Visible Bands

A discrete Fourier transform analysis of the adjusted image data sums is used to detect striping. Although the final version of the algorithm has not been established, a preliminary set of equations are given in Figure 21. By comparing appropriate elements of the power spectrum, any pattern in the data that occurs every mirror sweep is made apparent. Such a pattern indicates the presence of striping. More experimentation is needed to determine the particular elements of the spectrum that should be compared and to determine the correct threshold value that should be used in the comparison.

The destriping algorithm is performed only if the power-spectrum analysis so indicates. The equations for destriping are given in Figure 23. The algorithm is based on the assumption that, for every pair of detector numbers m and n, the mean and standard deviation of the pixel values from detector m must be the same as the mean and standard deviation of the pixel values from detector n.

$V_{i,d}$ = value of ith pixel from detertor d

$$P_d = \sum_{i=1}^{N} V_{i,d} \qquad Q_d = \sum_{i=1}^{N} V_{i,d}^2$$

g_d, b_d = gain and bias from calibration algorithm

$$\bar{P}_d = g_d P_d + N b_d \qquad \bar{Q}_d = g_d^2 Q_d^2 + 2 g_d b_d P_d + N b_d^2$$

$$\bar{P} = \sum_{d=1}^{D} \bar{P}_d \qquad \bar{Q} = \sum_{d=1}^{D} \bar{Q}_d$$

$$M_d = \frac{\bar{P}_d}{N} \qquad M = \frac{\bar{P}}{DN}$$

$$\sigma_d = \sqrt{\frac{\bar{Q}_d}{N} - M_d^2} \qquad \sigma = \sqrt{\frac{\bar{Q}}{DN} - M^2}$$

$$G_d = \frac{\sigma}{\sigma_d} = \text{gain} \qquad B_d = M - G_d M_d = \text{bias}$$

$$O_{i,d} = G_d V_{i,d} + B_d = \text{corrected pixel value}$$

Figure 23. Destriping Equations.

The first-degree polynomial function shown in Figure 21, when used on the pixel values from detector d, causes the resulting pixels to have mean M and standard deviation σ. One such polynomial is determined for each detector. This set of polynomials is used to radiometrically correct the entire frame. That is, the algorithm is global.

3.2.3 Radiometric Correction

Radiometric correction applies to each sample of image data the intensity adjustment determined by the radiometric calibration. The correction is applied as a gain and bias change as shown in equation (10):

$$I' = GI + B \tag{10}$$

where: I is the uncorrected image intensity value
I' is the radiometrically corrected value
G,B are the coefficients calculated in radiometric calibration

This linear transformation is also applied to the GCP Search areas before the Control Location Algorithm searches for control points (CPs).

Information necessary for radiometric correction is: radiometric calibration coefficients, the status of each detector, and the scene format center. The radiometric calibration coefficients will have been corrected for destriping, if necessary. As described in the previous subsection, the detector status values will be monitored and radiometric calibration coefficients modified for those detectors requiring a destriping correction. The detector status flag identifies lines for replacement. The scene format center (output from Geometric Error Modeling) will establish where on disk the image data is to be accessed, so that the output scenes can be framed correctly.

3.2.4 Geometric Correction/Temporal Registration

When a digital image of an area on the earth's surface is generated by a spaceborne sensor, the image will contain geometric distortions caused by the sensor platform, the sensor characteristics, and scene effects. The digital image data must be modified to remove these geometric distortions such that a point in the input image can be related to its true position on the earth's surface to a prescribed accuracy, generally one-half pixel. Control points, or recognizable features located in the image data, are used to correct these geometric distortions. Geometric correction and temporal registration are two versions of a process using the information provided by control points to develop a mathematical transformation between the correct and distorted versions of the image.

The difference between geometric correction and temporal registration is the definition of what constitutes a correct image. For geometric correction, position accuracy is defined as the ability to relate a point in the input image to its true position on the earth's surface as represented by some map projection. For temporal registration, registration accuracy is defined as the ability to overlay two images of the same ground point taken at different points in time.

The steps involved in geometric correction and temporal registration are:

a. Control Point Processing

b. Geometric Error Modeling

c. Space-to-Space Mapping

d. Geometric Interpolation.

Control point processing locates control points in the image data. Geometric error modeling uses these control point locations to compute geometric error model coefficients to define the mathematical relationships between the corrected and input images.

Space-to-Space mapping is the characterization of the relationship between the corrected image and a map. Geometric interpolation grid point creation is the final definition of the transformation between corrected and uncorrected images. These four steps are described in more detail in the following subsections.

3.2.4.1 Control Point Processing

Control point processing involves two major functions:

a. Control point location, a fully automatic function.

b. Construction and maintenance of a control point library, an offline operation involving manual selection of data.

Control points are used to augment tracking and spacecraft attitude data to precisely locate output image pixel coordinates. Control points consist of two types:

a. Geodetic control points (GCP) used for geometric correction.

b. Relative control points (RCP) used for temporal registration.

A GCP is a physical feature detectable in a scene, whose geodetic coordinates (latitude and longitude) are precisely known. GCPs are generally taken from USGS maps with a scale of 1:24,000. Typical GCPs are airports, highway intersections, land-water interfaces, and geological and field patterns.

A RCP is a physical feature taken from a reference image rather than a map. Typically, the reference image has already been geometrically corrected to a map projection. The geodetic coordinates of any feature in the reference image can be obtained by a straightforward calculation using the error models (geometric error models) developed in performing the geometric correction. A feature defined as a GCP can also be a RCP. The geodetic position of the RCP taken from the reference image will not, however, coincide with the geodetic coordinates of the GCP taken from a map. This is because of the error model used when performing the geometric correction.

The distinction, then, between geometric correction and temporal registration is the type of ground control used. The control point library will contain two types of GCP libraries:

a. RCP libraries

b. GCP libraries.

A given GCP library may contain window areas and ground locations that have been taken from several distinct scenes. An RCP library must have all data obtained from only one scene, designated as the reference scene. This is an important distinction between GCP and RCP libraries.

3.2.4.1.1 Control Point Location

Control points are stored in the library in terms of the geodetic coordinates (latitude and longitude). As the control point is accessed from the control point library, the coordinates are converted to line and pixel (sample) coordinates. The differences between the line and pixel coordinates of features stored in the library and input images become inputs to the geometric error model.

The location of a feature in the input image consists of two steps:

a. Search area identification.

b. Control location algorithm (CLA) application.

3.2.4.1.1.1 Search Area Identification

The Landsat orbit is adjusted to produce repeating ground tracks. Thus, there will be a fixed number of unique swaths with every control point assigned a swath number. This swath number will be on an associated ancillary data tape (ADT) or can be computed from the ephemeris data on the ADT. Ephemeris data, attitude control system (ACS) data, and the geodetic coordinates of the control points (CP) are used to predict the input space coordinates of each CP as shown in Figure 24.

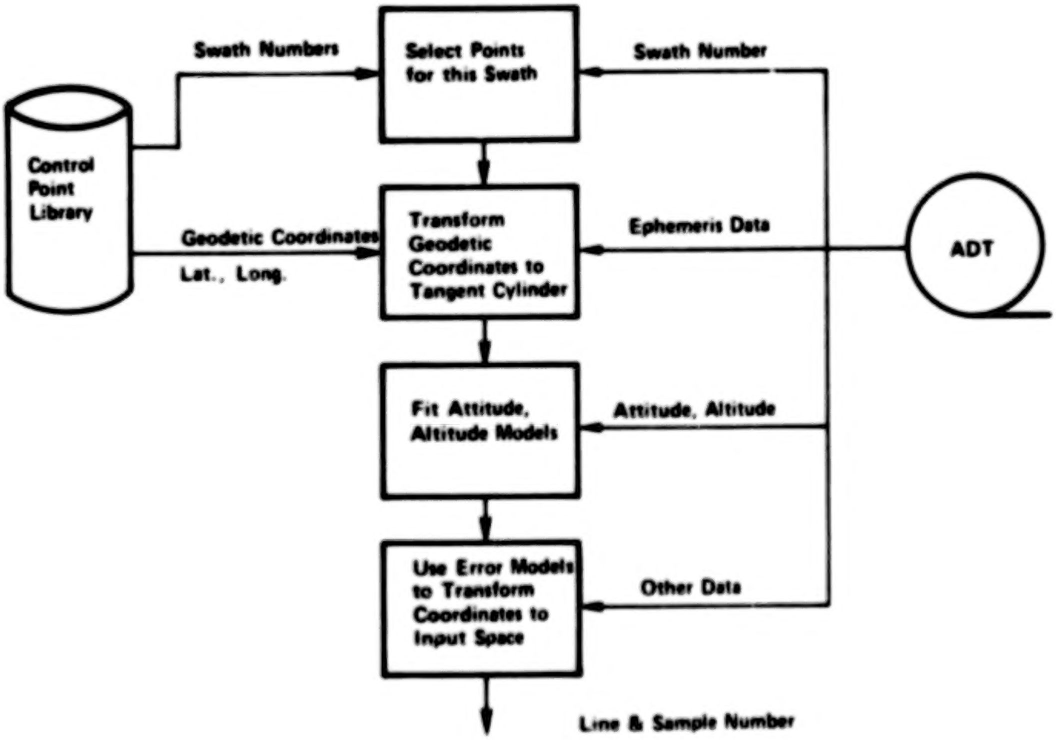
Swath Numbers
Select Points for this Swath
Swath Number
Control Point Library
Geodetic Coordinates
Lat., Long.
Transform Geodetic Coordinates to Tangent Cylinder
Ephemeris Data
ADT
Fit Attitude, Altitude Models
Attitude, Altitude
Use Error Models to Transform Coordinates to Input Space
Other Data
Line & Sample Number

Figure 24. Search Area Definition.

Errors in the ancillary data will cause errors in the predicted control point locations. Therefore, the arrays extracted from the input data stream must be relatively large (128 lines of 128 pixels are generally used). In addition, input image data that is extracted from the input must be corrected for high-frequency image distortions due to line length variation, earth rotation, and any detector sampling delay, before the control points are located in the search area. This is accomplished by defining two types of subimages: extraction areas and search areas. Extraction areas are large enough so that high-frequency effects can be removed using cubic convolution resampling. Search areas are extraction areas that have been radiometrically corrected and resampled to remove high-frequency effects. A table of extraction area upper left corner coordinates is generated for all control points. The search areas are then stored for input to the CLA.

3.2.4.1.1.2 Control Location Algorithm (CLA)

The control point location within a specified search area is accomplished by computing the discrete correlation of a window area, extracted from the control point library, with a search area as shown in Figure 25.

The correlation procedure is implemented using the FFT cross-correlation approach. Briefly, the approach is as follows:

a. Pad the zero-mean form of the search and window arrays to the next higher size which is an integral power of 2. The search area is 128 x 128 with the window area generally 32 x 32 as shown in Figure 26. The window area would then be zero padded to 128 x 128.

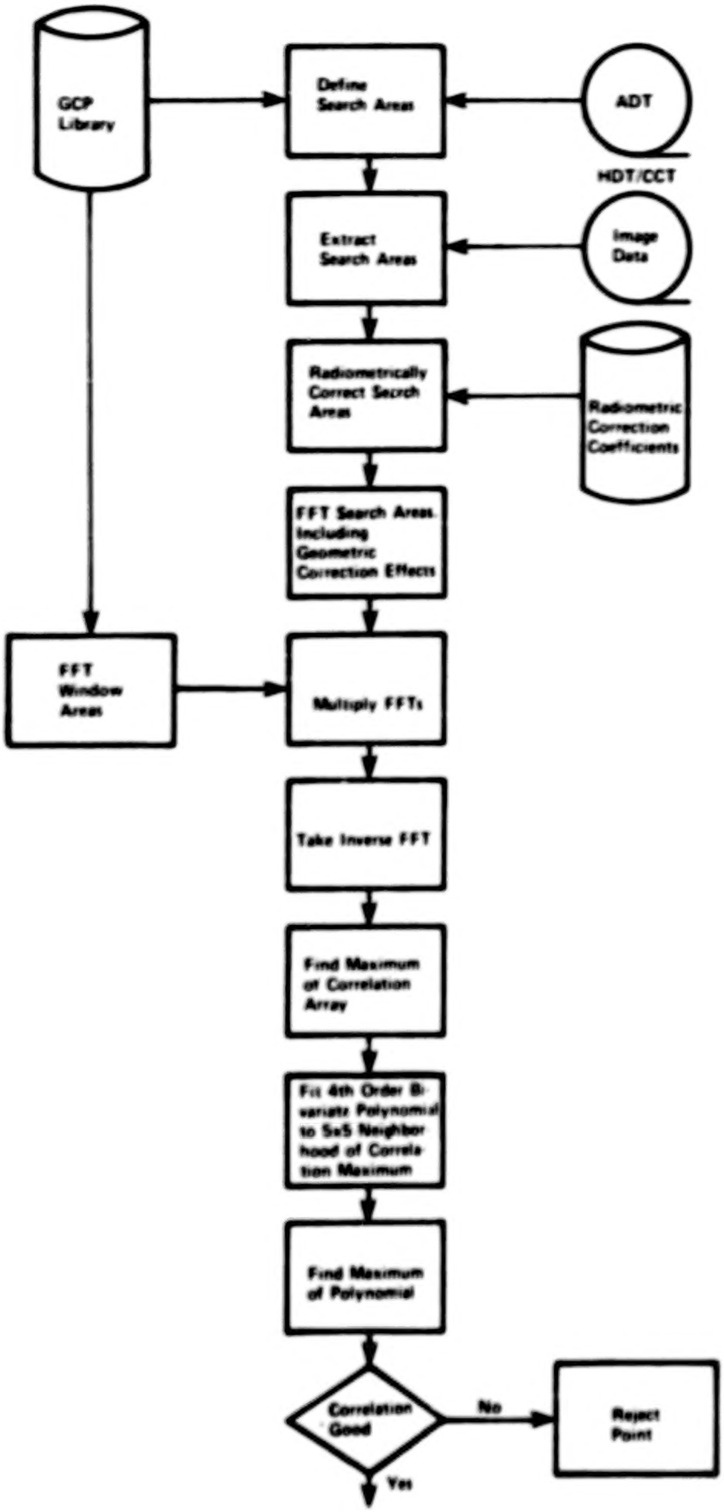
GCP Library
Define Search Areas
ADT
HDT/CCT
Extract Search Areas
Image Data
Radiometrically Correct Search Areas
Radiometric Correction Coefficients
FFT Search Areas Including Geometric Correction Effects
FFT Window Areas
Multiply FFTs
Take Inverse FFT
Find Maximum of Correlation Array
Fit 4th Order Bi-variate Polynomial to 5x5 Neighborhood of Correlation Maximum
Find Maximum of Polynomial
Correlation Good
No
Reject Point
Yes

Figure 25. Control Point Location.

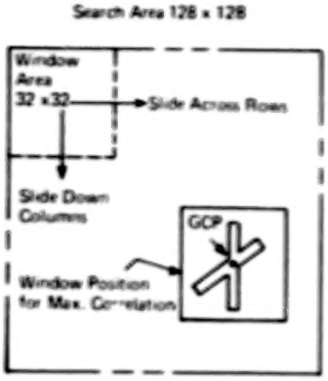
Search Area 128 x 128
Window Area 32 x 32
Slide Across Rows
Slide Down Columns
GCP
Window Position for Max. Correlation

Figure 26. CLA Correlation Processing.

b. Compute the FFT of the search and zero padded window areas, phase shifting the FFT of the search area to correct for the effects of yaw, line length variations, earth rotation, and sampling delay error.

c. Multiply the transform of the search area times the complex conjugate of the transform of the window area.

d. Compute the inverse transform of this product.

e. Unpad appropriately to obtain the desired correlation.

At this point in the location process, the search and window areas have been registered to the nearest integral pixel. An interpolating function is then fit around the correlation maximum and used to find the subpixel maximum of the correlation function. Figure 27 shows this procedure in one dimension and is accomplished as follows:

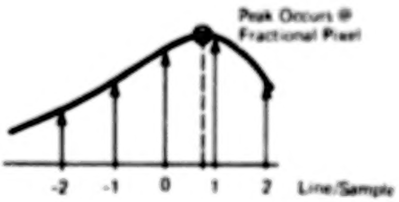
Peak Occurs @ Fractional Pixel
-2
-1
0
1
2
Line/Sample

Figure 27. Interpolation of Correlation Surface.

a. Select the 5 by 5 subarray of correlation points surrounding the nearest pixel registration in the correlation array previously generated.

b. Fit a bivariate fourth order polynomial to these correlation values using a least squares technique.

c. Locate the maximum of the polynomial.

d. Use the location of the maximum to determine the input image location of the final registration point.

The maximum of the fourth order bivariate polynomial must be determined numerically. Because of the polynomial form, Newton's method will be used. The polynomial maximum point shown in Figure 27 is the input image location relative to the upper left corner of the search area. Since erroneous correlation results can sometimes be obtained if the window area is not represented in the search area (e.g., the search area is cloud covered), the maximum value of the correlation is compared to a threshold value obtained from the autocorrelation function of the window. This comparison is shown in one dimension in Figure 28. Any registration failing this test is rejected.

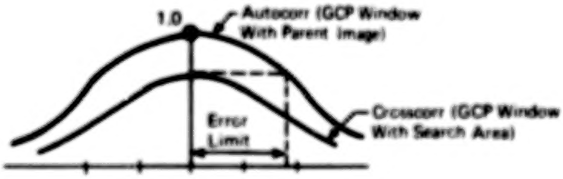
1.0
Autocorr (GCP Window With Parent Image)
Crosscorr (GCP Window With Search Area)
Error Limit

Figure 28. Registration Verification.

3.2.4.1.2 Construction and Maintenance of a Control Point Library

The control point library will contain, or must contain, a sufficient number of recognizable geodetic features that are reliable and known with sufficient accuracy to meet the position accuracy requirements. Large-scale maps must be used for accurate determination of geodetic coordinates, and such maps are frequently nonexistent or out-of-date. Patterns in the image data must be related to the maps, not only in the large (relatively easy) but also to subpixel accuracy (much more difficult). It is the ability of an analyst to accurately relate a feature in the image data to an exact point on a large-scale map which will be the limiting factor in the geometric correction accuracy.

The construction of a control point library consists of three main functions:

a. Map Point Location

b. Map Point Set Refinement

c. Machine-Locatable Point Selection.

Each is part of a man-machine interface consisting of an interactive operator-controlled dialog with the machine. The operator has at his disposal both an image and an alphanumeric display, a cursor control (via a joystick) on the image display, a function keyboard and an alphanumeric keyboard. See Figure 29 for an overview.

At the start of the Map Point Location phase, the geodetic coordinates of the CP are transformed with the aid of attitude/ephemeris data into the proper line and sample coordinates in the input sensor data. The exact relationship between the input sample space and geodetic coordinates is not well known at this step of the processing. Therefore, for each point, a large data array (512 lines x 512 sample) is extracted from the total scene to serve as a search area.

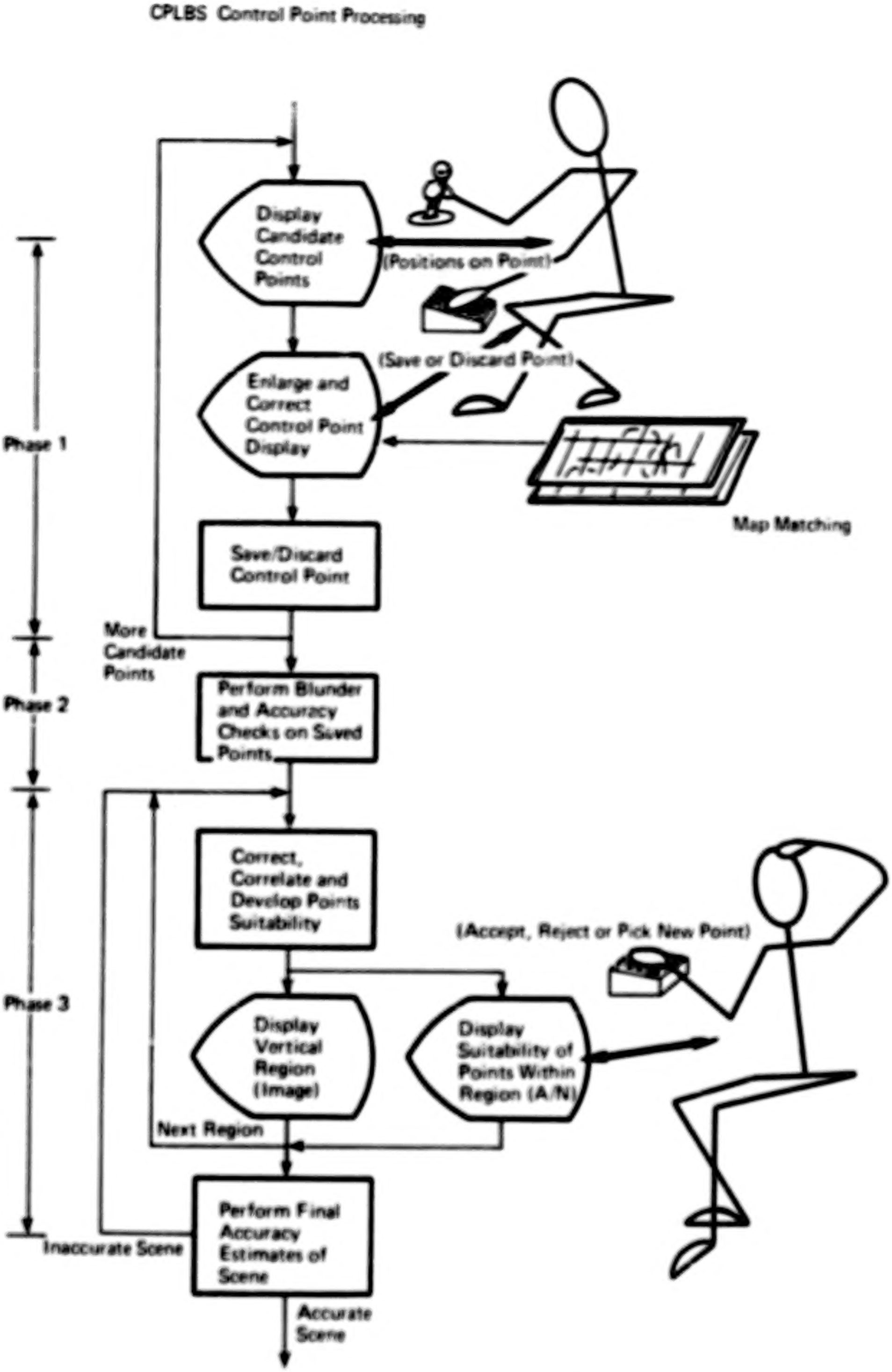
CPLBS Control Point Processing
Display Candidate Control Points
(Positions on Point)
(Save or Discard Point)
Enlarge and Correct Control Point Display
Map Matching
Save/Discard Control Point
Phase 1
More Candidate Points
Phase 2
Perform Blunder and Accuracy Checks on Saved Points
Phase 3
Correct, Correlate and Develop Points Suitability
(Accept, Reject or Pick New Point)
Display Vertical Region (Image)
Display Suitability of Points Within Region (A/N)
Next Region
Inaccurate Scene
Perform Final Accuracy Estimates of Scene
Accurate Scene

Figure 29. CPLBS Control Point Processing Overview.

The extracted data (512 x 512) is displayed for operator inspection. The operator locates the appropriate scene feature through the use of his joystick-cursor. The operator presses the appropriate function key which causes the m x m pixels about the cursor to be expanded, incorporating high-frequency corrections, to 512 x 512 pixels so that the display scale matches the corresponding map. If the Zoom Transfer Scope has a 4X magnification factor, then the m x m matrix will be 53 x 53 if the map scale is 1:24K. Another map scale will require the m x m to be a different size. With the aid of a Zoom Transfer Scope the operator can exactly superimpose the display feature with the map feature and enter the exact pixel location corresponding to the map coordinates. When all the candidate points have been processed and either identified or rejected, this phase is complete.

In the Map Point Set Refinement phase, attitude/altitude models for the scene are developed using the image and geodetic coordinates of the identified features combined with the attitude and ephemeris data provided for the scene. The attitude/altitude model is used to calculate regional estimates of accuracy to which the scene may be corrected. This accuracy check verifies that the error models may be used to compute acceptably accurate geodetic coordinates for points selected from the scene data.

The final phase is Machine-Locatable Point Selection which permits the operator to view the scene in large segments, allowing him to select scene features as candidate CP by positioning the cursor over them. The suitability of each feature for use in the Control Location Algorithm, and a measure of the curvature of its autocorrelation function, is presented to the operator for his acceptance or rejection. Any features accepted are geometrically corrected for local distortions. The geodetic coordinates are calculated from their image coordinates and the attitude/altitude model computed in the Map Point Set Refinement phase. An accuracy check is made to present the operator with an estimated error of the position coordinates. If the operator accepts the point, it is placed in the CP library as a

32 x 32 pixel matrix about the CP image coordinates. If the first two phases fail or are not used, the final phase may be still executed, provided data from past history is present as input to the attitude/altitude error models. An alternate consideration must be present, if maps are not available for the land areas in the image scene. This case would only use phase 3, and excludes the possibility of an exact geodetic correction. Any attitude/altitude corrections are made according to simpler error models. This last case refers to the control points obtained as relative control points (RCP).

The following algorithms are used in the Control Point Library Build System:

a. Mean and Standard Deviation of Pixel Intensity

b. Enhancement Table for Display Contrast

c. Expansion of Data

    Along Scan Corrections
    Cubic Convolution Interpolation

d. Accuracy Estimate

    Attitude/Altitude Error Model
    Blunder Check

e. Autocorrelation Matrix

f. Suitability Index.

The purpose of the blunder check is to eliminate operator error in matching the map points from the screen image to the map image.

3.2.4.2 Geometric Error Modeling

There are two basic approaches for generating geometric error model coefficients given the location of control points in the input image space. In the first approach, the functional form of the mapping between the uncorrected (input) and corrected images is assumed to be a bivariate polynomial. All geometric coefficients of the assumed function are computed through the use of the control points. In the second approach, geometric distortion models of each of the error sources are constructed with ancillary and a priori information used to evaluate as many of the model coefficients as possible. The remaining coefficients are evaluated from control points.

The Landsat series would require functions of a relatively high order (i.e., many coefficients) when using the direct function mapping approach. There is, however, an abundance of fairly accurate error information (e.g., mirror models, attitude measurements, and altitude estimates) available. Thus, the second approach requires fewer coefficients to be evaluated. Generally, the number of control points needed to attain a given accuracy increases as the number of coefficients to be determined increases. Therefore, the second approach has been selected for evaluating geometric distortion coefficients, and is currently being implemented by the Master Data Processor (MDP).

3.2.4.2.1 Error Sources

There are three principal error sources:

a. Sensor

b. Platform

c. Scene.

The particular errors and their magnitudes within each principal error source for Landsat-D are shown in Tables 7 and 8. These errors can be categorized as low-frequency or high-frequency errors. Low-frequency errors are errors whose rate of occurrence is of the order of a scene. High-frequency errors are errors whose rate of occurrence is of the order of a single sweep. High-frequency errors are compensated for during resampling. Tables 7 and 8 indicate the residual error following low-frequency error correction and then resampling. Figure 30 illustrates the effect on the image due to these error sources.

Table 7. TM Error Sources.

Error Types	Total Magnitude (Max) Meters		Magnitude After System Correction (Before Resampling) Meters		Magnitude After Resampling Meters	
	(Along-Scan) Cross-Track ΔY	(Cross-Scan) Along-Track ΔX	Cross-Track ΔY	Along-Track ΔX	Cross-Track ΔY	Along-Track ΔX
Sensor Errors						
Mirror Scan Linearity	28	38	3	3	3	3
Scan Line Length	15	-	15	-	Neg	-
Band-to-Band Offset	3750	-	15	-	3	-
Detector Sampling Delay	0	0	0	0	0	0
Panoramic Distortion	120	-	Neg	-	Neg	-
Differential Scale	0	0	0	0	0	0
Thermal (Not Modeled)	2.6	2.6	2.6	2.6	2.6	2.6
Platform Errors						
Attitude	370	470	1.5	1.5	1.5	1.5
Altitude	20	-	1	-	1	-
Velocity	-	10	-	1	-	1
Ephemeris	150	750	2.6	2.6	2.6	2.6
Scan Skew	-	0	-	0	-	0
Scene Errors						
Earth Rotation	13300	-	16	-	Neg	-
Perspective Geometry (Earth Curvature)	75	-	Neg	-	Neg	-
Map Projection	[1]1700	1700	Neg	Neg	Neg	Neg

[1] Only lat/long to tangent space, does not include map (UTM) to lat/long.

Table 8. MSS Error Sources.

Error Types	Total Magnitude (Max) Meters		Magnitude After System Correction (Before Resampling) (Meters)		Magnitude After Resampling Meters	
	(Along-Scan) Cross-Track ΔY	(Cross-Scan) Along-Track ΔX	Cross-Track ΔY	Along-Track ΔX	Cross-Track ΔY	Along-Track ΔX
Sensor Errors						
Mirror Scan Linearity	370	-	8	-	8	-
Scan Line Length	28	-	28	-	Neg	-
Band-to-Band Offset	80	-	60	-	3	-
Detector Sampling Delay	11	-	11	-	Neg	-
Panoramic Distortion	120	-	Neg	-	Neg	-
Differential Scale	60,720	?	Neg	-	Neg	-
Thermal (Not Modeled)	?	?	?	?	?	?
Platform Errors						
Attitude	370	370	6	6	6	6
Altitude	20	-	1	-	1	-
Velocity	-	10	-	1	-	1
Ephemeris	150	750	2.6	2.6	2.6	2.6
Scan Skew	-	80	-	Neg	-	Neg
Scene Errors						
Earth Rotation	13300	-	16	-	Neg	-
Perspective Geometry	75	-	Neg	-	Neg	-
Map Projection	1700	1700	Neg	Neg	Neg	Neg

MICROFILMED FROM
BEST AVAILABLE COPY

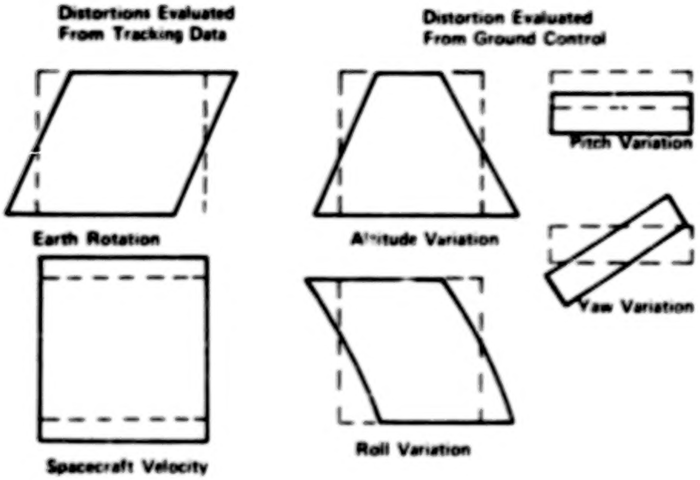
Distortions Evaluated From Tracking Data
Distortion Evaluated From Ground Control
Earth Rotation
Altitude Variation
Pitch Variation
Yaw Variation
Spacecraft Velocity
Roll Variation

a. Distortions Whose Effects Are Variable in Nature

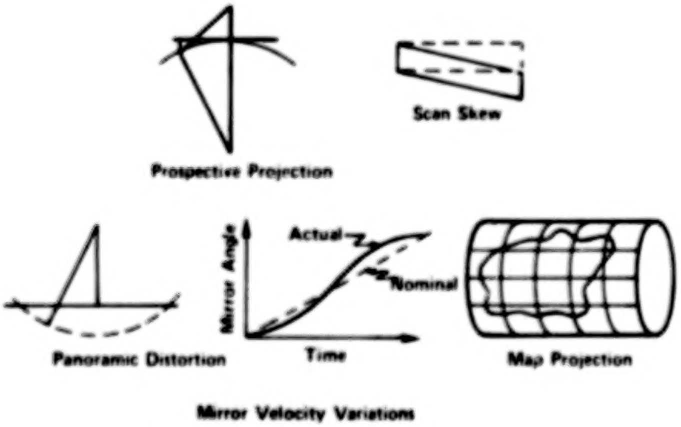
Prospective Projection
Scan Skew
Actual
Nominal
Mirror Angle
Time
Panoramic Distortion
Map Projection
Mirror Velocity Variations

b. Distortions Whose Effects Are Systematic in Nature

Figure 30. Scanning Sensor (TM & MSS) Geometric Distortions.

There are three geometric error modeling steps as shown in Figure 31. The first step maps the observed control point locations to the systematically corrected tangent space. All coefficients for the low-frequency errors not requiring control points are calculated in this step.

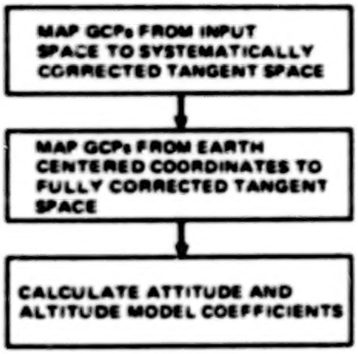
MAP GCPs FROM INPUT SPACE TO SYSTEMATICALLY CORRECTED TANGENT SPACE
MAP GCPs FROM EARTH CENTERED COORDINATES TO FULLY CORRECTED TANGENT SPACE
CALCULATE ATTITUDE AND ALTITUDE MODEL COEFFICIENTS

Figure 31. Error Modeling Steps.

The second step calculates the locations of the control points in the fully corrected tangent space. The nominal, earth-fixed coordinates of the control points are used in this step. The only difference between geometric correction and temporal registration occurs here. For geometric correction, the earth-fixed coordinates of the control points are based on map measurements; for temporal registration, they are based on a previously processed image.

The third step is to calculate the coefficients of the attitude and altitude error models. This is accomplished by comparing the coordinates of the control points in the two distinct tangent spaces. The GCP coordinate differences in the tangent plane are due solely to attitude and altitude errors. These differences (residuals) along with ADT-supplied attitude and altitude values, permit updated least-squares estimates of the attitude and altitude models to be computed.

Figure 32 illustrates this overall processing flow. Inputs available from the ancillary data tape (ADT) include scene nadir coordinates and time, spacecraft heading and velocity, and spacecraft attitude and altitude values centered around nadir time. The CP geodetic coordinates and image coordinates, determined previously by CP processing, are also input.

Additional computations needed for output image framing are also computed, since they make use of the updated attitude and altitude models.

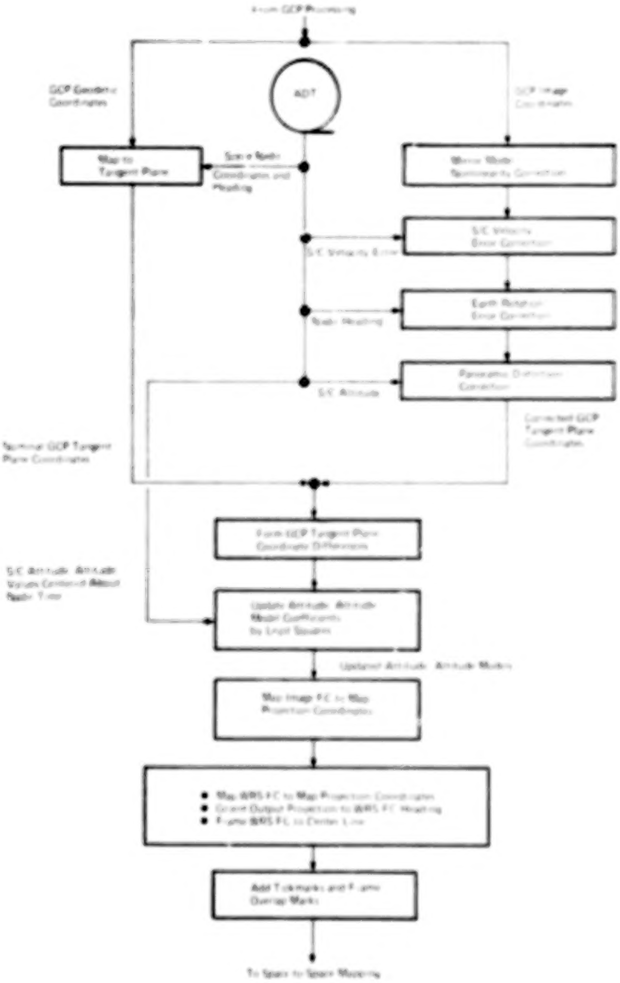
From GCP Processing
GCP Geodetic Coordinates
ADT
GCP Image Coordinates
Map to Tangent Plane
Scene Nadir Coordinates and Heading
Mirror Mode Nonlinearity Correction
S/C Velocity Error Correction
S/C Velocity Error
Earth Rotation Error Correction
Nadir Heading
Panoramic Distortion Correction
S/C Attitude
Corrected GCP Tangent Plane Coordinates
Nominal GCP Tangent Plane Coordinates
Form GCP Tangent Plane Coordinate Differences
S/C Attitude, Altitude Values Centered About Nadir Time
Update Attitude, Altitude Model Coefficients by Least Squares
Updated Attitude, Altitude Models
Map Image FC to Map Projection Coordinates
Map WRS FC to Map Projection Coordinates
Orient Output Projection to WRS FC Heading
Frame WRS FC to Center Line
Add Tickmarks and Frame Overlap Marks
To Space to Space Mapping

Figure 32. Geometric Error Model Coefficient Processing.

MICROFILMED FROM
BEST AVAILABLE COPY

First the image format center (FC) is mapped to output map coordinates for all map projections of interest. The world reference system (WRS) FC for the scene is similarly mapped, and its heading angle is used to orient the output projection. The line and sample coordinate differences are used to shift the image, so that the WRS FC falls on the center line at an integer pixel location. These steps will be described in more detail in the following subsections for the MSS and TM scanning mirror sensors.

3.2.4.2.2 Systematic Correction of Observed Control Point Locations

Systematic correction of the observed control point (CP) locations involves a series of coordinate transformations that begin with the input space and ends with the systematically corrected tangent space. The tangent space represents a cylinder tangent to the earth spheroid at the ground track of the spacecraft nadir. The last of the transformations defines an image in which all low-frequency, systematic, geometric errors have been removed.

3.2.4.2.2.1 Mirror Scan Velocity Profile and Panoramic Distortion

Mirror velocity -- The scanning mirror has a nonlinear sweep characteristic. Since data samples are taken at regular intervals of time, the varying mirror rate produces along-scan geometric distortion.

Panoramic distortion -- Data samples are taken at regular intervals of time (and, hence, nominally at regular angular intervals along the scan). However, the ground distance between samples is proportional to the tangent of the scan angle rather than to the angle itself. This effect produces along-scan geometric distortion.

In the conventional image coordinate system for Landsat imagery, the X-axis is tangent to the subsatellite tracks and positive in the direction of spacecraft motion (cross-scan). The Y-axis is orthogonal to the X-axis and positive in the direction of scan (along-scan). Let (X_1, Y_1) be the input image line and sample coordinates, respectively, before error modeling. Subscripted X and Y values indicate processing stages.

Compute equation (11):

$$X_1 = L - L_{nadir}$$

$$Y_1 = \frac{S - I_s + 1}{2} \qquad (11)$$

The distortions in the input image control point locations due to mirror scan nonlinearities and panoramic distortion are corrected by a model of equation (12):

$$X_2 = \begin{cases} X_1 & \text{FOR MSS} \\ X_1 + L_o + L_1 Y_1 + L_2 Y_1^2 + L_3 Y_1^3 & \text{FOR TM} \end{cases}$$

$$Y_2 = \frac{I_S H_o}{W_S} \text{ TAN } \left[K_o + Y_1 \left(K_1 + \frac{2\,\delta mm}{I_S} \right) + K_2 Y_1^2 + K_3 Y_1^3 + K_4 Y_1^4 \qquad (12)$$

Where:

I_S -- the nominal number of samples per input image line
H_o -- nominal spacecraft altitude (meters)

W_S -- nominal swath width (meters)

L_o, L_1, L_2, L_3, K_o, K_1, K_2, K_3, K_4 -- parameters of the mirror model (supplied by NASA)

θmm -- maximum mirror angle (radians)

3.2.4.2.2.2 Differential Scale Errors (MSS Only)

Distortions due to differential input and output scales are corrected by the model of equation (13):

$$X_3 = \frac{O_L}{I_L} X_2$$

$$Y_3 = \frac{O_S}{I_S} Y_2 \qquad (13)$$

where:

O_L, O_S -- the number of lines and samples per line in the output image

I_L, I_S -- the nominal number of lines and samples per line in the input image

X_2, Y_2 -- the input-image control point coordinates corrected for all systematic errors.

3.2.4.2.2.3 Scan Skew Error (MSS Only)

During the time that the MSS mirror completes one active scan, the spacecraft moves along the ground track. Thus, the ground swath scanned is not normal to the ground track but is slightly skewed. This produces cross-scan geometric distortion.

Cross-scan distortions caused by scan skew are corrected by the model of equation (14):

$$X_4 = X_3 + K_{ss}Y_3 \tag{14}$$

where K_{ss} is a constant determined by the amount of scan skew.

3.2.4.2.2.4 Spacecraft Velocity Error

If the spacecraft velocity departs from nominal, the ground track covered by a fixed number of successive mirror sweeps changes. This produces a cross-scan scale distortion.

Cross-scan distortions caused by spacecraft velocity errors are corrected by the model of equation (15):

$$X_5 = \left(1 + \frac{\Delta V}{V}\right) X_4 \tag{15}$$

where $\frac{\Delta V}{V}$ is the normalized spacecraft velocity error (obtained from ephemeris data supplied by NASA for the scene).

3.2.4.2.2.5 Earth Rotation Distortion

As successive scans are completed, the earth rotates beneath the sensor. The ground swath scanned by the mirror gradually migrates westward with a speed that is a function of spacecraft latitude.

Distortions due to earth rotation are corrected by the model of equation (16):

$$T_{ER} = \frac{T_s X_1}{N} + \frac{T_N Y_1}{I_S}$$

$$X_6 = X_5 + V_{RA} \left(T_{ER} + 20\right) -20 \; V_{RAN} \qquad (16)$$

$$Y_4 = Y_3 - V_{RC} \left(T_{ER} + 20\right) +20 \; V_{RCN}$$

where,

T_s -- time between mirror sweeps

T_m -- nominal number of samples per line

N -- lines scanned per sweep

V_{RA}, V_{RC}, V_{RAN} -- function of geodetic latitude of a control point, geodetic latitude of nadir, and spacecraft heading.

The earth rotation correction, as implemented by error modeling, is a global, continuous correction. The true earth rotation correction is a function of sweep number but is discontinuous in X. The difference is a fraction of a pixel from line to line.

The integral portion is applied by appending an appropriate number of "fill" pixels (bytes) to either end of each scan line. Rather than actually write the fill bytes on a partially processed output tape, each scan line is preceded by a left and right fill count necessary for properly aligning the data. The computation of the left and right fill pixels required for each scan line is accomplished during geometric interpolation. The fractional portion of the earth rotation correction is applied as a high-frequency correction during the resampling operation.

3.2.4.2.2.6 Perspective Geometry Error

Perspective projection -- For some applications, it is desired that Landsat images represent the projection of points on the earth upon a plane tangent to the earth, with all projection lines normal to the plane. The sensor data represent perspective projections; i.e., projections whose lines all meet at a point above the tangent plane. For the MSS, this produces only along-scan distortion.

Along-scan errors due to earth curvature and panoramic projection are corrected by the model of equation (17):

$$Y_5 = Y_4 - K_{EC}Y_3^3 - K_{EC}^2Y_3^5 \qquad (17)$$

where $K_{EC} = \frac{-1}{2R_E H_o}$

R_E -- the radius of the earth at the spacecraft nadir (meters) and H_o is as defined previously.

3.2.4.2.2.7 Map Projection Errors

A map projection is a formal mathematical definition of how the curved surface of the earth may be represented on a plane surface (i.e., the map). This produces nonlinear distortions in both the along-scan and the cross-scan.

3.2.4.2.3 Mapping Nominal Control Point Locations to the Tangent Space

The nominal control point locations are given in earth-centered coordinates (latitude and longitude). These locations are mapped into the fully corrected tangent space. This mapping of points in earth-centered coordinates into tangent space coordinates involves the following steps:

a. Calculate the earth-centered coordinates of the spacecraft nadir directly from the latitude and longitude coordinates of the nadir, as shown in Figure 33.

b. Calculate the values of the elements of the three rotation matrixes. These cause rotations of the coordinate axes, so that the resulting axes are parallel to the tangent-space coordinate axes. These equations are shown in Figure 34.

c. For each control point, the transformation equation in Figure 35 is evaluated.

3.2.4.2.4 Attitude/Altitude Modeling

The only Landsat errors to be evaluated with control points are the attitude and ephemeris measurement errors. These are related to position errors as shown in Figure 36. Since it is impossible to distinguish between small errors in pitch and roll and small errors in along-track and cross-track position (see Figure 37), the position errors are considered to be zero, and their effects are accounted for in the pitch and roll estimates. This produces the relations shown in

$$LC_0 = \mathrm{TAN}^{-1}\left(\frac{B^2\ \mathrm{TAN}\ LG_0}{A^2}\right)$$

$$R_0 = \sqrt{\frac{A^4 \cos^2 LG_0 + B^4 \sin^2 LG_0}{A^2 \cos^2 LG_0 + B^2 \sin^2 LG_0}}$$

$$X_0 = R_0 \cos G_0 \cos LC_0$$

$$Y_0 = R_0 \sin G_0 \cos LC_0$$

$$Z_0 = R_0 \sin LC_0$$

Figure 33. Earth-Centered Coordinates of Spacecraft Nadir.

$$M_A = \begin{bmatrix} \cos(\beta - \frac{\pi}{2}) & \sin(\beta - \frac{\pi}{2}) & 0 \\ -\sin(\beta - \frac{\pi}{2}) & \cos(\beta - \frac{\pi}{2}) & 0 \\ 0 & 0 & 1 \end{bmatrix}$$

$$M_L = \begin{bmatrix} \cos(\frac{\pi}{2} - LG_0) & 0 & -\sin(\frac{\pi}{2} - LG_0) \\ 0 & 1 & 0 \\ \sin(\frac{\pi}{2} - LG_0) & 0 & \cos(\frac{\pi}{2} - LG_0) \end{bmatrix}$$

$$M_G = \begin{bmatrix} \cos G_0 & \sin G_0 & 0 \\ -\sin G_0 & \cos G_0 & 0 \\ 0 & 0 & 1 \end{bmatrix}$$

Figure 34. Rotation Matrixes.

$$\begin{bmatrix} X_T \\ Y_T \\ Z_T \end{bmatrix} = M_A\ M_L\ M_G \begin{bmatrix} X_E - X_0 \\ Y_E - Y_0 \\ Z_E - Z_0 \end{bmatrix}$$

Figure 35. Earth-Centered to Tangent-Space Transformations.

Figure 38 and introduces an acceptably small error. The selected correction approach is referred to as attitude/altitude modeling.

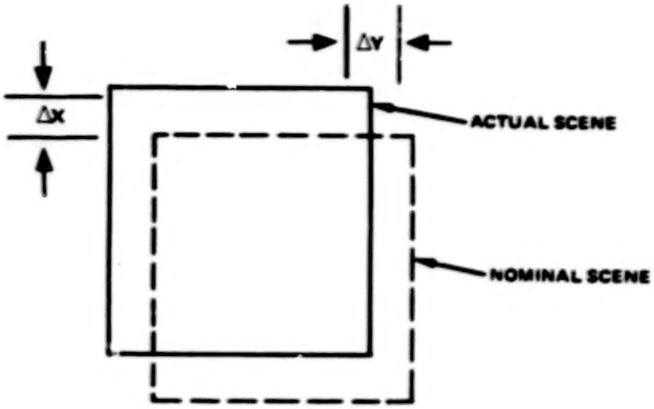
ΔY
ΔX
ACTUAL SCENE
NOMINAL SCENE

Figure 36. Effects of Attitude and Position (Ephemeris) Errors.

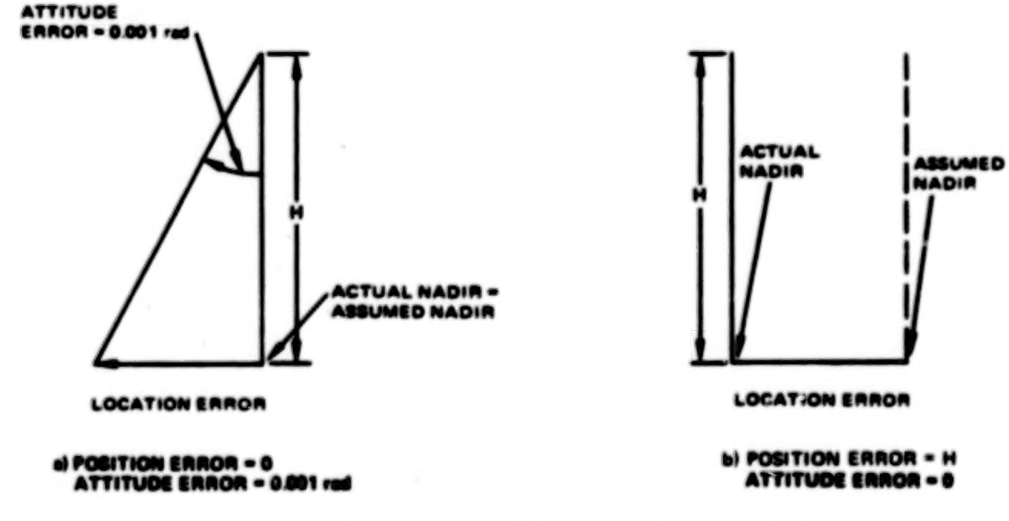
ATTITUDE ERROR = 0.001 rad
H
ACTUAL NADIR = ASSUMED NADIR
LOCATION ERROR
H
ACTUAL NADIR
ASSUMED NADIR
LOCATION ERROR

a) POSITION ERROR = 0
ATTITUDE ERROR = 0.001 rad

b) POSITION ERROR = H
ATTITUDE ERROR = 0

Figure 37. Equivalence of Attitude and Position Errors.

$$\begin{bmatrix} \Delta X \\ \Delta Y \end{bmatrix} = \begin{bmatrix} 0 & H & V & 0 \\ -\frac{H^2 + V^2}{H} & 0 & 0 & \frac{V}{H} \end{bmatrix} \begin{bmatrix} \phi \\ \theta \\ \psi \\ \Delta H \end{bmatrix}$$

Figure 38. Image Error Effects of Attitude and Altitude Errors.

Attitude/altitude modeling can be implemented in three different ways: scene, swath, or recursive swath. In scene modeling, an attitude/altitude model is constructed from control points located in that scene. In swath modeling, the model is constructed from control points located in several contiguous scenes. In recursive swath modeling, a swath attitude/altitude model is updated on a scene-by-scene basis as control points in a scene become available.

Scene modeling has the simplest mathematical form and computational procedure but requires the most control points, and is not capable of correcting a scene if there are no control points in the scene.

Both batch and recursive swath modeling require fewer control points on a per scene basis and can bridge a scene containing no control points. Each, however, has a more complex mathematical model than scene processing and requires more complicated computational procedures.

The **advantages** and disadvantages of these three approaches for Landsat-D are summarized in Table 9.

Table 9. Attitude/Altitude Error Modeling Approaches Comparison.

Approach Attribute	Scene	Batch Swath	Recursive Swath
Number control points required	Six per scene	Two per scene	Two per scene
Model complexity	Least complex	More complex	Most complex
Procedural complexity	Least complex	More complex	Most complex
Advanced data read required	One scene	One swath	One scene
Applicability	Always	Requires batch test	Requires continuous test
Bridging scenes with no control	No	Yes	Yes
Model available	After scene	After whole swath	After each scene

Batch swath modeling requires that the entire swath be searched for control points before the first scene in the swath can be corrected. Recursive swath modeling has the theoretical advantage of permitting each scene in the swath to be corrected with models based on only those control points found up to that point in the swath. However, simulations of Landsat-D performance have shown that, although it is possible to interpolate over large areas with acceptably small error, errors build up rapidly when the models are extrapolated past regions containing control points. Thus, the theoretical advantage of recursive swath modeling is not realizable in actual practice. Since recursive swath processing is procedurally more complex and hence more costly than batch processing, and since it has no practical advantage over batch swath processing, this approach was not pursued.

Swath modeling has several potential advantages, the principal ones being:

a. It is expected that fewer GCPs on a per-scene basis would be required for a given accuracy, since the greater vertical spread in the GCPs would mean smaller errors in the estimated coefficients and thus greater image accuracy.

b. An attitude/altitude model could be constructed for a scene containing no GCPs.

A simulation study further investigated swath attitude/altitude modeling. The number of GCPs was varied from 3 to 9, as was the distribution of the GCPs over a swath. The swath was defined as 11 contiguous 185 km X 185 km frames (or scenes).

The conclusion drawn from the simulation was that swath attitude/altitude modeling is feasible from an image accuracy point of view. However, due to procedural problems, swath modeling was rejected. The principal reasons for the rejection were:

a. Scene modeling must always be available; therefore, the potential savings in the number of GCPs would not be realized.

b. The variable length of swaths implies the need for tests and branches in the geometric correction function, complicating programming and making testing more difficult.

c. The output product requires that each scene have appended at its beginning the grids required for resampling. The grids cannot be computed until all necessary control points have been accessed from the image data and processed. This requires the entire swath be stored (11 frames), necessitating large amounts of mass memory.

Attitude/altitude modeling, on a scene-by-scene basis, will be described for the Landsat series spacecraft, as implemented by the Master Data Processor.

3.2.4.2.4.1 Modeling of Landsat-1,-2, and-C Sensor Attitude and Altitude

The differences between nominal and corrected input-image control point coordinates, along with all applicable ephemeris and attitude data, are processed by a weighted least-squares estimator, which computes the format center coordinates and the coefficients of the attitude and altitude models.

The order of the attitude/altitude model depends on the frequency and accuracy of the measurements and the region over which the model is considered valid (i.e., a scan or a swath). Landsat-1, -2, and -C attitude data has reasonably good rate data and poor absolute location (on the order of 0.1° error). Attitude estimates and tracking station altitude estimates are at 1-second intervals over the time interval of interest. Spacecraft roll, pitch, and yaw variations are described by cubic functions of time (4 X 3 coefficients), and spacecraft altitude variations by a linear function of time (two coefficients). The mathematical model is shown in equation (18):

$$\begin{bmatrix} \phi \\ \theta \\ \psi \\ \Delta H \end{bmatrix} = \begin{bmatrix} 1 & t_i & t_i^2 & t_i^3 & 0 & 0 & 0 & 0 & 0 & 0 & 0 & 0 & 0 & 0 \\ 0 & 0 & 0 & 0 & 1 & t_i & t_i^2 & t_i^3 & 0 & 0 & 0 & 0 & 0 & 0 \\ 0 & 0 & 0 & 0 & 0 & 0 & 0 & 0 & 1 & t_i & t_i^2 & t_i^3 & 0 & 0 \\ 0 & 0 & 0 & 0 & 0 & 0 & 0 & 0 & 0 & 0 & 0 & 0 & 1 & t_i \end{bmatrix} \begin{bmatrix} (\phi_0, \phi_1, \phi_2, \phi_3)^T \\ (\theta_0, \theta_1, \theta_2, \theta_3)^T \\ (Y_0, Y_1, Y_2, Y_3)^T \\ (h_0, h_i)^T \end{bmatrix} = B_i\underline{C} \qquad (18)$$

The measurement error model for the i th GCP is shown in equation (19):

$$\begin{bmatrix} \Delta X_i \\ \Delta Y_i \end{bmatrix} = \begin{bmatrix} 0 & H_i & Y_i & 0 \\ \dfrac{H^2+Y_i^{\,2}}{H} & 0 & 0 & \dfrac{Y_i}{H} \end{bmatrix} B_i\underline{C} = A_i B_i \underline{C} \qquad (19)$$

3.2.4.2.4.2 Modeling of Landsat-D Sensor Attitude and Altitude

The Landsat-D altitude control system will provide two observations per second of roll, pitch, and yaw from a reference direction. The observations will have good absolute location (on the order of 0.01° error); however, the reference direction is slowly drifting with time (about 10^{-6} degrees per second). The reference direction can be considered a constant for periods of time equivalent to a scene.

Spacecraft altitude measurements, two observations per second, will be available from ground tracking stations or the Global Positioning System (GPS). The altitude error will change slowly due to the nature of the orbital motion and orbit determination and can also be modeled as a constant over an interval of time corresponding to a scene. Spacecraft attitude and altitude models are shown in equation (20):

$$\begin{bmatrix} \phi \\ \theta \\ \Psi \\ \Delta H \end{bmatrix} = \begin{bmatrix} 1 & 0 & 0 & 0 \\ 0 & 1 & 0 & 0 \\ 0 & 0 & 1 & 0 \\ 0 & 0 & 0 & 1 \end{bmatrix} \begin{bmatrix} \phi_o \\ \theta_o \\ \Psi_o \\ h_o \end{bmatrix} = B\underline{C} \qquad (20)$$

The measurement error model for the i th GCP is shown in equation (21):

$$\begin{bmatrix} \Delta X_i \\ \Delta Y_i \end{bmatrix} = \begin{bmatrix} 0 & H_i & Y_i & 0 \\ -\dfrac{H^2 + Y_i^2}{H} & 0 & 0 & \dfrac{Y_i}{H} \end{bmatrix} \begin{bmatrix} 1 & 0 & 0 & 0 \\ 0 & 1 & 0 & 0 \\ 0 & 0 & 1 & 0 \\ 0 & 0 & 0 & 1 \end{bmatrix} \begin{bmatrix} \phi_o \\ \theta_o \\ \Psi_o \\ h_0 \end{bmatrix} = A_i B_i{}^{(0)}\underline{C} \qquad (21)$$

3.2.4.2.4.3 Weighted Least-Squares Estimator for Attitude and Altitude

The equations for the weighted least-squares computation are shown in equation (22):

$$Z = (X_1, Y_1 \ldots\ldots X_N, Y_N)^T \qquad \text{Observation Vector}$$

$$M = \begin{bmatrix} A_1 & B_1 \\ A_2 & B_2 \\ \cdot & \cdot \\ \cdot & \cdot \\ \cdot & \cdot \\ \cdot & \cdot \\ A_N & B_N \end{bmatrix} \qquad \text{N GCPs} \qquad (22)$$

$$Z = M\,\underline{C} \qquad \text{Equations of Condition}$$

$$(M^T M)\underline{C} = M^T \underline{Z} \qquad \text{Normal Equations}$$

$$\underline{C} = (M^T V^{-1} M)^{-1} M^T \underline{Z} \qquad \text{Weighted least-squares solution}$$

V is weighting matrix

$$\text{Cov}\underline{C} = (M^T V^{-1} M)^{-1} \qquad \text{Covariance matrix}$$

The weighting matrix, V, allows for the possibility that some control points may be known more accurately than others.

The information necessary for the attitude/altitude weighted least-squares estimator is:

a. The observed control point locations (x_i, y_i, t_i) corrected for systematic distortions

b. The nominal control point locations (X_i, Y_i) as stored in the control point library

c. The attitude measurement system (AMS) estimates $(\phi_j, \theta_j, \psi_j, t_j)$

d. The tracking station or ephemeris predict altitude estimates (H_k, t_k)

e. The weighting coefficients based on the expected errors (V_c, V_a, V_h).

The subscripts i, j, and k indicate that the measurement values are known at different times. The modeling approach is shown in Figure 39.

3.2.4.3 Space-to-Space Mapping

The geometric error models lead directly to explicit, correction transformations from input to output space. The corresponding inverse transformation, however, from output space to input space is only implicit. Space-to-Space mapping is the process by which a known location in the input space is mapped through geometric distortion models to the corresponding input space location.

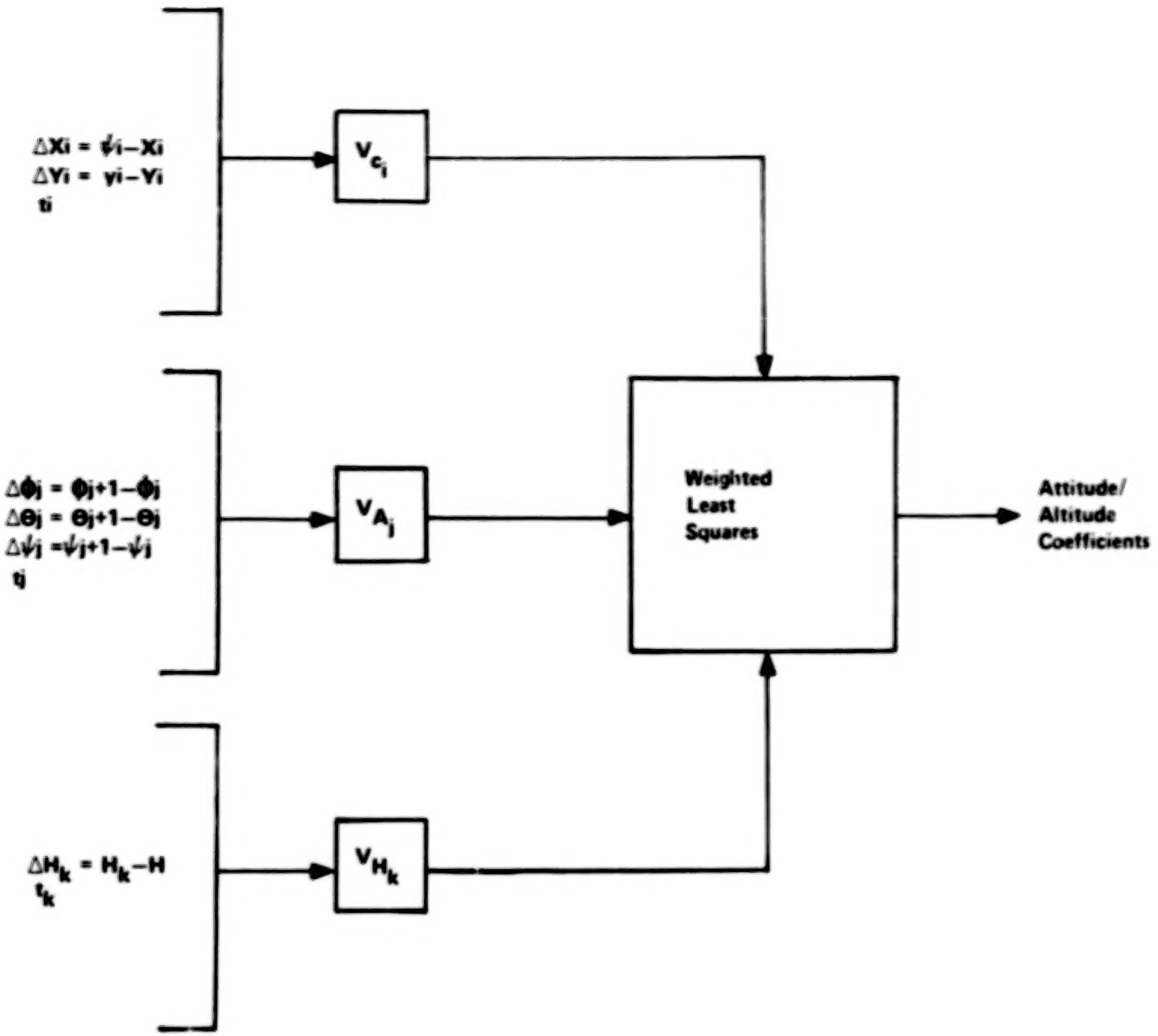
ΔXi = ẋi−Xi
ΔYi = yi−Yi
ti
V_{c_i}
Δφj = φj+1−φj
Δθj = θj+1−θj
Δψj = ψj+1−ψj
tj
V_{A_j}
ΔH_k = H_k−H
t_k
V_{H_k}
Weighted
Least
Squares
Attitude/
Altitude
Coefficients

Figure 39. Modeling Approach for Attitude/Altitude Estimates.

The space-to-space mapping processing steps are shown in Figure 40. The procedure is:

a. A rectangular array of grid points is defined in the output space. The spacing of this array is selected to keep interpolation errors less than an acceptable limit in the presence of the anticipated worst-case geometric distortions. This array is invariant for a given map projection, output image, and pixel size.

b. Using the equations of the map projection of the output image, the grid points are transformed to geodetic coordinates (latitude and longitude) and then to a tangent plane centered at the format center of the input image.

c. The tangent plane grid points are mapped (T_1) to the input space by the approximate output-to-input mappings.

d. The resulting input points are **mapped** (I_T) to the output space, using the exact input-to-output transformations (from the geometric error model).

e. The residuals between the nominal and mapped grid points are used to adjust the input space coordinates in a linear manner; this process is repeated.

f. It is estimated that, at most, three interactions will be required to produce a set of input space grid locations, which, when mapped through the input-to-output mapping, will result in the desired rectangular array of output space grid points.

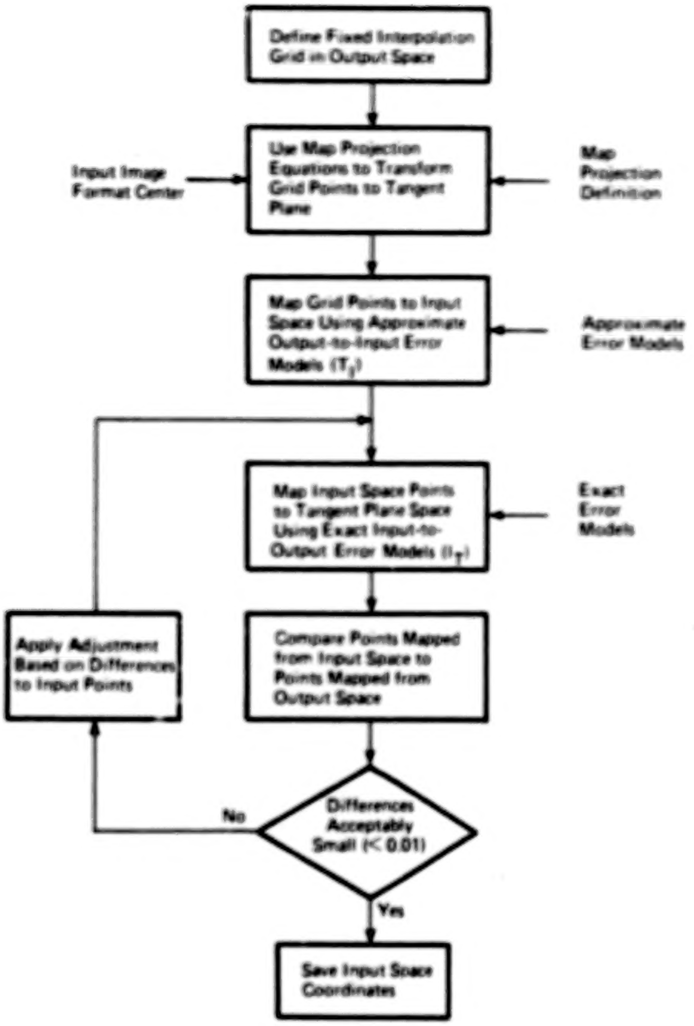
Define Fixed Interpolation Grid in Output Space
Input Image Format Center
Use Map Projection Equations to Transform Grid Points to Tangent Plane
Map Projection Definition
Map Grid Points to Input Space Using Approximate Output-to-Input Error Models (T_I)
Approximate Error Models
Map Input Space Points to Tangent Plane Space Using Exact Input-to-Output Error Models (I_T)
Exact Error Models
Apply Adjustment Based on Differences to Input Points
Compare Points Mapped from Input Space to Points Mapped from Output Space
No
Differences Acceptably Small (< 0.01)
Yes
Save Input Space Coordinates

Figure 40. Space-to-Space Mapping.

The accurate input-to-output transformations are correct for all known sources of error, except line-length variations and the fractional position of earth rotation error, which are accounted for as high-frequency corrections in the resampling function.

The output of the space-to-space mapping function is a table of line and pixel coordinates in the input space corresponding to the coordinates of the rectangular array of grid points in the output space. The current MDP system will execute this series of steps for each required map projection. Since the computational load required to implement the space-to-space mapping is a function of the total number of grid points needed for resampling, alternate methods of generating the required grid points for multiple map projections have been investigated.

One alternate approach is shown in Figure 41 for the Landsat-D mapping requirements. Landsat-D requires that grid points be created for three projections: Lambert Conformal Conic (LCC), Space Oblique Mercator (SOM), and Universal Transverse Mercator (UTM)/Polar Stereographic (PS). The approach involves developing the grids for the LCC as previously described. However, once a primary grid point correspondence has been determined for the LCC map projection, it can be used to determine other map projection grids by evaluating a composition of known functions. Figure 42 illustrates the spaces and functions involved. The function f_1 is evaluated by using cubic interpolation between the primary and grid points. The map projection functions U_G, S_G, and G_L are assumed to be known; the function f_2 is then a composition of S_G, G_L, and f_1. This composition of functions technique requires fewer calculations than implementing the iterative technique three times.

Currently, the MDP implements the UTM/PS or SOM map projection. Each map projection has certain desirable characteristics, with the user selecting the projection best suiting his requirements. In a Transverse Mercator

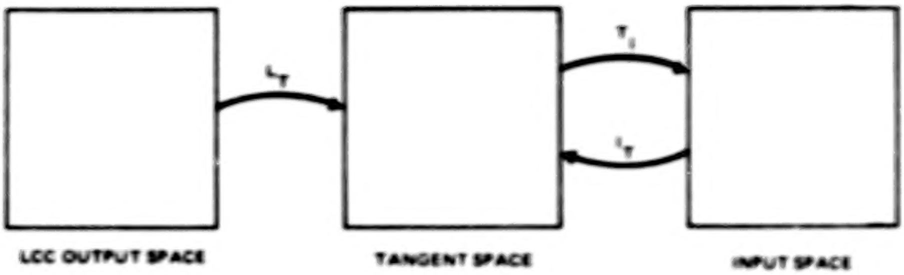
LCC OUTPUT SPACE
TANGENT SPACE
INPUT SPACE
L_T
T_I
I_T

Figure 41. Iterative Technique for LCC Space-to-Space Mapping.

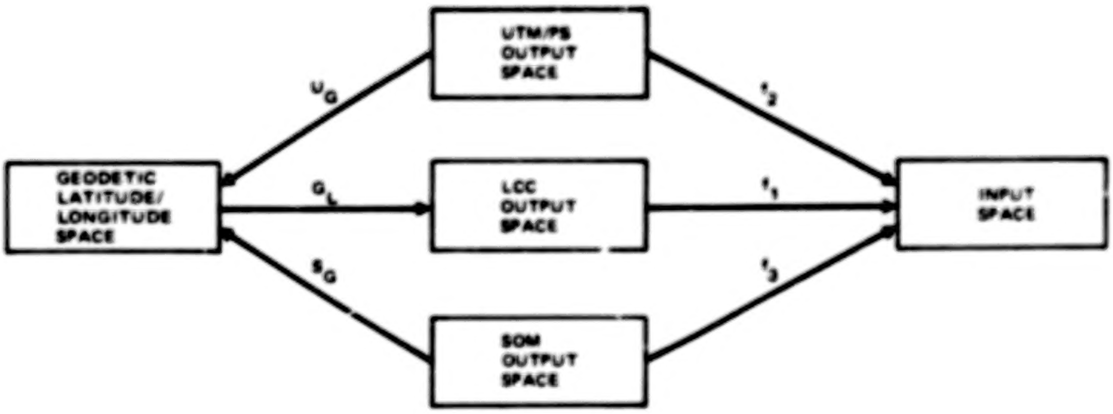
GEODETIC LATITUDE/ LONGITUDE SPACE
UTM/PS OUTPUT SPACE
LCC OUTPUT SPACE
SOM OUTPUT SPACE
INPUT SPACE
U_G
G_L
S_G
f_2
f_1
f_3

Figure 42. Space-to-Space Mapping Functions.

projection, the earth is projected onto a cylinder whose axis falls within the equatorial plane. The line of tangency between earth and the cylinder is along a longitude meridian. The Universal Transverse Mercator shown in Figure 43 takes the cylinder's axis and rotates it in 6-degree steps within the equatorial plane. This provides a close fit of the earth's surface with the cylinder over ± 3 degrees from the longitude of tangency which now becomes the central meridian of a 6-degree UTM zone. Surface coordinates are measured in meters from the central target meridian (easting) and meters from the equator (northing). The northing and easting coordinates, together with the zone number, define a point on earth's surface in UTM. Although it is not defined above 80^{o} latitude, the UTM projection has the advantage of being a Cartesian coordinate system with identical units of measure along each axis. There is a disadvantage in terms of distortions due to projecting areas from one zone into the adjacent zone. This occurs at higher latitudes (above 60^{o}) where the spacecraft heading angle increases at a rapid rate and the zone widths decrease, causing a rapid traversing of zones. Polar areas are thus excluded from the UTM system in favor of the Polar Stereographic projection.

The Polar Stereographic projection shown in Figure 44 is defined north of 65^{o}N latitude or south of 65^{o}S latitude, the distortion regions of the UTM projection. The projection is a Cartesian system centered at the North Pole (for points north of 65^{o}N latitude) or at the South Pole (for points south of 65^{o}S latitude). Points are expressed in Polar Stereographic coordinates as an ordered triplet, (X, Y, P), where X and Y are Cartesian coordinates, P is +1 for points north of 65^{o}N latitude, and -1 for points south of 65^{o}S latitude. P can alternatively be expressed as 'N' for the North Pole; 'S' for the South Pole.

The Space Oblique Mercator (SOM) projection involves a cylinder whose circumference is tangent to the satellite ground track as shown in Figure 45.

CONTENTS

Section — Page

1 SUMMARY 1 **1/B4**

2 INTRODUCTION 2 **1/B5**

2.1 Background 2 **1/B5**

2.2 Scope 8 **1/B11**

3 DIGITAL IMAGE PROCESSING OF EARTH OBSERVATION SENSOR DATA 10 **1/B13**

3.1 General Overview 10 **1/B13**

3.2 MSS and TM Functional Description 11 **1/B14**

3.2.1 Data Reformatting 15 **1/C4**

3.2.2 Radiometric Calibration 23 **1/C12**

3.2.3 Radiometric Correction 42 **1/E3**

3.2.4 Geometric Correction/Temporal Registration 43 **1/E4**

3.2.5 Resampling for Scanner Sensors 88 **2/A12**

3.3 Return Beam Vidicon (RBV) 99 **2/B11**

3.3.1 RBV Functional Overview 100 **2/B12**

3.3.2 Radiometric Calibration and Correction 104 **2/C3**

3.3.3 Geometric Correction 110 **2/C9**

3.3.4 Resampling for RBV 119 **2/D4**

3.4 Heat Capacity Mapper Mission (HCMM) 120 **2/D5**

3.4.1 Heat Capacity Mapper (HCM) Functional Description 121 **2/D6**

3.4.2 HCM Phase I Processing 123 **2/D8**

3.4.3 Radiometric Calibration Processing . . . 124 **2/D9**

3.4.4 Radiometric Correction 128 **2/D13**

3.4.5 Geometric Correction 133 **2/E4**

Section		Page	
3.4.6	Resampling for HCM	140	2/E11
3.5	Analysis of Geometric Correction/Temporal Registration Errors	141	2/E12
3.5.1	Landsat-D TM and MSS Error Analysis . .	143	2/E14
3.5.2	Input and Internal Errors	145	2/F3
3.6	Classification	158	2/G5
3.6.1	Introduction	158	2/G5
3.6.2	LACIE Overview	163	2/G10
3.6.3	Classification Approaches	167	3/A3
3.6.4	Baseline Classification Process	171	3/A7
3.6.5	On-Board Classification Configuration Analysis	176	3/A13
4	CONCLUSIONS AND RECOMMENDATIONS	209	3/E2
Appendix A	TM AND MSS DATA REFORMATTING STUDY	213	3/E6
Appendix B	ERROR ANALYSIS	233	3/G5
Appendix C	EFFECT OF DATA STRIPING ON CLASSIFICATION ACCURACY	249	4/A10
Appendix D	EFFECT OF LANDSAT ORBITAL CHARACTERISTICS ON ON-BOARD CLASSIFICATION	278	4/E1

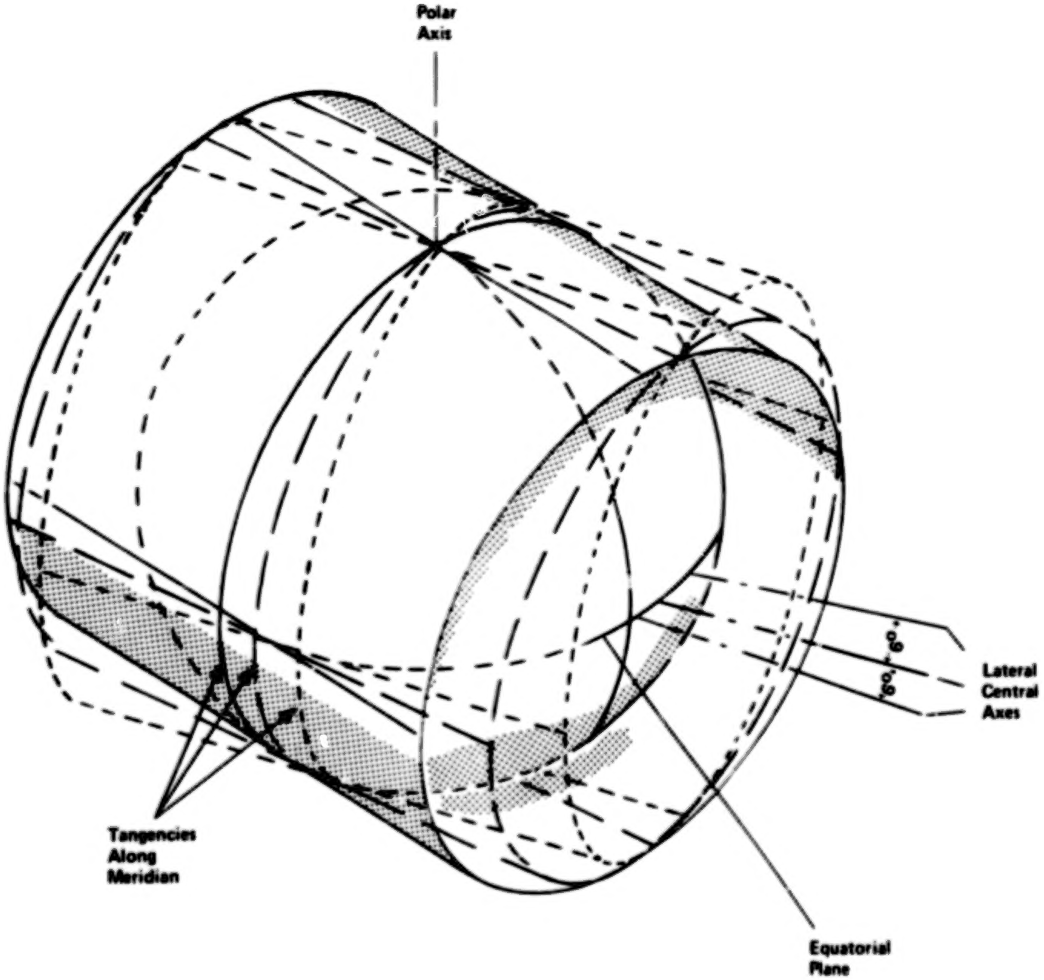
Polar Axis
6°
6°
Lateral Central Axes
Tangencies Along Meridian
Equatorial Plane

Figure 43. Universal Transverse Mercator Projection.

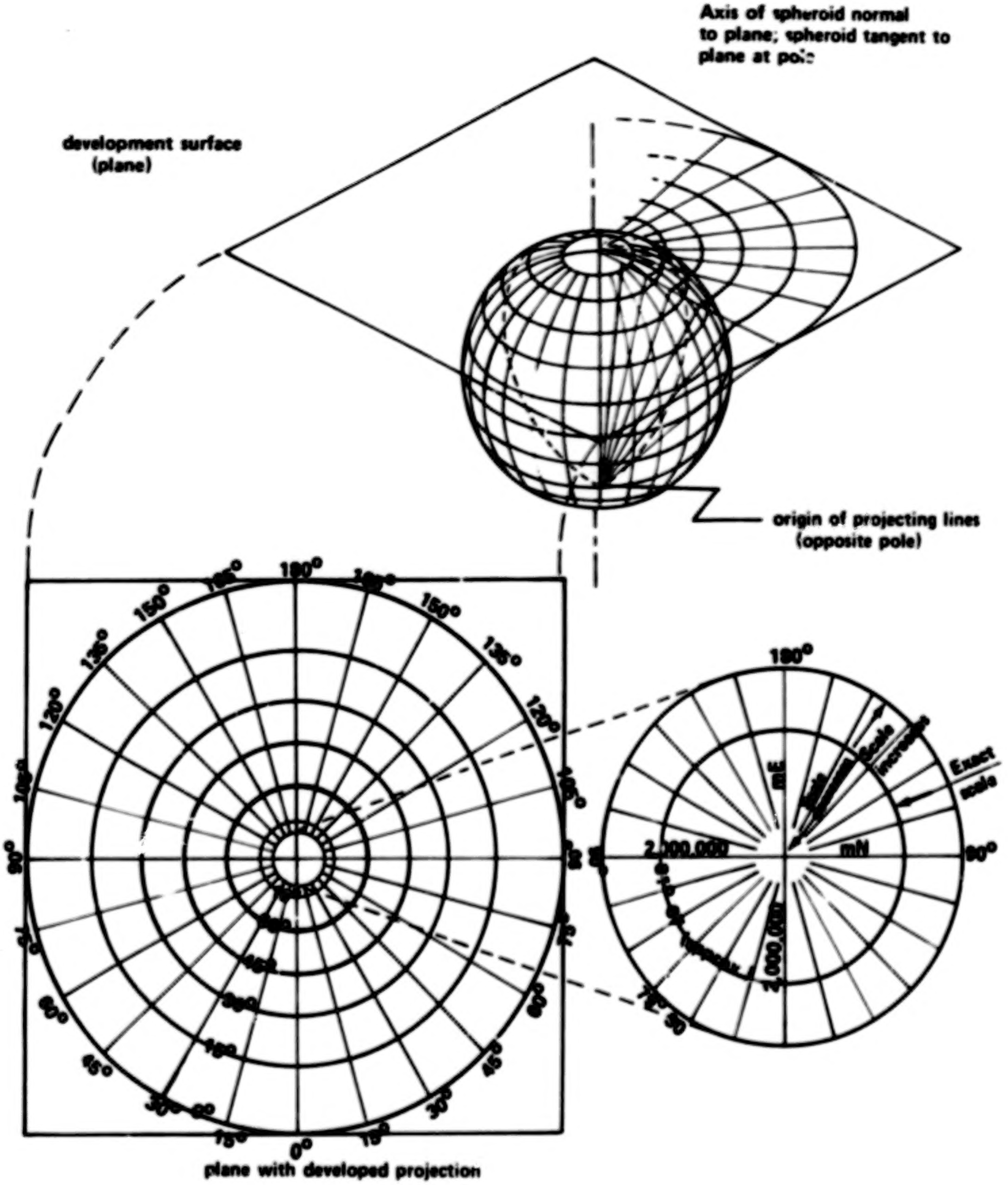

Axis of spheroid normal to plane; spheroid tangent to plane at pole
development surface (plane)
origin of projecting lines (opposite pole)
180°
150°
135°
120°
105°
90°
75°
60°
45°
30°
15°
0°
180°
mN
2,000,000
mE
Scale increases
Exact scale
plane with developed projection

Figure 44. Polar Stereographic Projection.

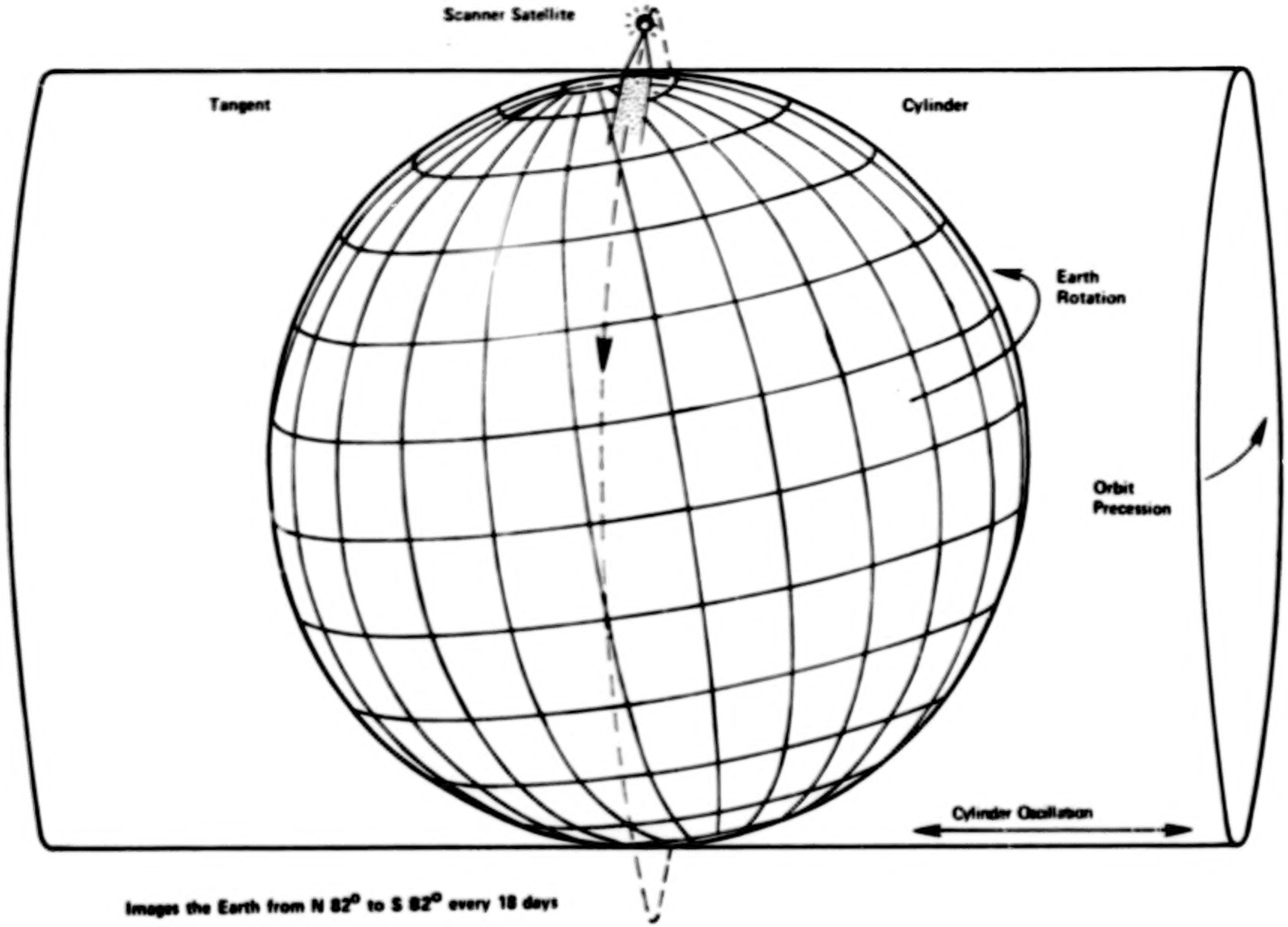
Scanner Satellite
Tangent
Cylinder
Earth Rotation
Orbit Precession
Cylinder Oscillation

Images the Earth from N 82° to S 82° every 18 days

Motions Involved: °Scanner sweep °Satellite orbit °Earth rotation °Orbit Precession

Figure 45. Space Oblique Mercator Projection.

A truly circular feature on the figure of the earth will have a slightly elliptical form to it on the SOM projection, depending on its position on the orbit. However, since the geometric conditions which create this slight deviation from conformality can be expressed mathematically, the relationships between the figure of the earth and the SOM projection are still rigorous.

The Lambert Conformal Conic (LCC) is the projection of the earth spheroid onto a cone whose axis coincides with the polar axis of the spheroid as shown in **Figure 46. The cone is secant to earth, intersecting along two** parallels of latitude which are on the same side of the equator. Meridians appear as straight lines radiating from a point beyond the mapped area. Latitude parallels appear as arcs of concentric circles which are centered at the point from which the meridians radiate. The projection is especially suited for maps having a predominating east-and-west dimension.

3.2.4.4 Geometric Interpolation

The Geometric Interpolation function takes the primary grid points (defined as G points) output from space-to-space mapping and interpolates between them to provide secondary grids for horizontal (G3 points) and vertical resampling (G2 points).

The position in input space (line and sample) of each output space pixel is arrived at by using a set of interpolations. At any interpolation stage, errors can be considered to arise from two sources: an error in the location of the primary grid points, and an error caused by truncation of the interpolation series (i.e., using linear interpolation to approximate a cubic function). A series of cubic and linear interpolations, using the primary grid points, provides a computationally efficient, yet accurate, procedure for establishing the G2 and G3 secondary grids. Since the line and sample positions of a pixel are determined using a different set of interpolations, the following discussion for the TM treats each separately. The MSS grids are

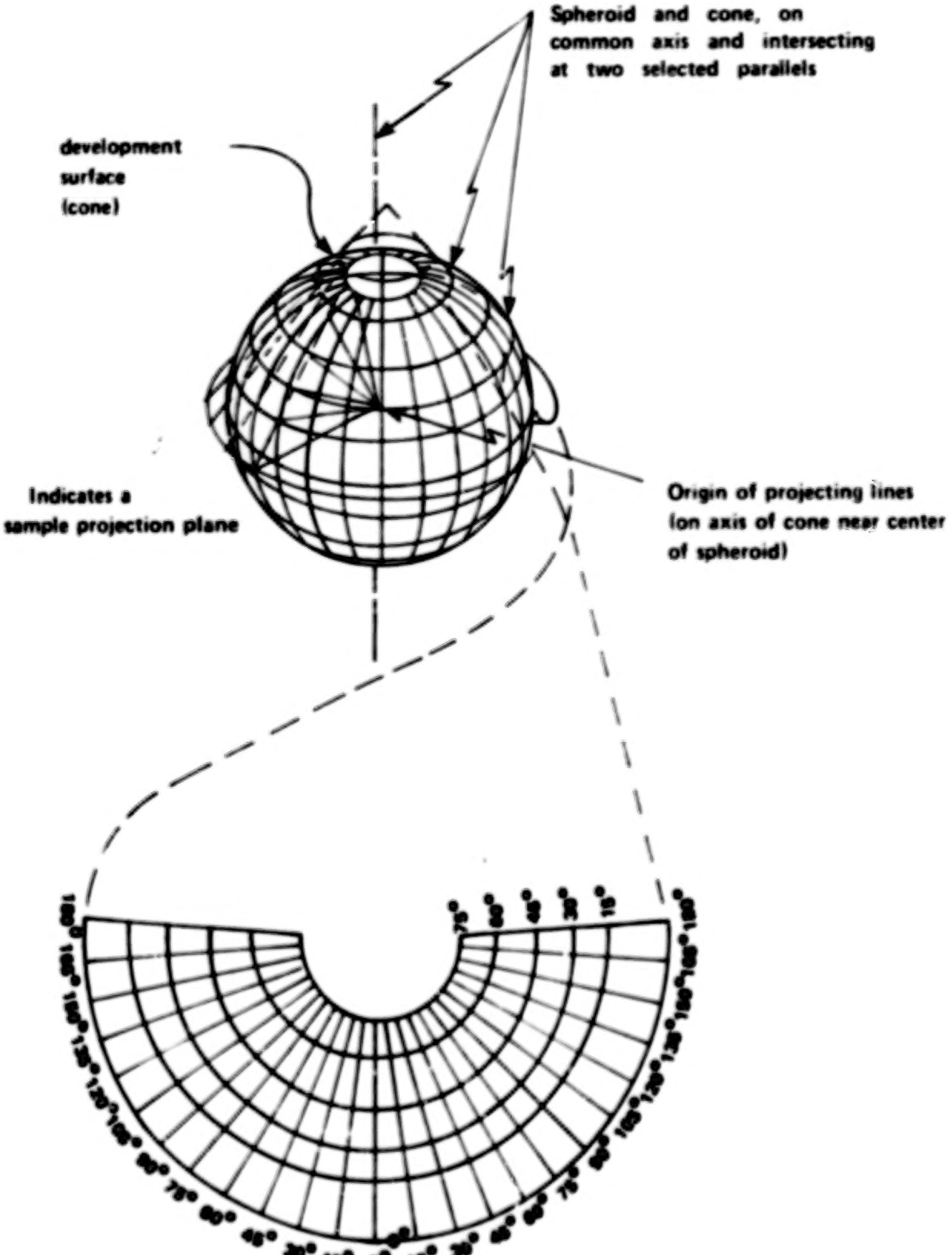
Spheroid and cone, on common axis and intersecting at two selected parallels
development surface (cone)
Indicates a sample projection plane
Origin of projecting lines (on axis of cone near center of spheroid)
flattened cone with developed projection

Figure 46. Lambert Conformal Conic Projection.

determined in the same way; however, the number of secondary grid points will be less due to the larger MSS pixel.

3.2.4.4.1 Sample Position Interpolations

The first interpolation, shown in Figure 47, is performed along each row of the primary grid points (G points) to obtain an intermediate set of points. These intermediate points across the primary rows define a G1 output space column. The G1 output space columns are found using cubic interpolation and are spaced 60 pixels apart in output space.

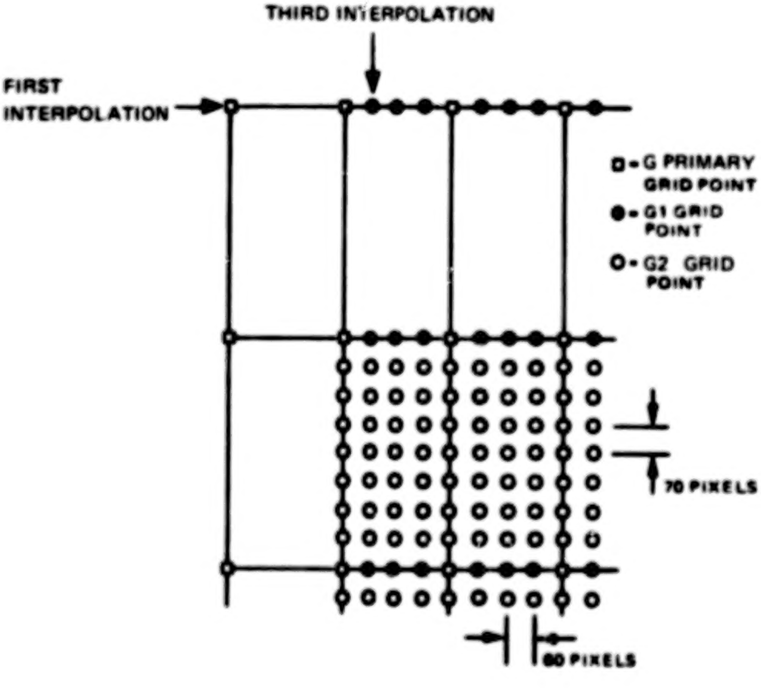
THIRD INTERPOLATION
FIRST INTERPOLATION
□ - G PRIMARY GRID POINT
● - G1 GRID POINT
○ - G2 GRID POINT
70 PIXELS
60 PIXELS

Figure 47. Output Space Grid Point Locations.

A second cubic interpolation with divided differences, shown in Figure 48, is used to obtain the intersection of the G1 output space columns with the input space rows. These points are defined as the G3 points and are spaced by 48 input space rows. This produces the G3 secondary grid used for horizontal resampling. The G3 secondary grid is 140 rows (spaced by 48 input space rows) by 120 columns (spaced by 60 output space pixels).

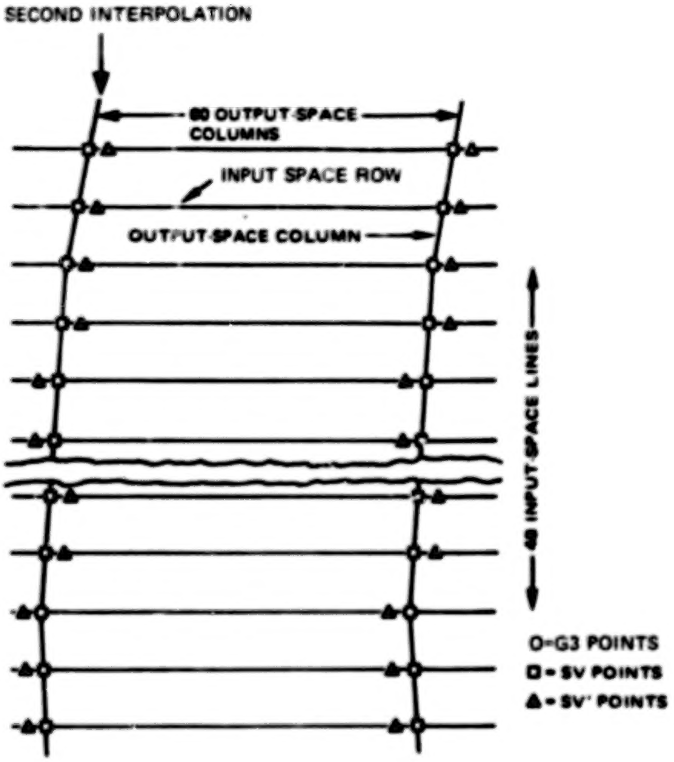
SECOND INTERPOLATION
60 OUTPUT SPACE COLUMNS
INPUT SPACE ROW
OUTPUT SPACE COLUMN
48 INPUT SPACE LINES
O=G3 POINTS
□=SV POINTS
△=SV' POINTS

Figure 48. Input Space Grid Point Locations.

A linear interpolation is now used to determine the intersection of the G1 output space columns with the intermediate 48 input space lines. The resulting SV points (intersections of the G1 output space columns with all input space rows) represent hybrid space. Figure 48 also illustrates the positive or negative shift of the SV points following high-frequency scan line adjustments (accomplished as part of horizontal resampling). A second linear interpolation between G3 points along an input space row generates the pixel position for hybrid space. These linear interpolations are part of horizontal resampling.

3.2.4.4.2 Line Position Interpolation

A third cubic interpolation, shown in Figure 47, is performed along a G1 output space column to obtain the intersections of the output space column and output space rows. The resulting line positions are defined as the G2 points and are spaced by 60 pixels along an output row and 70 pixels across output space rows. The G2 secondary grid is 97 rows (spaced by 70 pixels) by 120 columns (spaced by 60 pixels).

Linear interpolation between G2 points along an output space column determines the intersection of the intermediate 70 output space rows. This linear interpolation is part of vertical resampling.

The output of geometric interpolation is, then, two sets of grids used to control horizontal and vertical resampling. In addition, the number of output space fill pixels to the left and right of the output line and the number of fill pixels to be appended to input space image data before resampling will be output. This zero pixel fill will be added to the input image data as the image data is read in from tape for full processing.

3.2.5 Resampling for Scanner Sensors

A requirement normally imposed upon image processing when the image is in digital form is that the output pixel lattice be regular, or equi-spaced in the output space. The output picture element will almost always have nonintegral line and sample coordinates in the input space as shown in Figure 4.. It is necessary to interpolate over input space intensity values to generate each output pixel. This process of interpolation has been customarily denoted as resampling.

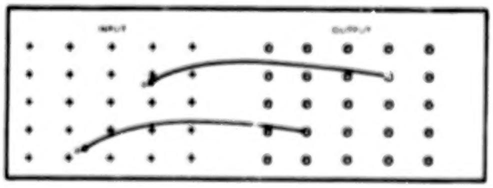

Figure 49. Locating Output Points in Output Space.

Resampling consists of two related processes:

a. Determining the geometric location in the input space of each output pixel.

b. Determining the intensity value to be assigned to each output pixel.

The geometric location of an output pixel in the input space is obtained by using a linear interpolation between secondary grid points output from the geometric interpolation functions. Prior to the linear interpolation, the secondary grid points will be adjusted for the high-frequency effects. Two methods of assigning the intensity value to each output pixel are: nearest neighbor (NN) and cubic convolution (CC). NN simply finds the input pixel closest to the output pixel location and assigns that intensity value to the output pixel sample as shown in Figure 50.

Cubic convolution is a family of resamplers that approximate the SINC, or $\frac{\text{SIN X}}{\text{X}}$ function. The SINC function is the theoretical perfect resampler, but requires an infinite number of terms. Cubic convolution substitutes a truncated piecewise cubic approximation to the SINC function. The four-point cubic convolution resampler is commonly used and is implemented in the MDP.

Cubic convolution is divided into two steps as shown in Figure 51. The first step resamples horizontally or along an input row. The second step resamples vertically along an output column to obtain the final output pixel intensity. Both resampling steps use a nested form of the cubic convolution interpolation algorithm given by equation (23):

$$I_k' = I_k + d_k (I_{k+1} - I_{k-1} + d_k (2I_{k-1} - 2I_k + I_{k+1} - I_{k+2} + d_k (I_{k+2} - I_{k+1} + I_k - I_{k-1}))) \tag{23}$$

where,

I_k' = the interpolated image data for the kth sample

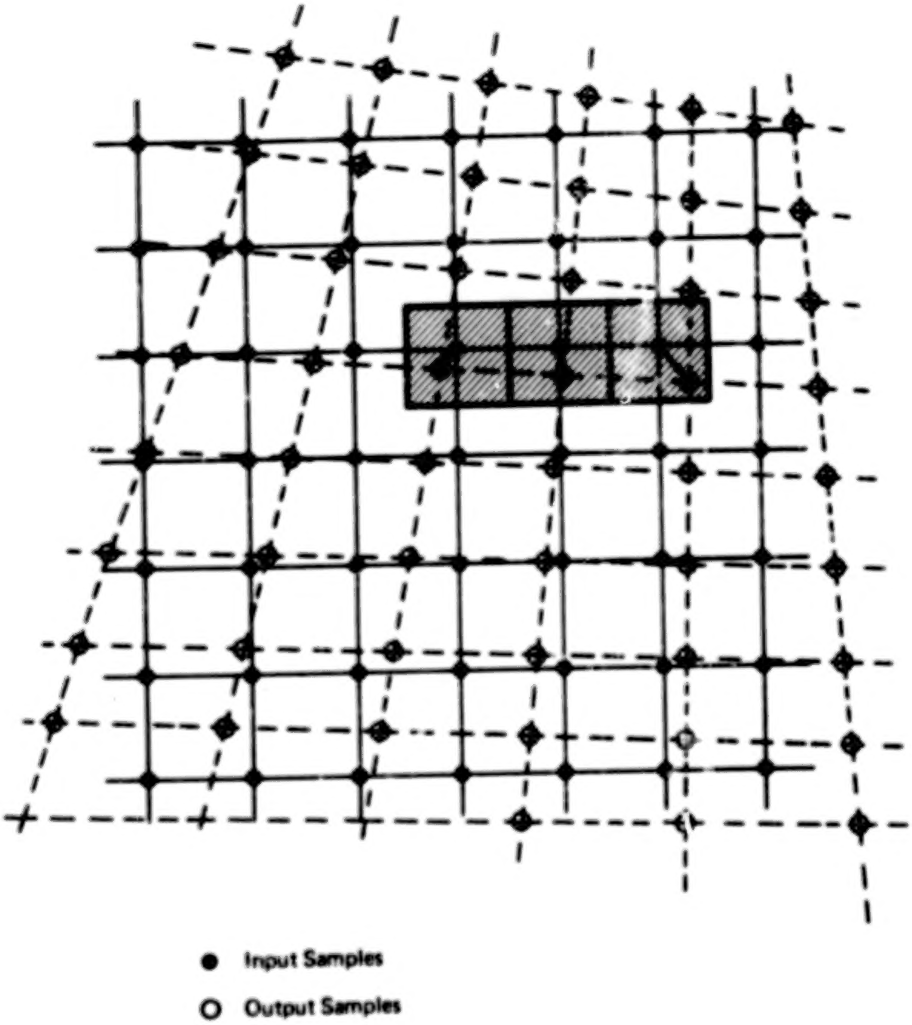
● Input Samples
○ Output Samples

Figure 50. Nearest Neighbor Assignment.

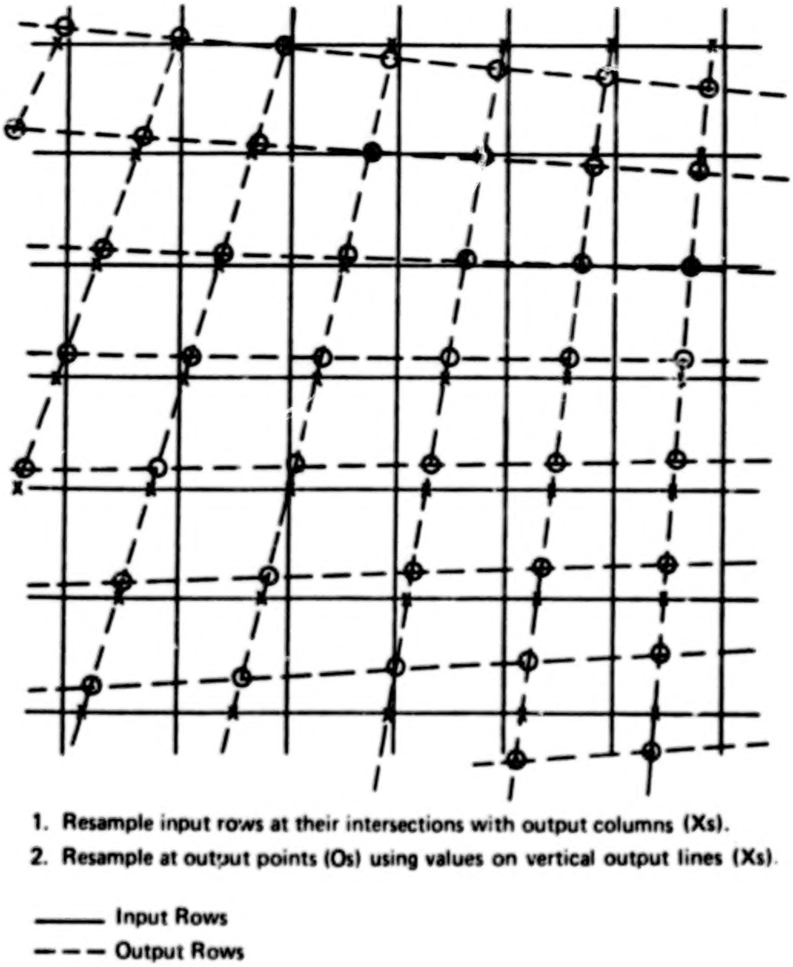

1. Resample input rows at their intersections with output columns (Xs).
2. Resample at output points (Os) using values on vertical output lines (Xs).

—— Input Rows
– – – Output Rows

Figure 51. Resampling Model for Cubic Convolution.

I_k = image data of the kth sample

d_k = the normalized displacement between I'_k and $I_k (0 \le d_k \le 1)$

Figure 52 illustrates the samples used to create a point horizontally (I'_3) and then vertically (I).

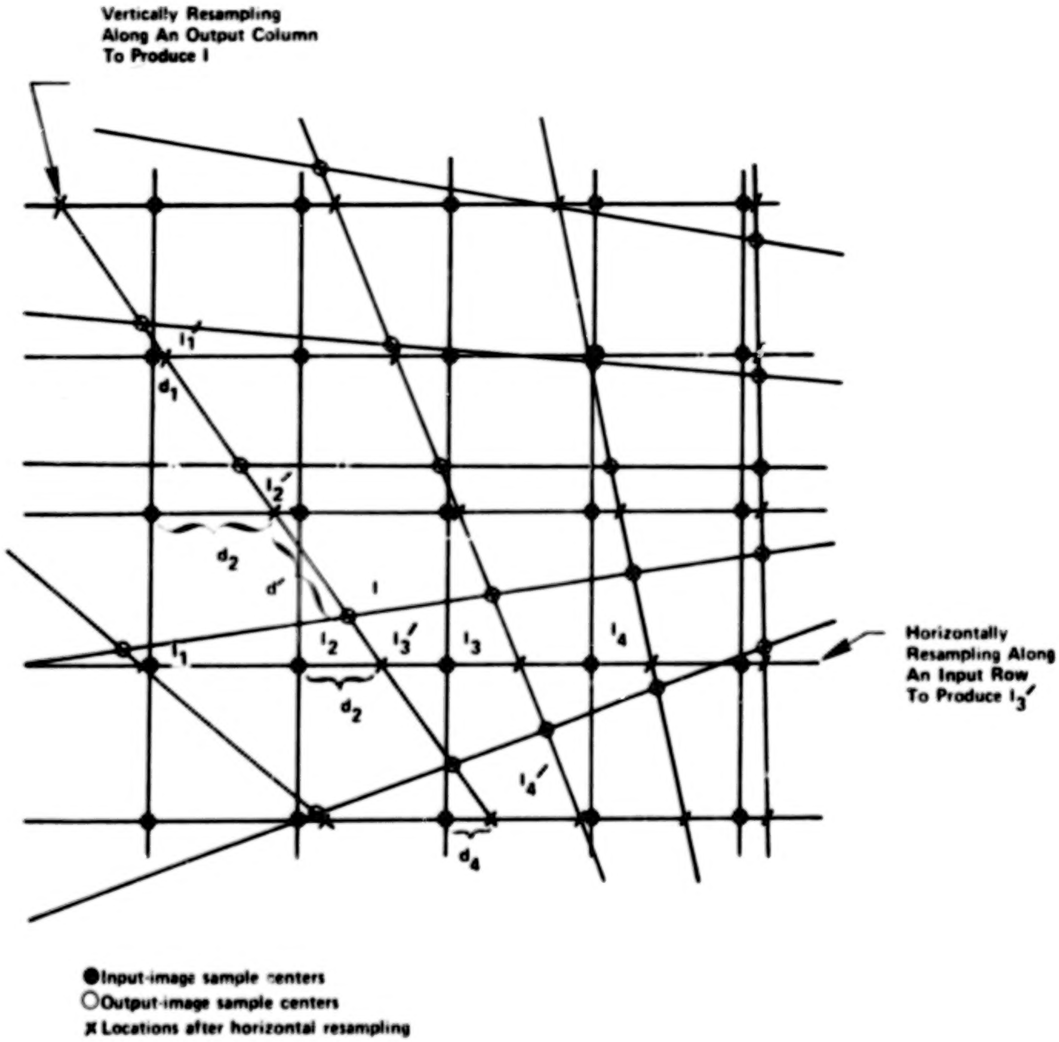
Vertically Resampling Along An Output Column To Produce I
I1'
d1
I2'
d2
d'
I
I1
I2
I3'
I3
I4
d2
I4'
d4
Horizontally Resampling Along An Input Row To Produce I3'
● Input-image sample centers
○ Output-image sample centers
✗ Locations after horizontal resampling

Figure 52. Cubic Convolution Resampling Scheme.

Figure 53 shows the relationships of the various parameters to the SINC function.

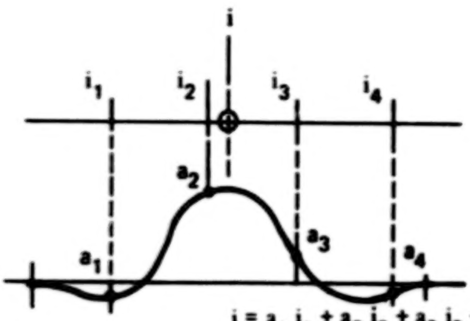

$$i = a_1 i_1 + a_2 i_2 + a_3 i_3 + a_4 i_4$$

Cubic Convolution Polynomial

$$f(x) = 1 - 2|x|^2 + |x|^3 \qquad 0 \leq |x| \leq 1$$

$$= 4 - 8|x| + |x|^2 - |x|^3 \qquad 1 < |x| \leq 2$$

$$= 0 \qquad < |x|$$

Figure 53. Cubic Convolution Interpolation.

Horizontal resampling applies the one-dimensional cubic convolution interpolation to the intersections of the output space columns and input space rows (horizontal intersection points) to form a hybrid image space. Hybrid space provides an interim staging area in the construction of a fully corrected image. Vertical resampling is then applied along output space columns to the intersection of output space columns and output space rows (vertical intersection points) to produce the final output image space.

3.2.5.1 Resampling Parameter Preparation

Image data, as received from the sensor, will not have any applied geometric corrections. Based on provided ancillary data, separate sets of geometric data are computed during the geometric error modeling (subsection 3.2.4.2) and space-to-space mapping functions (subsection 3.2.4.3). These sets of geometric data (the secondary grid values) will reflect the primary geometric corrections necessary for presenting the imagery in any one of three different map projections. However, high-frequency effects still remain and must be removed. These high-frequency effects consist of:

a. Band-to-band registration offsets (function of the physical light pipe arrangement)

b. Scan line length variations from nominal

c. Detector-to-detector offsets (due to a finite sampling interval)

d. Mirror velocity profile

e. Sweep-to-sweep offsets (due to the combination of earth rotation scene latitude, and n lines at a time scanning).

These high-frequency effects can be removed by shifting the G3 grid points along the input scan line in either a positive or negative direction.

Now, any high-speed logic unit used to implement the resampling algorithm operates most efficiently if the data is sequenced through in a repetitive manner. This requires that the image data be partitioned, on a line-by-line basis, so that some number of pixels may be resampled and output in a repetitive manner. Associated with each input line, then, is an initial displacement x_o (see Figure 54) measured from an input pixel, and an incremental displacement Δx. These parameters (x_o, Δx) are used to recursively calculate successive interpolation displacements using equation (24) for each line:

$$x_k = x_{k-1} + \Delta x \qquad (24)$$

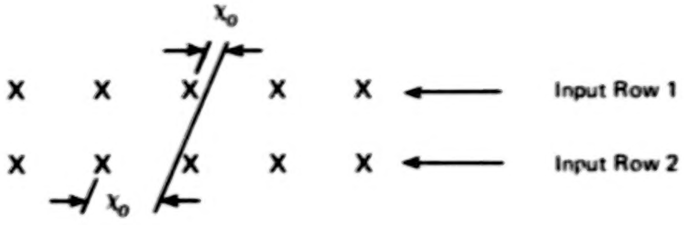

Figure 54. Initial Position of Output Column at Different Points.

The incremental displacement, Δx, is constant within a partition, but can vary with line number as shown in Figure 55. A table, for each input line in a subscene, must be developed that identifies the number of partitions (where breaks occur), the initial input pixel index, the initial interpolation displacement (x_0), the incremental displacement (Δx), and the number of pixels output along each row in each partition. Having defined these parameters, maximum advantage can be taken of any high-speed logic unit.

3.2.4.2 Horizontal Resampling

Four of the secondary G3 grid points will be input for horizontal resampling. These grid points have a horizontal separation of 60 output pixels and a

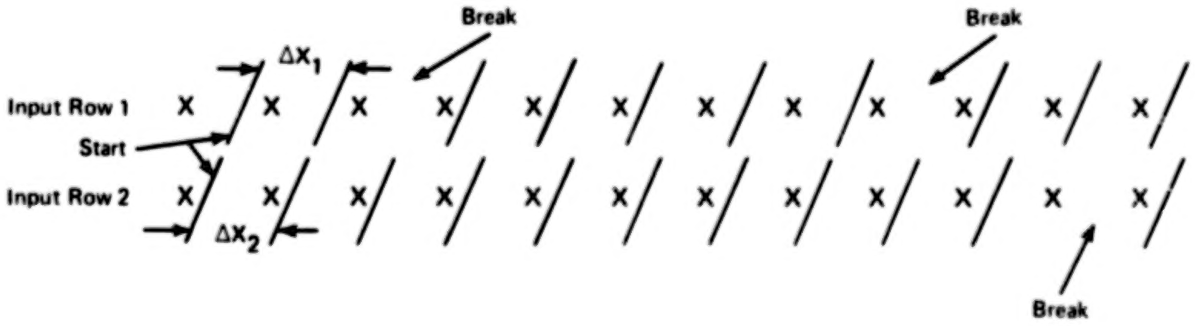

Figure 55. Output Columns Process at Different Rates.

vertical separation of 48 input rows. The end points of each input row are determined using a linear interpolation between pairs of the secondary grid points (see Figure 56). These end points are then shifted to correct the high-frequency effects shown as the wavy lines on Figure 56.

Next, the location of the 60 pixels along each input row are determined by using a linear interpolation between the high-frequency corrected end points. All pixel locations are now determined within the subinterval encased by the four secondary input grid points. The intensity value assigned to each pixel location is determined using the resampling algorithm.

The wavy columns that result from the horizontal resampling become straight columns in hybrid space. Remember that hybrid space consists of the input space rows and the output space columns.

3.2.5.3 Vertical Resampling

When vertical resampling is implemented (shown in Figure 57), four of the secondary G2 grid points will be input. These define points in the hybrid space that have integer pixel locations (located on the hybrid space column) but noninteger output space row values. The task is to define the locations on the pixel columns of the output space row intersection.

The G2 grid points are separated by 60 output space columns and 70 output space rows. A linear interpolation between the VRS points determines the end points of the 60 output space columns. Using these end points, the 70 intermediate output space row locations are also determined by a linear interpolation.

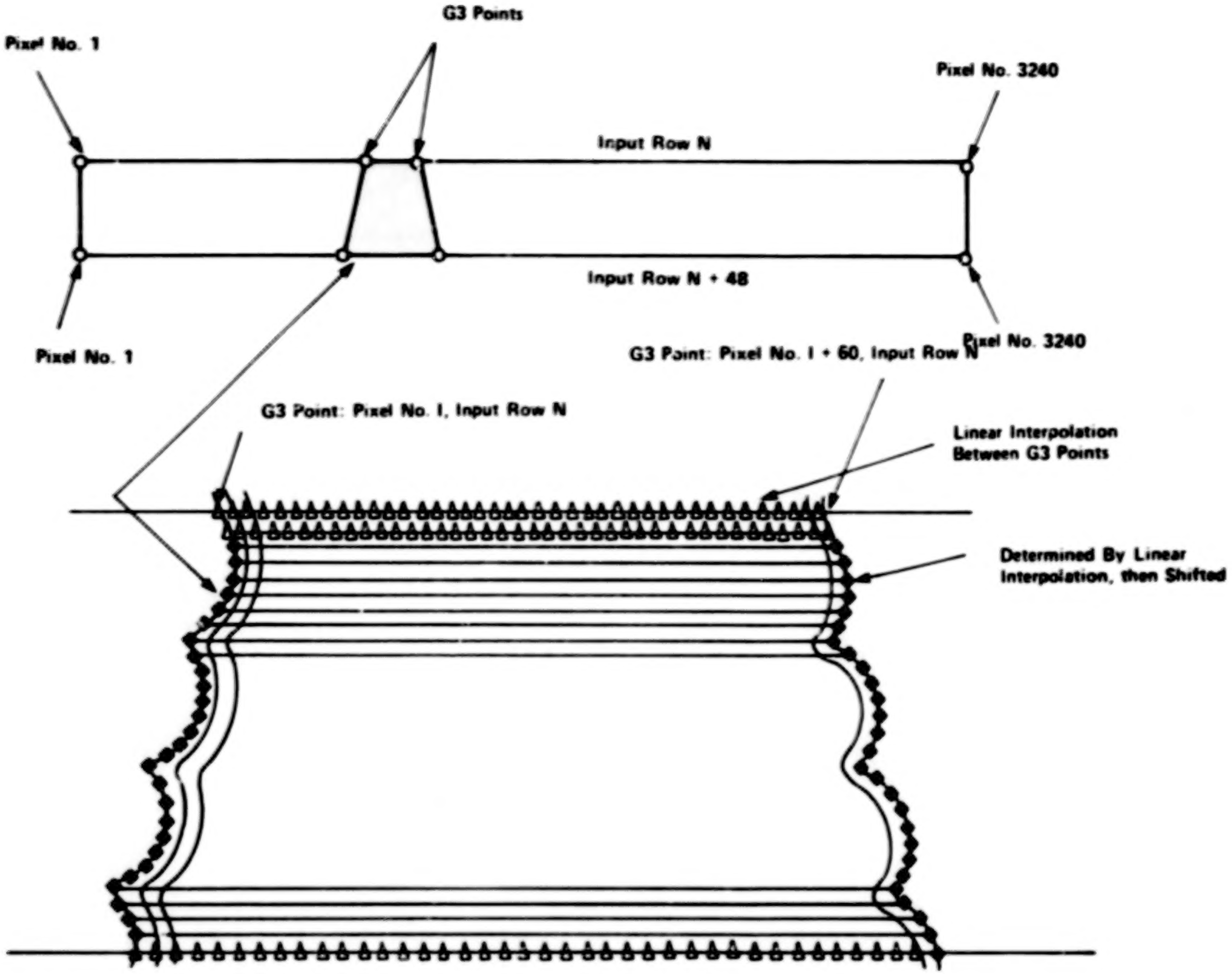
G3 Points
Pixel No. 1
Pixel No. 3240
Input Row N
Input Row N + 48
Pixel No. 1
Pixel No. 3240
G3 Point: Pixel No. I + 60, Input Row N
G3 Point: Pixel No. I, Input Row N
Linear Interpolation Between G3 Points
Determined By Linear Interpolation, then Shifted

Figure 56. Horizontal Resampling.

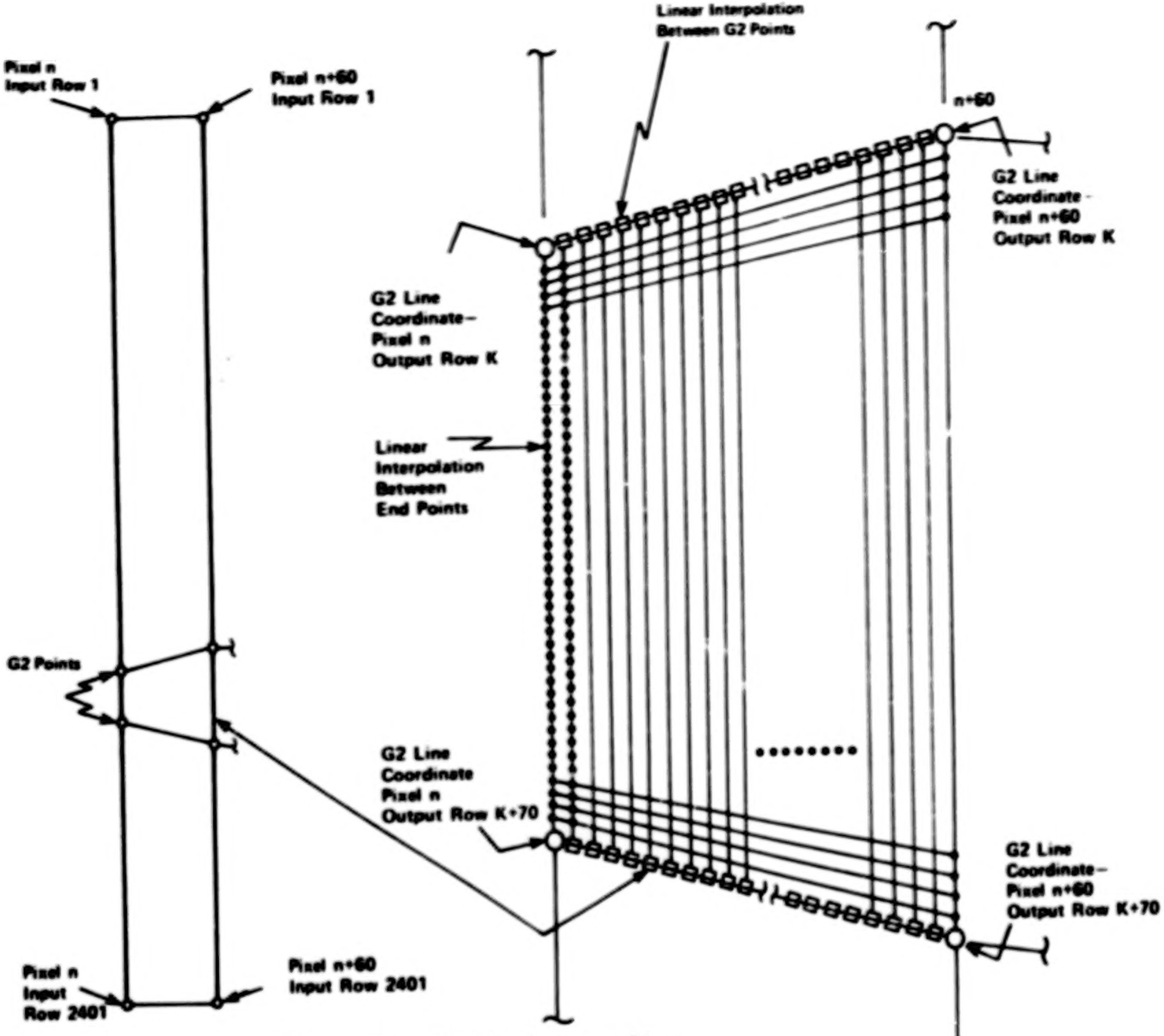
Linear Interpolation
Between G2 Points
Pixel n
Input Row 1
Pixel n+60
Input Row 1
n+60
G2 Line
Coordinate -
Pixel n+60
Output Row K
G2 Line
Coordinate -
Pixel n
Output Row K
Linear
Interpolation
Between
End Points
G2 Points
G2 Line
Coordinate
Pixel n
Output Row K+70
G2 Line
Coordinate -
Pixel n+60
Output Row K+70
Pixel n
Input
Row 2401
Pixel n+60
Input Row 2401

Figure 57. Vertical Resampling.

3.3 RETURN BEAM VIDICON (RBV)

The RBV uses conventional lenses and shutters, with vidicons for image scanning and storing prior to transmission of the image data to ground stations.

The Landsat-1 and -2 RBV is a three-band, three-camera television system, the Landsat-C RBV is a single-band, two-camera television system. The characteristics of each system are summarized in Table 10. This discussion will be only concerned with the Landsat-C two-camera configuration; however, the processing of the RBV data for Landsat-1 and -2 is functionally identical.

Table 10. Comparison of Landsat-C/RBV with Landsat-1 and-2/RBV.

Item	Landsat 1 & 2/RBV	Landsat-C/RBV
Number of Cameras	3	2
Ground Coverage/Frame	185x185 km	183x98 km
Ground Coverage/Camera	185x185 km	98x98 km
Spectral Coverage	Camera 1: 475-575 mμ Camera 2: 580-680 mμ Camera 3: 690-830 mμ	Each Camera: 505-750 mμ
Readout	Staggered for 3 Cameras	Staggered for 2 Cameras
Nominal Exposure Time	12 ms	5.6 ms
Cycle Time	25 sec	12.5 sec
Video Bandwidth	3.2 MHz	3.2 MHz
Read Time	3.5 sec total	3.5 sec Total

One RBV scene will consist of four subframes covering an equivalent region on the earth of 180 km by 183 km as shown in Figure 58. The two RBV cameras are tilted to provide side-by-side pictures of the earth spacecraft/earth motion and with the 3.5-second time interval between Camera 1 and Camera 2 exposures. RBV and MSS output image format centers are defined relative to the World Reference System (WRS) format centers in such a way that, nominally, corrected RBV data arrays will be in registration with the corresponding portions of corrected MSS data arrays. The RBV signal is analog on entry into the preprocessor. This analog signal is then digitized at 6 bits per sample to create an input image array of 4500 video samples per line, 4125 lines per subframe with a 18.2 by 23.8 meter pixel as shown in Figure 59. This subframe represents a 98 by 98 km region on the surface of the earth. The output image array is 5322 samples per line, 5322 lines per subframe with a 19 by 19 meter pixel, also shown in Figure 59.

3.3.1 RBV Functional Overview

The application of radiometric and geometric corrections to RBV image data is performed as shown in Figure 60 and described in the following paragraphs. Image data is read from the input HDT and written to disk. Reseau search areas are extracted, reseau located, and RBV internal geometric distortions modeled. Ancillary data are read from the Ancillary Data Tape (ADT) and used, along with the internal geometric distortion models, to estimate control point locations in the input image data.

Control point search areas are extracted from the image data on disk, and the Control Location Algorithm used to determine the control point locations within the search areas. Control point locations, ancillary data, and internal distortion models are employed in Geometric Error Modeling to estimate spacecraft attitude. The spacecraft attitude and the internal distortion models form a basis for the geometric output-to-input image transformation in Space-to-Space Mapping.

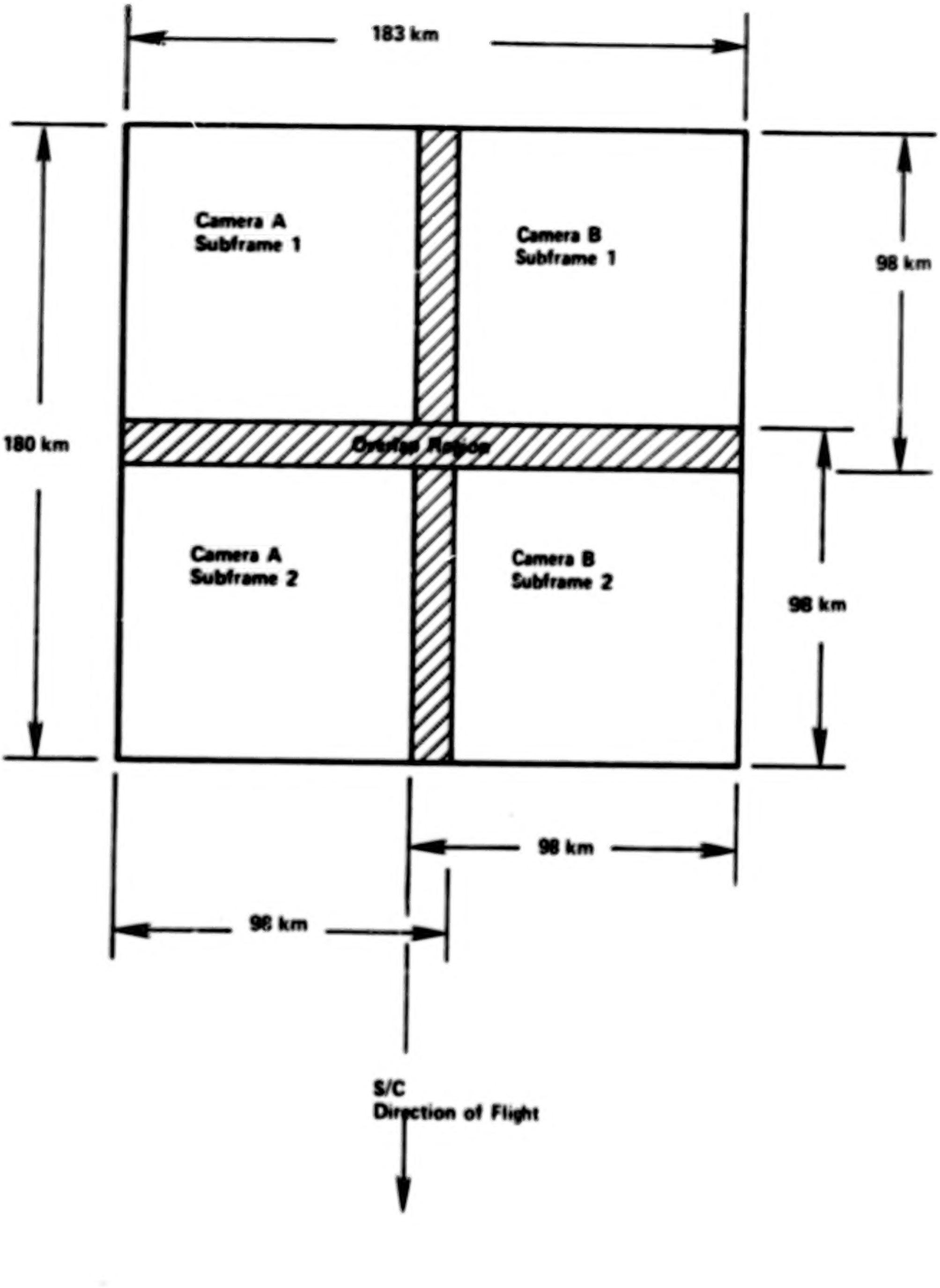
183 km
Camera A
Subframe 1
Camera B
Subframe 1
98 km
180 km
Overlap Region
Camera A
Subframe 2
Camera B
Subframe 2
98 km
98 km
98 km
S/C
Direction of Flight

Figure 58. One RBV Scene Consists of Four Subframes.

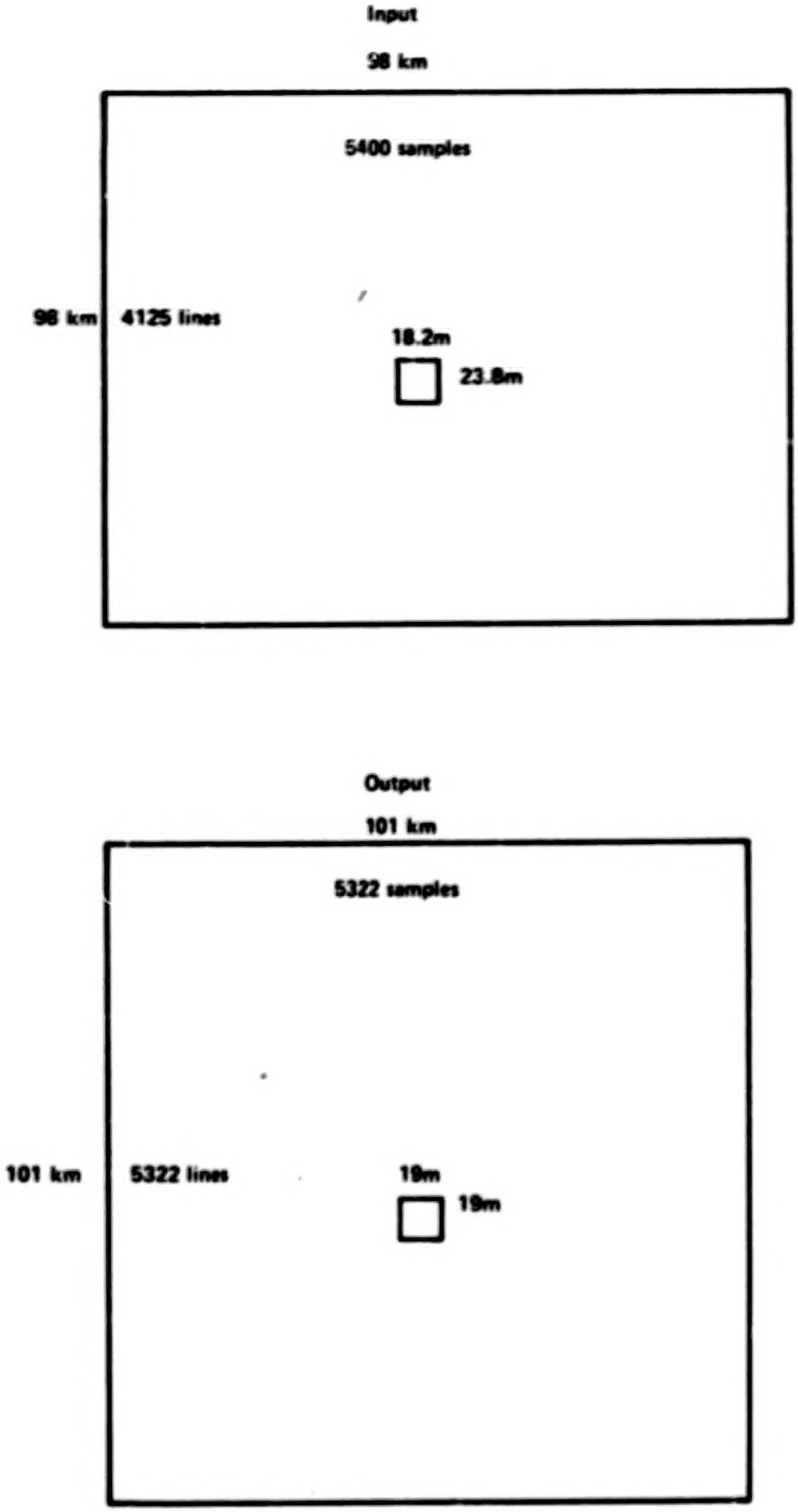
Input
98 km
5400 samples
98 km
4125 lines
18.2m
23.8m
Output
101 km
5322 samples
101 km
5322 lines
19m
19m

Figure 59. Input and Output Data Arrays.

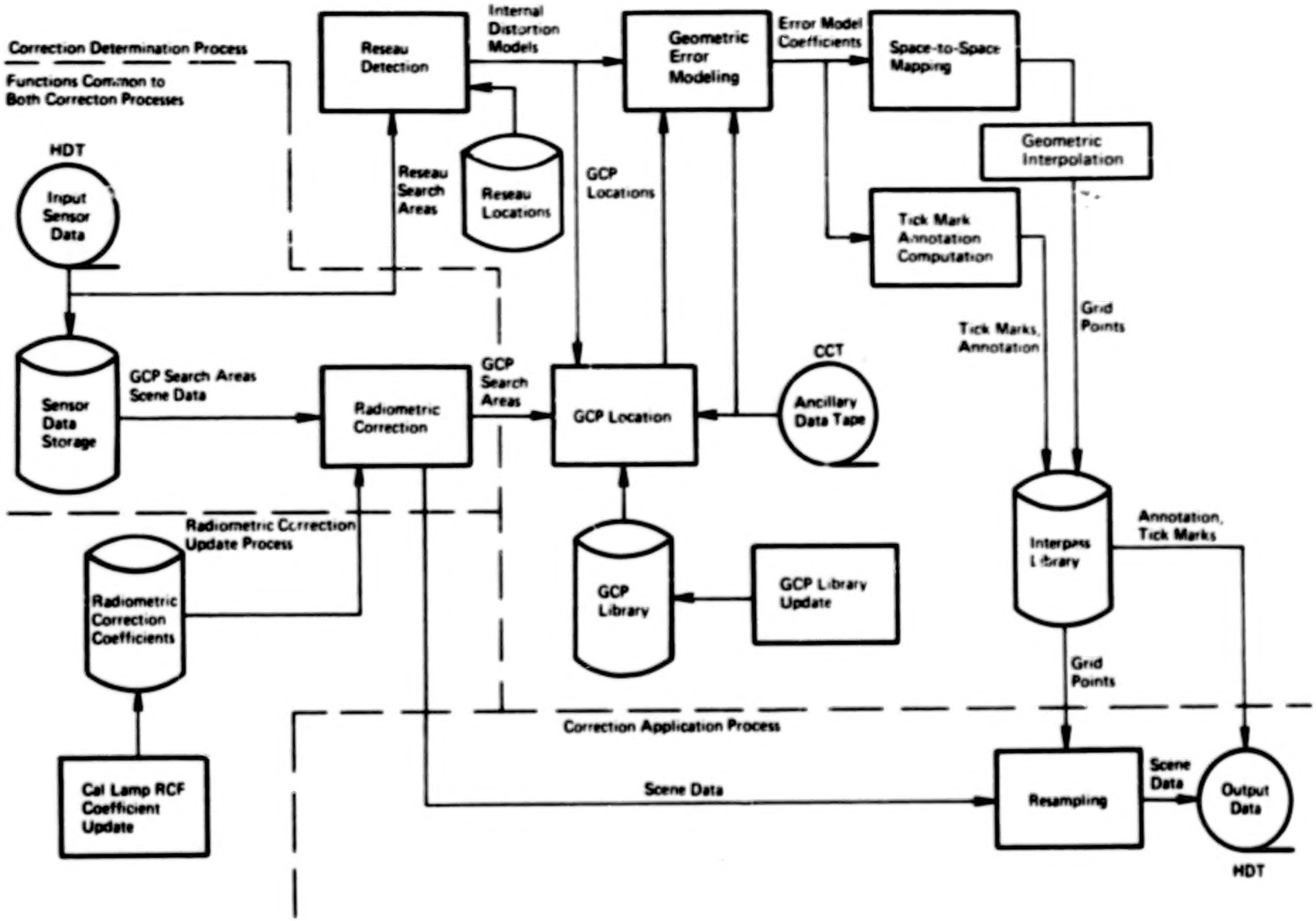
Correction Determination Process
Functions Common to Both Correcton Processes
HDT
Input Sensor Data
Reseau Detection
Reseau Search Areas
Reseau Locations
Internal Distortion Models
GCP Locations
Geometric Error Modeling
Error Model Coefficients
Space-to-Space Mapping
Geometric Interpolation
Tick Mark Annotation Computation
Sensor Data Storage
GCP Search Areas Scene Data
Radiometric Correction
GCP Search Areas
GCP Location
CCT
Ancillary Data Tape
Tick Marks, Annotation
Grid Points
Interpass Library
Annotation, Tick Marks
Radiometric Correction Update Process
Radiometric Correction Coefficients
GCP Library
GCP Library Update
Grid Points
Correction Application Process
Cal Lamp RCF Coefficient Update
Scene Data
Resampling
Scene Data
Output Data
HDT

Figure 60. RBV Functional Processing Overview.

The input image data is then radiometrically corrected and resampled to transform input data to the selected output map projection with geometric errors eliminated. Output image data, with tick marks and annotation, are written onto an HDT.

As a separate process, calibration lamp data in the form of images from the spacecraft are used to update the radiometric correction coefficients (calibration lamp processing is performed only occasionally, e.g., once per week).

3.3.2 Radiometric Calibration and Correction

The RBV data suffer from significant shading (nonuniform response) effects. Since the objective of RBV correction is to modify the image data intensity to compensate for the spatially variable response characteristics, a method has been developed that mathematically structures the RBV image into correction zones. (A sufficient number of such zones must be established to have a nearly continuous radiometric response function.) Each zone has a unique radiometric correction table to be used for compensation of the RBV errors. In effect, RBV radiometric correction is performed in two stages. The first part is the radiometric correction coefficient computation. This step includes prelaunch processing of Hovis Sphere radiometric data to get an initial set of calibration and occasional (once a week) processing of radiometric calibration lamp images from the spacecraft to update the correction coefficients. The second part is the radiometric correction coefficient application or the actual radiometric correction of RBV imagery.

The radiometric correction coefficient computation begins with the preprocessing of the Hovis Sphere as shown in Figure 61. The Hovis Sphere is a uniform radiance source. An 18 x 18 array of points are defined across the RBV. Each point is measured when illuminated by 10 different radiance levels from the Hovis Sphere. A linear least squares estimate, using the 10 radiance measurements, of gain and bias calibration values is computed at each of the 324 points.

The zoning of the image is illustrated in Figure 62. Global, eighth-order

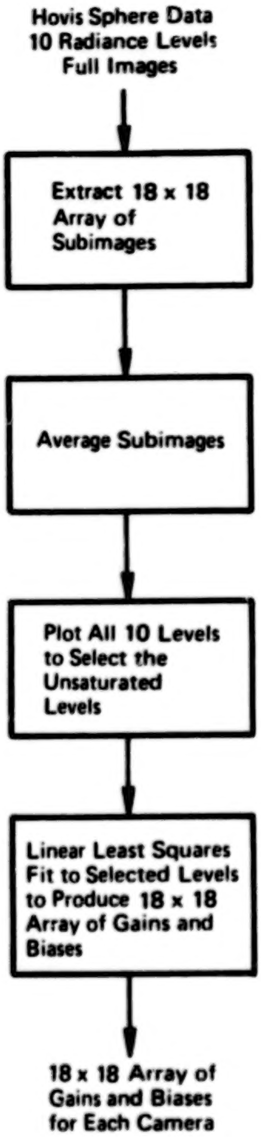
Hovis Sphere Data
10 Radiance Levels
Full Images
Extract 18 x 18 Array of Subimages
Average Subimages
Plot All 10 Levels to Select the Unsaturated Levels
Linear Least Squares Fit to Selected Levels to Produce 18 x 18 Array of Gains and Biases
18 x 18 Array of Gains and Biases for Each Camera

Figure 61. Preprocessing of Hovis Sphere Data.

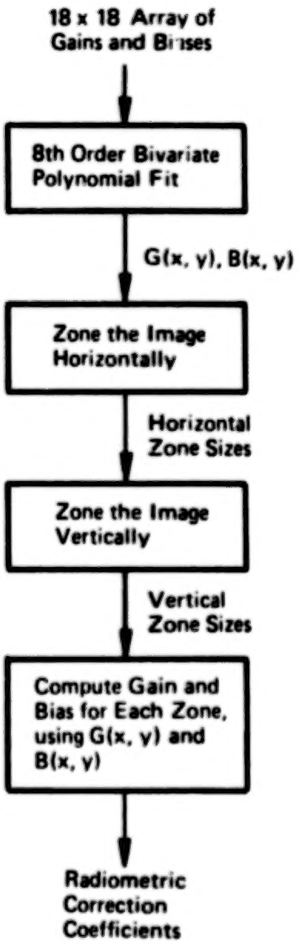
18 x 18 Array of Gains and Biases
8th Order Bivariate Polynomial Fit
G(x, y), B(x, y)
Zone the Image Horizontally
Horizontal Zone Sizes
Zone the Image Vertically
Vertical Zone Sizes
Compute Gain and Bias for Each Zone, using G(x, y) and B(x, y)
Radiometric Correction Coefficients

Figure 62. Zoning the Image.

bivariate polynomials of gains and bias are computed as least-squares estimates using the 18 x 18 array of gains and biases previously computed.

The zoning of the image is accomplished as two one-dimensional problems. First, the horizontal zones are computed, then the vertical zones. Horizontal zoning is accomplished as shown in Figure 63. For each of several lines in the image (seven are shown in the figure), the zone sizes are computed. The zone sizes are determined by measuring the variation in radiometric distortions along each line. Using the eighth-order polynomials of gains (G(x,y)) and bias (B(x,y)) previously computed, compute for the first zone each x (line) and y (where y equals the sample location of the leftmost column of the 324 calibration points) the output intensity value at extremes of the digital range (0 and 63). Now increment y by 2 pixels, determine the new gain and bias for the seven lines, and recompute the output intensity values. If the difference of the output intensity values exceeds a threshold at either the low (0) or high (63), intensity level for any of the lines tested, a zone boundary has been reached. Otherwise, y is incremented by two pixels with each iteration until one of the lines exceeds the threshold. The vertical zoning is accomplished in a similar manner but computed for a set of samples rather than a set of lines. For each zone, gain and bias coefficients are computed using the global eighth-order gain and bias polynomials and coordinates of the center of the zone.

Calibration lamp data is used to detect changes in RBV camera response and to update the radiometric correction coefficients. The first set of calibration lamp images is calibrated using the Hovis Sphere coefficients and serves as a baseline from which all future camera response changes are determined (see Figure 64).

From the first calibration Lamp Image (CLI) a 18 x 18 array of small (20 pixel by 20 pixel) subimages, centered at the intensity sampling points is extracted. An average intensity value is computed for each subimage. For each of the two intensity levels--calibration 0 and calibration 1

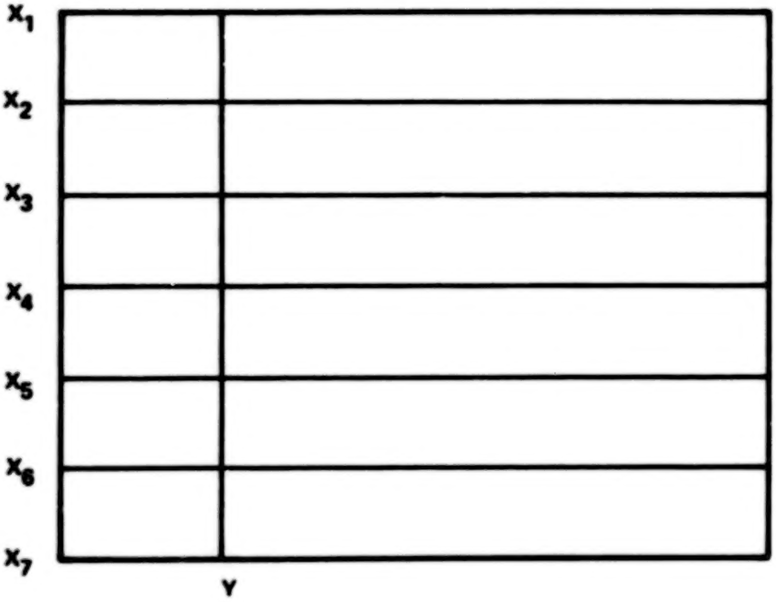
X_1
X_2
X_3
X_4
X_5
X_6
X_7
Y

$I_0 = G(X,Y)\,[0 + B(X,Y)]$

$I_{63} = G(X,Y)\,[63 + B(X,Y)]$

$J_0 = G(X,Y+2)\,[0 + B(X,Y+2)]$

$J_{63} = G(X,Y+2)\,[63 + B(X,Y+2)]$

If $| I_0 - J_0 | > T$ or $| I_{63} - J_{63} | > T$.

Y is a zone boundary.

$G_{ij} = P_G\,(X_i, Y_j)$

$B_{ij} = P_B\,(X_i, Y_j)$

Figure 63. Horizontally Zoning the RBV Image.

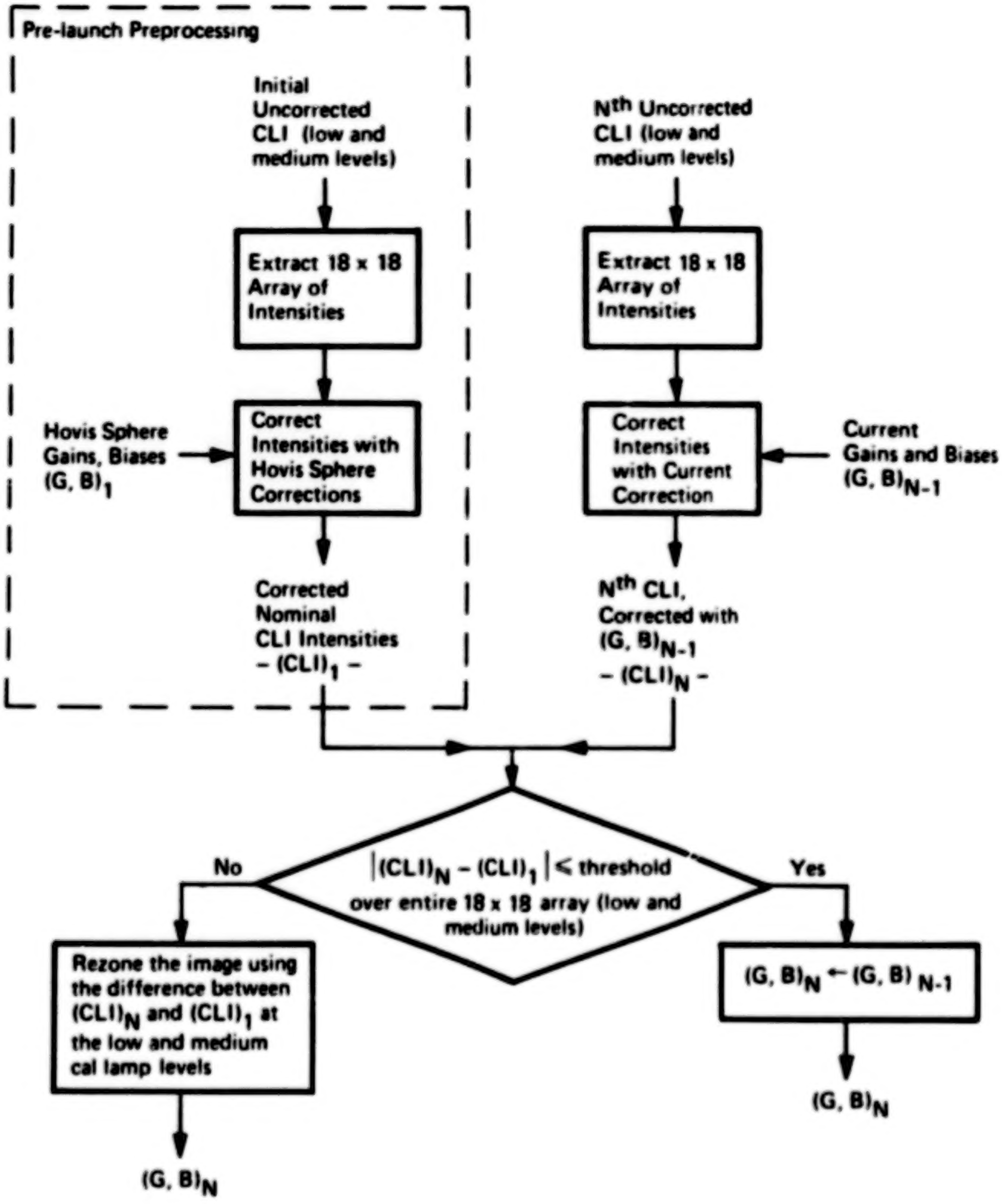
Pre-launch Preprocessing
Initial Uncorrected CLI (low and medium levels)
Extract 18 x 18 Array of Intensities
Hovis Sphere Gains, Biases (G, B)1
Correct Intensities with Hovis Sphere Corrections
Corrected Nominal CLI Intensities - (CLI)1 -
Nth Uncorrected CLI (low and medium levels)
Extract 18 x 18 Array of Intensities
Correct Intensities with Current Correction
Current Gains and Biases (G, B)N-1
Nth CLI, Corrected with (G, B)N-1 - (CLI)N -
|(CLI)N - (CLI)1| ≤ threshold over entire 18 x 18 array (low and medium levels)
No
Yes
Rezone the image using the difference between (CLI)N and (CLI)1 at the low and medium cal lamp levels
(G, B)N
(G, B)N ← (G, B)N-1
(G, B)N

Figure 64. Calibration Lamp Image Processing.

(calibration 2 tends to be saturated because of its high level)--the 18 x 18 array of intensities is corrected using the gains and biases computed from Hovis Sphere data. The output of this preprocessing step is an 18 x 18 array of corrected nominal CLI intensities--(CLI_1)--for each of two calibration levels.

Operationally, each time a CLI is processed, an 18 x 18 array of small subimages is extracted and averaged to produce a 18 x 18 array of intensities. These intensities are corrected using the current radiometric coefficients and tested against the corrected nominal CLI intensities. If the camera response has changes, a new 18 x 18 array of gains and biases is computed using the differences between current and corrected nominal CLI intensities, new eighth-order polynomials are computed, and the image is rezoned. The zoning technique is precisely the zoning of Figure 62 (the zoning that was done on the Hovis Sphere data). If the camera response has not changed, current zoning and coefficients are not changed.

The radiometric correction of RBV images is performed by applying the gain and bias for a given zone to all the input image intensity values in that zone (see Figure 65).

As part of radiometric correction the resulting pixel values are checked. Any values which are greater than 63 are made equal to 63. (This assumes that miminum value is 0.)

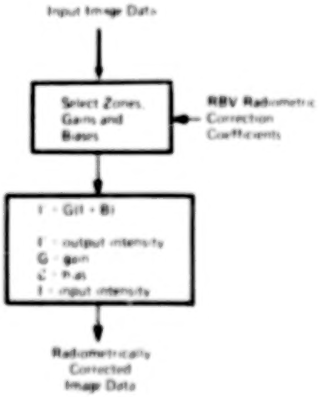
Input Image Data
Select Zones, Gains and Biases
RBV Radiometric Correction Coefficients
I' = GiI + Bi
I' = output intensity
G = gain
B = bias
I = input intensity
Radiometrically Corrected Image Data

Figure 65. Radiometric Correction Coefficient Application.

3.3.3 Geometric Correction

The functional flow of geometric correction is presented in Figure 66.

Geometric correction is divided into correction determination and correction application. Correction determination begins with the location of reseau marks in the input data. Control point search areas are then extracted from the input data, corrected for internal RBV geometric errors (determined from the reseau marks), corrected for radiometric distortions, and are input to the Control Location Algorithm (CLA). The CLA uses an FFT implementation of cross-correlation between windows of image data surrounding the control points and the image data. Error Modeling uses ancillary data and the control point locations to estimate spacecraft attitude. Space-to-Space Mapping computes a grid point correspondence that accurately represents the geometric transformation applied to the input data (including the selected map projection). The computed geometric corrections are then applied to the input data in the resampling process.

3.3.3.1 Reseau Detection

A reseau pattern composed of a 9 x 9 array of opaque cruciform marks is inscribed on the RBV faceplate to provide the means of determining the geometric distortion introduced by the sensor. The mathematical characterization of the sensor-caused error in a given image requires the detection and precise location of the nominally black reseau marks in that image. The vector differences between the actual locations and the undistorted locations of the reseau marks are used to compute the coefficients of bivariate mapping polynomials used to represent the internal errors of the RBV.

The internal geometric errors of the RBV are expected to be very stable. A 64 x 48 pixel area centered at the last known location of the reseau (shown in Figure 67) is sufficiently large to ensure that it contains the reseau and is used as a search area for the reseau.

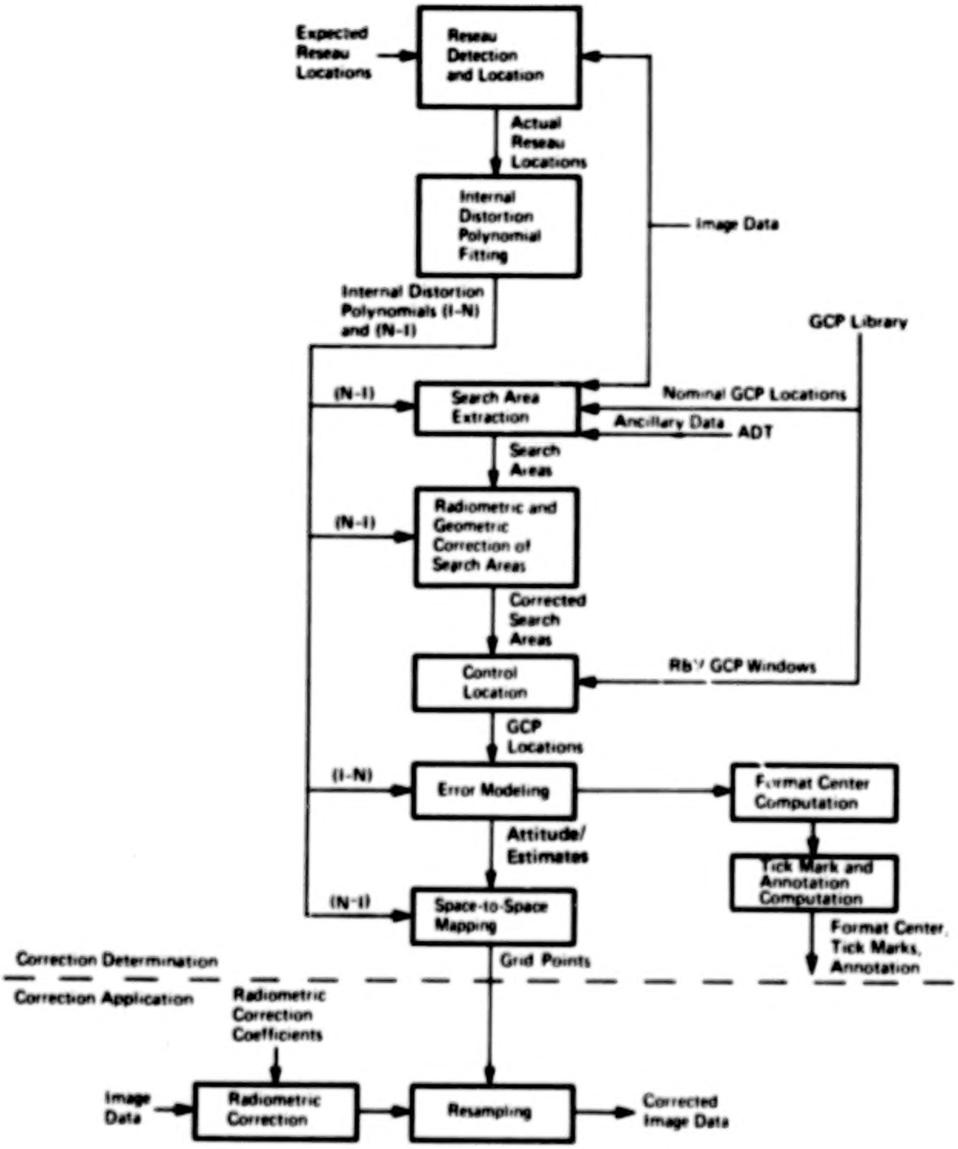
Expected
Reseau
Locations
Reseau
Detection
and Location
Actual
Reseau
Locations
Internal
Distortion
Polynomial
Fitting
Image Data
Internal Distortion
Polynomials (I-N)
and (N-I)
GCP Library
(N-I)
Search Area
Extraction
Nominal GCP Locations
Ancillary Data
ADT
Search
Areas
(N-I)
Radiometric and
Geometric
Correction of
Search Areas
Corrected
Search
Areas
Control
Location
RBV GCP Windows
GCP
Locations
(I-N)
Error Modeling
Format Center
Computation
Attitude/
Estimates
Tick Mark and
Annotation
Computation
(N-I)
Space-to-Space
Mapping
Format Center,
Tick Marks,
Annotation
Correction Determination
Grid Points
Correction Application
Radiometric
Correction
Coefficients
Image
Data
Radiometric
Correction
Resampling
Corrected
Image Data

Figure 66. Geometric Correction.

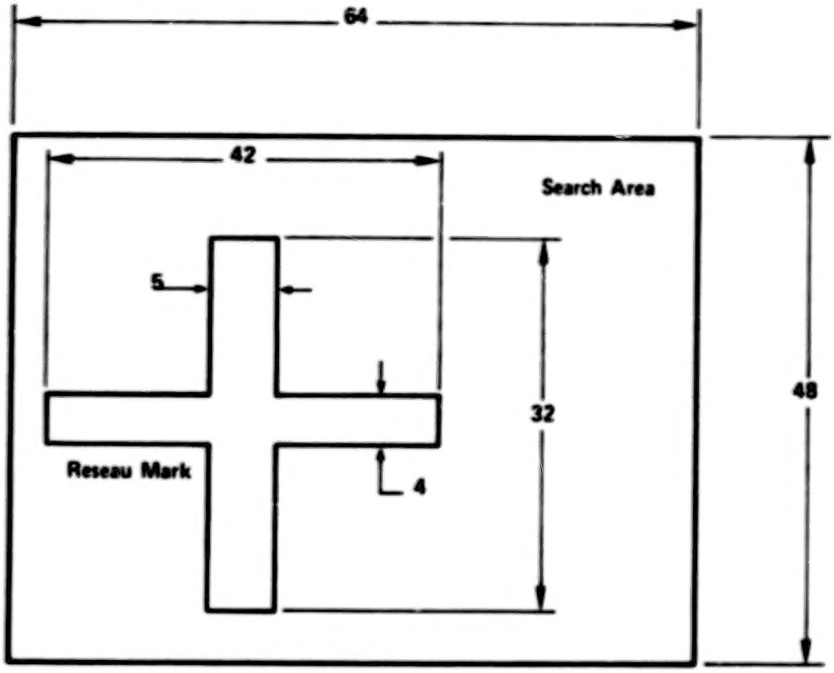

Figure 67. Shape and Size of Reseau Within the Search Area.

The reseau detection routine developed by IBM is based on the following operational sequence:

a. The last known locations of reseau marks are inputs to the program.

b. Within search areas of 64 x 48 pixels, each centered about a previous reseau mark location, individual row and column sums of pixel gray levels are computed. This operation is called "shadow casting." Thus, along the nth column, the sum would be as shown in equation 25

$$S_n = \sum_{m=1}^{48} g_{mn} \tag{25}$$

where g_{mn} is the gray level of the pixel located at the mth row and the nth column of the 64 x 48 search area.

c. The reseau mark contained within a search area is detected by the application of the detection algorithm to the row and column sequences $\left\{S_m\right\}$ and $\left\{S_n\right\}$

This algorithm finds the lowest column sum and tentatively calls this the column center of the reseau. It then computes threshold values based on the lowest sum and the background intensity. The reseau is considered to be all contiguous sums in the neighborhood of the lowest sum that are lower than the threshold. A similar procedure is used for row sums.

The steps of the algorithm, described with reference to the typical set of row or column sums in Figure 68, are as follows:

a. Tentatively call the lowest sum, S_k, the reseau center.

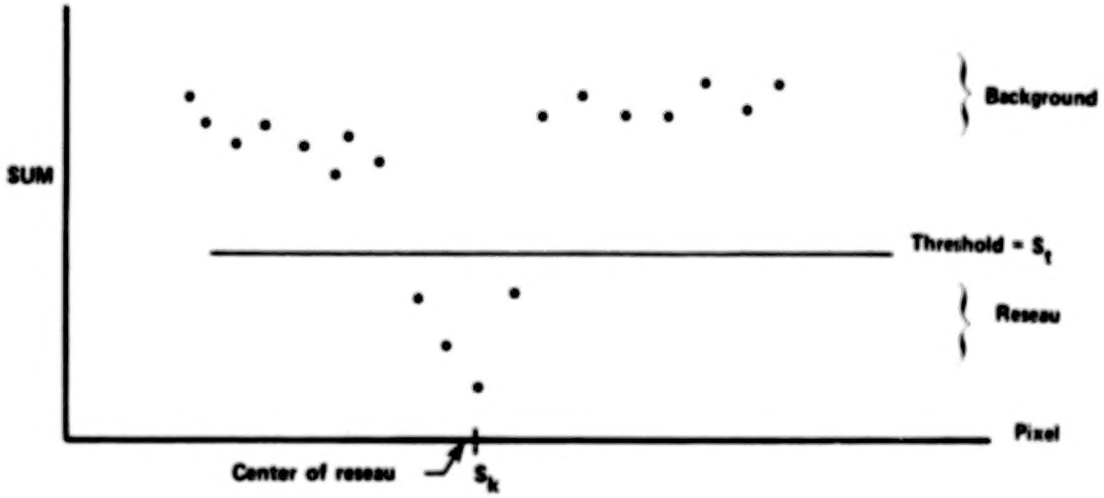

Figure 68. Typical Set of Row or Column Sums.

b. Next, compute a local average background intensity the following way:

> Move to the right of S_k three sums and the next four sums are background.
>
> Move to the left of S_k three sums and the next four sums are background. Average the eight background sums to get the local average background intensity (call it S_a).

c. Compute the average of S_k and S_a using equation 26. Call this a threshold, S_t.

$$S_t = (S_a + S_k)/2.0 \tag{26}$$

d. All sums below the threshold near S_k are reseau pixels.

e. If there is an odd number of pixels in the reseau, the correct center is the middle pixel of the reseau. If there is an even number of pixels in the reseau, the center is the pixel just left of the middle, i.e.,

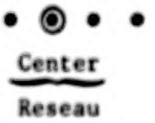

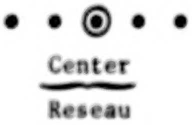

As described, this lowest sum algorithm finds 81 of 81 reseau. However, it defines a reseau location even if there was no reseau in the search area. Obviously, a check is necessary to detect false reseau. The false reseau check is based primarily on the following:

a. Real reseau are 3 to 7 pixels wide -- if we detect a reseau narrower than 3 or wider than 7 pixels, reject it.

b. Real reseau are much darker than the background, so the algorithm insists that a reseau pixel must be, on the average, at least 8 intensity levels (out of 64) darker than the background. That is, $S_a - S_k$ must be greater than 8 x (32-4) = 244.

Both of these checks use data routinely collected during the search for the reseau, and so take very little extra computing time. Used together they are extremely effective.

The reseau detection program was checked on 486 reseau marks (that is, 972 searches, one search through column sums and one search through row sums for each reseau). Every true reseau was found. Visual examination of the reseau showed the algorithm was finding the correct reseau center. A further confirmation of the algorithm's accuracy is the fact that the algorithm computed the average reseau width to be between 4 and 5 pixels. This agrees with visual evidence.

The reseau detection program was tested on 486 false reseau. That is, the program was asked to search for reseau in 486 search areas that contained no reseau. Of the 972 searches for the 486 false reseau, the program accepted only 3 of the 972 as being reseau. The probability of accepting a false row or column when on reseau is present in the search area is thus approximately 0.003, and the probability of accepting a false reseau is (3/972) (3/972) = approximately 0.00001. On the average, if the program looked only in search areas that contained no reseau through more than 1000 images, it would reject all but one of the false reseau.

3.3.3.2 Internal Distortion Modeling

Two pairs of fifth-order polynomials (84 coefficients) are least squares fit to the reseau marks. One pair represents the transformation from input to nominal reseau locations (I-N polynomials) and the other is from nominal to input (N-I polynomials). The two polynomial pairs, I-N and N-I, are used in Search Area Extraction, Error Modeling, and Space-to-Space Mapping.

3.3.3.3 Search Area Extraction and Correction

This process is performed in two steps: extraction and correction. Search area extraction is the process of estimating where in the input image space of each RBV camera control points will be found. It is expected that six points per RBV image will be adequate. To minimize correlation errors in Control Point Location, search areas are radiometrically and geometrically corrected (for distortion).

3.3.3.4 Control Location

The Control Location Algorithm (CLA) developed by IBM for the MDP will be used. The MDP CLA processes search areas of 128 x 128 pixels, while the search areas required for RBV processing are 384 x 384 pixels. Therefore, within these areas, 3 x 3 groups of samples are averaged to produce 128 x 128 sample arrays. The MDP CLA is used to correlate these arrays with 32 x 32 sample window arrays (formed by averaging 3 x 3 groups of samples over 96 x 96 sample arrays of RBV input data) taken from the RBV Control Point Library.

This coarse search is used to determine the approximate location of each control point in the input image data. Each approximate location is used to define the center of a 128 x 128 sample array of full-resolution RBV data. The MDP CLA is used to correlate these arrays with 32 x 32 sample window arrays of full-resolution RBV data taken from the RBV Control Point Library. The results of this fine search are used in the Error Modeling calculations.

3.3.3.5 Geometric Error Modeling

The functional flow of Geometric Error Modeling is presented in Figure 69.

Error modeling computes a pair of fifth-order bivariate polynomials to describe NBV internal distortions. Control point input image locations, produced by the CLA, are mapped through this polynomial pair to an internally-corrected set of coordinates. Nominal control point locations (latitude and longitude) from the control point library are mapped to the tangent space and then onto the nominal input space by analytical formulas. The differences in input and nominal Control Point Locations are assumed to be due solely to satellite attitude. Since the RBV is a framing sensor, classical three-parameter resection can be performed to estimate attitude: one each of roll, pitch, and yaw is produced. In the resection, Attitude Monitoring System (AMS) and tracking station estimates of attitude and altitude are input. They are then refined by the control point information. If insufficient control points are input to Geometric Error Modeling, the output defaults to AMS estimates of attitude.

If an RBV Control Point Library does not exist, but the MSS scene corresponding to a given RBV scene has been processed, an alternative attitude determination procedure shall be possible. The attitude models estimated during the processing of the MSS scene are input to the RBV correction process -- no RBV control points are located. Attitude determination is reduced to evaluating the MSS attitude polynomials at the time of the RBV image. This procedure is presented in Figure 70.

This alternative process will not be as accurate as processing with a true RBV control point library, but it does provide a reliable method by which RBV images can be corrected with reasonable accuracy in the absence of RBV control points. Therefore, this optional processing mode shall be implemented as part of the RBV processing system.

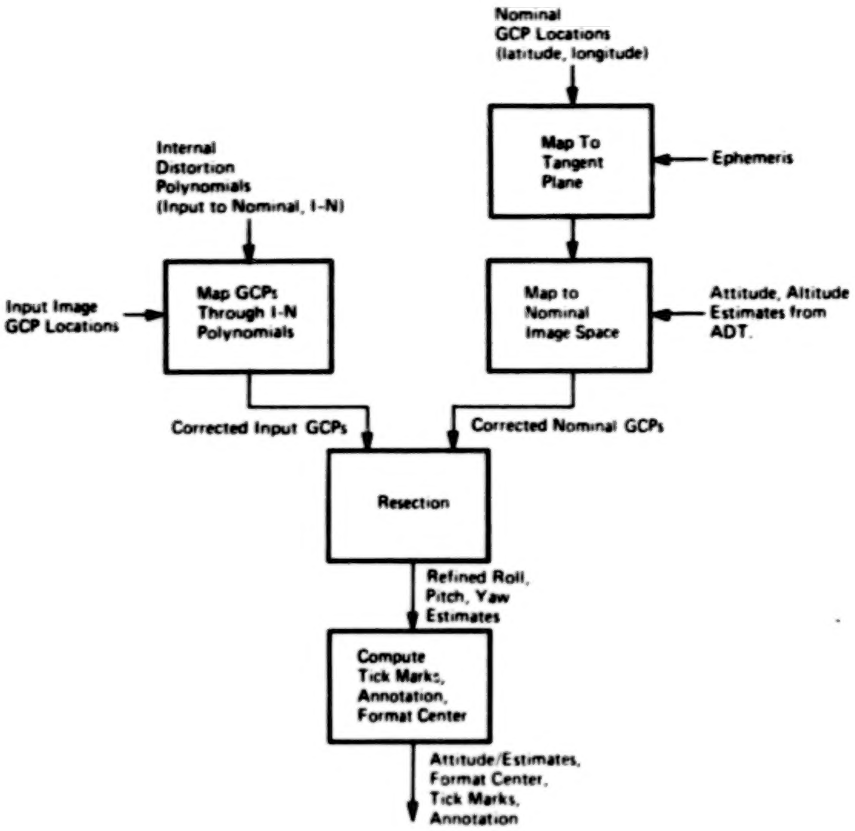
Nominal GCP Locations (latitude, longitude)
Internal Distortion Polynomials (Input to Nominal, I-N)
Map To Tangent Plane
Ephemeris
Input Image GCP Locations
Map GCPs Through I-N Polynomials
Map to Nominal Image Space
Attitude, Altitude Estimates from ADT.
Corrected Input GCPs
Corrected Nominal GCPs
Resection
Refined Roll, Pitch, Yaw Estimates
Compute Tick Marks, Annotation, Format Center
Attitude/Estimates, Format Center, Tick Marks, Annotation

Figure 69. Geometric Error Modeling.

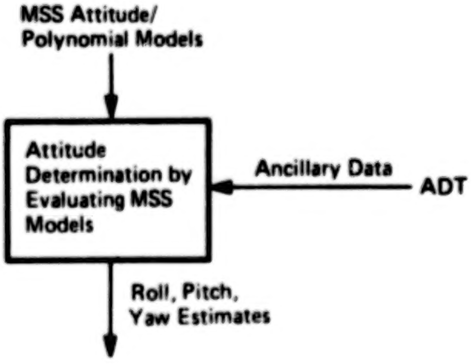
MSS Attitude/ Polynomial Models
Attitude Determination by Evaluating MSS Models
Ancillary Data
ADT
Roll, Pitch, Yaw Estimates

Figure 70. Alternative Attitude Determination Procedure.

3.3.3.6 Space-to-Space Mapping

The internal and external distortion correction models computed in Geometric Error Modeling are applied to a set of standard primary output space grid points to obtain corresponding pairs of coordinates L, S in the input image space. This procedure is functionally identical to the TM and MSS procedure described in subsection 3.2.4.3.

3.3.3.7 Geometric Interpolation

Cubic interpolation functions are applied to the input space coordinates of the primary grid point net to determine coordinates for a secondary, finer net. Linear interpolation is then used to compute the intersections of the near-vertical columns defined by the secondary grid points with the horizontal lines of the input data array. These operations are identical to that required for the TM and MSS scanning sensors and are further described in subsection 3.2.4.4.

3.3.4 Resampling for RBV

Since the points of the output array, when mapped to the input space, do not coincide generally with points on the input space sample lattice, the input space must be "resampled" at the computed locations of the output data points. Two algorithms (Cubic Convolution and Nearest Neighbor), discribed in subsection 3.2.5, are provided to perform this function. Both algorithms incorporate the final determination of the input space coordinates of each output sample (based on the data computed in Geometric Interpolation) as well as the determination of output sample intensity values.

3.4 HEAT CAPACITY MAPPER MISSION (HCMM)

The Heat Capacity Mapping Radiometer (HCMR) collects data in two bands (channels; 0.5 to 1.1 micron (visible and near IR) and 10.5 to 12.2 micron (IR), providing measurements of reflected solar energy and equivalent black body temperature. Since the S/C does not have an on-board data recording capability, sensor data can only be collected within range of an acquisition site (i.e., 5-10 minutes). The realtime HCMR analog data will be recorded on tape at the acquisition sites and shipped to GSFC for data processing. This analog data is then digitized at 8 bits per sample to create an input image array of 1500 samples/line, 1500 lines per frame, with a 500m by 500m pixel at nadir. This data will be radiometrically and geometrically corrected with 420m square pixels output.

The secord phase of the data processing deals with the registration of day and night thermal infrared data. Features will be identified in both the day and night data and the night thermal images remapped to overlay day images.

The registered day and night thermal infrared data will be archived at GSFC and used to produce day/night temperature difference data.

Processed data will be available in three formats:

a. Black-and-white imagery as 241 mm prints or transparencies

b. Computer-compatible tapes (CCTs) of calibrated and geometrically corrected data

c. Computer-compatible tapes of calibrated but geometrically uncorrected data.

3.4.1 Heat Capacity Mapper (HCM) Functional Description

HCM data correction and registration incorporates three distinct processing phases (see Figure 71). Phase I is the systematic correction of the HCMM image data. In this phase the input to the system is a continuous swath of unprocessed HCMM image data. These data are broken into frames and radiometric and systematic geometric corrections are applied. The output is square output images. All collected HCMM image data are processed through Phase I.

Phase II is the selection and systematic correction of overlapping day/night image pairs. The input to Phase II consists of one or more day/night pairs of unprocessed HCMM image tapes, where each pair has been found to contain an intersecting image area which is a candidate for day/night registration. From these the system generates an output tape containing pairs of day/night imagery. These pairs are fully processed (i.e., radiometric and systematic corrections are applied) and each frame is elongated to provide the complete area of overlap. Film is made of each pair of elongated frames to aid in control point selection during Phase III.

Phase III is the actual registration of day/night images. The input to Phase III is the tape of fully processed day/night image pairs created in Phase II. Under operator control, each image is displayed on the display terminal. Using the film images created from the Phase II output as a guide, the operator locates the control points in each displayed image and indicates their locations to the system using the cursor of the display terminal. Identifying information associated with each control point is entered so that the system can pair up conjugate points. When all the control points for an image pair have been located, the system registers the day images to the corresponding night image. The output of Phase III, derived from the registered images, consists of a pixel difference image and an apparent thermal inertia image. Thus far, only Phase I has been implemented on the MDP. The following sections will describe in more detail the Phase I processing functions.

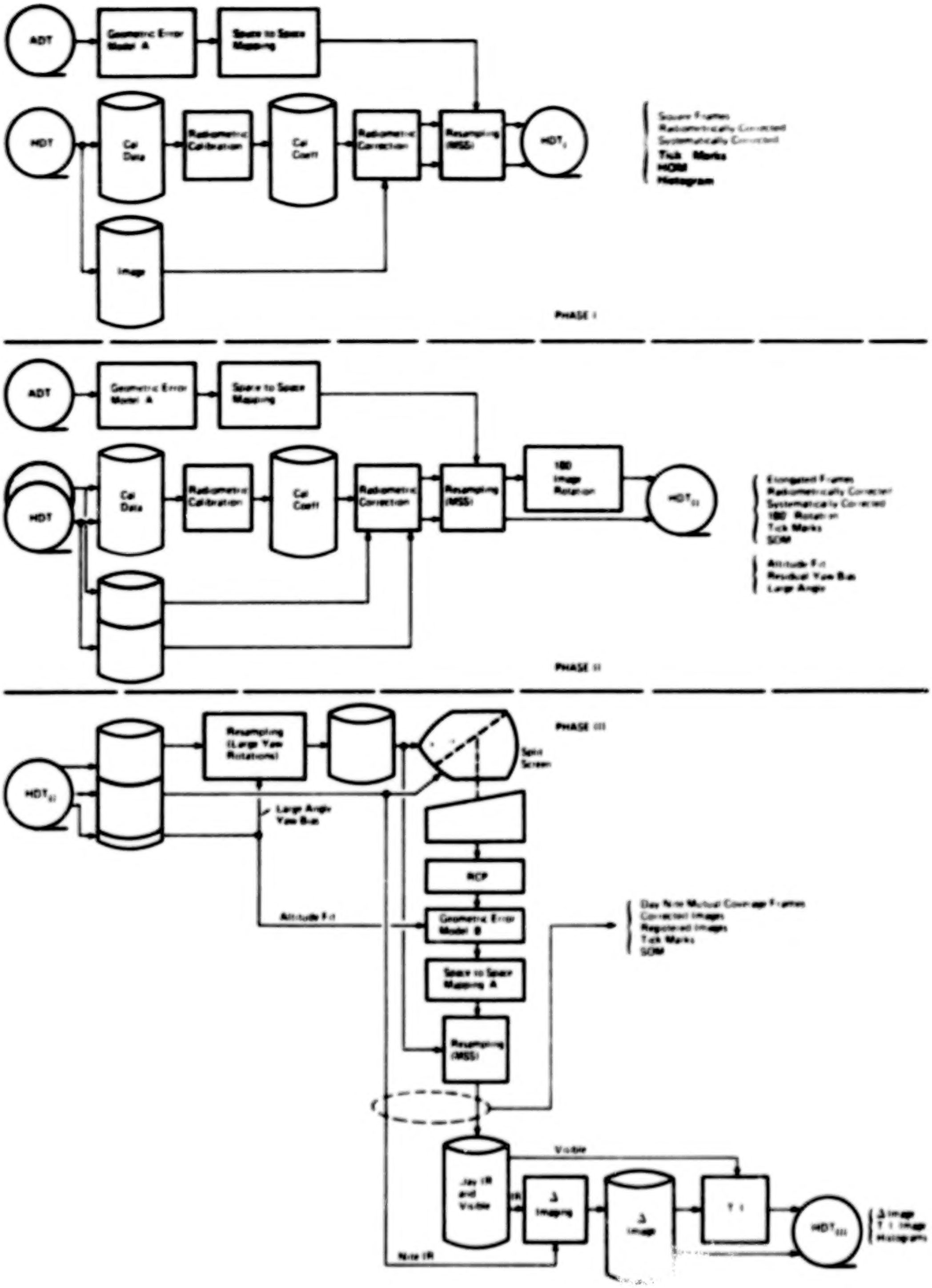
ADT
Geometric Error Model A
Space to Space Mapping
HDT
Cal Data
Radiometric Calibration
Cal Coeff
Radiometric Correction
Resampling (MSS)
HDT$_I$
Square Frames
Radiometrically Corrected
Systematically Corrected
Tick Marks
HCMM
Histogram
Image
PHASE I
ADT
Geometric Error Model A
Space to Space Mapping
HDT
Cal Data
Radiometric Calibration
Cal Coeff
Radiometric Correction
Resampling (MSS)
180 Image Rotation
HDT$_{II}$
Elongated Frames
Radiometrically Corrected
Systematically Corrected
180 Rotation
Tick Marks
SOM
Attitude Fit
Residual Yaw Bias
Large Angle
PHASE II
PHASE III
HDT$_{II}$
Resampling (Large Yaw Rotations)
Split Screen
Large Angle Yaw Bias
RCP
Attitude Fit
Geometric Error Model B
Space to Space Mapping A
Resampling (MSS)
Day Nite Mutual Coverage Frames
Corrected Images
Registered Images
Tick Marks
SOM
Visible
Day IR and Visible
IR
Δ Imaging
Δ Image
T I
HDT$_{III}$
Δ Image
T I Image
Histogram
Nite IR

Figure 71. Functional Diagram of HCMM Data Processing System.

MICROFILMED FROM
BEST AVAILABLE COPY

3.4.2 HCM Phase I Processing

The HCM processing system, shown in Figure 72, accepts the image data, radiometrically corrects the samples and, optionally, geometrically corrects the data to a Hotine Oblique Mercator (HOM) projection. The transformation grids will be generated using data from the S/C attitude measurements only. The output pixels, radiometrically and geometrically corrected, are output as rectangular frames (808.0 km x 693.4 km) or as an elongated frame. The elongated frame shows an 808.8 km width and can be as long as necessary to show the entire requested swath of input data, up to 5509 km.

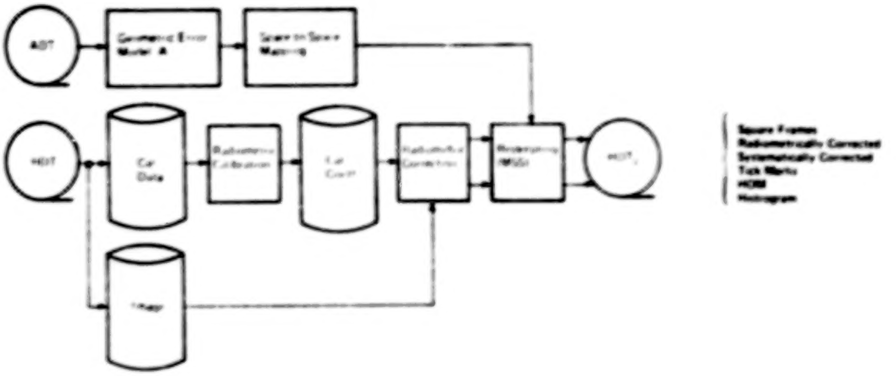
ADT
Geometric Error Model A
Scan to Scan Mapping
HDT
Cal Data
Radiometric Calibration
Cal Coeff
Radiometric Correction
Resampling
Image
Square Frames
Radiometrically Corrected
Systematically Corrected
Tick Marks
Histogram

Figure 72. HCMM Functional Flow.

Both fully processed and partially processed image data will be output from HCMM processing to a high density tape. Partially processed image data will consist of pixel values which have been radiometrically corrected but have not been geometrically corrected (i.e., not resampled). Fully processed image data will consist of pixel values which have been both radiometrically and geometrically corrected.

Image data is input (in BIL format) and processed on a swath basis. A swath is the maximum amount of contiguous sample data that can be gathered from the S/C. This can be as many as 10220 sensor scans of 1500 samples each (per

MICROFILMED FROM
BEST AVAILABLE COPY

each band). Image and calibration data are read from an input HDT and staged to disk for subsequent processing. Image data is being collected from both bands during the descending (nighttime) and ascending (daytime) nodes; however, only IR data is processed from the nighttime data. Ascending node data will be reversed from its input orientation in order that the frames of both day- and night-gathered data will have a northward orientation.

3.4.3 Radiometric Calibration Processing

Correction of earth scan radiometric values is necessary to remove distortions introduced between the detector voltage output and the presentation of data to the processing. In addition, the corrected radiometric value must be transformed to represent normalized albedo for Channel 1 and radiance intensities for Channel 2. A cubic polynomial is generated to account for the distortion and transformation.

The generation of the cubic polynomial coefficients is the radiometric calibration, while application of the function is radiometric correction. Figure 73 indicates the radiometric calibration inputs for channels 1 and 2.

The calibration process for channel 1 (visible band) is shown in Figure 74. Each major frame of image data contains a set of calibration data. Included in the calibration data are calibration wedges, the count levels resulting from introducing known voltage levels into the electronics system. There are two wedges for each channel, one injected at the input to the sensor amplifier and one at the output of the amplifier.

The input calibration wedge is used to develop a cubic polynomial (δ_i represents the coefficients), by a least squares procedure, which transforms received scan count to output sensor voltage. The transformation from voltage to normalized albedo for channel 1 is via a prespecified quadratic polynomial (α_i represents the coefficients). The β_i and α_i coefficients of the two polynomials are combined to form one cubic polynomial, giving normalized albedo from received scan count.

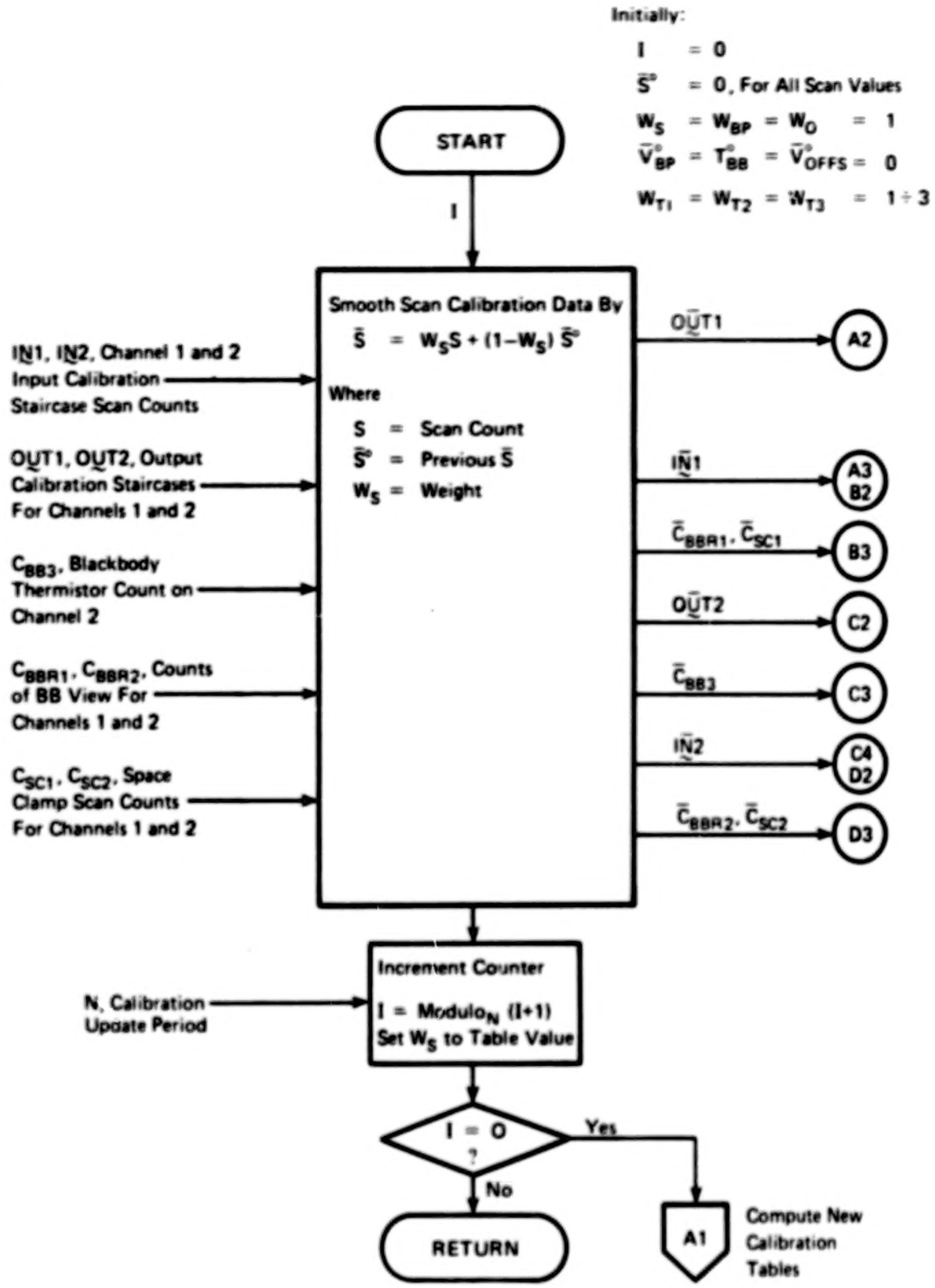
Initially:
$I = 0$
$\bar{S}^{\circ} = 0$, For All Scan Values
$W_S = W_{BP} = W_O = 1$
$\bar{V}^{\circ}_{BP} = T^{\circ}_{BB} = \bar{V}^{\circ}_{OFFS} = 0$
$W_{T1} = W_{T2} = W_{T3} = 1 \div 3$
START
I
Smooth Scan Calibration Data By
$\bar{S} = W_S S + (1-W_S)\,\bar{S}^{\circ}$
Where
S = Scan Count
$\bar{S}^{\circ}$ = Previous $\bar{S}$
W_S = Weight
IN1, IN2, Channel 1 and 2 Input Calibration Staircase Scan Counts
OUT1, OUT2, Output Calibration Staircases For Channels 1 and 2
C_{BB3}, Blackbody Thermistor Count on Channel 2
C_{BBR1}, C_{BBR2}, Counts of BB View For Channels 1 and 2
C_{SC1}, C_{SC2}, Space Clamp Scan Counts For Channels 1 and 2
OUT1
A2
IN1
A3
B2
$\bar{C}_{BBR1}$, $\bar{C}_{SC1}$
B3
OUT2
C2
$\bar{C}_{BB3}$
C3
IN2
C4
D2
$\bar{C}_{BBR2}$, $\bar{C}_{SC2}$
D3
N, Calibration Update Period
Increment Counter
$I = \text{Modulo}_N\,(I+1)$
Set W_S to Table Value
I = O ?
Yes
No
RETURN
A1
Compute New Calibration Tables

Figure 73. Radiometric Calibration Inputs.

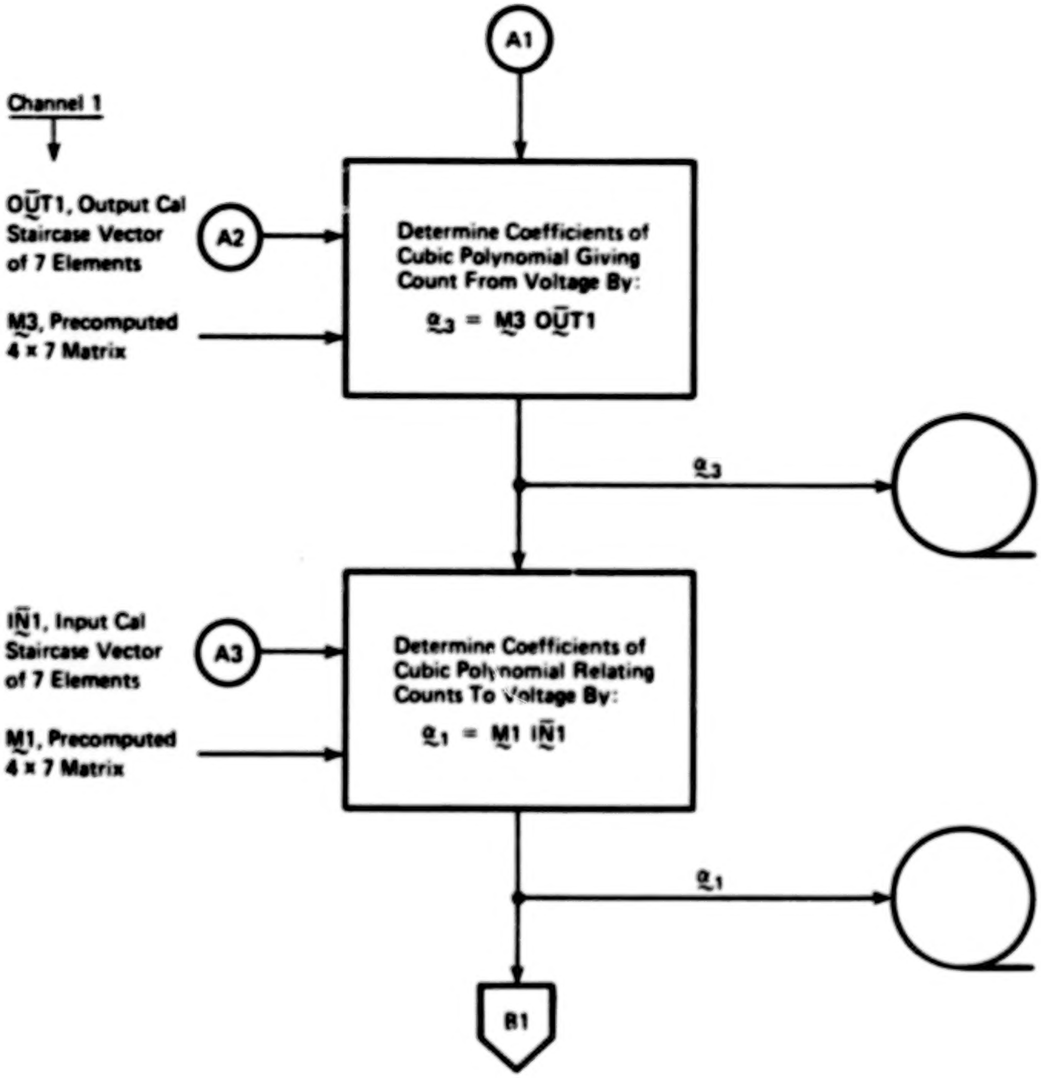
A1
Channel 1
OUT1, Output Cal Staircase Vector of 7 Elements
A2
M3, Precomputed 4 × 7 Matrix
Determine Coefficients of Cubic Polynomial Giving Count From Voltage By:
$\alpha_3 = M3\ OUT1$
α_3
IN1, Input Cal Staircase Vector of 7 Elements
A3
M1, Precomputed 4 × 7 Matrix
Determine Coefficients of Cubic Polynomial Relating Counts To Voltage By:
$\alpha_1 = M1\ IN1$
α_1
B1

Figure 74. Channel 1 Radiometric Calibration (Sheet 1 of 2).

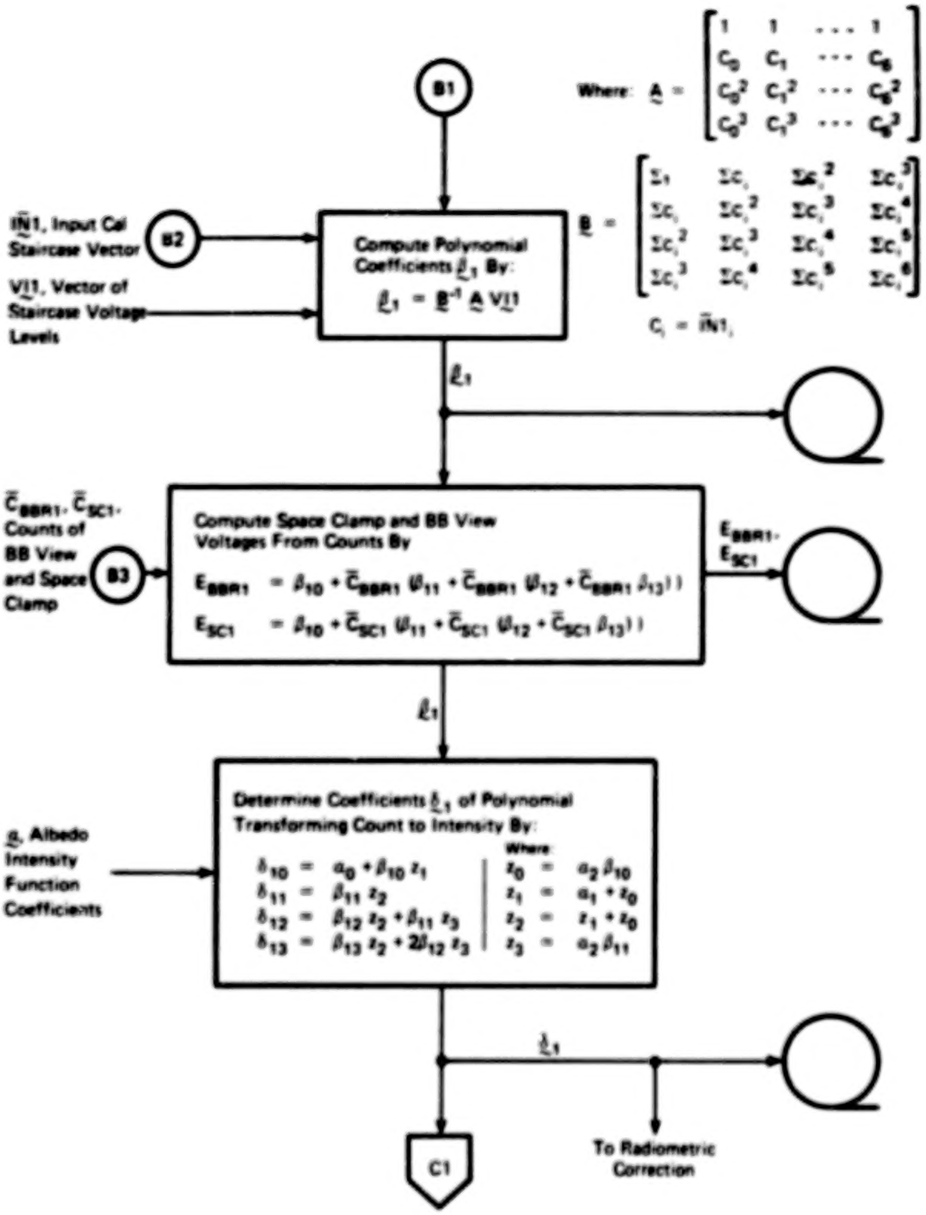
B1
Where: $\underset{\sim}{A} = \begin{bmatrix} 1 & 1 & \cdots & 1 \\ C_0 & C_1 & \cdots & C_6 \\ C_0^2 & C_1^2 & \cdots & C_6^2 \\ C_0^3 & C_1^3 & \cdots & C_6^3 \end{bmatrix}$
$\underset{\sim}{B} = \begin{bmatrix} \Sigma_1 & \Sigma c_i & \Sigma c_i^2 & \Sigma c_i^3 \\ \Sigma c_i & \Sigma c_i^2 & \Sigma c_i^3 & \Sigma c_i^4 \\ \Sigma c_i^2 & \Sigma c_i^3 & \Sigma c_i^4 & \Sigma c_i^5 \\ \Sigma c_i^3 & \Sigma c_i^4 & \Sigma c_i^5 & \Sigma c_i^6 \end{bmatrix}$
$C_i = \overline{IN}1_i$
$\underset{\sim}{IN}1$, Input Cal Staircase Vector
B2
$\underset{\sim}{VI}1$, Vector of Staircase Voltage Levels
Compute Polynomial Coefficients $\underset{\sim}{\beta}_1$ By:
$\underset{\sim}{\beta}_1 = \underset{\sim}{B}^{-1} \underset{\sim}{A} \underset{\sim}{VI}1$
$\underset{\sim}{\beta}_1$
$\overline{C}_{BBR1}$, $\overline{C}_{SC1}$, Counts of BB View and Space Clamp
B3
Compute Space Clamp and BB View Voltages From Counts By
$E_{BBR1} = \beta_{10} + \overline{C}_{BBR1} (\beta_{11} + \overline{C}_{BBR1} (\beta_{12} + \overline{C}_{BBR1} \beta_{13}))$
$E_{SC1} = \beta_{10} + \overline{C}_{SC1} (\beta_{11} + \overline{C}_{SC1} (\beta_{12} + \overline{C}_{SC1} \beta_{13}))$
E_{BBR1}, E_{SC1}
$\underset{\sim}{\beta}_1$
$\underset{\sim}{a}$, Albedo Intensity Function Coefficients
Determine Coefficients $\underset{\sim}{\delta}_1$ of Polynomial Transforming Count to Intensity By:
$\delta_{10} = a_0 + \beta_{10} z_1$
$\delta_{11} = \beta_{11} z_2$
$\delta_{12} = \beta_{12} z_2 + \beta_{11} z_3$
$\delta_{13} = \beta_{13} z_2 + 2\beta_{12} z_3$
Where:
$z_0 = a_2 \beta_{10}$
$z_1 = a_1 + z_0$
$z_2 = z_1 + z_0$
$z_3 = a_2 \beta_{11}$
$\underset{\sim}{\delta}_1$
C1
To Radiometric Correction

Figure 74. Channel 1 Radiometric Calibration (Sheet 2 of 2).

The procedure for channel 2 shown in Figure 75 is somewhat different. Included in the calibration data is a scan of an internal black body source, plus thermistor sensor readings of the black body and mounting plate temperatures. These temperature readings are used to compute the black body radiance, via the Planck equation. The radiance value and black body scan are then used to define a linear transformation of sensor voltage output to radiance. A third transformation from radiance to displayed intensity is done by a prespecified quadratic polynomial. The three polynomials are combined to form one cubic polynomial, defined by the 62 coefficients, giving output intensity as a function of received scan count.

The output calibration wedge is used mainly as a check on amplifier linerarity. The received count levels are used to develop a cubic polynomial giving count as a function of sensor voltage. This is the inverse of the transformation developed above from the input wedge which gave sensor voltage as a function of count. A similar polynomial is developed for the input wedge, and the two sets of coefficients are output for offline comparison and determination of amplifier linearity.

The output wedge is also used in channel 2 calibration to determine the voltage of a thermistor sensing the black body temperature.

Smoothing of the input calibration data is added to reduce noise added to the signals and to reduce the frequency of radiometric calibration. Calibration is performed every N scan lines, where N is restricted to $1 < N < 12$. When N is changed, the value of a smoothing constant will be adjusted to provide an effective averaging of N scan lines. In addition to smoothing of calibration scan data, smoothing of telemetry voltages is performed within the calibration process.

3.4.4 Radiometric Correction

Radiometric correction is the application of the cubic polynomial developed above to the received earth scan values. The process in shown in Figure 76

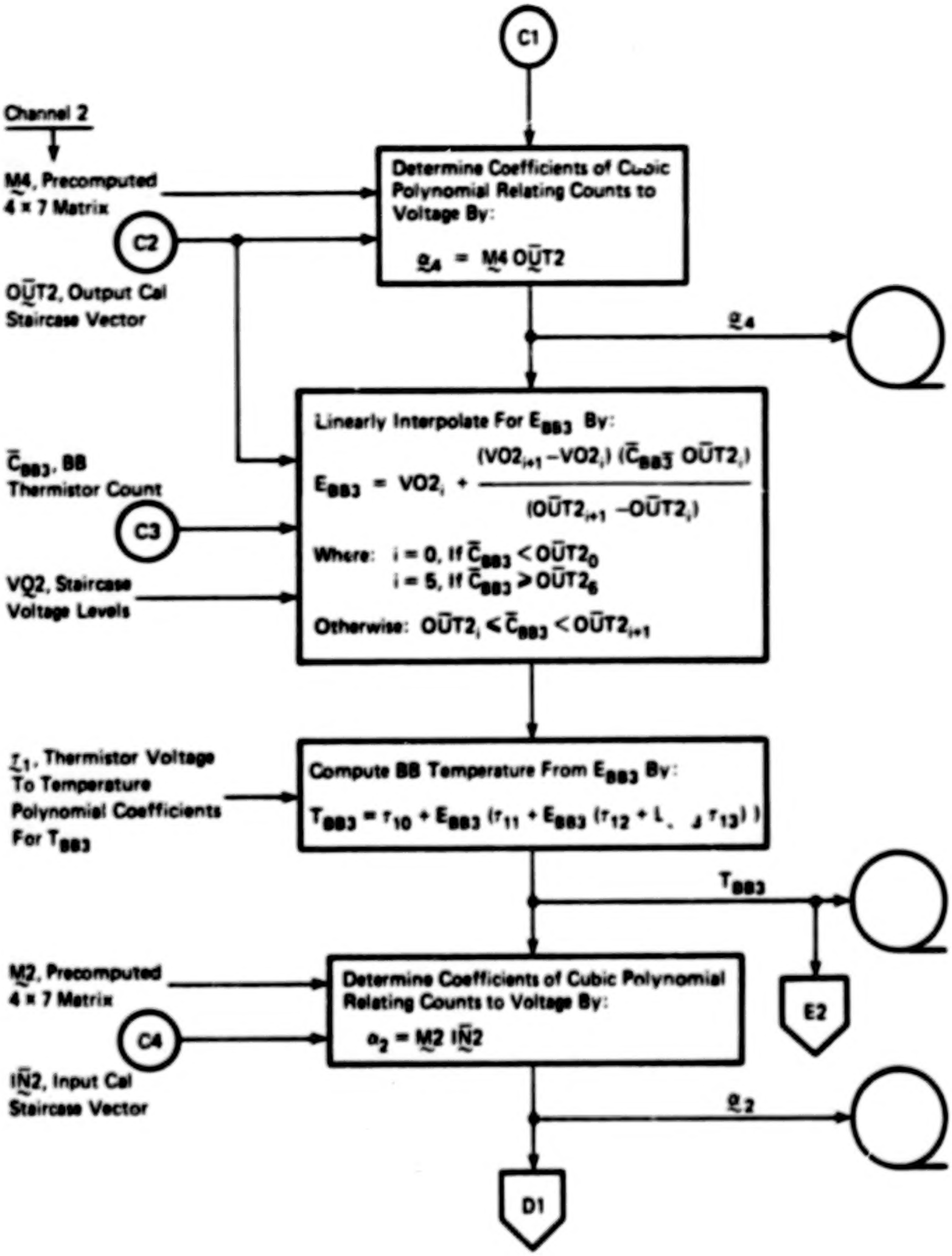
C1
Channel 2
M4, Precomputed 4 × 7 Matrix
C2
OUT2, Output Cal Staircase Vector
Determine Coefficients of Cubic Polynomial Relating Counts to Voltage By:
$a_4 = M4\ \overline{OUT}2$
a_4
$\bar{C}_{BB3}$, BB Thermistor Count
C3
VO2, Staircase Voltage Levels
Linearly Interpolate For E_{BB3} By:
$E_{BB3} = VO2_i + \frac{(VO2_{i+1} - VO2_i)(\bar{C}_{BB3} - \overline{OUT}2_i)}{(\overline{OUT}2_{i+1} - \overline{OUT}2_i)}$
Where: $i = 0$, If $\bar{C}_{BB3} < \overline{OUT}2_0$
$i = 5$, If $\bar{C}_{BB3} > \overline{OUT}2_6$
Otherwise: $\overline{OUT}2_i < \bar{C}_{BB3} < \overline{OUT}2_{i+1}$
τ_1, Thermistor Voltage To Temperature Polynomial Coefficients For T_{BB3}
Compute BB Temperature From E_{BB3} By:
$T_{BB3} = \tau_{10} + E_{BB3}(\tau_{11} + E_{BB3}(\tau_{12} + E_{BB3}\tau_{13}))$
T_{BB3}
E2
M2, Precomputed 4 × 7 Matrix
C4
IN2, Input Cal Staircase Vector
Determine Coefficients of Cubic Polynomial Relating Counts to Voltage By:
$a_2 = M2\ \overline{IN}2$
a_2
D1

Figure 75. Channel 2 Radiometric Calibration (Sheet 1 of 4).

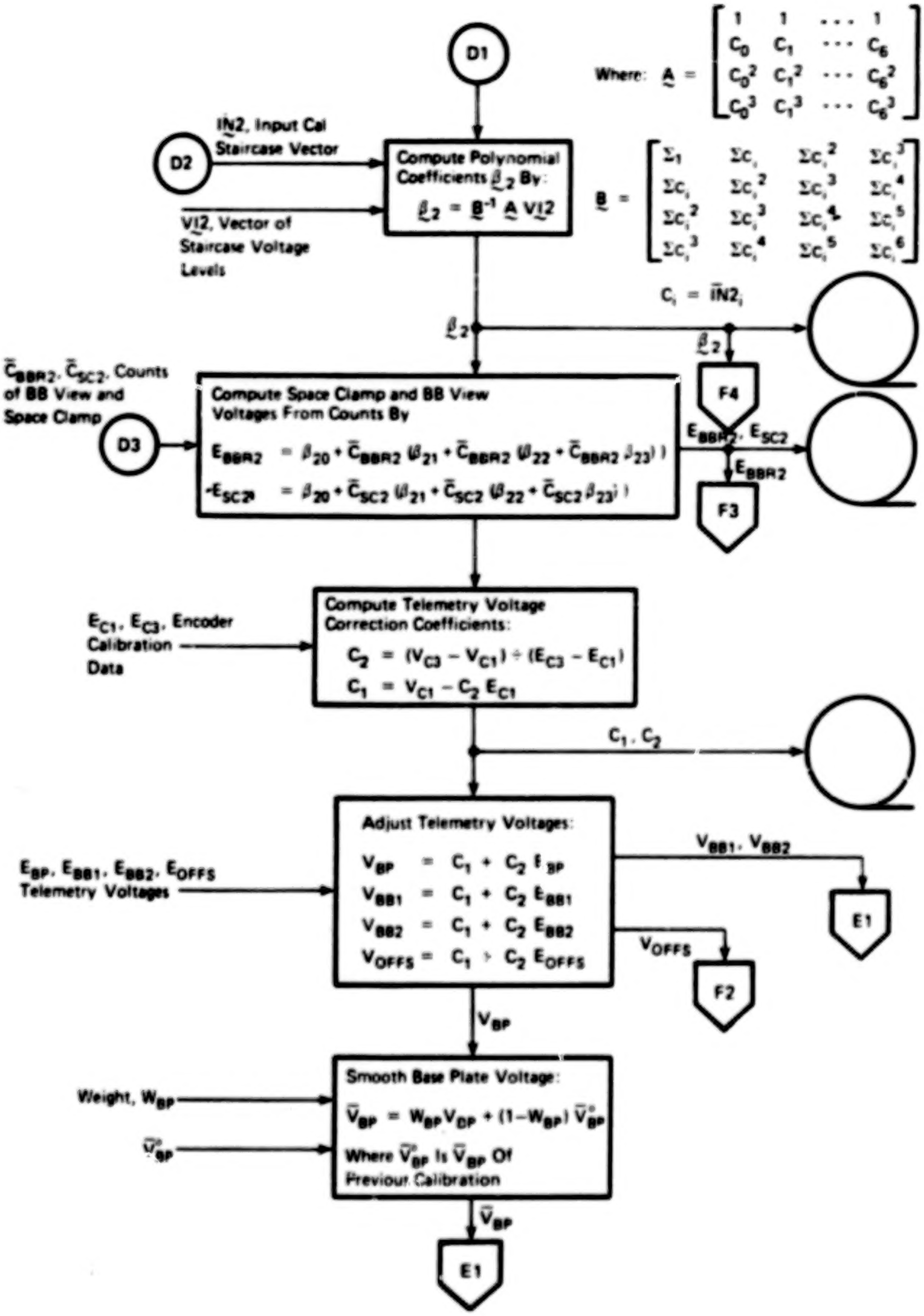
D1
Where: A = [1 1 ... 1; C0 C1 ... C6; C0² C1² ... C6²; C0³ C1³ ... C6³]
IN2, Input Cal Staircase Vector
D2
Compute Polynomial Coefficients β2 By:
β2 = B⁻¹ A VI2
VI2, Vector of Staircase Voltage Levels
B = [Σ1 ΣCi ΣCi² ΣCi³; ΣCi ΣCi² ΣCi³ ΣCi⁴; ΣCi² ΣCi³ ΣCi⁴ ΣCi⁵; ΣCi³ ΣCi⁴ ΣCi⁵ ΣCi⁶]
Ci = IN2i
β2
β2
F4
C̄BBR2, C̄SC2, Counts of BB View and Space Clamp
D3
Compute Space Clamp and BB View Voltages From Counts By
EBBR2 = β20 + C̄BBR2 (β21 + C̄BBR2 (β22 + C̄BBR2 β23))
ESC2 = β20 + C̄SC2 (β21 + C̄SC2 (β22 + C̄SC2 β23))
EBBR2, ESC2
EBBR2
F3
EC1, EC3, Encoder Calibration Data
Compute Telemetry Voltage Correction Coefficients:
C2 = (VC3 − VC1) ÷ (EC3 − EC1)
C1 = VC1 − C2 EC1
C1, C2
EBP, EBB1, EBB2, EOFFS Telemetry Voltages
Adjust Telemetry Voltages:
VBP = C1 + C2 EBP
VBB1 = C1 + C2 EBB1
VBB2 = C1 + C2 EBB2
VOFFS = C1 + C2 EOFFS
VBB1, VBB2
E1
VOFFS
F2
VBP
Weight, WBP
V̄°BP
Smooth Base Plate Voltage:
V̄BP = WBP VBP + (1−WBP) V̄°BP
Where V̄°BP Is V̄BP Of Previous Calibration
V̄BP
E1

Figure 75. Cahnnel 2 Radiometric Calibration (Sheet 2 of 4).

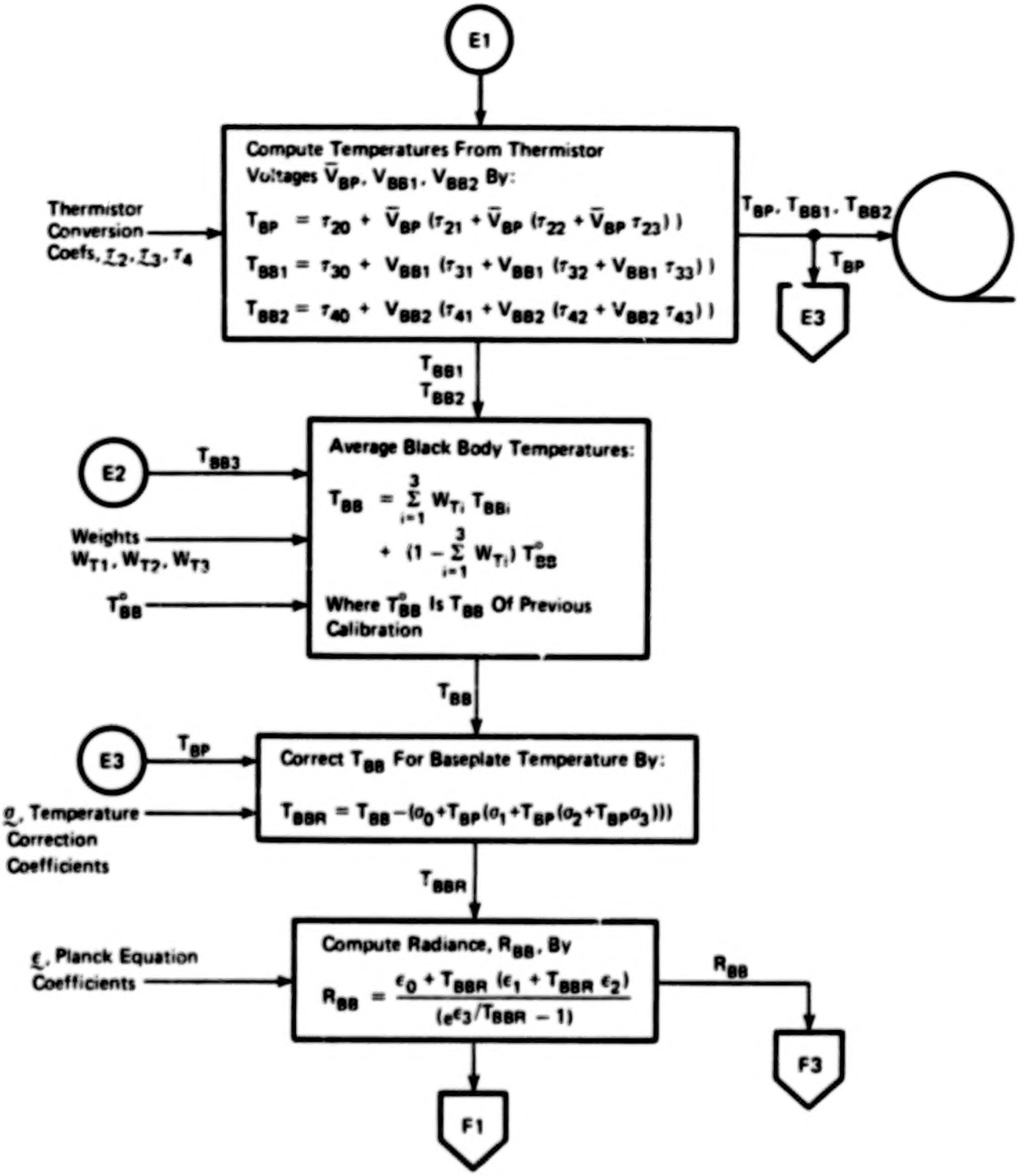
E1
Compute Temperatures From Thermistor Voltages $\bar{V}_{BP}$, V_{BB1}, V_{BB2} By:
$T_{BP} = \tau_{20} + \bar{V}_{BP}(\tau_{21} + \bar{V}_{BP}(\tau_{22} + \bar{V}_{BP}\tau_{23}))$
$T_{BB1} = \tau_{30} + V_{BB1}(\tau_{31} + V_{BB1}(\tau_{32} + V_{BB1}\tau_{33}))$
$T_{BB2} = \tau_{40} + V_{BB2}(\tau_{41} + V_{BB2}(\tau_{42} + V_{BB2}\tau_{43}))$
Thermistor Conversion Coefs, $\underset{\sim}{\tau}_2$, $\underset{\sim}{\tau}_3$, τ_4
T_{BP}, T_{BB1}, T_{BB2}
T_{BP}
E3
T_{BB1}
T_{BB2}
E2
T_{BB3}
Average Black Body Temperatures:
$T_{BB} = \sum_{i=1}^{3} W_{Ti} T_{BBi} + (1 - \sum_{i=1}^{3} W_{Ti}) T_{BB}^{\circ}$
Weights W_{T1}, W_{T2}, W_{T3}
T_{BB}°
Where T_{BB}° Is T_{BB} Of Previous Calibration
T_{BB}
E3
T_{BP}
Correct T_{BB} For Baseplate Temperature By:
$T_{BBR} = T_{BB} - (\alpha_0 + T_{BP}(\alpha_1 + T_{BP}(\alpha_2 + T_{BP}\alpha_3)))$
$\underset{\sim}{\alpha}$, Temperature Correction Coefficients
T_{BBR}
Compute Radiance, R_{BB}, By
$R_{BB} = \frac{\epsilon_0 + T_{BBR}(\epsilon_1 + T_{BBR}\epsilon_2)}{(e^{\epsilon_3/T_{BBR}} - 1)}$
$\underset{\sim}{\epsilon}$, Planck Equation Coefficients
R_{BB}
F3
F1

Figure 75. Channel 2 Radiometric Calibration (Sheet 3 of 4).

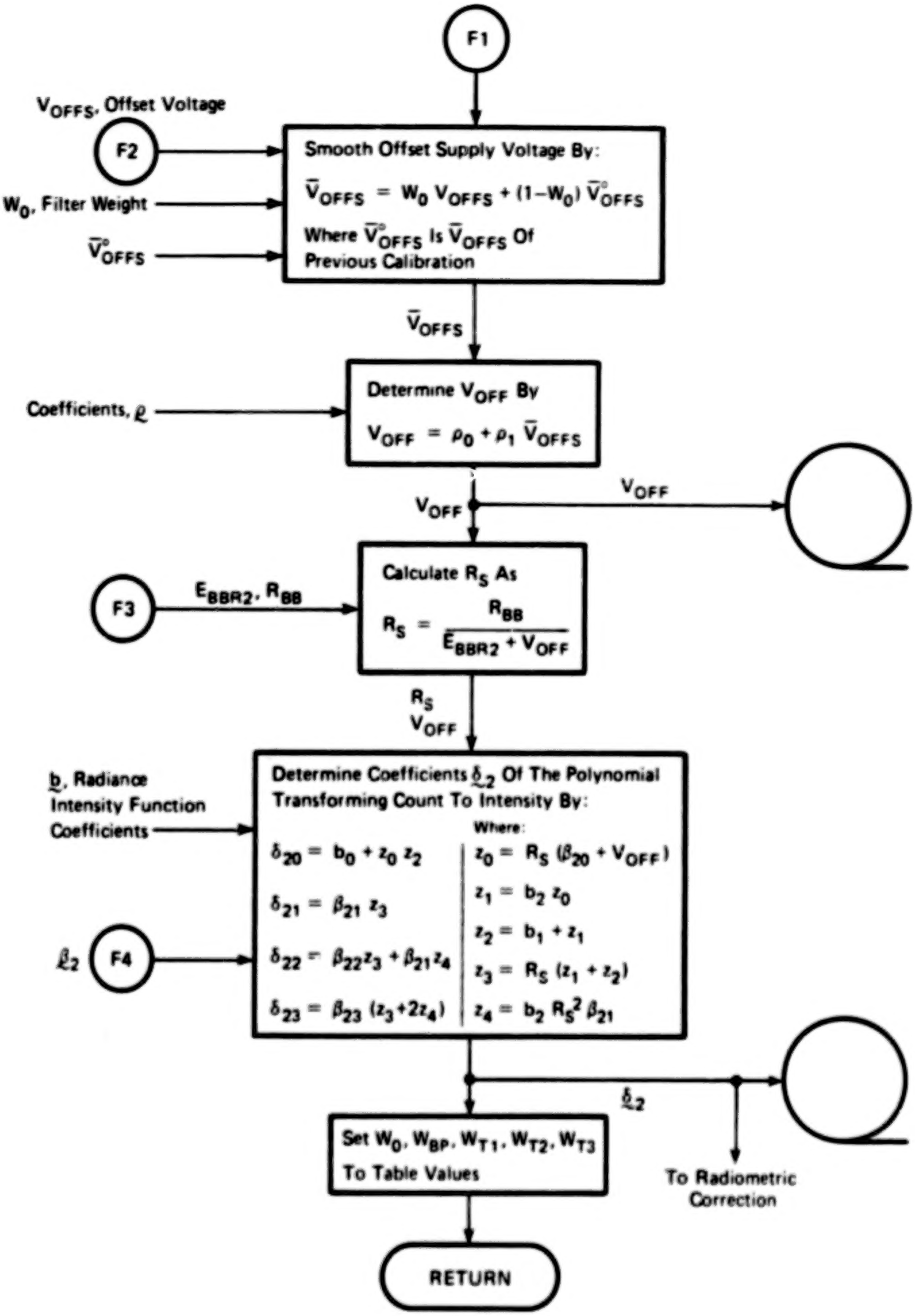
F1
V_{OFFS}, Offset Voltage
F2
W_0, Filter Weight
$\bar{V}^{\circ}_{OFFS}$
Smooth Offset Supply Voltage By:
$\bar{V}_{OFFS} = W_0 V_{OFFS} + (1-W_0)\bar{V}^{\circ}_{OFFS}$
Where $\bar{V}^{\circ}_{OFFS}$ Is $\bar{V}_{OFFS}$ Of Previous Calibration
$\bar{V}_{OFFS}$
Coefficients, $\underset{\sim}{\rho}$
Determine V_{OFF} By
$V_{OFF} = \rho_0 + \rho_1 \bar{V}_{OFFS}$
V_{OFF}
V_{OFF}
F3
E_{BBR2}, R_{BB}
Calculate R_S As
$R_S = \frac{R_{BB}}{E_{BBR2} + V_{OFF}}$
R_S
V_{OFF}
$\underset{\sim}{b}$, Radiance Intensity Function Coefficients
$\underset{\sim}{\beta}_2$
F4
Determine Coefficients $\underset{\sim}{\delta}_2$ Of The Polynomial Transforming Count To Intensity By:
$\delta_{20} = b_0 + z_0 z_2$
$\delta_{21} = \beta_{21} z_3$
$\delta_{22} = \beta_{22} z_3 + \beta_{21} z_4$
$\delta_{23} = \beta_{23}(z_3 + 2z_4)$
Where:
$z_0 = R_S(\beta_{20} + V_{OFF})$
$z_1 = b_2 z_0$
$z_2 = b_1 + z_1$
$z_3 = R_S(z_1 + z_2)$
$z_4 = b_2 R_S^2 \beta_{21}$
$\underset{\sim}{\delta}_2$
Set W_0, W_{BP}, W_{T1}, W_{T2}, W_{T3} To Table Values
To Radiometric Correction
RETURN

Figure 75. Channel 2 Radiometric Calibration (Sheet 4 of 4).

and is the same for channels 1 and 2. The process consists of two steps. First, the radiometric value of each pixel in a scan line is transformed via a cubic polynomial. A different set of coefficients is used for each band and set of N scan lines. If necessary, (for daytime images), the pixel ordering is also reversed in this step. Next, all transformed values less than 0 are clipped to 0, and all values greater than 255 are clipped to 255. This process is simple mathematically, but relatively time consuming because it must be applied to every input sample.

3.4.5 Geometric Correction

Geometric correction of the HCCM image data (as with MSS and TM data) involves

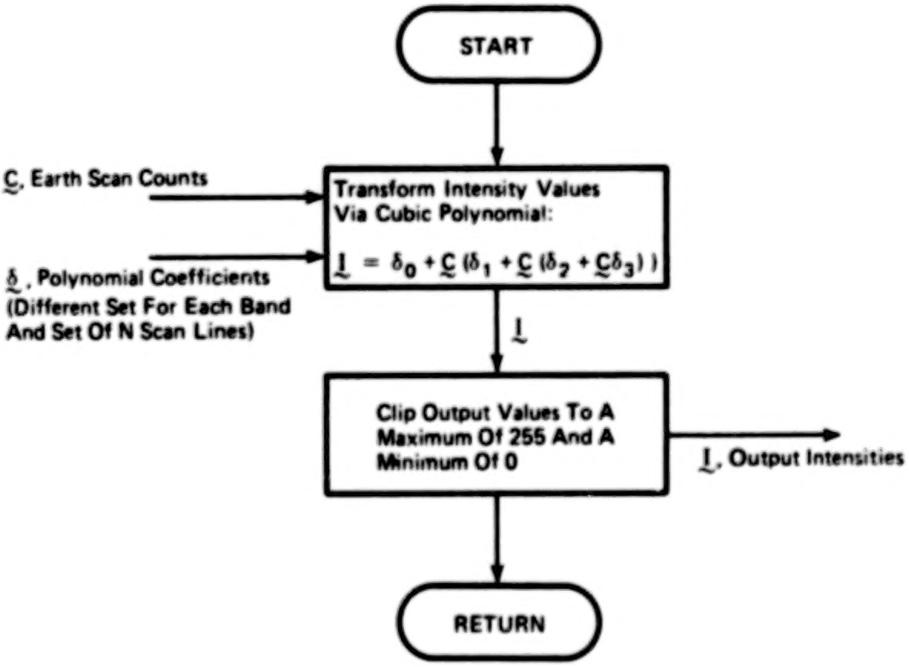
START
C, Earth Scan Counts
δ, Polynomial Coefficients (Different Set For Each Band And Set Of N Scan Lines)
Transform Intensity Values Via Cubic Polynomial:
$I = \delta_0 + C(\delta_1 + C(\delta_2 + C\delta_3))$
I
Clip Output Values To A Maximum Of 255 And A Minimum Of 0
I, Output Intensities
RETURN

Figure 76. Radiometric Correction Process.

developing a mathematical transformation to transform the input image samples to a geometrically correct output space.

As described in subsection 3.2.4, geometric correction of MSS and TM data involves four steps:

a. Control Point Processing

b. Geometric Error Modeling

c. Space-to-Space Mapping

d. Geometric Interpolation.

Control points, or recognizable features locatable in the input image data, are used to develop very precise attitude/altitude models necessary for removing the geometric distortions present in MSS and TM image data. However, these sensors have considerable redundancy in CPs and the CPs are referenced to maps. With HCMM, neither the number or distribution of recognizable CPs is sufficient to support a MSS/TM like attitude/altitude model. Furthermore, the resolution of HCMM (500 m) is much less than MSS or TM such that the accuracy of the end result is expected to be worse.

In addition, the HCMM attitude control system differs substantially from the Landsat spacecraft, expecially with regards to the magnitude of the attitude excursions and unlike the Landsat application, attitude data is available for only small fractions of an orbit, i.e., 10 minutes rather than continuously. The HCMM attitude specifications give the maximum yaw excursion as less than ±2 degrees and the maximum pitch and roll excursions as less than ±0.5 degrees. The maximum attitude rate is less than 0.01 degrees per second for all three axes. It was further revealed that the Attitude Control System (ACS) data supplied by GSFC on the Ancillary Data Tape (ADT) had reduced the random noise in the raw data to the maximum extent possible. Further reduction by the MDP (smoothing) was not likely and, in fact, may lose some of the fidelity produced by GSFC processing and recorded on the ADT.

After consideration of the above factors, it was decided that the current geometric error modeling approach implemented for the MSS and TM be replaced with a linear interpolation of the attitude and altitude values supplied by GSFC ADT. The remaining functions necessary for geometric correction (i.e., space-to-space mapping and geometric interpolation) are described in the following subsections.

3.4.5.1 Space-To-Space Mapping

The space-to-space mapping procedure for HCCM is similar to the procedure used for the MSS and TM scanning sensors described in subsection 3.2.4.3. A rectangular array of grid points are defined in the output space during the system design. The spacing of this array is selected to keep the interpolation errors less than an acceptable limit in the presence of the anticipated worst case distortions. This array is invariant for a given map projection and output image and pixel size.

An iterative mapping procedure is used to compute the input space coordinates of the rectangular array of grid points defined in output space. The iterative requirement stems from the uncertainty of the exact time at which a point on the ground is imaged by the sensor.

This intermediate mapping for the HCCM will be to tangent cylinder, whereas the iteration involved an intermediate step mapping of the grid points to a tangent plane for MSS and TM. This tangent cylinder is inertially fixed with its axis normal to the orbital plane as shown in Figure 77. The line of tangency with the geosphere passes through the nadir at scene center time of the scene designated as the HRC scene. The nadir forms the origin of the tangent space coordinate (SC, YC, ZC) shown in Figure 78. XC is a curvilinear coordinate along the line of tangency traced out by the radius vector of the satellite. Time is measured from scene center time. This tangent cylinder serves as a swath long intermediate mapping surface. When mapping

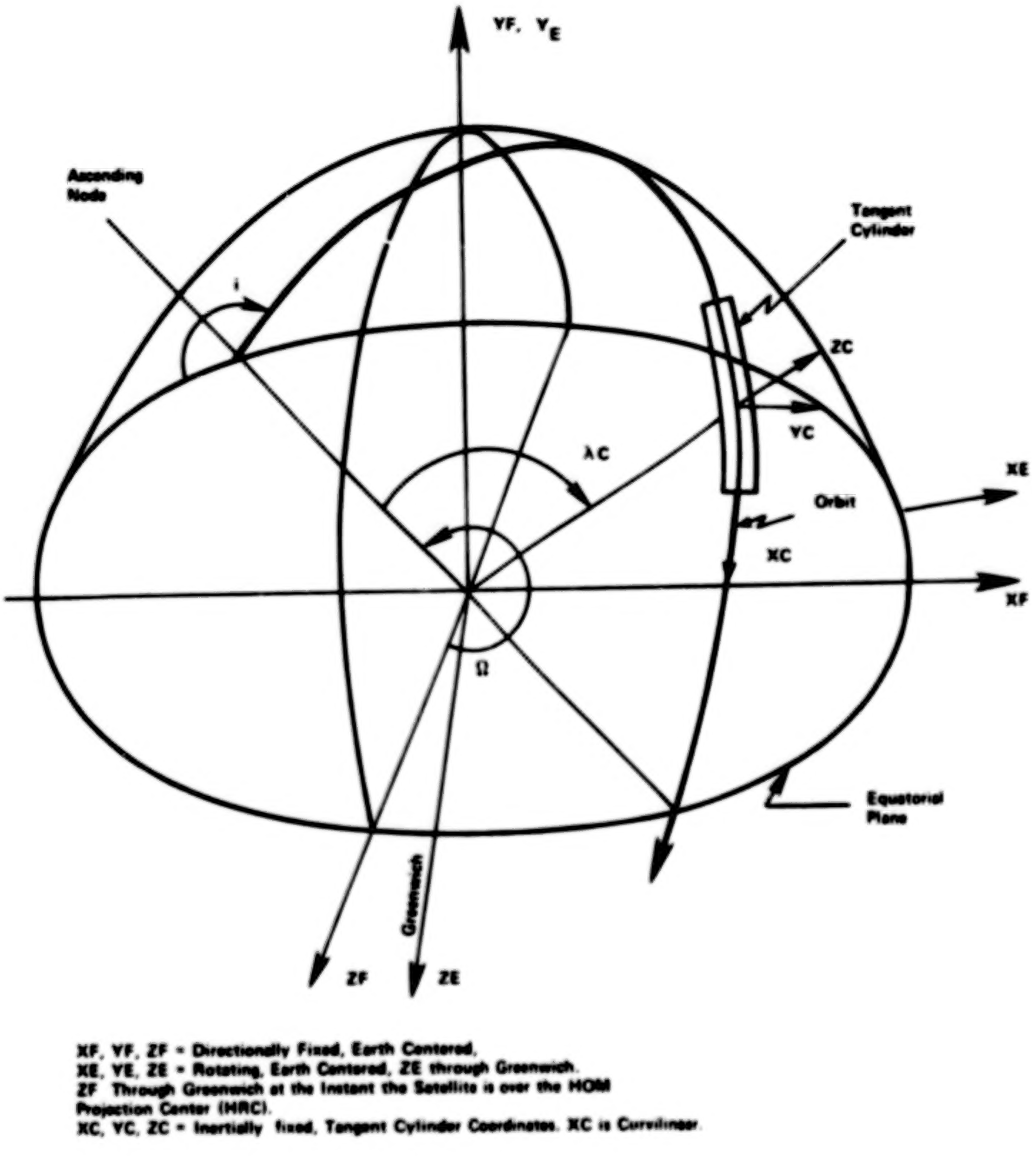
YF, Y_E
Ascending Node
i
Tangent Cylinder
ZC
YC
λC
XE
Orbit
XC
XF
Ω
Equatorial Plane
Greenwich
ZF
ZE

XF, YF, ZF = Directionally Fixed, Earth Centered,
XE, YE, ZE = Rotating, Earth Centered, ZE through Greenwich.
ZF Through Greenwich at the Instant the Satellite is over the HOM Projection Center (HRC).
XC, YC, ZC = Inertially fixed, Tangent Cylinder Coordinates. XC is Curvilinear.

Figure 77. Space-to-Space Mapping Coordinate Frames.

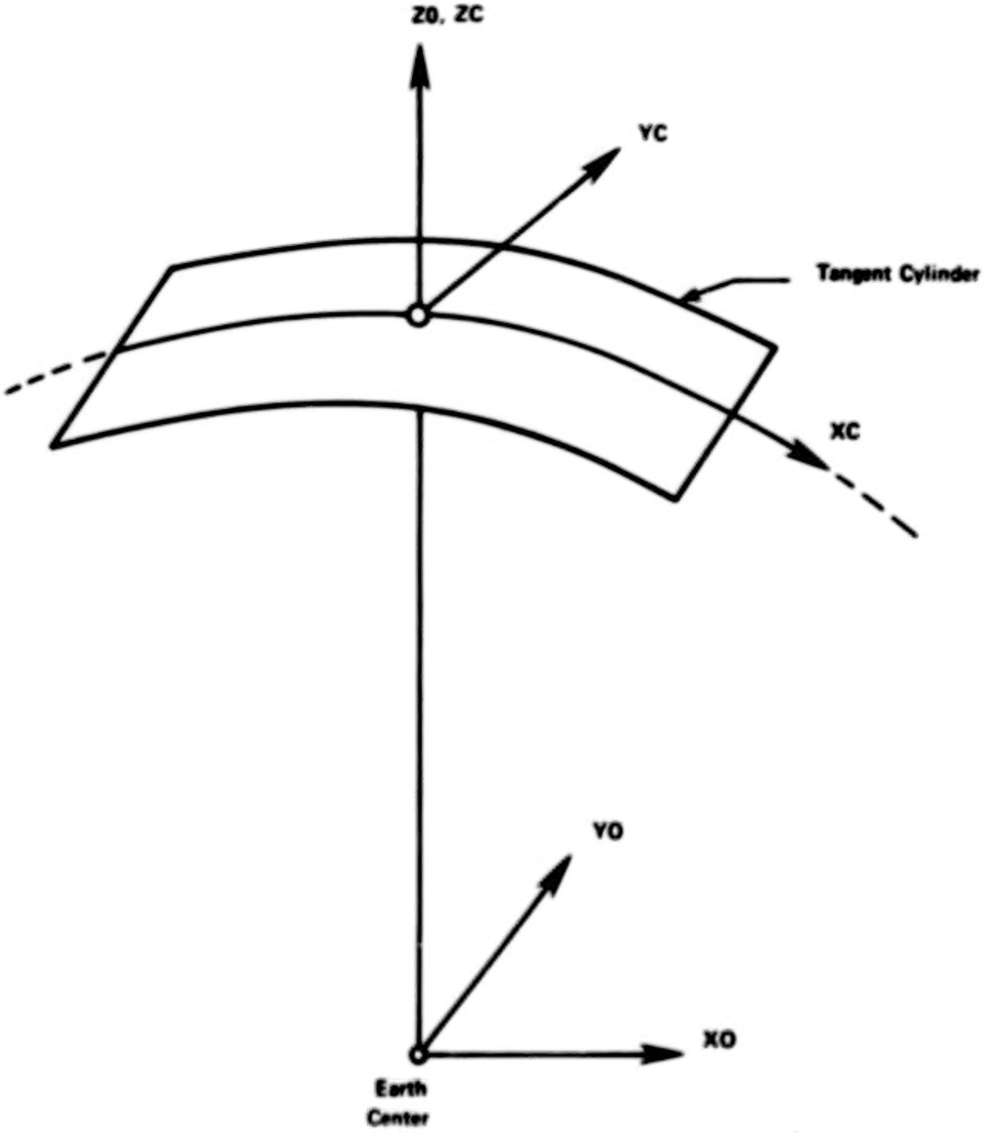
Z0, ZC
YC
Tangent Cylinder
XC
YO
XO
Earth
Center

Figure 78. Tangent Cylinder Coordinates.

a single grid point from the tangent cylinder into the input image, each individual iteration for the grid point will use a locally defined tangent plane.

The output of the space-to-space mapping function is a 44 x 23 grid of pixels containing the input space coordinates of the spatial interpolation grid points presented in Hotine Oblique Mercator (HOM) projection. This array provides the input to the geometric interpolation function.

The projection of HOM is defined by its latitude and longitude. These are available as the latitude and longitude of the nadir (at scene center time) of the frame specified as center frame on ADT. The azimuth of the projection axis through the projection center, AZO, measured from true North completes the definition of HOM coordinates. AZO is a function of the projection center latitude, orbital inclination and period. AZO is computed for each specified projection center latitude.

The origin of the HOM coordinates (U, V)is not located at the projection center (see Figure 79). The location of the origin is created when the parameters of the radius function of the parallels of the aposphere (an immediate mapping surface) are computed to minimize distortion at the center of the map. The HOM coordinates are defined with U increasing toward the North, V negative West of the projection axis, and positive East of it.

3.4.5.2 Geometric Interpolation

The geometric interpolation procedure for HCCM is similar to the procedure used for the MSS and TM scanning sensors described in subsection 3.2.4.4. The only difference is the number of grid points input to an output from the geometric interpolation function. The sequence of operations and the order of the polynomial interpolators is the same.

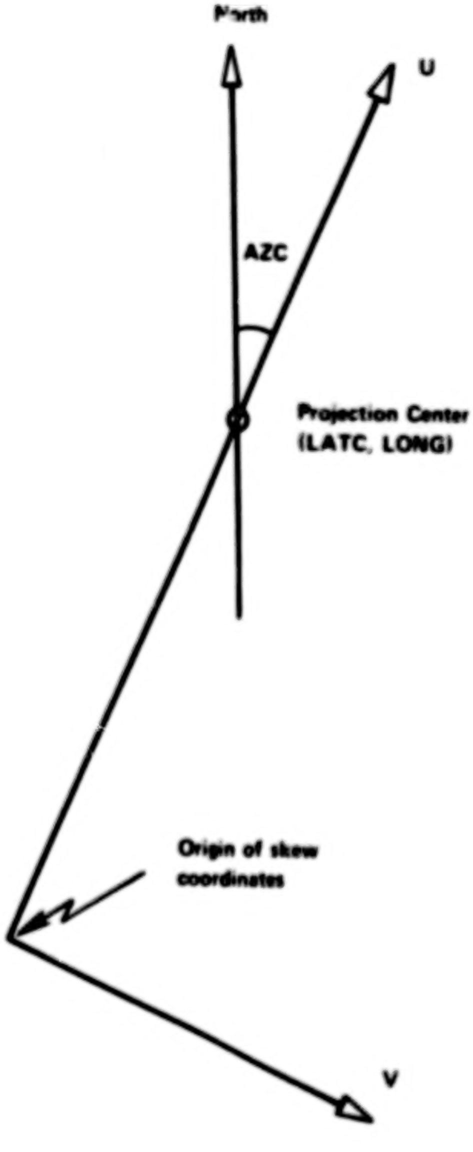
North
U
AZC
Projection Center
(LATC, LONG)
Origin of skew
coordinates
V

Figure 79. HOM Coordinates.

The 44 x 23 grid of pixels output from the space-to-space mapping function will be interpolated to generate the secondary grid points necessary for resampling. As with the MSS and TM scanning sensors, horizontal resampling requires the locations of the intersections of output space pixel columns with input space lines (G3 points); vertical resampling requires the locations of the intersections of output pixel rows with hybrid space (G2 points).

The same set of G2 and G3 grid points is generated for both the "square" or elongated output frames. The geometric interpolation function computes the necessary information to choose the correct subsets and initialize the resampling functions. In addition, the line group number (a line group is six input scan lines) of the beginning of input data for each frame and the number of fill pixels to the left and right of the image for each output space row are computed.

The output will consist of two sets of secondary grids. A 285-row by 81-column grid for horizontal resampling (G3) and a 325-row by 81-column grid for vertical resampling (G2). Each value is contained in one 32-bit word.

3.4.6 Resampling for HCM

The resampling procedure for HCCM is identical to the procedure used for MSS and TM scanning sensors as described in subsection 3.2.5. The HCCM resampling algorithms will allow for distortions of up to 25 percent in the cross track direction (any length segment of samples will not be stretched or compressed by more than 25 percent), and a maximum horizontal line droop of less than 3.6° (a horizontal output space line mapped to the input space will be distorted from the horizontal by less than 3.6°). The corresponding values for the MSS and TM sensors are: generally 1 to 5 pixel stretch or compression in line length, and a horizontal line droop of less than 1.5°.

3.5 ANALYSIS OF GEOMETRIC CORRECTION/TEMPORAL REGISTRATION ERRORS

The principal steps in the Geometric Correction (GC) process are shown in Figure 80. Temporal Registration (TR) differs from Geometric Correction in that Relative Control Points (derived from a single image) are used to compute error models instead of Geodetic Control Points (GCPs). Errors in these processes (GC and TR) are of three kinds:

a. Input

b. Internal

c. Propagated.

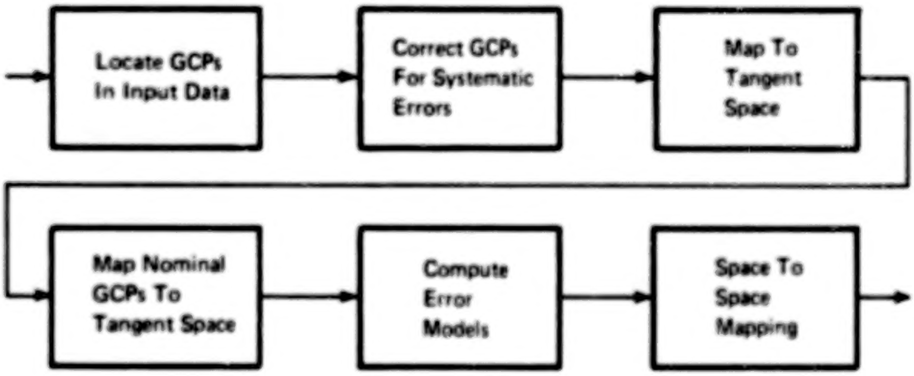
Locate GCPs In Input Data
Correct GCPs For Systematic Errors
Map To Tangent Space
Map Nominal GCPs To Tangent Space
Compute Error Models
Space To Space Mapping

Figure 80. Overview of Geometric Correction Process.

Input errors are derived from information external to the process. Internal errors are the result of the approximation made in the mathematical models used in the Geometric Error Modeling to remove systematic errors (subsection 3.2.4.2). Propagated errors are transmitted by a process.

The purpose of the error analysis is to identify and assign values to these error sources and to predict what their effects will be on image positional accuracy thereby verifying that the proposed system will meet the accuracy specifications.

The method of predicting image errors evolved from the methods used by IBM in the All-Digital Precision Processing of ERTS Images Study (NASA Contract 5-21716) and the EOS Attitude Control/Ground System Study (NASA Contract NAS5-21947). Subsequent processing of Landsat-1 and -2 images has shown the accuracy predictions to be in reasonable agreement with the image actually obtained.

Extensive Monte Carlo simulations were performed in the studies cited with initial and internal errors propagated through the GC/TR process to generate resulting image errors. Analyses of these simulations as well as analysis of Landsat-1 and -2 data indicated the following:

a. Image errors are normally distributed

b. Image errors in either UTM or latitude/longitude coordinates are close enough to the corresponding errors in the tangent space so that it is sufficient to predict the error in the tangent space.

c. Tangent space errors due to GCP location errors can be reliably estimated by propagating the covariance matrix of GCP location errors through the attitude/altitude model.

Subsection 3.2.4 discussed the two basic approaches to the use of control points in correcting image data. The selected approach uses ancillary and a priori information to evaluate as many distortion coefficients as possible. The only errors that remain to be evaluated with control points are the attitude and ephemeris measurement errors. The error analysis approach can therefore be summarized in the following steps.

a. Determine the effect of all error sources on GCP location and derive the GCP location error by combining the effects in a root-sum-of squares.

b. Propagate the GCP location error through the attitude/altitude model to determine the error in the tangent space due to GCP location.

c. Combine the errors due to interpolation (creating the secondary resampling grids from the primary grids) and resampling with the propagated error in the tangent space to obtain the estimate of the 1 σ value of the image error.

3.5.1 Landsat-D TM and MSS Error Analysis

An error analysis was performed for Landsat-D using the procedure just outlined and developed for Landsat-1, -2, and -C. Landsat-D carries two scanning sensors, the Thematic Mapper (TM) and the Multispectral Scanner (MSS). The errors relating to both of these sensors are discussed in the following paragraphs.

Figure 81 illustrates the grouping of consecutive corrections and/or transformations involved in the Landsat-D TM and MSS error analysis. The inputs to the error analysis are the true GCP geographic coordinates, true GCP image, coordinates (line and sample), and the true ephemeris (nadir location). Each input is subject to errors as listed in Table 11. The GCP image coordinates are corrected for all systematic errors as indicated by the GCPCOR box. The sensitivity matrix relating the Δ x, Δ y errors in the image GCPs to the Δ x, Δ y errors in the same points after the corrections indicated

Table 11. Input Errors, Meters (1 Sigma).

Error Type	Thematic Mapper	MSS
UTM map	7.4	7.4
UTM measurement	5	5
Map matching	3	8
Control location	3	8
Error in $\Delta V/V$	Negligible	

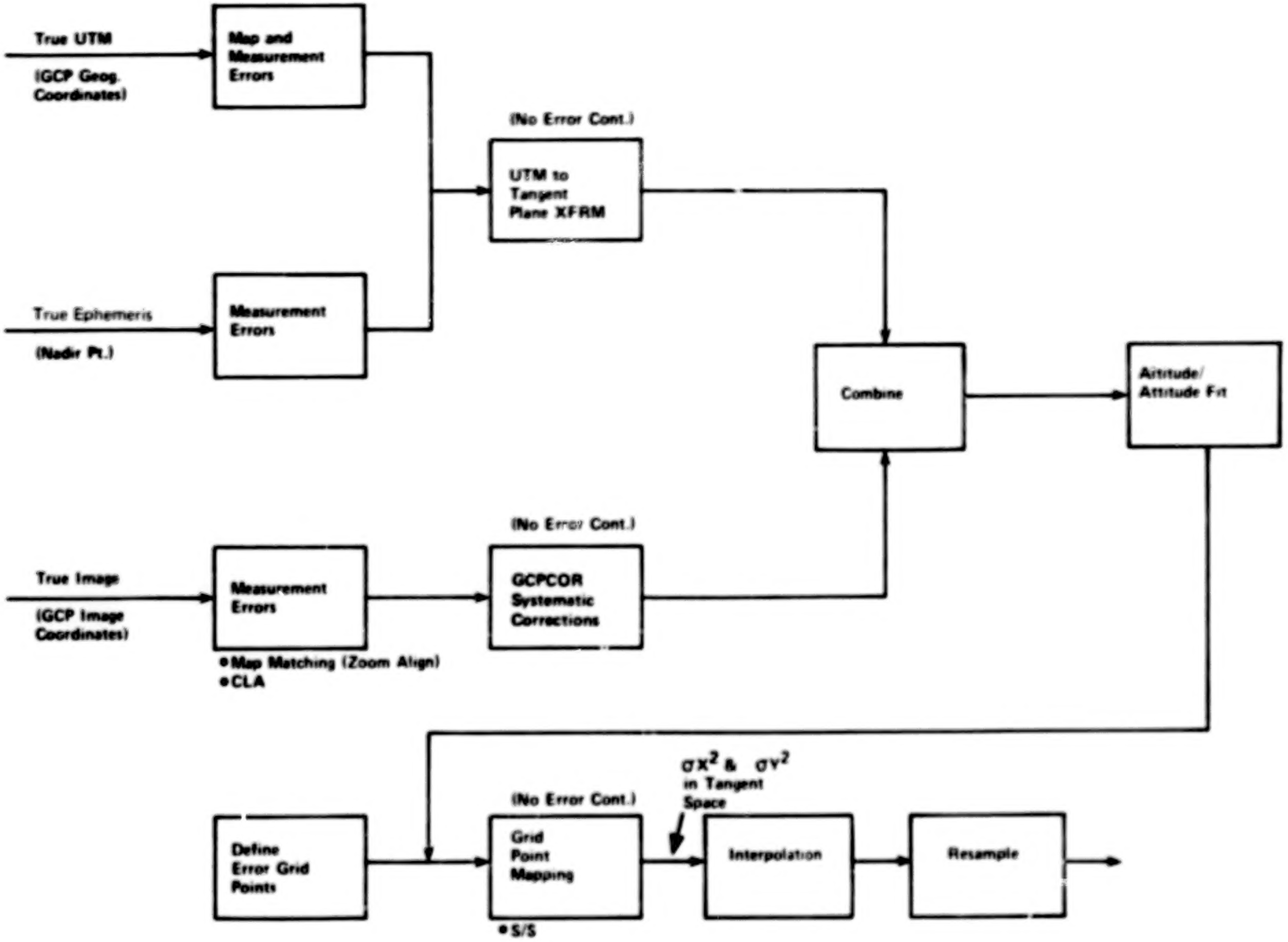
True UTM
(GCP Geog. Coordinates)
Map and Measurement Errors
True Ephemeris
(Nadir Pt.)
Measurement Errors
(No Error Cont.)
UTM to Tangent Plane XFRM
Combine
Attitude/ Attitude Fit
True Image
(GCP Image Coordinates)
Measurement Errors
• Map Matching (Zoom Align)
• CLA
(No Error Cont.)
GCPCOR Systematic Corrections
Define Error Grid Points
(No Error Cont.)
Grid Point Mapping
• S/S
σx² & σy² in Tangent Space
Interpolation
Resample

Figure 81. MSS Precision Processing: Error Analysis of Geometric Correction.

in Figure 81 are sought for each error source. The elements of the sensitivity matrix (a function of the operating state sector) are partial derivatives of the values of output variables of a process with respect to the input variables. The components of the state vector are the attitude and altitude parameters.

Also shown in Figure 81 are a set of uniformly distributed error check grid points. The output to input mapping of each of these grid points is subject to space-to-space mapping errors, error due to the cubic and linear interpolation of the grid points, and the error due to the resampling. As previously mentioned, the error check grid points include 90 percent of the area of the output image.

Figure 82 illustrates in detail the functions involved in the GCPCOR box and the grid point mapping box shown in Figure 81.

The error estimate is used to predict the image errors. The error has computed at a given point has two components: the x (cross-scan) and y (along-scan) direction. Each component is multiplied by 1.645, which corresponds to the 90 percent of a normal distribution. Error estimates are calculated at a grid of points covering 90 percent of the output image as shown in Figure 83. The grid shown is 5 x 5, a size proven to be adequate for Landsat-1, -2, and -C. The maximum error in either direction over the grid is determined. If this value is less than 0.5 pixel for GC or 0.3 pixel for TR, the image may then be considered to have satisfactory accuracy, since 90 percent of the pixels in the image would have geometric errors less than this maximum.

3.5.2 Input and Internal Errors

Input error sources and their 1 sigma values are shown in Table 8. The

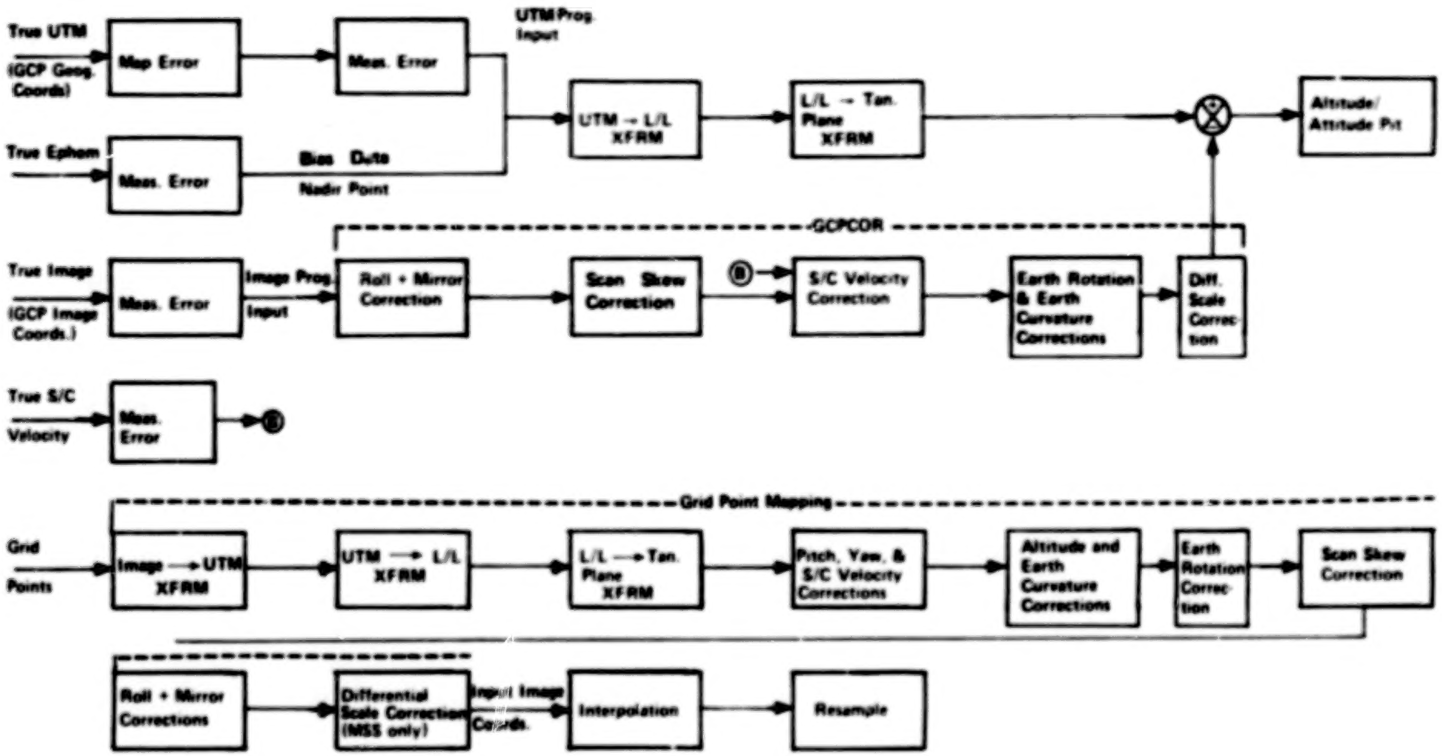
True UTM
(GCP Geog. Coords)
Map Error
Meas. Error
UTM Prog. Input
True Ephem
Meas. Error
Bias Data
Nadir Point
UTM → L/L XFRM
L/L → Tan. Plane XFRM
Attitude/ Attitude Fit
GCPCOR
True Image
(GCP Image Coords.)
Meas. Error
Image Prog. Input
Roll + Mirror Correction
Scan Skew Correction
B
S/C Velocity Correction
Earth Rotation & Earth Curvature Corrections
Diff. Scale Correction
True S/C Velocity
Meas. Error
B
Grid Point Mapping
Grid Points
Image → UTM XFRM
UTM → L/L XFRM
L/L → Tan. Plane XFRM
Pitch, Yaw, & S/C Velocity Corrections
Altitude and Earth Curvature Corrections
Earth Rotation Correction
Scan Skew Correction
Roll + Mirror Corrections
Differential Scale Correction (MSS only)
Input Image Coords.
Interpolation
Resample

Figure 82. TM and MSS Precision Processing: Geometric Correction.

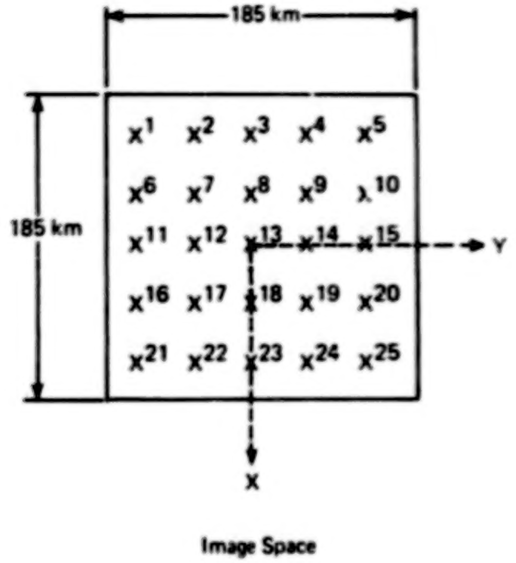

Figure 83. Grid at Which Image Errors are Computed.

value of the UTM map error was derived from the National Map Accuracy Standards, which specify that 90 percent of map points must be located within a tolerance of 1/50 inch for scales of 1:20,000 and smaller. Geodetic Control Points (GCPs) are located on 1:24,000 maps, 1/50 inch corresponds to 12.2 meters. This represents a 1 sigma value of 7.4 meters (12.2 ÷ 1,645). The UTM measurement error value was derived from map scaling experiments. The error in manually measuring the location of a GCP on the map is 5 meters from the experiments. The map matching error represents the ability of an analyst to register (superimpose) the control point identified on a map with the same feature located in the input image using the zoom transfer scope. Once the analyst registers the control point, the line and sample values of the control point are entered into the Control Point Library. The control location error is the error introduced when using the control location algorithm (CLA) to locate the control point in the input image. The map matching and control location error value correspond to 0.1 pixel, experimentally observed in Landsat-1 and -2 image processing. Spacecraft velocity errors are obtained from the Goddard Space Flight Center Operational Orbit Support Branch and are negligible.

Table 12 lists the errors due to thermal vibrational effects which cannot be modeled and will, therefore, contribute to GCP location error. For convenience, the residual error after the mirror model correction has been applied, which technically is an internal error, is also given in Table 12. The error magnitudes were derived on the basis of extensive simulations of the spacecraft thermal and vibrational behavior and Thematic Mapper simulations.

Table 12. Unmodeled Errors (Meters).

Error Type	Thematic Mapper		MSS	
	Along-Track ΔX	Cross-Track ΔY	Along-Track	Cross-Track
Mirror model	3	3	8	8
Flight Segment errors				
Thermal distortion–**sensor**	1.5	1.5	4	4
Thermal dirtortion–**structure**	1.5	1.5	4	4
Thermal distortion–**ACS**	1.5	1.5	4	4
Response to sensor motion	0	1.5	0	4
ACS subsystem	1.5	1.5	4	4

The possible sources of internal error; that is, the error resulting from approximations in the mathematical models are listed in Table 13. These models are either transformations or functions applied to remove the systematic errors. A previous IBM analysis performed for the all-digital processing of ERTS Images Study Contract NAS5-21716 of each of the transformations or corrections involved indicated the error to be essentially zero.

Table 13. Internal Error Sources Checked.

- Transformation from UTM, PS, or LCC to latitude/longitude
- Transformation from latitude/longitude to tangent space
- Scan skew correction
- Earth rotation correction
- Earth curvature correction
- Differential scaling correction (MSS only)
- Format center computation
- Transformation from image to MAP

The error sources listed in Tables 11, 12, and 13 may be combined in a root-sum-of squares fashion to give the (1-sigma) value of the control location error shown in Table 14, which must be propagated through the attitude/altitude model. For Geometric Correction, all the error sources must be combined. For Temporal Registration, the location of the relative control points is exact, therefore, only the control location error and the errors in Table 12 need be considered.

Table 14. GCP Location Error (Meters).

	Geometric Correction		Temporal Registration	
	ΔX	ΔY	ΔX	ΔY
Thematic Mapper	10.8	10.9	5.2	5.4
MSS	18.4	18.8	13.9	14.4

The input errors (Table 11) will be reduced by a factor related to the square root of the number of control points processed. In addition, as the number of GCPs is increased (assuming a good GCP distribution) the uncertainty in the attitude/altitude is reduced and the propagated error is therefore less.

To the propagated error must be added the image errors, committed in producing the output image, due to interpolation and resampling, and the ephemeris error. These values are given in Table 15. The resampling and interpolation errors are derived from a study performed for the Master Data Processor (MDP). Each is computed so that the magnitude of the errors is less than 0.1 pixel.

Table 15. Interpolation and Resampling Error (Meters).

Error Source	Thematic Mapper	MSS
Interpolation	2	2
Cubic convolution	1.2	2.3
Ephemeris effect on attitude	2.4	2.4

3.5.2.1 Expected Accuracy of Output Digital Products (TM and MSS)

The control point location errors, previously described, are propagated through the altitude/attitude model according to equation 27:

$$\begin{pmatrix} \sigma^2_{\Delta x} & \sigma_{\Delta x \Delta y} \\ \sigma_{\Delta x \Delta y} & \sigma^2_{\Delta y} \end{pmatrix} = A_i B_i^{(o)} \mathrm{Cov}\ \underline{C}\ (A_i B_i^{(o)})^T \qquad (27)$$

The $\sigma^2_{\Delta x}$ and $\sigma^2_{\Delta y}$ terms are the covariances of the errors in the X and Y directions of the tangent space. Cov $\underline{C}$ is the covariance matrix of the errors in the coefficients of the attitude/altitude model, and the product of the A and B matrices is the sensitivity matrix which relates deviations in tangent space location to deviations from nominal spacecraft attitude and altitude.

The 1-sigma errors $\sigma_{\Delta x}$ and $\sigma_{\Delta y}$ depend on the number and the distribution of the control points used to determine the coefficients of the attitude/altitude model. Various distributions of control points for a given number of control points have been simulated and the expected values of the propagated error computed. In all cases, control points were located in the outer vertical quarters of a scene and as evenly divided as possible between the left and right quarters.

Figure 84 illustrates the results of propagating control location errors through the attitude/altitude model for Landsat-D. The expected behavior of a decrease in propagated error as the number of control points increases is evident. The propagated error is computed at a 5 X 5 grid of points covering 90 percent of an image. The propagated error at each point is multiplied by 1.645 (which, since the error distribution is normal, gives a realistic upper bound for the error at that point), and the maximum value in both directions over this grid is reported.

The total maximum image error was obtained by combining in a root-sum-of-squares manner the propagated error, errors due to interpolation and

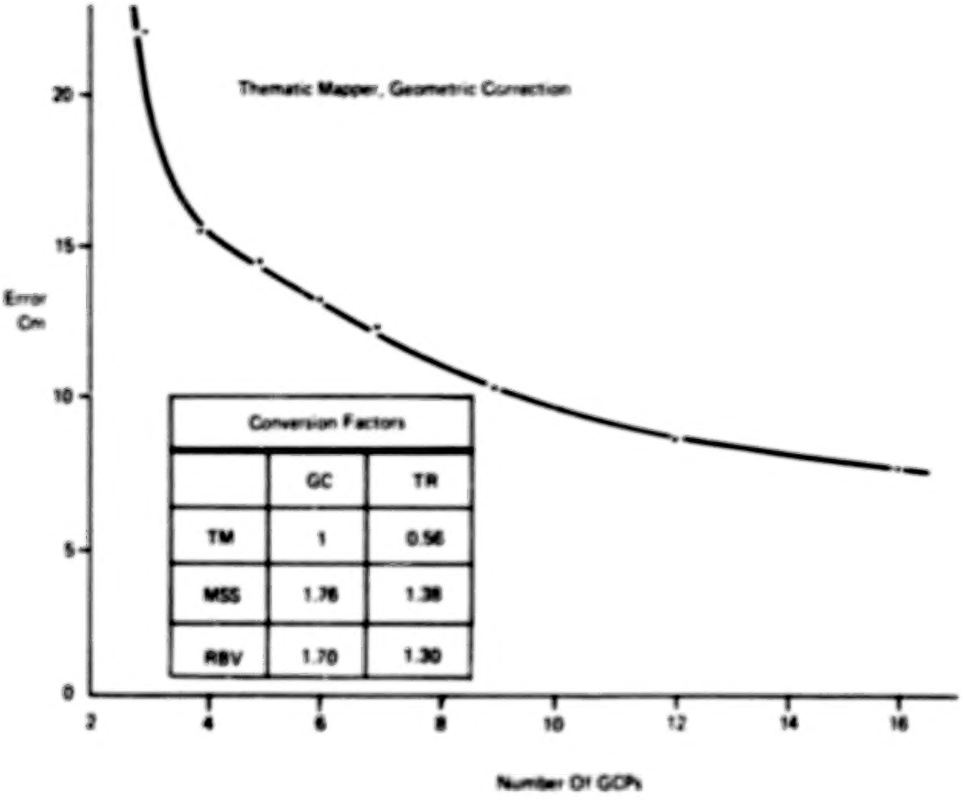

Conversion Factors		
	GC	TR
TM	1	0.56
MSS	1.76	1.38
RBV	1.70	1.30

Figure 84. Maximum Error (Meters) Over 90 Percent Grid vs. Number of GCPs.

resampling, and the ephemeris errors incorporated in the attitude estimates. The total image error for both sensors in both temporal registration and geometric correction using six control points is given in Table 16. As shown in Figure 84, six control points per scene are sufficient to meet the TM position accuracy requirement of 0.5 pixel. The conversion factor is applied to the ordinate (error term) to get the maximum error for the MSS. A similar analysis was run for Landsat-1, -2 and -C, resulting in twelve control points per scene to meet the MSS accuracy requirement of 0.5 pixel.

Table 16. Predicted Total Image Error, Pixels.

Sensor	Process	
	GC	TR
Thematic Mapper	0.43	0.27
MSS	0.29	0.23

*Maximum of X-, Y-direction error over 90% grid

3.5.2.2 Landsat-1, -2, and -C RBV Error Analysis

Most of the input and internal error data, as well as the procedure for calculating propagated errors, is the same for the RBV and the MSS processors. The MSS and TM error analyses were previously discussed. The following represents the error analysis procedure for the Landsat-C RBV sensor.

Figure 85 illustrates the grouping of consecutive corrections and/or transformations for purposes of the error analysis. The inputs to the error analysis are the true GCP geographic coordinates, true GCP image coordinates (line and sample), and the true ephemeris (nadir location). Each input is subject to errors as listed in Table 17. These error sources and their values are the same as those for the MSS, except the spacecraft velocity measurement has been deleted, since it would not be applicable to the RBV process.

Measurement and location errors in reseau points, not applicable to the scanning sensors, have been included in Table 17. The GCP image coordinates are corrected for internal RBV geometric errors (determined from the reseau marks) as indicated by the Reseau Mapping box. The sensitivity matrix re-

Table 17. Input Errors (Meters) (1 sigma).

Error Type	Error, Meters 1σ
UTM Map	7.4
UTM Measurement	5.0
Map Matching	8.0
Control Location	8.0
Nominal Reseau Measurement	1.3 (.066x19 m)
Image Reseau Location	5.5 (.289x19)
RSS	15.98

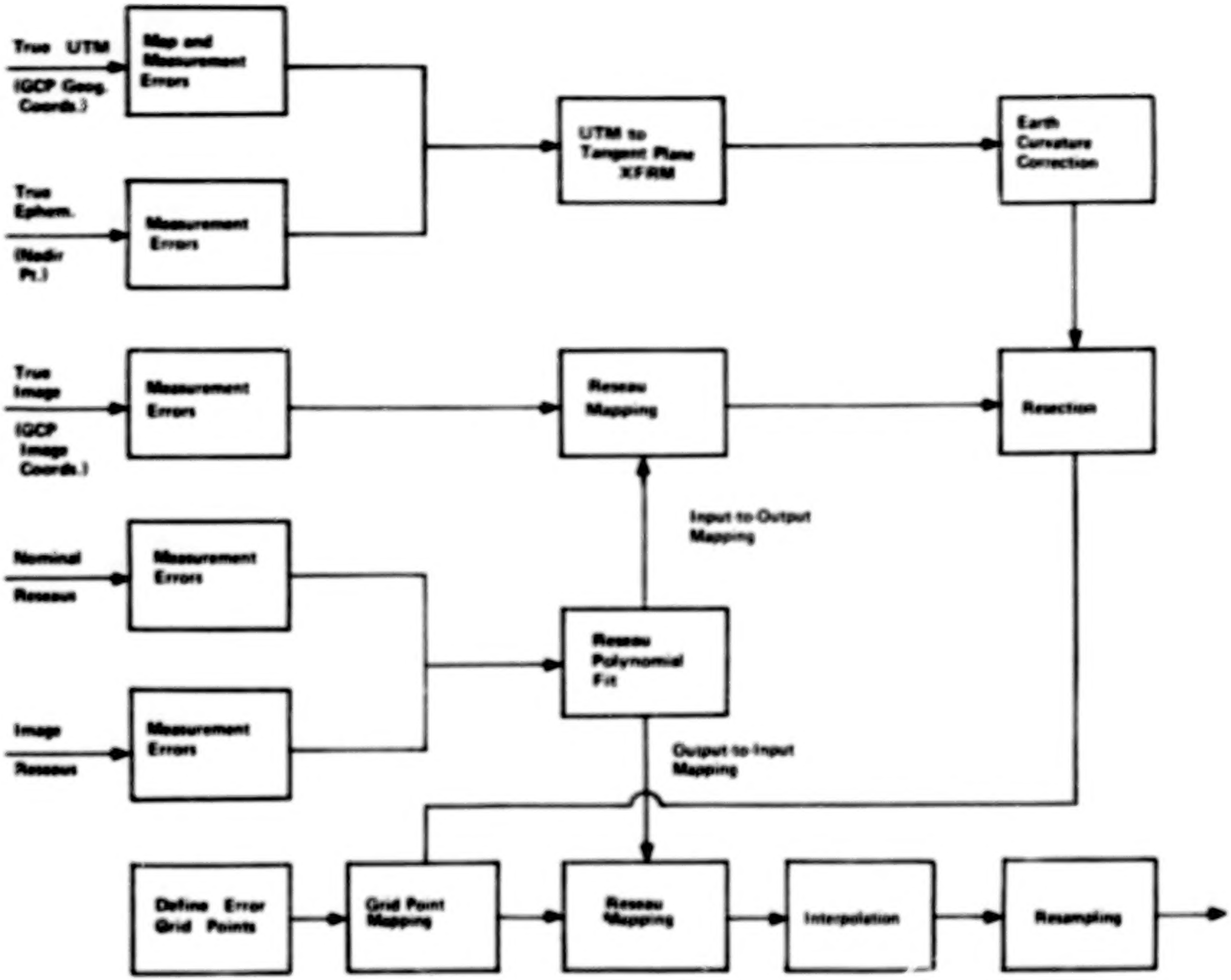
True UTM
(GCP Geog. Coords.)
Map and Measurement Errors
True Ephem.
(Nadir Pt.)
Measurement Errors
UTM to Tangent Plane XFRM
Earth Curvature Correction
True Image
(GCP Image Coords.)
Measurement Errors
Reseau Mapping
Resection
Input to Output Mapping
Nominal Reseaus
Measurement Errors
Reseau Polynomial Fit
Image Reseaus
Measurement Errors
Output to Input Mapping
Define Error Grid Points
Grid Point Mapping
Reseau Mapping
Interpolation
Resampling

Figure 85. RBV Precision Processing-Error Analysis of Geometric Correction.

lating the Δx, Δy errors in the image GCPs to the Δx, Δy errors in the same points after the set of corrections indicated in Figure 85 are sought for each error source. The elements of the sensitivity matrix are partial derivatives of the values of output variables (attitude coefficients) with respect to the input variables. Since the RBV is a framing sensor, classical three-parameter resection can be performed to estimate the attitude coefficients: one each for roll, pitch, and yaw.

A set of uniformly distributed error check grid points are also indicated as input to the grid point mapping. The output-to-input mapping of each of these grid points is subject to space-to-space mapping errors, error due to the cubic and linear interpolation of the grid points, and the error due to the resampling. The error check grid points includes 90 percent of the area of the output image.

Figure 86 indicates in more detail the applied corrections shown in Figure 85.

3.5.2.3 Input and Internal Errors

The input errors and their 1 sigma values are shown in Table 17. The input errors are constants or distributions based on information external to the RBV processing system. The error sources and their values are the same as those for the MSS, except that spacecraft velocity measurement has been deleted, since it is not applicable to the RBV process. The nominal reseau measurement error and the image reseau location errors in reseau points, not applicable to the MSS process, are included in Table 17. Nominal reseau location measurements are provided to the nearest 0.001 mm, which equals 0.066 pixels. The image reseau location error corresponds to 0.29 pixel, experimentally observed in Landsat-1 and -2.

Internal errors result from mathematical approximations and are listed in Table 18. These models are either transformations or functions applied to

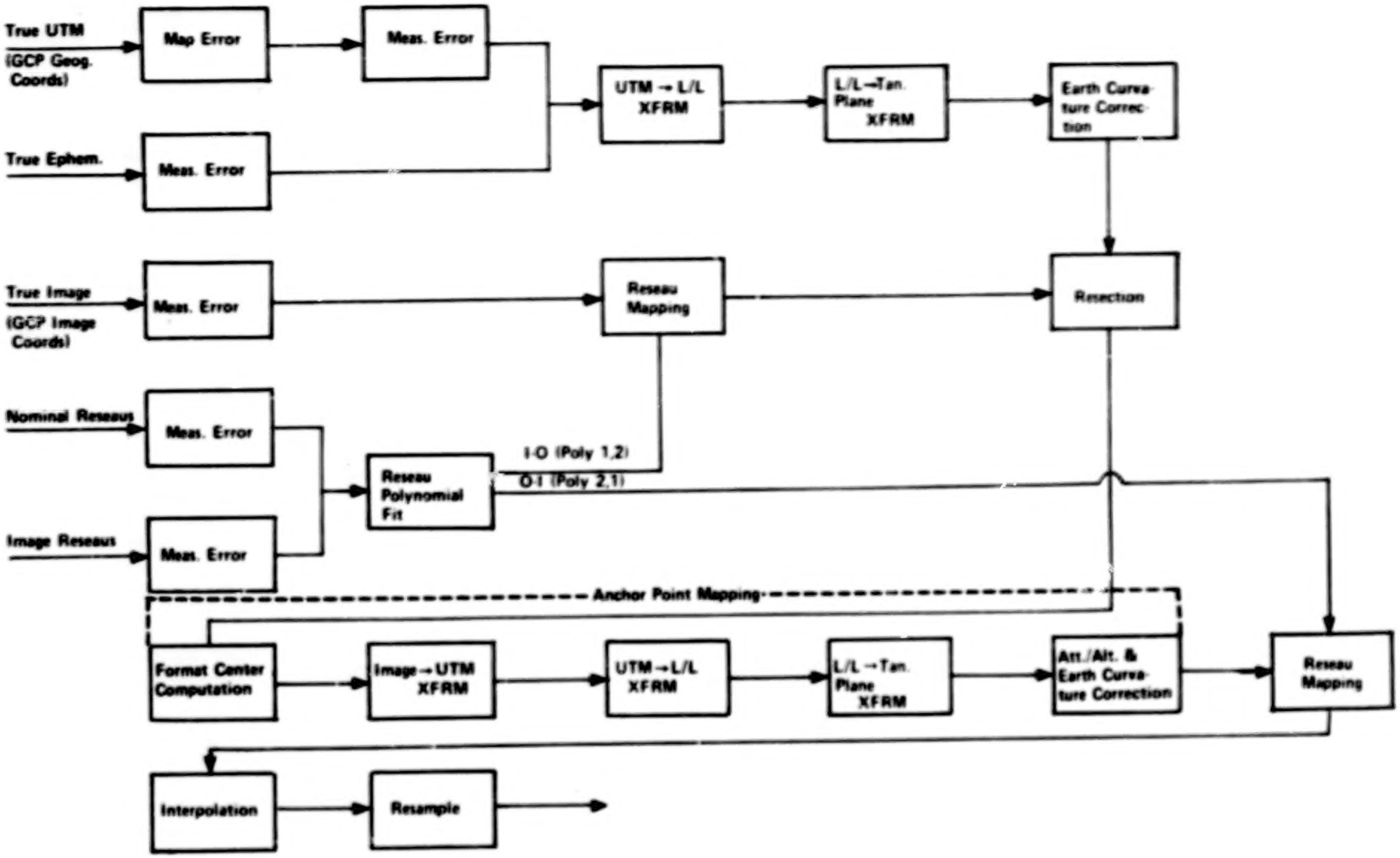
True UTM
(GCP Geog. Coords)
Map Error
Meas. Error
UTM → L/L XFRM
L/L → Tan. Plane XFRM
Earth Curvature Correction
True Ephem.
Meas. Error
True Image
(GCP Image Coords)
Meas. Error
Reseau Mapping
Resection
Nominal Reseaus
Meas. Error
Image Reseaus
Meas. Error
Reseau Polynomial Fit
I-O (Poly 1,2)
O-I (Poly 2,1)
Anchor Point Mapping
Format Center Computation
Image → UTM XFRM
UTM → L/L XFRM
L/L → Tan. Plane XFRM
Att./Alt. & Earth Curvature Correction
Reseau Mapping
Interpolation
Resample

Figure 86. RBV Precision Processing-Geometric Correction.

Table 18. Internal Error Sources*

Description
Transformation from UTM, PS, or SOM to latitude/longitude coordinates
Transformation from latitude/longitude to Tangent Space
Earth Curvature Correction
Resection
Format center computation
Transformation from image map
Transformation from input to nominal Reseau and nominal Reseau to input (distortion polynomials)

*Each Contributes Negligible Error

remove the systematic errors. The analysis performed for the all-digital processing of ERTS Images Study (Contract NAS5-21716) of each of the transformations or corrections involved indicated the error to be essentially zero for the first six error sources. The internal distortion polynomials (two pairs of 5th-order polynomials) represent the transformation from input to nominal reseau locations and nominal reseau location to input. Computer simulations currently indicate this error to be approximately 0.4 pixel in each axis.

The error sources listed in Tables 17 and 18 may be combined in a root-sum-of-squares fashion to yield the one-sigma value of the control location error shown in Table 19 which must be propagated through the attitude model.

For geometric correction, all the error sources must be combined. For temporal registration, the location of the relative control points is exact, therefore, only the control location error and the reseau errors (image and nominal) need be considered.

To the propagated error must be added the image errors due to interpolation and resampling errors, previously given in Table 15.

Table 19. GCP Location Errors (Meters).

Sensor	Geometric Correction		Temporal Registration	
RBV	ΔX	ΔY	ΔX	ΔY
	18.4	18.4	14.0	14.0

3.5.2.4 Expected Accuracy of Output Digital Products (RBV)

The control point location errors are propagated through the attitude/altitude model as outlined for the TM and MSS. The attitude is a constant for the RBV exposure time. Since the attitude model used for Landsat-D was also a constant the curve of Figure 84 can be scaled to illustrate the resulting propagated error as a function of the number of GCPs used. The total maximum image error was obtained by combining in a root-sum-of-squares manner the propagated error, the errors due to interpolation, and resampling errors. The total image errors, for the Landsat-C RBV in both temporal registration and geometric correction using six control points are given in Table 20. As shown, the performance requirements are met.

Table 20. Predicted Total Image Error, Pixels*

Sensor	Process	
	GC	TR
RBV	.98	.75

*Maximum of X-, Y-direction error over 90 percent grid

3.6 CLASSIFICATION

3.6.1 Introduction

Some fundamental concepts associated with the physics and mathematics of remote sensing classification are described.

Energy can be defined as the ability to do work. In the process of doing work, energy must be transferred frequently from one body to another or from one place to another. There are three basic ways in which energy can be transferred. These are the processes of conduction, convection, and radiation. The transfer of energy by electromagnetic radiation is of most significance to use here. It is the only form of energy transfer that can take place through free space. Remote sensing is accomplished through the transfer of energy that is either emitted or reflected from the radiating object to the sensors. The sensors, in turn, reconstitute this energy into an image detectable by normal sense organs, usually the eye.

Virtually all energy detected by remote sensing systems undergoes certain fundamental processes. It is radiated by a source, propagated through the atmosphere, interacted with a target, reemitted, and passed back through the atmosphere before being sensed.

Electromagnetic radiation is propagated through the earth's atmosphere almost at the speed of light in a vacuum. Unlike a vacuum in which nothing happens, the atmosphere may affect not only the speed of radiation but also its frequency, its intensity, its spectral distribution, and its direction.

One very serious effect of the atmosphere is the scattering of radiation by atmosphere particles. The three most important types of scattering are

Rayleigh scatter, Mie scatter, and nonselective scatter. Rayleigh scatter is largely due to molecules and other very small particles many times smaller than the wavelength of radiation under consideration. This type of scatter is inversely proportional to the fourth power of the wavelength. All scatter is accomplished through absorption and reemission of radiation by atoms and molecules.

Mie scatter takes place when there are essentially spherical particles present in the atmosphere with diameters approximately the wavelength of radiation being considered. For visible light, water vapor, dust, and other particles ranging from a few tenths of a micron to several microns in diameter are the main scattering agents.

When there are particles in the atmosphere several times the diameter of the radiation being transmitted, the scattering process is nonselective with respect to wavelength. Thus, water droplets, which make up clouds, scatter all wavelengths of visible light equally well, causing the cloud to appear white.

Certain wavelengths of radiation are affected far more by absorption than by scatter. This is particularly true of infrared and wavelengths shorter than visible light. Absorption occurs when energy of the same frequency as the resonant frequency of an atom or a molecule is absorbed, producing an excited state. If, instead of reemitting a photon of the same wavelength, the energy is transformed into heat and is subsequently reemitted at a longer wavelength, absorption occurs.

Several things may happen when electromagnetic radiation strikes a potential target. Some of the energy is reflected or scattered, and the rest enters the target to be propagated as a refracted wavefront. Reflection is the most important process to be considered here and refers to the process whereby radiation "bounces off" an object. Actually the process is considerably more complicated, involving reradiation of photons in unison by atoms or molecules. Reflection exhibits fundamental characteristics which are important in remote sensing. In specular reflection the surface from which the radiation is reflected is essentially smooth, and the angles of incidence and reflection are always equal. If the surface is rough, the reflected rays go in many directions, depending on the orientation of the smaller, reflecting surfaces. These surfaces are considered to be diffuse reflectors. The entire process whereby radiation is reflected, or reradiated, depends upon wavelength and it is this dependency upon which remote sensing classification depends.

Figure 87 plots a typical spectral signature for wheat. Figure 88 shows the variation in intensity response for an assortment of biological materials as determined by a 12-channel scanner covering wavelengths from 0.41 microns to about 2.0 microns in channels 1-11 and 9.3 to 11.7 microns in channel 12. Successful classification of materials depends on the ability to discriminate between such signatures and to accurately identify the desired class.

Much effort sponsored by NASA, USDA, DOI, universities and industry has been focussed on determining what useful information can be extracted from such imagery. Many efforts involve attempts at classification of crops, forests, etc. The most ambitious experiment called LACIE (Large Area Crop Inventory Experiment) has been in progress for 3 years with the goal of estimating winter wheat production in the United States to within 90 percent accuracy 90 percent of the time. Recent reports (at the LACIE Symposium in October 1978) indicate progressively better results as procedures and techniques have evolved.

The classification process itself in these studies is accomplished by comparing (in a statistical sense) information derived from an input pixel with similar data derived from known sample patterns or signatures.

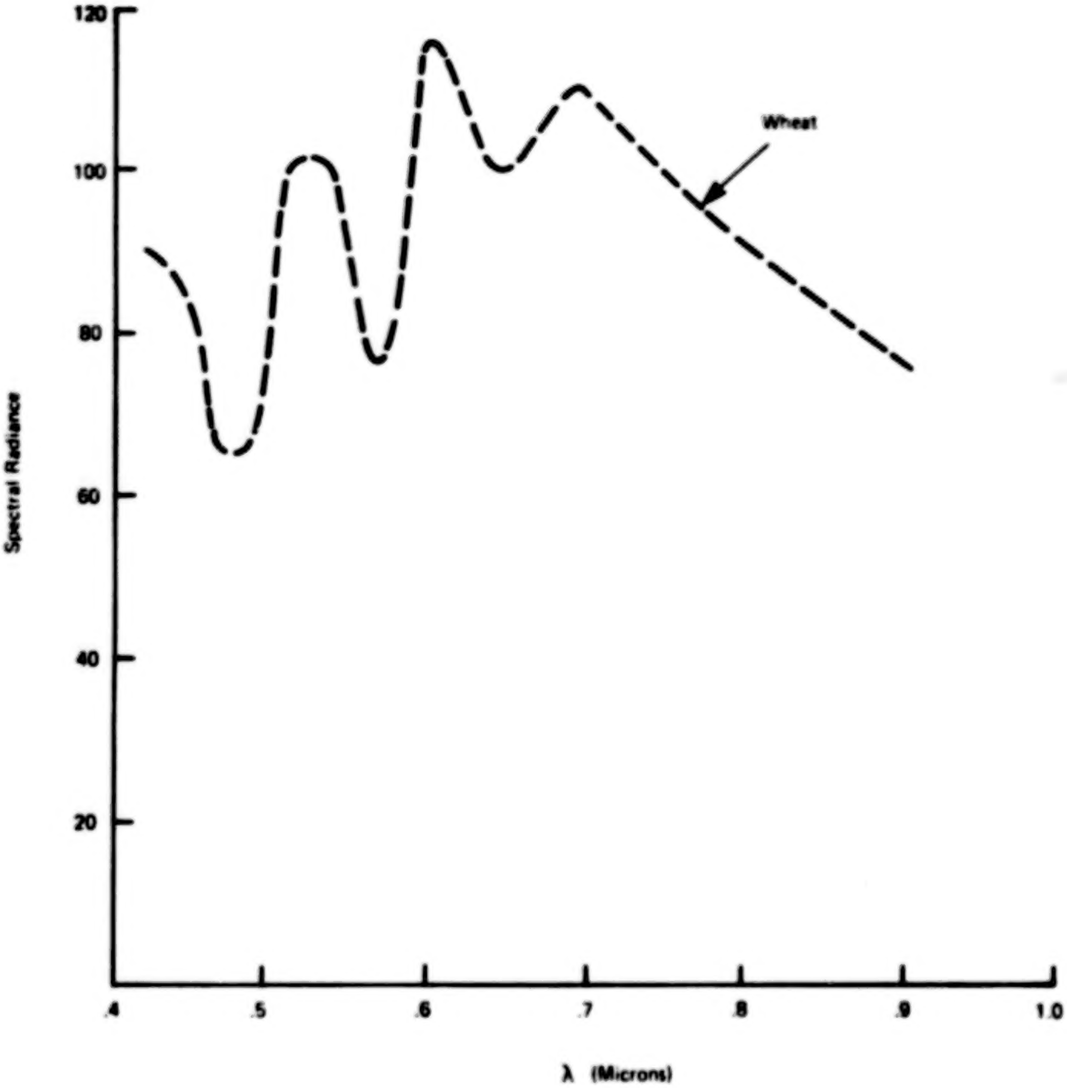

Figure 87. Typical Spectral Signatures for Wheat.

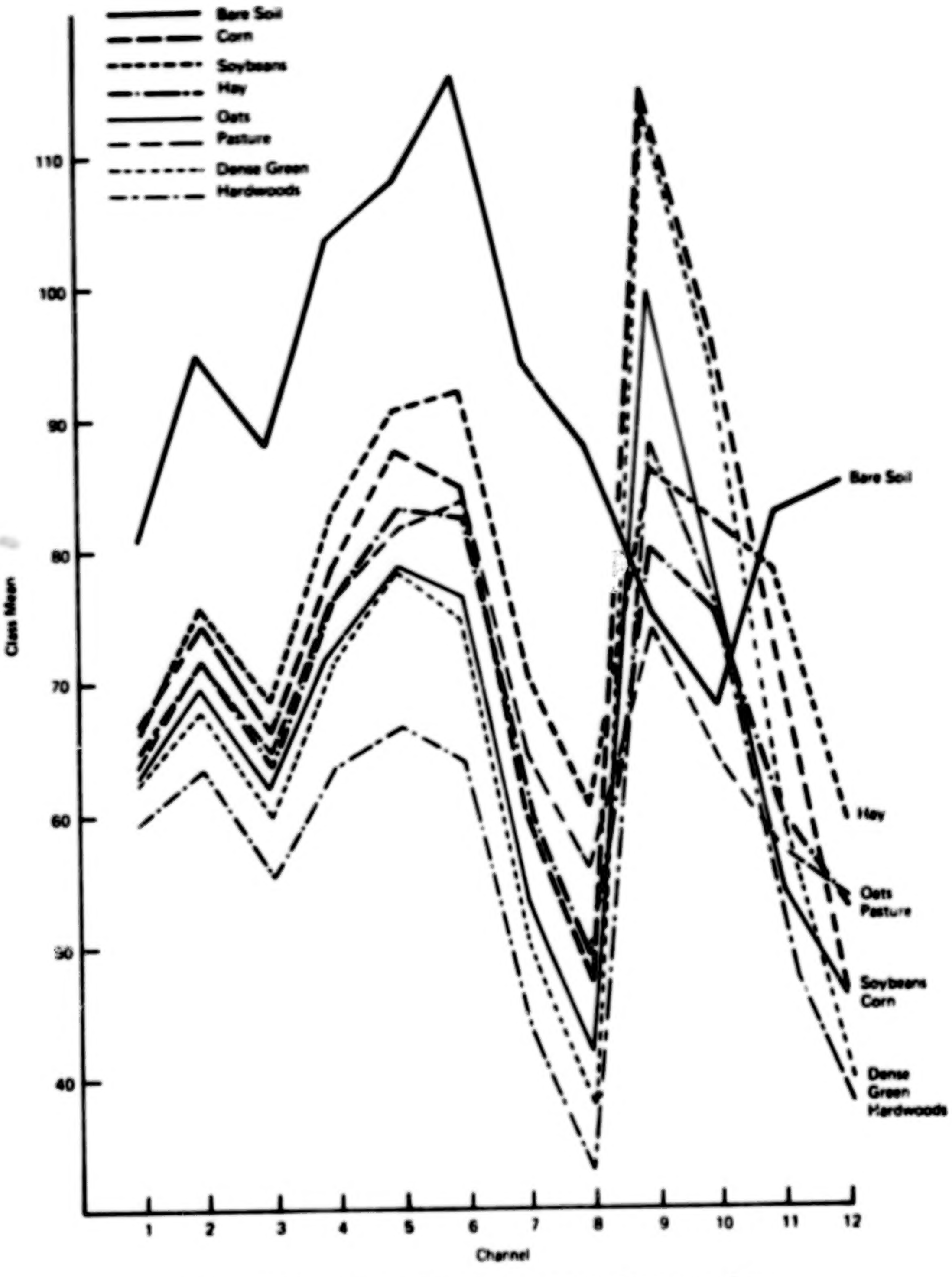

Figure 88. Variation in Spectral Response for Various Biological Materials

The signatures are derived from training sets. It is very important that such training sets, and the resultant signatures, be truly representative of the object class and its dispersion. Then, based upon a comparison between representative signatures and input data (test sets), decisions are made as to the nature of the data.

3.6.2 LACIE Overview

One procedure from LACIE for extracting information from remotely sensed data is summarized in the following paragraphs.

Figure 89 presents a functional overview of LACIE system operations. The Landsat sensor data are transmitted to a ground station and then to the Goddard Space Flight Center. The received images at Goddard are 185 km by 185 km, much larger than needed by LACIE. Goddard extracts the LACIE sites (segments) of 5 x 6 nautical miles (117 scan line by 196 pixel) from the larger image on demand. The segments are radiometrically corrected and geometrically corrected to a reference image.

The tapes of the sites extracted by Goddard are sent to the Johnson Space Center (JSC) and logged into a history data base, which is a file of all image orders sent to or filled by Goddard. The data are also converted into sets of multispectral graphic images (four visible bands for each site) for the photointerpreters (PIs) and then stored, in its original digital form, in the image data base for the analysts.

The photointerpreters, working from standard USDA documentation, identify fields of given crops in about 20 percent of the images. Both the vertices and crop classification of each field are stored in a fields data base by site number. They also are used to produce a fields-overlay tape, which

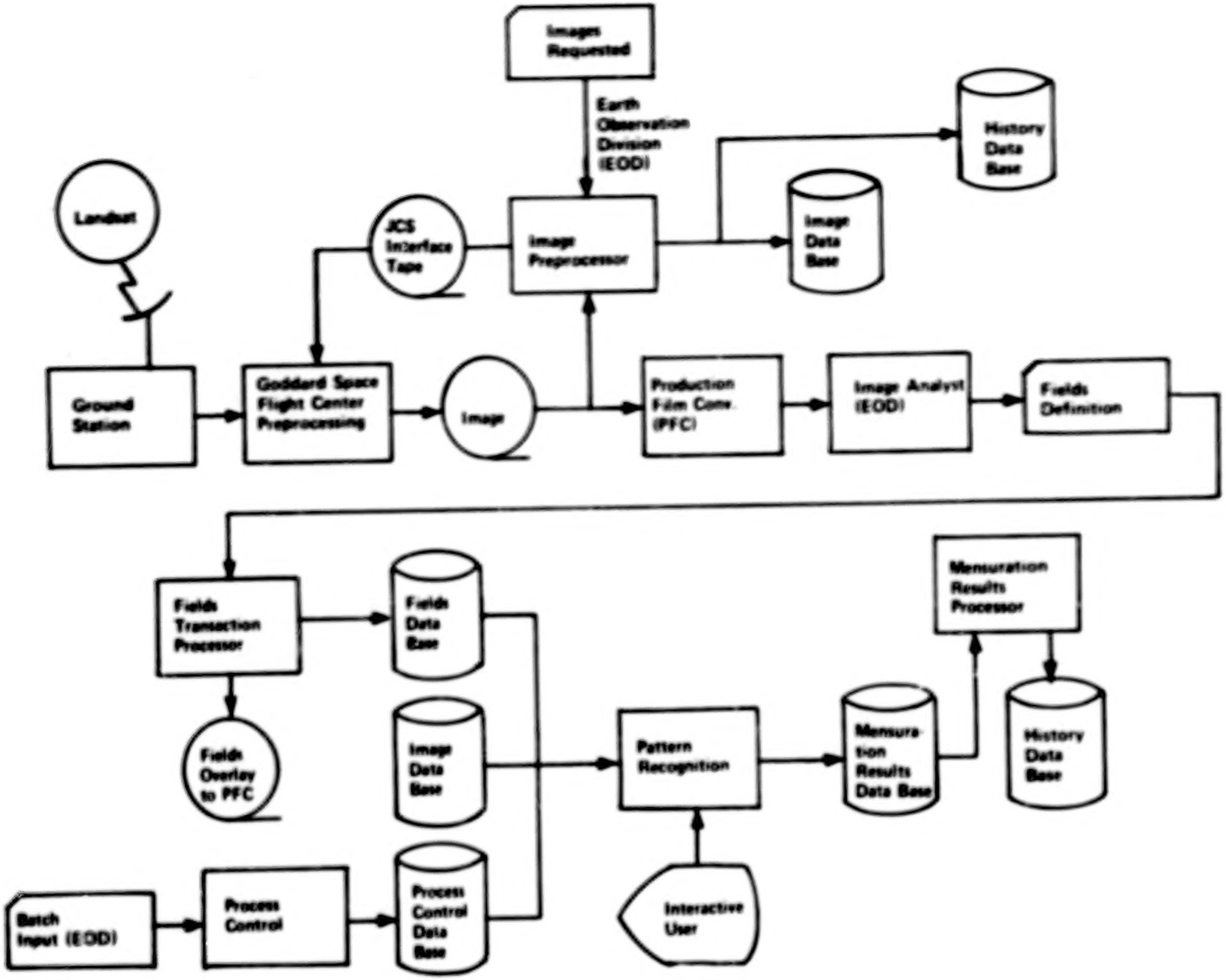
Images Requested
Earth Observation Division (EOD)
History Data Base
Landsat
JCS Interface Tape
Image Preprocessor
Image Data Base
Ground Station
Goddard Space Flight Center Preprocessing
Image
Production Film Conv. (PFC)
Image Analyst (EOD)
Fields Definition
Fields Transaction Processor
Fields Data Base
Mensuration Results Processor
Fields Overlay to PFC
Image Data Base
Pattern Recognition
Mensuration Results Data Base
History Data Base
Batch Input (EOD)
Process Control
Process Control Data Base
Interactive User

Figure 89. LACIE Overview.

provides the PI with a set of site pictures that define all the fields that have been identified. The PI uses these pictures in updating their judgments every time a new set of images of the site is acquired.

All of these operations support the system's primary function, which is the development of statistical signatures of the fields that have been identified, and the use of these signatures to classify those fields not identified. This operation is basically one of pattern recognition, with the patterns being statistical ones. The pattern-recognition function is organized into two types of fields and sites. The fields identified by the photointerpreter, the ones used to generate statistical signatures, are called training fields; the sites in which they are located are called training sites. The fields that have not been processed by the photointerpreters, which means that their crop contents are unknown, are called test fields. A test field may be either the unknown area of a training site or the entirety of a site that contains training fields. The sites that contain no training fields are called test sites, and consist of 80 percent of the sites on which no photointerpretation work is done.

The statistical crop signatures generated from the training fields consist of the mean vectors and covariance matrices of the pixels in up to four acquisitions (sets of multispectral images). At the very least, the composite is a spectral one, consisting of the four multispectral images in a single acquisition. At most, the composite is temporal as well as spectral, consisting of multiple sets of images acquired at multiple points in time. The largest composite from which a signature can be generated consists of 16 channels of data (four acquisition times, each containing images in four spectral bands).

When the training and test fields lie within the same site, the operation is called local classification. When a recognition site is being classified, which involves the use of a signature generated from a training field in a different site, the operation is called signature extension classification. The difference between the two operations lies in the statistical techniques used.

It became apparent during the early phase of the LACIE program that the most critical task performed by the analyst (PI) was training field selection rather than training field labeling. The analyst selects fields to be labeled, and there were indications that his selection was biased towards those fields he could identify with confidence. It was believed, therefore, that the use of analyst-selected training fields should be discarded. Tests indicated that the most desirable form of training field would be a single pixel. This has led to what is now called Procedure 1. Approximately 80 dots or pixels are selected uniformly throughout a segment and labeled as wheat or nonwheat.

A clustering analysis of the segment is made and the analyst-labeled dots used to label the clusters as wheat or nonwheat and thereby produce a classification. A final step uses more analyst-labeled dots to correct for the effect of classifier bias (but does not correct for analyst bias).

This procedure has proven to be successful and is the approach currently implemented by LACIE for local classification.

Two characteristics of the LACIE system pose particularly interesting problems, both associated with the pattern-recognition function. One of these characteristics is that the only way of achieving the productivity needed is by keeping the very large image data base online in its entirety and organizing it in a way that allows large sets of data to be retrieved very rapidly. A single classification operation can require the retrieval of as much as 368,000 bytes of data, and twice that amount can be called for in a single signature-extension operation.

CONTENTS

Section Page

1 SUMMARY 1 1/B4
2 INTRODUCTION 2 1/B5
2.1 Background 2 1/B5
2.2 Scope 8 1/B11
3 DIGITAL IMAGE PROCESSING OF EARTH OBSERVATION SENSOR DATA 10 1/B13
3.1 General Overview 10 1/B13
3.2 MSS and TM Functional Description 11 1/B14
3.2.1 Data Reformatting 15 1/C4
3.2.2 Radiometric Calibration 23 1/C12
3.2.3 Radiometric Correction 42 1/E3
3.2.4 Geometric Correction/Temporal Registration 43 1/E4
3.2.5 Resampling for Scanner Sensors 88 2/A12
3.3 Return Beam Vidicon (RBV) 99 2/B11
3.3.1 RBV Functional Overview 100 2/B12
3.3.2 Radiometric Calibration and Correction 104 2/C3
3.3.3 Geometric Correction 110 2/C9
3.3.4 Resampling for RBV 119 2/D4
3.4 Heat Capacity Mapper Mission (HCMM) 120 2/D5
3.4.1 Heat Capacity Mapper (HCM) Functional Description 121 2/D6
3.4.2 HCM Phase I Processing 123 2/D8
3.4.3 Radiometric Calibration Processing. . . 124 2/D9
3.4.4 Radiometric Correction 128 2/D13
3.4.5 Geometric Correction 133 2/E4

Section Page

3.4.6 Resampling for HCM 140 **2/E11**
3.5 Analysis of Geometric Correction/Temporal Registration Errors 141 **2/E12**
3.5.1 Landsat-D TM and MSS Error Analysis . . 143 **2/E14**
3.5.2 Input and Internal Errors 145 **2/F3**
3.6 Classification 158 **2/G5**
3.6.1 Introduction 158 **2/G5**
3.6.2 LACIE Overview 163 **2/G10**
3.6.3 Classification Approaches 167 **3/A3**
3.6.4 Baseline Classification Process 171 **3/A7**
3.6.5 On-Board Classification Configuration Analysis 176 **3/A13**
4 CONCLUSIONS AND RECOMMENDATIONS 209 **3/E2**
Appendix A TM AND MSS DATA REFORMATTING STUDY 213 **3/E6**
Appendix B ERROR ANALYSIS 233 **3/G5**
Appendix C EFFECT OF DATA STRIPING ON CLASSIFICATION ACCURACY 249 **4/A10**
Appendix D EFFECT OF LANDSAT ORBITAL CHARACTERISTICS ON ON-BOARD CLASSIFICATION 278 **4/E1**

The other characteristic of LACIE's pattern-recognition function that poses a problem is the difficulty of the statistical process that must be done. One part of the difficulty lies in the time frame in which LACIE must produce crop-inventory results. Because of time constraints (a 14-day period was desired to acquire data and complete the analysis), small fields, and other photointerpretive limitations, the statistics used for the classification operations are often based on a small sample. Another part of the problem is that crop signatures are affected by atmospheric haze, sun illumination angle, soil color, level of crop maturity, and farming practices. Even within a single site, these factors usually vary enough to produce a significant amount of statistical uncertainty. Both of these problems need to be addressed when considering on-board multispectral classification.

3.6.3 Classification Approaches

Based on examining the structure of typical remotely sensed data it seems that the probability of correct classification is a function of several factors. Some of these factors are:

a. Classification rule -- for example is it very complete or is it an approximation.

b. Number of classes -- the more classes an observation can be assigned to could increase the probability of making an error.

c. Number of channels -- too few channels may not provide enough information and too many channels may actually decrease the probability of making a correct decision.

d. Location of channels along the electromagnetic spectrum.

e. Sample mean and covariance matrix.

3.6.3.1 Classification/Similarity Functions

Several techniques are used for the actual classification of pixel data. Analysis has demonstrated that all the most widely used spectral similarity functions are only approximations to the maximum likelihood classification rule, with the assumption that the observation vector is an element of multivariate normal distribution.

A similarity function is used as a criterion to determine if one observation vector is similar to another observation vector. If the two vectors are similar, they are considered to be elements of the same set.

In the Earth Resources application, the observation vector consists of the average intensity of the electromagnetic radiation in each of the wavelength intervals. Since the measurement vector consists of intensity as a function of wavelength, the similarity function is described as a spectral similarity function. The various types of spectral similarity functions that have been used in Earth Resources applications range from the quadratic form to the Euclidean distance measure.

The likelihood function of an n-dimensional, random-variable x is defined as the direct product of the probability density function of a set of m observations, equation (28). If the random variable x is an element of a multivariate normal distribution, the probability density function is described by equation (29). In the classification procedure, x is assigned to the set associated with the μ_j and Σ_j for which $L(x)$ is maximized; this is equivalent to minimizing equation (30). The maximum likelihood criterion, equation (30), requires several operations. This effect is made more dramatic by the amount of data being collected. The computational complexity of equation (30) can be decreased by approximating the covariance matrix Σ, by a simpler form. Three such approximations, designated as S_2, S_3, and S_4, are described in Table 21.

$$L(x)=\prod_{i=1}^{m} p(x_i) \tag{28}$$

$$p(x)=(2\pi)^{-n/2}|\Sigma|^{-1/2}\exp\{-1/2(x-\mu)^T\Sigma^{-1}(x-\mu)\} \tag{29}$$

$$S_1=\log|\Sigma_j| + (x-\mu_j)^T \Sigma_j^{-1}(x-\mu_j) \qquad j=1,k \tag{30}$$

Table 21. Similarity Functions and Statistical Implications.

ASSUMPTION	SIMILARITY FUNCTION	STATISTICAL IMPLICATIONS
$\Sigma=\Sigma$	$S_1 = \log\|\Sigma\| + (x-\mu)^T\Sigma^{-1}(x-\mu)$	• Data Set is accurately described.
$\Sigma=\Sigma_d$	$S_2 = \log\|\Sigma_d\| + (x-\mu)^T\Sigma_d^{-1}(x-\mu)$	• Principal axes of the equiprobable contour are assumed to be parallel with the measurement coordinates.
$\Sigma=\sigma^2 I$	$S_3 = \log \sigma^2 + \frac{(x-\mu)^T(x-\mu)}{\sigma^2}$	• Probability of occurrence is independent of the angle between the observation vector and the measurement coordinates.
$\Sigma = I$	$S_4 = (x-\mu)^T(x-\mu)$	• Hyperellipsoid is approximated by a hypersphere with a radius of 1.

Table 22. Processing Times for Various Similarity Functions.

NO. PIXELS PER LINE	TIME REQUIRED TO PROCESS ONE LINE (SECONDS)				TIME RATIO S_1/S_i		
	S_1	S_2	S_3	S_4	S_1/S_2	S_1/S_3	S_1/S_4
100	.0586	.0340	.0279	.0251	1.722	2.102	2.330
250	.1463	.0849	.0695	.0627	1.723	2.104	2.333
500	.2925	.1697	.1389	.1253	1.724	2.105	2.335
750	.4387	.2545	.2083	.1879	1.724	2.106	2.335
1000	.5848	.3392	.2777	.2504	1.724	2.106	2.335

NOMENCLATURE

k	number of classes to which x can be assigned
L	likelihood function
n	dimension of the random variable x
$p(x_i)$	probability density function of the i^{th} sample of the random variable x
S_1	similarity function corresponding to a full covariance matrix
S_2	similarity function corresponding to a diagonal covariance matrix
S_3	similarity function corresponding to a covariance matrix described as a constant times the identity matrix
S_4	similarity function corresponding to an identity covariance matrix
x	$n \times 1$ random variable
μ	$n \times 1$ mean vector of $p(x)$
ξ_1	first principal axis of the equiprobable contour
ξ_2	second principal axis of the equiprobable contour
Σ	$n \times n$ covariance matrix

MICROFILMED FROM
BEST AVAILABLE COPY

The motivation for the approximation is to decrease the time required to process that data. Table 22 illustrates the difference in processing times for each of the algorithms on an IBM System/360 Model 75 for a case where there are 4 channels, n=4 and 10 classes, k=10.

Other techniques now being actively used include clustering.

3.6.3.2 Cluster Analysis

Clustering is a method of partitioning a set of data into homogeneous subsets. This is achieved by extremizing a functional, J, which is a function of a similarity function, S_f, the number of clusters, N, and the parameters of the clusters, θ. For discrete data, J can be expressed in equation (31) as:

$$J = \sum_{i=1}^{N} \sum_{X_j \in C_i} S_f(X_j, \theta_i) \tag{31}$$

There are various similarity functions, typical ones include:

Similarity Function	Interpretation
$\sum_{K=1}^{n} \lvert X_{jK} - \mu_{jK} \rvert$	staircase distance
$(X_j - \mu_i)^T (X_j - \mu_i)$	unweighted Eculidean norm
$(X_j - \mu_i)^T K_i^{-1} (X_j - \mu_i)$	weighted Euclidean norm

One of the most significant problems in cluster analysis is determining the correct number of clusters in the data set (cluster convergence).

For the purpose of this study, the precise classification technique used is less critical than the recognition of the large calculation load implied by any of the above processes. Also, as in many computationally demanding problems, the actual process is highly repetitive absorbing large amounts of computer capacity but, even worse, requiring complex, high-rate and high-volume data handling systems. With this perspective, a baseline classification system using a maximum-likelihood classification rule was defined for use in configuration planning.

3.6.4 Baseline Classification Process

Currently, the classification procedure is accomplished on the ground, as with LACIE. Translating the classification function to the spacecraft will involve implementing the same functions as LACIE. Demonstrating that the entire classification process can be accomplished on-board is best shown using an evolutionary procedure. Functions are systematically integrated into the on-board system while continuing to perform the same function on the ground. This allows a direct comparison to be made between functions implemented on-board and at the ground.

The baseline classification process (Figure 90) is derived from various experiments including LACIE. The input data stream is formatted to a convenient form and the segments to be classified are extracted from the full sensor stream.

The segments are radiometrically corrected based on latest calibration data. The data are geometrically corrected to allow registration with previous data (multitemporal registration). Training fields are defined and classification statistics are gathered. This process is called training.

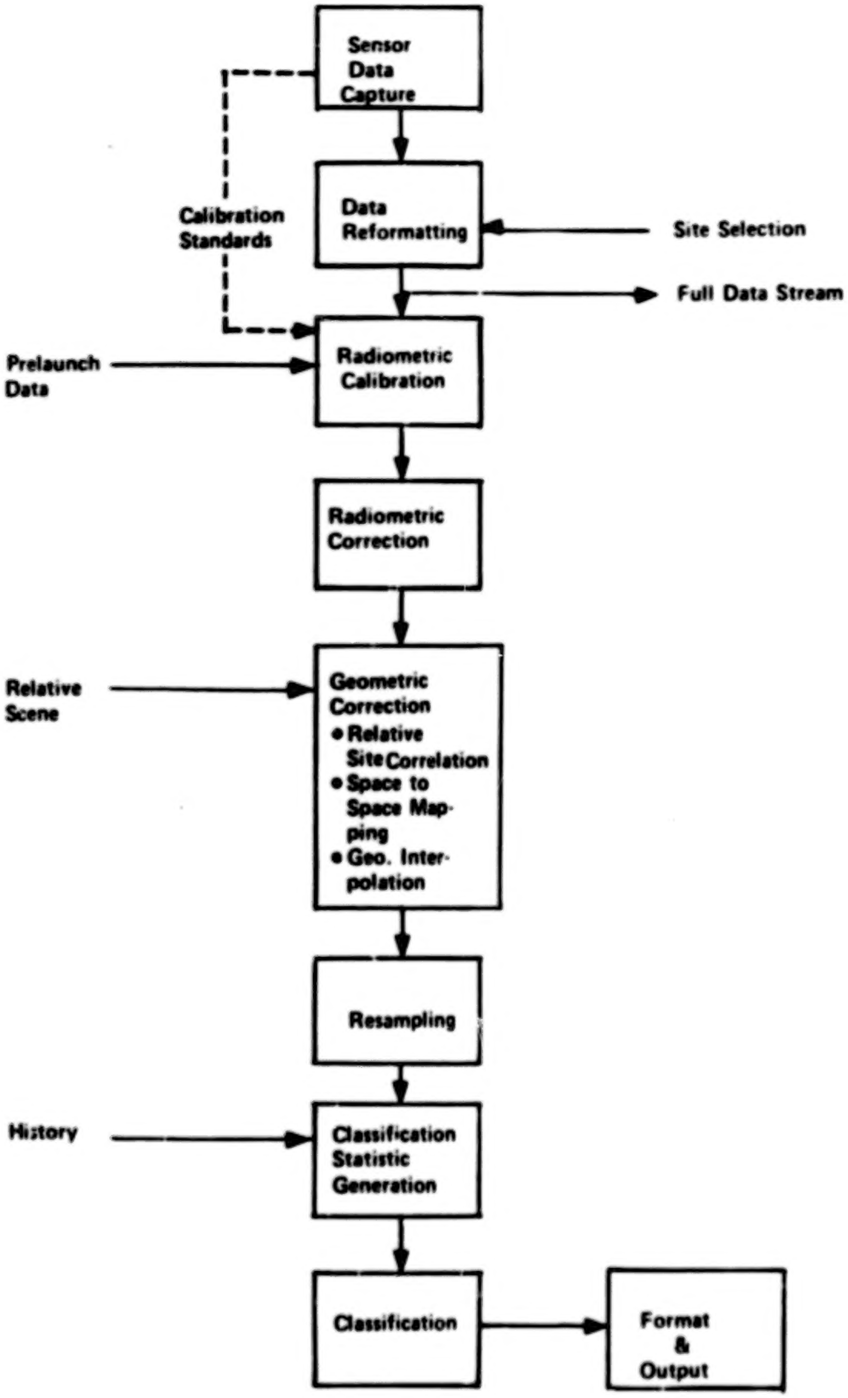
Sensor Data Capture
Calibration Standards
Data Reformatting
Site Selection
Full Data Stream
Prelaunch Data
Radiometric Calibration
Radiometric Correction
Relative Scene
Geometric Correction
• Relative Site Correlation
• Space to Space Mapping
• Geo. Interpolation
Resampling
History
Classification Statistic Generation
Classification
Format & Output

Figure 90. Processing Functions for Multispectral Classification.

Given the information in the training fields, data are classified using a maximum-likelihood classifier. The data are then conveniently formatted and released for further processing.

The sensor parameters of the Landsat-C Multispectral Scanner, shown in Table 23, have been assumed for the analysis. Estimates of the processing load in terms of cycles/pixel classified were developed using actual measurements (including overhead) from the GSFC Master Data Processor System. Classification and classification statistics generation were estimated from LACIE experience since MDP is not programmed for those functions. These loads are shown in Table 24. Note that the classification load, estimated for four channels (bands) and eight classes dominates the rest of the problem with over 70 percent of the requirement. Eight configurations capable of accomplishing on-board classification were established. Each configuration is a different mix of functions allocated between space and the ground as shown in Table 25. These configurations are described and their advantages and disadvantages discussed in the following sections.

Certain assumptions, common to all eight configurations, have been made for this comparison. These assumptions are:

a. All sensor data (image and nonimage) are recorded on tape on-board the spacecraft.

b. These data are transmitted to the ground with the selected data segments classified at the ground using the identical functions implemented on-board. The results will be compared to establish the accuracy of the on-board system.

Table 23. Sensor Parameters of the Landsat-C.

Function	(1) Required Processing (cycles/pixel)	Percentage of Total Processing
Radiometric Calibration	1.4	0.8
Radiometric Correction	5.0	2.7
GCP Locate	1.4	0.8
(2)GEM/S-S/Geo. Interpolation	5.0	2.7
(3)Resampling	36.0	19.4
(5)Classification Statistics	4.5	2.4
Classification	132.0	71.2
(4)Data Reformatting	-	-
Total	185.3	100.0

NOTES:

(1) Cycle is a multiply + add operation

(2) 1 map projection

(3) Includes radiometric correction

(4) Assumes accessing RAM and/or queing on tape or disk

(5) Training field pixels equal to 20% of pixels classified

Table 24. Processing Requirements.

Parameters	Value
SW = Swath Width (m)	185,000
R_L = Along Scan Line Resolution (m)	80 (240)
R_P = Along Scan Path Resolution (m)	30 (240)
V = Spacecraft Ground Track Vel (m/sec)	6750
N_b = Number of Bands	4 Visible + (1 IR)
N_{bp} = Number of Bits Per Pixel	6
Sr = Samples per Pixel in Scan Direction	1.4
N_P = Number of Pixels Classified	≈ 10% of scene
N_C = Number of Classes	8

$$\text{Data Rate} = \frac{S_W}{R_L} \times \frac{V}{R_P} \times N_b \times N_{bp} \times Sr = 6.74 \times 10^6 \text{ bps}$$

Table 25. Processing Functions Computed On-Board or at Ground.

Function	Configuration															
	1		2		3		4		5		6		7		8	
	Gr.	On Bd.	Gr.	On Bd.	Gr.	On Bd.	Gr.	On Bd.	Gr.	On Bd.	Gr.	On Bd.	Gr.	On Bd.	Gr.	On Bd.
Data Reformatting		✓		✓		✓		✓		✓	NA	NA	NA	NA	NA	NA
Radiometric Calibration	✓			✓		✓		✓		✓	NA	NA	NA	NA	NA	NA
Radiometric Correction		✓		✓		✓		✓		✓	NA	NA	NA	NA	NA	NA
Geometric Correction GCP Locate GEM S/S Geo. Interpolation	✓		✓		✓			✓		✓	✓			✓		✓
Resampling	✓		✓			✓		✓		✓	✓			✓		✓
Class. Statistics Generation	✓		✓		✓		✓			✓	✓		✓			✓
Classification		✓		✓		✓		✓		✓		✓		✓		✓

NA -- Not Applicable

c. The selected segments to be classified will be stored on-board and processed as time is available (not in realtime). Approximately 10 percent of the total data accumulated by the sensor will be classified.

d. All configurations perform the classification function on-board.

3.6.5 On-Board Classification Configuration Analysis

Eight on-board configurations have been defined and analyzed. The configurations differ in terms of the functions implemented on-board the spacecraft. The advantages and disadvantages of each of the eight configurations are summarized in Table 26. The factors considered were:

a. Data compaction
b. Turnaround time
c. On-board processing requirements
d. On-board storage requirements
e. Geometric accuracy
f. Classification accuracy
g. On-board complexity
h. Amount of ancillary data required.

The sensor input data rate establishes the available processing time per pixel (i.e., a 1×10^6 bit per second rate allows 0.125 microseconds for an 8-bit pixel). Generally, only a small percentage of the total data collected by the sensor is ever classified. In addition, these data are multichannel (many bands) with the output of the classifier the class code assigned to the classified pixel. These factors combine to determine the relative data compaction for any configuration.

BLANK PAGE

BLANK PAGE

Table 26. On-Board Configuration Comparisons.

	Configurations							
Configuration Features	1	2	3	4	5	6	7	8
Turnaround Time	27 sec/98.88 min	54 sec/98.88 min	54 sec/98.88 min	54 sec/98.88 min	27 sec.	54 sec/98.88 min	54 sec/98.88 min	27 sec.
Processing Reqmts.	73.9%	74.7%	94.1%	97.6%	100%	71.2%	94.1%	96.5%
On Board Storage (bits)								
RAM	486K	486K	486K	486K	243K	30K	30K	30K
Disk or Tape	[1] 13×10^6/[2] 292.5×10^6	$39 \times 10^6/292.5 \times 10^6$	$39 \times 10^6/292.5 \times 10^6$	$39 \times 10^6/292.5 \times 10^6$	19.5×10^6	$39 \times 10^6/292.5 \times 10^6$	$39 \times 10^6/292.5 \times 10^6$	19.5×10^6
Geometric Accuracy	[3] 3 pixel	3 pixel	< 1 pixel	< 1 pixel	< 1 pixel	3 pixel	< 1 pixel	< 1 pixel
Classification Accuracy	Low/medium	Low/medium	Low/medium	Low/medium	High	Low/medium	Low/medium	High
On Board Complexity	Low	Low	Medium	Medium	High	Low	Medium	High
Ancillary Data Required	1,2,3,5	1,2	1,2,4,5	1,2,5,6	7	1,2	1,2,5,6	7

NOTES:

[1] 2 sample segment

[2] 3 sample segments in each of 15 scenes.

[3] Relative to an 80 m MSS pixel

Ancillary Data From Ground

1. Classification statistics
2. Sample segment ID
4. Resampling grids
3. Radiometric calibration coefficients
5. Search area ID
6. Attitude/ephemeris data
7. Training site locations

MICROFILMED FROM
BEST AVAILABLE COPY

All eight configurations analyzed have an 80:1 data compaction ratio. This is based on the following: 10 percent of the pixels are classified, there are four bands of input data with eight classes output (3 bits), each input pixel is 6 bits. The output data rate, assuming an input rate of R bits per second would be R x 10% x 1/4 X 3/6 or R/80 bits per second.

The turnaround time involves the elapsed time between the receipt of the raw data at the sensor and the generation of the output product (i.e., the classification of the pixel). The amount of operator/interpreter intervention in the data flow increases this turnaround time. As an example, any time spent in analyzing the imagery to identify training sites and develop the classification statistics is inserted into the transmission loop thereby imposing a reduction in throughput of the system.

The selected processing approach must accommodate all required functions within the allotted time (i.e., 125 microseconds for an 8-bit pixel in the example cited). This speed can be achieved by a single high-speed device or by distributing the load between similar, lower-speed processors. A higher data rate can be achieved by increasing the speed of a single device or increasing the number of processing elements over which the processing is distributed. Thus, system complexity increases proportionally to the pixel rate.

The sensitivity to the number of bits per pixel primarily depends on the multiplication method used in the processor. If the multiplications are done by ROM table lookup, the amount of ROM required varies with the number of bits in the words to be multiplied. Conversely, if a PLA or hardware multiplier is used, the complexity is proportional to the number of bits (at least for less than 16 bits).

The processing requirements listed in Table 26 represent the percentage of the total processing load accomplished on-board for the 10 percent of the pixels of a scene actually classified. As previously mentioned, the classification function is by far the largest consumer of processing resources, thus the percentage remains high for all configurations.

If the sensor data is to be processed in realtime, certain information must be available. This information includes: radiometric calibration coefficients, resampling grids, and classification statistics. If information must be extracted from the image data and processed prior to classification of the data (such as the control points necessary for resampling grids) then the sample segments to be classified must be stored until this ancillary data is available. In addition, the image data may not be in the proper format, again necessitating data storage.

Two types of on-board storage are shown in Table 26: RAM and disk or tape. The RAM provides the high-speed working storage while the disk or tape provides the lower speed, high data volume capability. Conceivably, bubble memory could also be used for the high-data volume requirement.

The geometric accuracy of the processed data is a function of the correction process implemented on-board. Using ground control points, the absolute geometric accuracy achievable is 0.5 pixel. Using the measured attitude and ephemeris data as provided by the current Landsat-D spacecraft, the absolute geometric accuracy is about 9 pixels relative to a TM pixel or 3 pixels relative to an MSS pixel.

Classification accuracy is a function of the temporal and spatial separation between the classification statistics and the image data being classified. The more representative the statistics, the more accurate the classification. As previously mentioned, the selection of an appropriate set of training fields has been a major problem for the LACIE system.

The complexity of the system is directly related to the degree of geometric correction performed on-board and the procedure used to establish the classification statistics. A useful trade-off to be considered is: spacecraft cost/complexity versus cost/complexity of a number of ground stations.

The ancillary data required reflects the amount of interaction between the ground and the on-board system.

3.6.5.1 Configurations 1a and 1b

Configuration 1a, shown in Figure 91, performs data reformatting (BIP to BIL), radiometric correction, and image classification of selected sample segments on-board. The radiometric calibration coefficients, classification training site statistics, and sample segment ID are computed on the ground and transmitted to the on-board system.

The format of the data is important in terms of the ease of accommodating various functions. Radiometric correction applies the same gain and bias correction to each pixel of a detector, thus a BIL format is preferable. Classification is performed on each individual pixel using information from each band, thus the BIP format is required. Resampling requires contiguous pixels from a detector; however, one set of resampling grids are used for all bands. The data can be resampled in BIL format, stored, and output to the classification function in the BIP format.

All the radiometric coefficients and correction factors are established for a sensor during ground calibration and prelaunch testing. Then during the spacecraft checkout period, about three weeks after launch, these coefficients are verified. The coefficient set includes the gains, offsets, calibration light levels, and channel to channel shading factors and their sensitivities to temperature. The factors most likely to change due to launch vibrations are the internal calibration shading factors. Checking the ratios of odd and even cells using one light level will verify the calibration shading

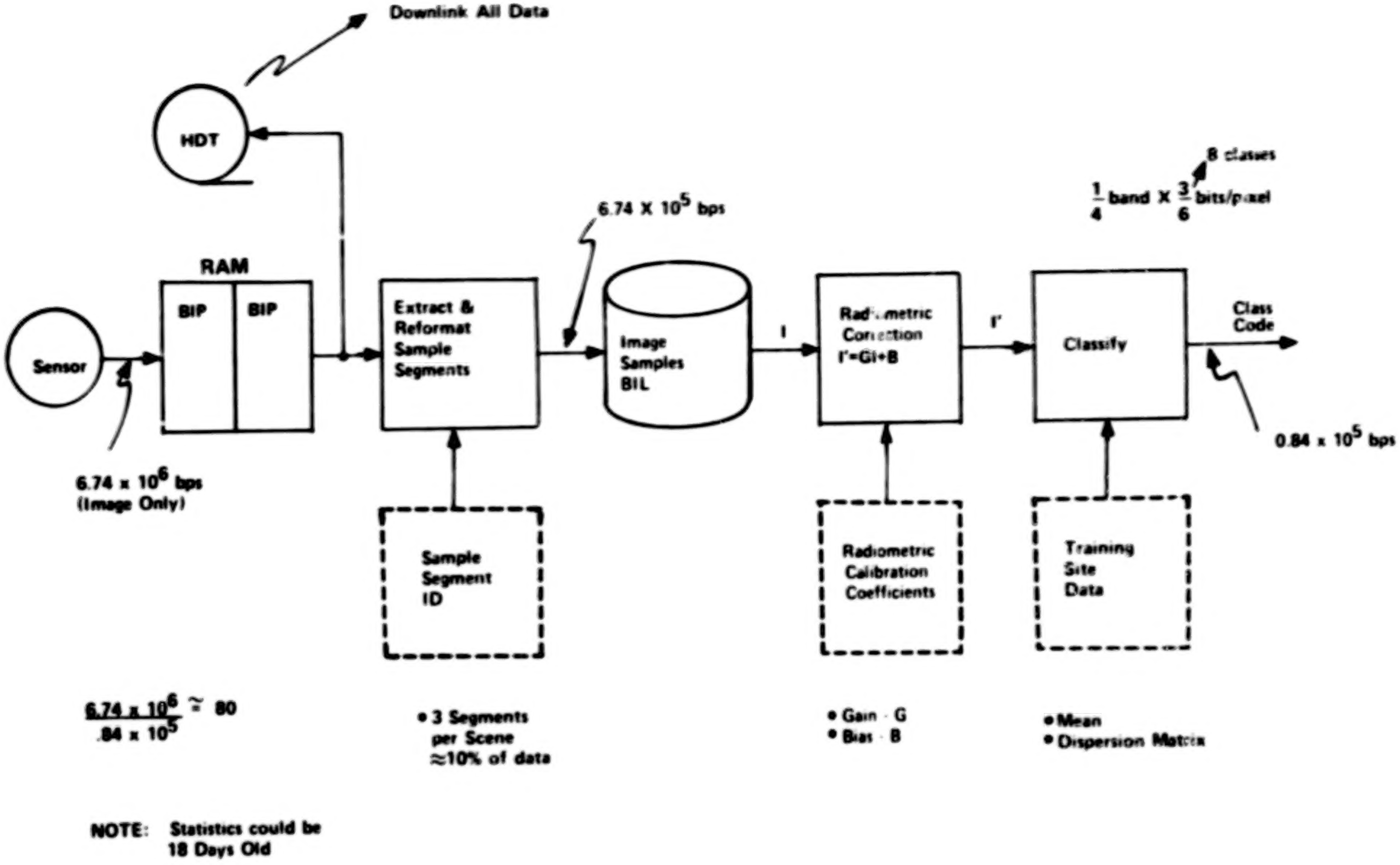
Downlink All Data
HDT
RAM
BIP
BIP
Sensor
6.74 x 10^6 bps (Image Only)
Extract & Reformat Sample Segments
6.74 X 10^5 bps
Image Samples BIL
I
Radiometric Correction I'=GI+B
I'
8 classes
1/4 band X 3/6 bits/pixel
Classify
Class Code
0.84 x 10^5 bps
Sample Segment ID
Radiometric Calibration Coefficients
Training Site Data
6.74 x 10^6 / .84 x 10^5 ≃ 80
• 3 Segments per Scene ≈10% of data
• Gain - G
• Bias - B
• Mean
• Dispersion Matrix
NOTE: Statistics could be 18 Days Old

Figure 91. Configuration 1a--Function Data Flow.

factors. Calibration coefficients and temperature correction factors are determined by cycling through the known internal lamp levels. Variations from the prelaunch coefficients are analyzed. If an environmental disturbance has occurred, the complete calibration coefficient set is reinitialized.

An operational data base is maintained on-board consisting of coefficients G and B (the gain and bias coefficients) that will be applied to the data as radiometric corrections. There will be a G and B coefficient for each detector. Then for each band there will be a set of correction factors that modify these coefficients as a function of focal plane temperature. The number of factors required in any one band should not exceed about 20 with any one factor applicable over a range of temperatures. These factors are in the form of a table lookup.

The internal lamp levels will be cycled through once during any turn-on period. The sun signal will be taken once every orbit. These data are summarized and reviewed by a radiometric systems analyst once a day. If a problem is detected, the calibration coefficients will be updated or the focal plane temperature correction factors modified by changing the table look-up entries.

The image data are transmitted to the ground and reviewed using a procedure similar to that currently implemented by the LACIE system. Training sites are identified and the statistical parameters of interest (means and covariance matrices) computed. Sample segments are identified as test sites of interest. These sample segments will of necessity contain a region larger than the test site to allow for the attitude and position uncertainties in the data. The sample segment locations (line and sample number in the image space plus expected time) along with the training site statistics are transmitted to the spacecraft.

Success of current classification approaches (including LACIE) has been limited to the vicinity of local areas near the training sites (usually tens of kilometers) unless account is taken of systematic variations imposed on the signatures by the conditions of measurement (atmospheric haze, cloud cover, and sun illumination angle) and parameters of measurement (sensor characteristics). Test sites are always taken from the same scene as the training sites.

Image data from a specific scene must be viewed by an operator prior to determining the training site statistics. Due to the time required to identify and compute the training site statistics, test sites within that same scene cannot be classified until 18 days later (9 days with 2 satellites) when the spacecraft again views the same scene. Although the data would be classified as it is collected (27 sec or 1 scene time turnaround assumed) with storage only necessary for 2 sample segments (13×10^6 bits) this 18-day delay would most likely result in poor classification accuracy based on LACIE experience.

This loss of classification accuracy could be reduced by providing sufficient on-board storage of the sample segments until the classification statistics can be made available to the on-board system. Appendix D indicates the effect of the orbital parameters on satellite in-view time. The spacecraft is in-view of the continental U.S. three orbits per day. Storing all sample segments for one orbit would allow sufficient time for the classification statistics to be computed and uplinked to the spacecraft 1 orbit (98.88 min) later. Assuming three sample segments from each scene (≈ 10 percent of the data) and 15 scenes per orbit (over the continental U.S.) results in a storage requirement of 292.5×10^6 bits, a large amount of on-board storage. Any sample segments falling outside the continental U.S. would add to this amount. Once the classification statistics are available, the stored sample segments can be classified. This on-board storage eliminates the temporal delay between computing the statistics and applying the statistics thereby improving classification accuracy. As noted in Appendix D, the available in-view time could be extended with TDRSS, again reducing storage.

Classification accuracy can be improved, therefore, by increasing on-board storage with the on-board storage minimized by extending the spacecraft in-view time.

The image data must be radiometrically corrected prior to classification to correct for sensor-induced errors that would otherwise appear as scene radiance variations. Data reformatting to accommodate radiometric correction (BIP to BIL) requires sufficient on-board storage to allow the data shuffling required for reformatting and to bring the pixels into spatial registration. Appendix A outlines the reformatting process and indicates the storage required to accomplish the reformatting and radiometric correction. As indicated in Appendix A, RAM is used for working storage while tape or disk provides the medium for accumulating the entire segment. There is 486K of RAM required. This assumes the sample segments are acquired serially within a scene (i.e., each sample segment contains a different set of 512 lines). Multiple segments accessed from the same lines would increase the amount of RAM.

The output of the classification function is the class code for each input image pixel of a sample segment, thus the pixel intensity values are lost. The image positional accuracy (true position at the ground) is determined by the attitude and ephemeris uncertainties. Appendix B indicates that with the MMS attitude determination system and the GPS positional accuracies, an image positional accuracy of 3 pixels (relative to the MSS) can be achieved. Attaining an image positional accuracy of less than 3 pixels can only be achieved by using ground control points. The location of ground control points in the input image space involves correlating a search area known to contain a control point with a stored replica of the control point (see subsection 3.2.4.1). This correlation is performed on the pixel intensity values and must be accomplished prior to classifying the data.

Configuration 1b, shown in Figure 92, adds to the on-board processing the control location algorithm function. This will allow ground control points to be located to the nearest input image pixel. The 5 x 5 matrix of correlation values surrounding the control point maximum correlation value can be downlinked to the ground along with the class codes of each pixel. The remaining steps required to develop the anchor points do not require intensity values but just represent a shift of the input image points. The secondary grid points are generated from these shifted anchor points and the position of each input image pixel can be computed.

The correct class code could be assigned to a geometrically correct frame by using the nearest neighbor algorithm applied to the previously classified data.

In summary, the advantages and disadvantages of configurations 1a and 1b are summarized as follows:

Advantages:

1. 80:1 reduction in data rate
2. Reduces the ground station data processing requirements by 73.9 percent
3. Useful in applications that are temporally stable (i.e., forest/nonforest delineation).

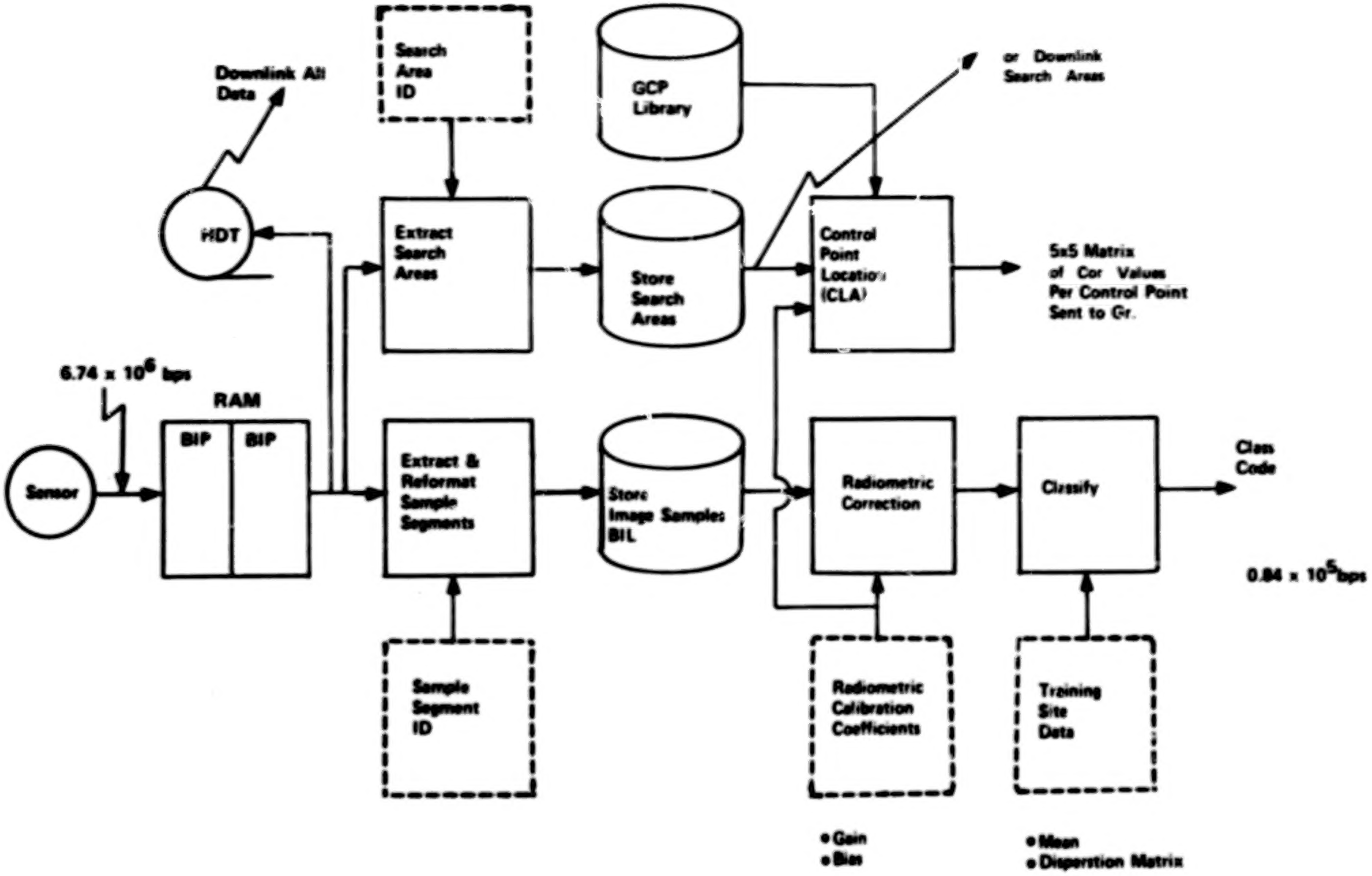
Search
Area
ID
GCP
Library
Downlink All
Data
or Downlink
Search Areas
HDT
Extract
Search
Areas
Store
Search
Areas
Control
Point
Locatio
(CLA
5x5 Matrix
of Cor Values
Per Control Point
Sent to Gr.
6.74 x 10^6 bps
RAM
BIP
BIP
Sensor
Extract &
Reformat
Sample
Segments
Store
Image Samples
BIL
Radiometric
Correction
Classify
Class
Code
0.84 x 10^5 bps
Sample
Segment
ID
Radiometric
Calibration
Coefficients
Training
Site
Data
• Gain
• Bias
• Mean
• Dispersion Matrix

Figure 92. Configuration 1b--Functional Data Flow.

Disadvantages:

1. Pixel intensity values necessary for locating GCPs in image data are lost*
2. Classification statistics could include a temporal delay of 9 to 18 days unless additional on-board storage is provided resulting in low classification accuracy
3. System not able to immediately adjust to radiometric changes
4. Requires a radiometric system analyst at the ground
5. Geometric accuracy only good to three pixels.

3.6.5.2 Configuration 2

Configuration 2, shown in Figure 93, performs data reformatting (BIP to BIL), radiometric calibration, radiometric correction, and image classification on-board. The classification training site statistics are computed on ground and transmitted to the on-board system.

This configuration differs from the first in that the in-flight calibration system monitoring the aging process of the sensors is on-board. The calibration coefficients (gain and bias) will be updated and the focal plane temperature correction factors modified based on an on-board monitoring process. Included within this monitoring process is the implementation of algorithms for striping control as described in subsection 3.2.2.4. In addition, the periodic calibration of the in-flight calibration system, using solar observations, is on-board.

---

*Configuration 1a only.

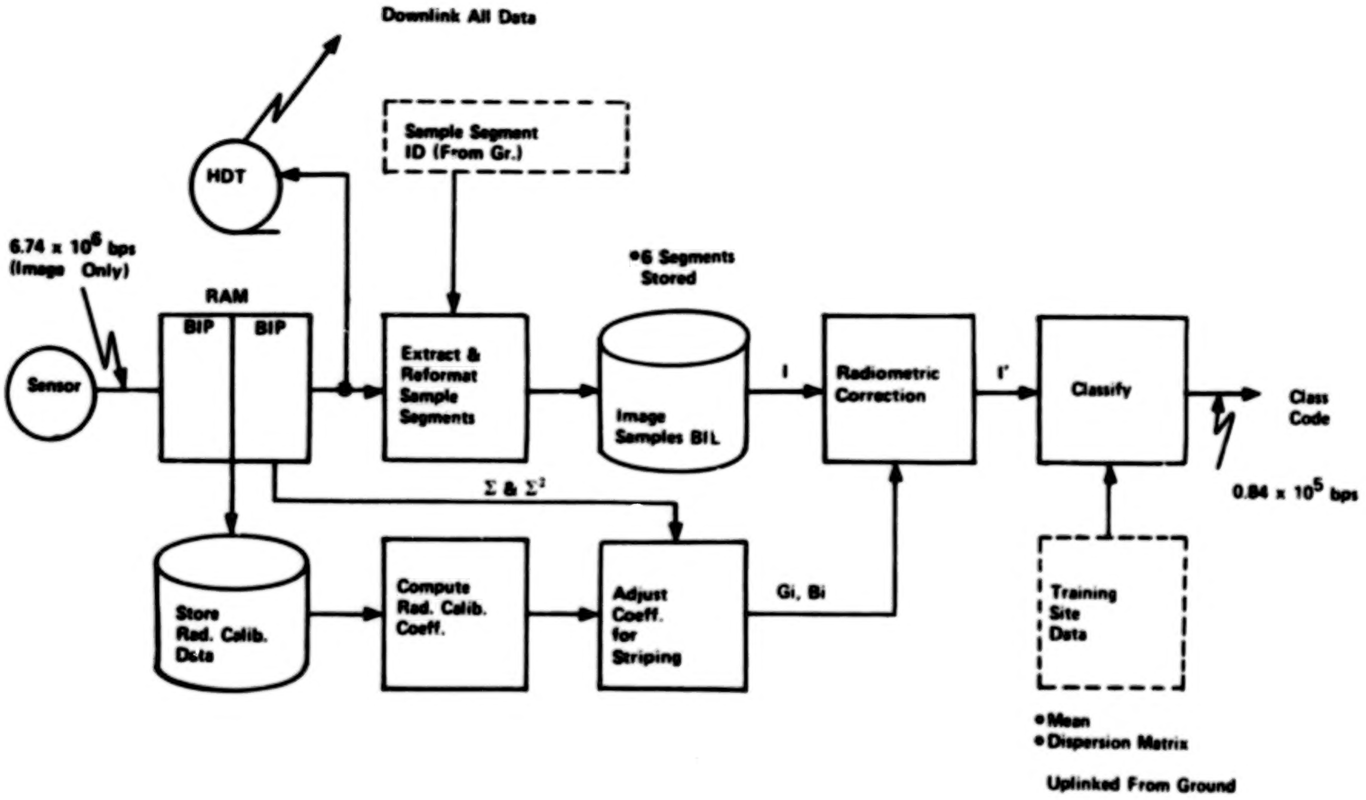
Downlink All Data
HDT
Sample Segment ID (From Gr.)
6.74 x 10^6 bps (Image Only)
RAM
BIP
BIP
Sensor
Extract & Reformat Sample Segments
•6 Segments Stored
Image Samples BIL
I
Radiometric Correction
I'
Classify
Class Code
0.84 x 10^5 bps
Σ & Σ²
Store Rad. Calib. Data
Compute Rad. Calib. Coeff.
Adjust Coeff. for Striping
Gi, Bi
Training Site Data
•Mean
•Dispersion Matrix
Uplinked From Ground

Figure 93. Configuration 2--Functional Data Flow.

Data striping has an undesirable effect when generating photographic products. It can, in some cases, be a hindrance to photo interpretation. It is felt that striping can also be detrimental to multispectral classification applications because spectral signatures of the digital data are artificially altered by the striping. IBM has conducted an experiment to determine the effect data striping has on classification accuracy. This experiment is described in Appendix D. The experiment indicated no effect on classification accuracy due to data striping; however, additional experiments should be conducted before any definite conclusion can be drawn.

As noted in subsection 3.2.2.4, improved techniques for prelaunch calibration of the on-board calibration system and implementation of good calibration algorithms are expected to remove all striping. However, to ensure that striping is completely removed, an automatic scene-dependent destriping algorithm can be implemented as described in subsection 3.2.2.4. After the radiometric correction coefficients have been computed but before they have been applied to the image data, the coefficients are used to modify the sums (Σ) of the pixels in each scan line. The modified sums are then digitally analyzed (using the sums squared, Σ^2) to determine whether striping is present in the corrected data. If striping is detected, the previously computed radiometric coefficients are modified. If striping is not detected, the radiometric coefficients are used without modification.

Computing the radiometric calibration coefficients on-board reduces the interaction between the ground and the on-board system. The need for analyses of the radiometric calibration on the ground is eliminated as is the need for periodically updating the coefficients from the ground. The system can more readily respond to sensor-induced errors or to earth platform-related effects such as changes of radiometric intensity with viewing angle.

The on-board storage requirements will be increased over configuration 1 since the sum (Σ) and sum squared (Σ^2) of pixel intensity values over an entire scene are needed to detect and correct for striping.

The sample segments to be classified over an entire scene must be stored while the radiometric calibration coefficients are being computed. Onboard storage will be provided for sample segments within two scenes or 39×10^6 bits. This allows the image data from one scene to be radiometrically corrected and classified while the radiometric coefficients are being computed for the second scene.

The turnaround time between the sensing and classification of the image data is equivalent to the two-scene delay (54 seconds) providing the classification statistics are available. However, as described for configuration 1, the classification accuracy would be low due to the temporal difference between the computation of the classification statistics and their use in the classification algorithm.

Classification accuracy can be improved by increasing the turnaround time (to 98.88 minutes) and the on-board storage (292.5×10^6 bits) as with configuration 1.

As with configuration 1, the image positional accuracy is determined by the attitude and ephemeris uncertainties. Ground control points must be processed to attain a positional accuracy of less than three pixels. The location of control points is accomplished using the detector radiance values correlated with a stored replica of the control point. Once the data is classified, the intensity values are lost and only the pixel class code transmitted.

This configuration has an advantage over the first configuration in that the data are correctly radiometrically adjusted as the sensor characteristics change. There is no delay between a sensor change and the ability of the system to respond to a change as there is with the first configuration in which an analyst is involved.

The advantages and disadvantages of configuration 2 are summarized as follows:

a. Advantages:

1. 80:1 reduction in data rate
2. Reduces the ground station data processing requirements by 75.3 percent
3. System immediately adjusts to radiometric changes
4. Eliminates the need for a radiometric system analyst at the ground. Only occasional monitoring required.

b. Disadvantages:

1. Pixel intensity values necessary for locating GCPs in the image data are lost
2. Classification statistics could include a temporal delay of 9 to 18 days unless additional on-board storage is provided resulting in low classification accuracy
3. Geometric accuracy only good to three pixels
4. Sample segments from two scenes would be stored on-board to allow for striping correction.

3.6.5.3 Configuration 3

Configuration 3, shown in Figure 94, performs data reformatting (BIP to BIL), radiometric calibration, radiometric correction, resampling, and image classification on-board. Geometric correction (computing the resampling grids), and the computation of the classification training site statistics are computed on the ground and transmitted to the on-board system.

Geometric accuracy can be improved by resampling the image data prior to data classification. Introducing resampling at the spacecraft allows data known to be at the same geometric position to be distributed to a number of ground stations rather than each ground station providing its own resampling capability.

This allows data from two different sensors to be correlated and also permits multitemporal analysis of data obtained from the same sensor of the same scene. Appendix B has shown that geometric accuracy will not be better than 3 pixels using the present attitude uncertainties of 0.01° per axis and a positional uncertainty, as provided by the Global Positioning System (GPS), of 10 meters. Attaining an uncertainty of 1 pixel or less without using ground control points requires the spacecraft attitude to be known to about 0.001° or an order of magnitude improvement over the present AMS system to be used with Landsat-D.

Computation of the resampling grids necessary for resampling requires precise knowledge of the attitude and altitude of the spacecraft. Resolution of the attitude and altitude to the required accuracy is achieved by using GCPs. Subsection 3.2.4.2.4 has shown that over a scene the attitude for Landsat-1, -2, and -C can be modeled by a cubic function of time, and the altitude by a linear function of time. The attitude and altitude for Landsat-D are both modeled as constants over a scene and linear over a swath.

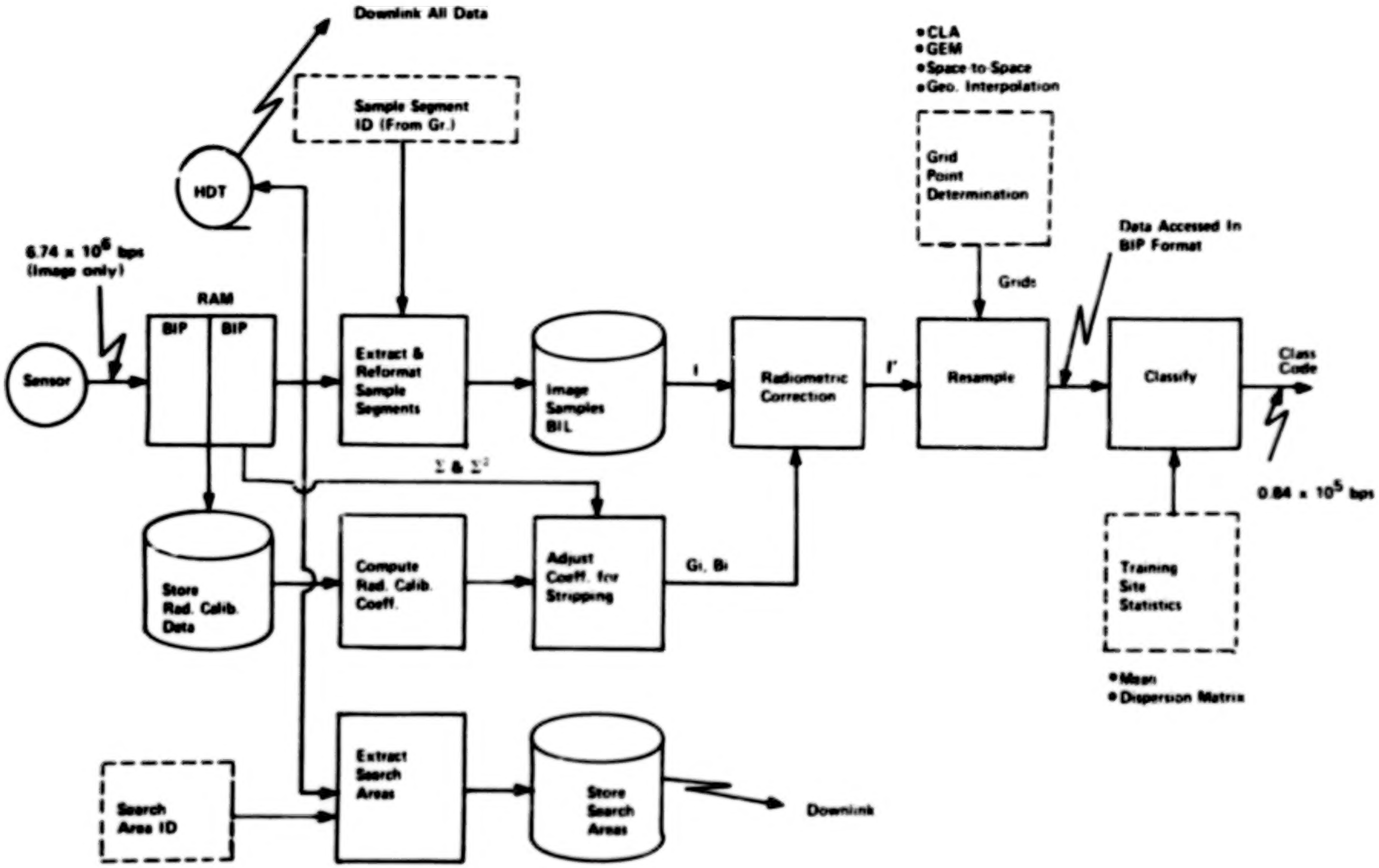
Downlink All Data
Sample Segment ID (From Gr.)
HDT
6.74 x 10^6 bps (Image only)
RAM
BIP
BIP
Sensor
Extract & Reformat Sample Segments
Image Samples BIL
I
Radiometric Correction
I'
Resample
• CLA
• GEM
• Space-to-Space
• Geo. Interpolation
Grid Point Determination
Grids
Data Accessed In BIP Format
Classify
Class Code
0.84 x 10^5 bps
Σ & Σ²
Store Rad. Calib. Data
Compute Rad. Calib. Coeff.
Adjust Coeff. for Stripping
Gi, Bi
Training Site Statistics
• Mean
• Dispersion Matrix
Search Area ID
Extract Search Areas
Store Search Areas
Downlink

Figure 94. Configuration 3a--Funcational Data Flow.

Note that the present Landsat series spacecraft collects the image data from one scene in about 27 seconds and is in-view of the tracking station for regions within the continental U.S. about 7 minutes. For Landstat-D and subsequent spacecraft with very low attitude drift rates (on the order of 10^{-6} degrees per second), the linear attitude and altitude model will be accurate for all sample segments taken during this 7-minute period.

On-board storage must be provided for the sample segments equivalent to the time necessary to create the resampling grids. The present ground implementation approach processes all control points within a scene (batch processes) to determine the attitude/altitude coefficients. Rather than batch processing, the ground control points could be processed recursively. As each ground control point comes in-view of the sensor, a search area is extracted by the on-board system and downlinked to the ground. The attitude/altitude model coefficients would then be updated at the ground. Using the recursive approach, and assuming the high frequency components of the attitude to be insignificant, would provide resampling grids accurate over two scenes. This means that the resampling grids for sample segments in scene N+2 could be uplinked based on control points from scene N. This would eliminate holding sample segments on-board while the resampling grids were being computed.

The recursive approach to creating the resampling rather than the batch approach grids could minimize on-board data storage. However, the image data must be held to allow sufficient time for the classification statistics to be computed, thus the resampling grids may as well be computed at the ground.

The advantages and disadvantages of configurations 3a are summarized as follows:

a. Advantages:

1. 80:1 reduction in data rate

2. Reduces the ground station data processing requirements by 94.7 percent

3. Provides a geometric accuracy of better than one pixel.

b. Disadvantages:

1. Classification statistics could include a temporal delay of 9 to 18 days unless additional onboard storage is provided resulting in low classification accuracy

2. Sample segments from two scenes would be stored onboard to allow for striping correction.

3.6.5.4 Configuration 4

Configuration 4, shown in Figure 95, performs data reformatting (BIP to BIL), radiometric calibration, radiometric correction, geometric correction, resampling, and image classification on-board the spacecraft. The location of sample segments to be classified, location in input image space of search areas containing control points, and ancillary data necessary for geometric correction will be uplinked to the on-board processing system. Training sites are identified on the ground and training site statistics computed and uplinked to the on-board system.

This configuration differs from the previous one in that the computation of the secondary grids necessary for geometric correction is accomplished

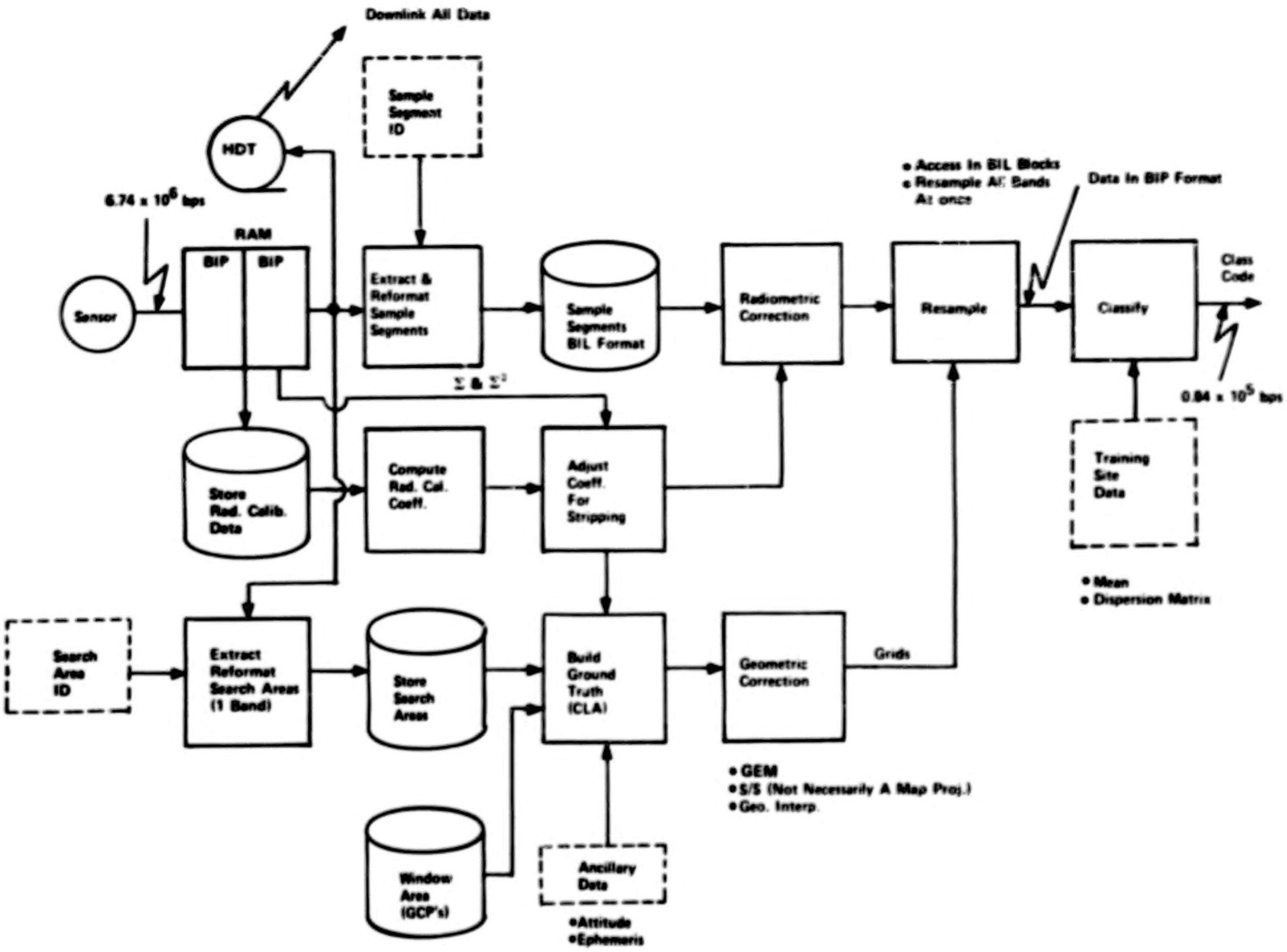
Downlink All Data
Sample Segment ID
HDT
6.74 x 10^6 bps
RAM
BIP
BIP
Sensor
Extract & Reformat Sample Segments
Sample Segments BIL Format
Radiometric Correction
• Access In BIL Blocks
• Resample All Bands At once
Data In BIP Format
Resample
Classify
Class Code
0.84 x 10^5 bps
Σ & Σ²
Store Rad. Calib. Data
Compute Rad. Cal. Coeff.
Adjust Coeff. For Stripping
Training Site Data
• Mean
• Dispersion Matrix
Search Area ID
Extract Reformat Search Areas (1 Band)
Store Search Areas
Build Ground Truth (CLA)
Geometric Correction
Grids
• GEM
• S/S (Not Necessarily A Map Proj.)
• Geo. Interp.
Window Area (GCP's)
Ancillary Data
• Attitude
• Ephemeris

Figure 95. Configuration 4--Functional Data Flow.

on-board. This includes the control location algorithm, geometric error model, space-to-space mapping, and geometric interpolation functions. Note that the space-to-space mapping function does not have to be relative to a map projection but can be relative to an earth-centered frame. This would eliminate two of the transformations needed for accommodating a selected map projection, transforming the image format center (World Reference System) geodetic latitude and longitude coordinates to map projection coordinates and transforming the primary grid coordinates (centered at the format center) to map projection coordinates.

Computing the secondary grids necessary for geometric correction on-board eliminates the time delay introduced by ground computation of the grids and reduces the amount of data uplinked to the spacecraft. The secondary grids are computed in four separate steps:

a. Control Location Algorithm (CLA)
b. Geometric Error Model (GEM)
c. Space-to-Space Mapping (S/S)
d. Geometric Interpolation.

The control points are located in the input image space using the CLA as described in subsection 3.2.4.1.1. This cross-correlation approach locates the control point to a one-pixel accuracy and is readily implemented on-board the spacecraft. The interpolating function (a bivariate fourth-order polynomial) is used to find the subpixel location of the control point. This function is somewhat complex to implement on-board.

Geometric error modeling, described in subsection 3.2.4.2, involves applying known distortion models (usually a polynomial) to correct the observed control points for systematic errors, then using these corrected control points in a weighted least-squares estimator to determine attitude and altitude error model coefficients. GEM requires double precision, floating-point, matrix operation (including the matrix inverse) to achieve the required accuracy.

As previously mentioned, the map transformations required in space-to-space mapping would be eliminated reducing the computational load (for space-to-space) by about a factor of two. This function is also currently implemented in double precision, floating-point arithmetic.

The geometric interpolation function requires a series of cubic and linear interpolations using the primary grid points. Currently, double-precision, floating-point arithmetic is implemented. Recent reviews of this function have revealed that this function could be implemented in single precision, with fixed-scaling arithmetic.

On-board storage requirements would be increased over configuration 3 to provide storage of the ground control points. This is not a significant increase, however, since each control point is represented by a 32 x 32 array of intensity values from 1 band or 1K words per GCP.

The primary disadvantage of this configuration, as with the previous, is the temporal separation between the classification statistics and the data being classified.

Configuration 4b (Figure 96) illustrates an alternate method for providing the grids necessary in resampling. The attitude/altitude coefficients (determined during geometric error modeling) are used in the space-to-space mapping function to map grid points to the input space. As previously mentioned, if the attitude were known to an accuracy of about .001° from the spacecraft system, and the ephemeris were known to 10 meters (GPS), the grids could be computed on-board. This would eliminate the CLA, GEM, and most of the space-to-space mapping functions. The primary grids would be

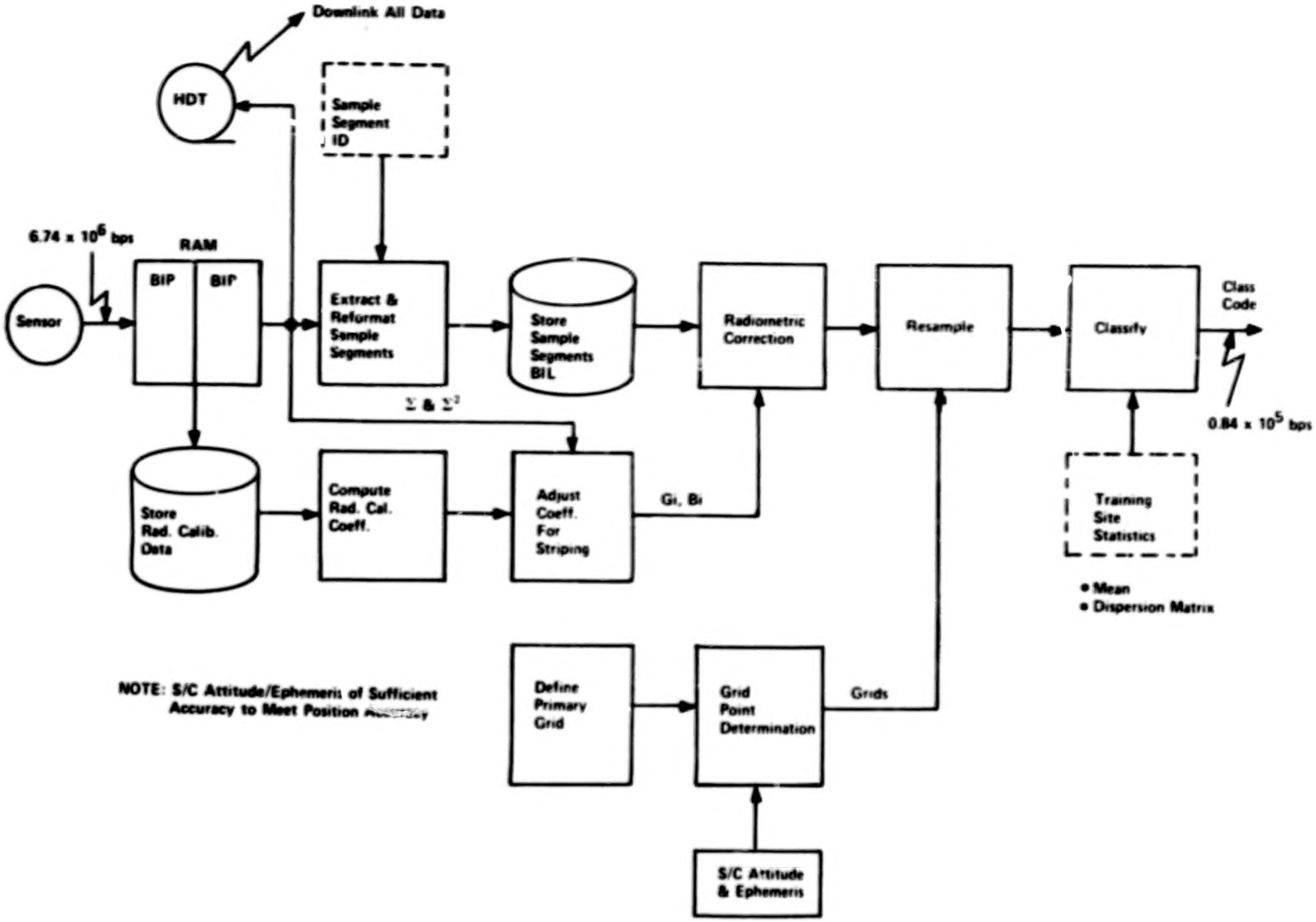
Downlink All Data
HDT
Sample Segment ID
6.74 x 10^6 bps
RAM
BIP
BIP
Sensor
Extract & Reformat Sample Segments
Store Sample Segments BIL
Radiometric Correction
Resample
Classify
Class Code
0.84 x 10^5 bps
Σ & Σ²
Store Rad. Calib. Data
Compute Rad. Cal. Coeff.
Adjust Coeff. For Striping
Gi, Bi
Training Site Statistics
• Mean
• Dispersion Matrix
Define Primary Grid
Grid Point Determination
Grids
S/C Attitude & Ephemeris

NOTE: S/C Attitude/Ephemeris of Sufficient Accuracy to Meet Position Accuracy

Figuration 96. Configuration 4b--Functional Data Flow.

adjusted for attitude and altitude, and corrected for the systematic errors, and geometrically interpolated to provide the resampling grids.

The advantages and disadvantages of configuration 4a and 4b are summarized as follows:

a. Advantages:

   1. 80:1 reduction in data rate

   2. Reduces the ground station data processing requirements by 97.6 percent.

   3. Provides a geometric accuracy of better than one pixel.

b. Disadvantages -- same as configuration 3.

3.6.5.5 Configuration 5

Configuration 5, shown in Figure 97, performs all processing functions on-board the spacecraft: data reformatting (BIP to BIL), radiometric calibration, radiometric correction, geometric correction, resampling, classification statistics generation, and image classification. The training site boundaries necessary for computing the classification statistics and ephemeris data required for locating control points will be uplinked to the spacecraft. The location of the sample segments to be classified, the location of search areas in the input image space containing control points, and the window areas are all stored on-board the spacecraft.

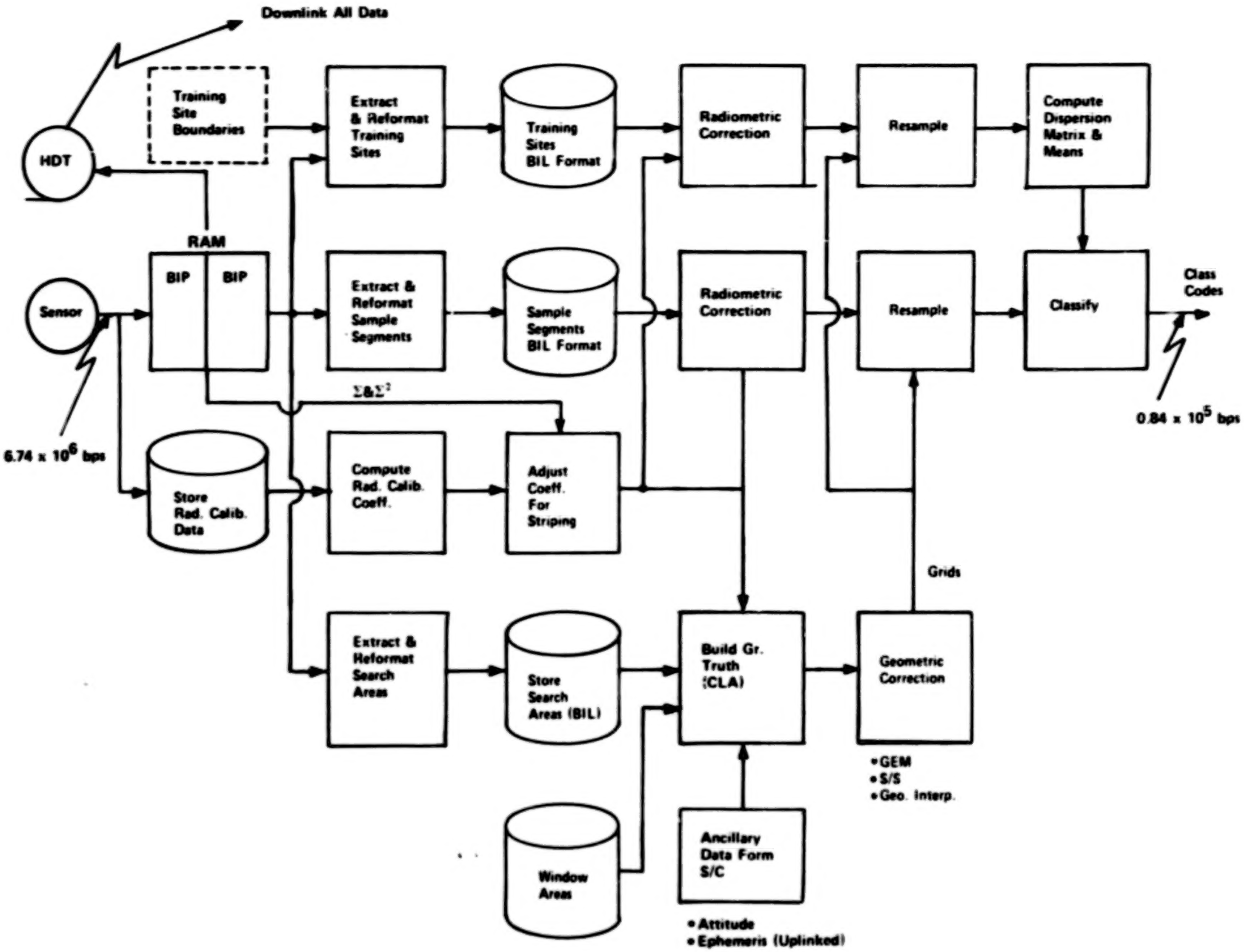
Downlink All Data
Training Site Boundaries
HDT
Extract & Reformat Training Sites
Training Sites BIL Format
Radiometric Correction
Resample
Compute Dispersion Matrix & Means
RAM
BIP
BIP
Sensor
Extract & Reformat Sample Segments
Sample Segments BIL Format
Radiometric Correction
Resample
Classify
Class Codes
Σ&Σ²
6.74 x 10⁶ bps
0.84 x 10⁵ bps
Store Rad. Calib. Data
Compute Rad. Calib. Coeff.
Adjust Coeff. For Striping
Grids
Extract & Reformat Search Areas
Store Search Areas (BIL)
Build Gr. Truth (CLA)
Geometric Correction
•GEM
•S/S
•Geo. Interp.
Window Areas
Ancillary Data Form S/C
• Attitude
• Ephemeris (Uplinked)

Figure 97. Configuration 5--Functional Data Flow.

This configuration offers the greatest potential in terms of classification accuracy, and turnaround time. It also represents the most complex on-board implementation. The training site boundaries would be provided in geodetic coordinates (latitude and longitude). The training site would be extracted from the input image data (all bands) and reformatted BIP to BIL. The extracted region would encompass an area larger than the training site to allow for geometric distortions. These data are radiometrically corrected and resampled to coincide with the known training site boundaries. This resampling process could be especially important for training sites containing a small number of pixels. The dispersion matrix and mean values are determined for the various training sites.

The resampling grids, necessary for resampling the sample segments and the training sites, are computed on-board using attitude information directly from the on-board spacecraft AMS and ephemeris uplinked from the spacecraft tracking net. As with the previous three configurations, the radiometric calibration coefficients are computed on-board, adjusted (if necessary) for striping, and used in radiometric correction.

A certain amount of on-board mass storage is required to provide the time latency necessary for computing the radiometric coefficients, resampling grids, and classification statistics. Storing the sample segments of one scene would be adequate to allow for striping correction and computing the resampling grids. If striping correction were not implemented and control points were recursively processed rather than batch processed, the storage could be reduced by at least a factor of 2.

Classification accuracy would be high since the statistics are being computed in near realtime. Here the turnaround time should be no more than 1 scene time (27 seconds) while the spacecraft is in view.

The advantages and disadvantages of configuration 5 are summarized as follows:

a. Advantages:

1. 80:1 reduction in data rate
2. Reduces the ground station data processing requirements by 100 percent.
3. Provides a geometric accuracy of better than one pixel
4. Turnaround time is essentially 27 seconds (equivalent to one scene)
5. Classification accuracy high since classification statistics contain no temporal delay relative to the test sites.

b. Disadvantages -- System represents a complex on-board implementation.

3.6.5.6 Configurations 6, 7, and 8

Configurations 6, 7, and 8, shown in Figures 98, 99, and 100, respectively, all incorporate radiometric calibration and correction within the sensor electronics. This simplifies the sensor data flow and eliminates the need for data reformatting (BIP to BIL), thereby significantly reducing the on-board storage requirements. Also, since classification requires the data be in a BIP format, the image data can be accessed directly from the sensor input buffer and classified. An optional check for data striping is shown within the dashed lines of the Figures 98 and 99 if striping proves to be a problem. As in previous configurations, all three sample segments

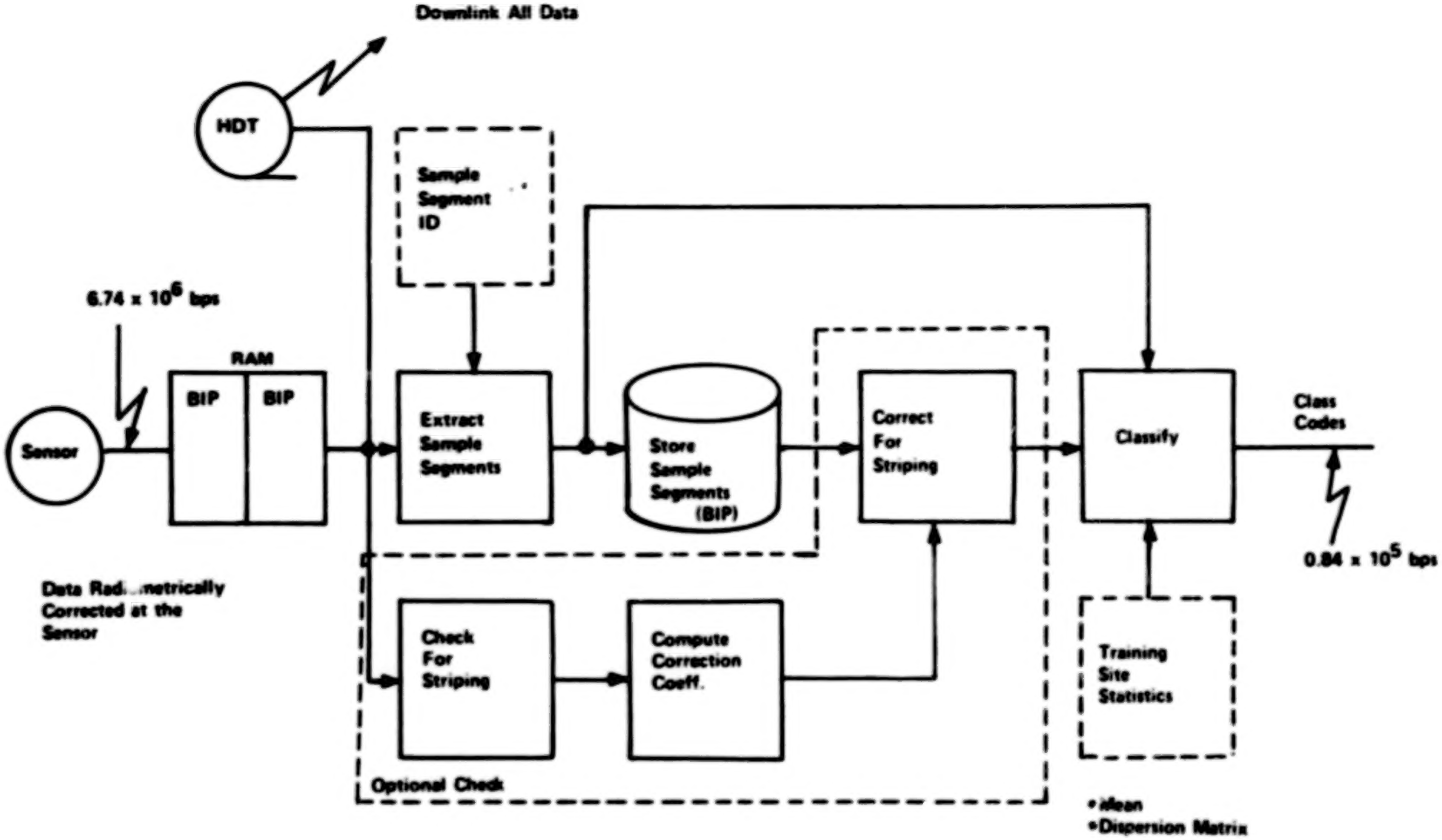
Downlink All Data
HDT
Sample Segment ID
6.74 x 10^6 bps
RAM
BIP
BIP
Sensor
Extract Sample Segments
Store Sample Segments (BIP)
Correct For Striping
Classify
Class Codes
0.84 x 10^5 bps
Data Radiometrically Corrected at the Sensor
Check For Striping
Compute Correction Coeff.
Optional Check
Training Site Statistics
•Mean
•Dispersion Matrix

Figure 98. Configuration 6--Functional Data Flow.

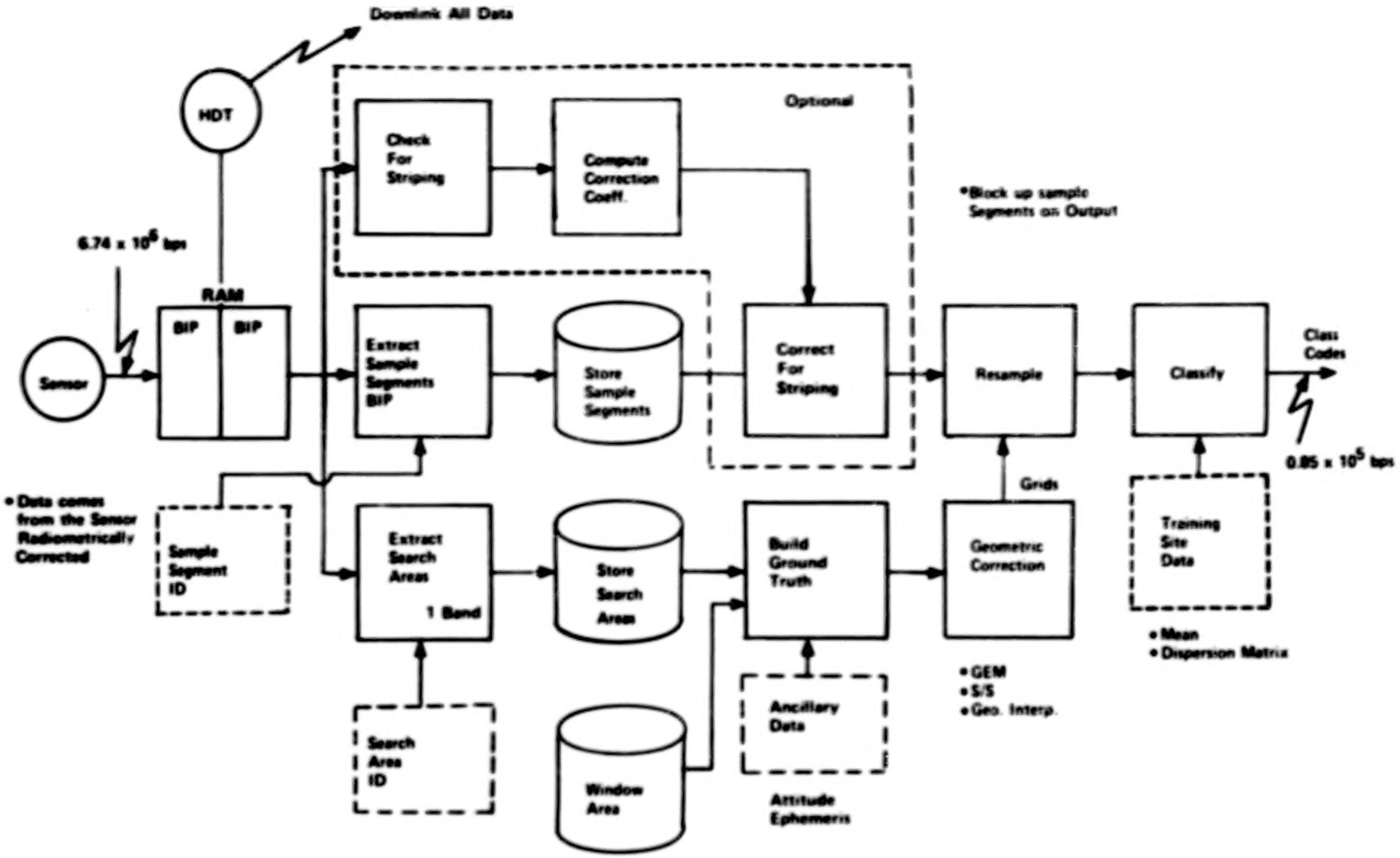
Downlink All Data
HDT
Optional
Check For Striping
Compute Correction Coeff.
*Block up sample Segments on Output
6.74 x 10^6 bps
RAM
BIP
BIP
Sensor
Extract Sample Segments BIP
Store Sample Segments
Correct For Striping
Resample
Classify
Class Codes
0.85 x 10^5 bps
Grids
• Data comes from the Sensor Radiometrically Corrected
Sample Segment ID
Extract Search Areas
1 Band
Store Search Areas
Build Ground Truth
Geometric Correction
Training Site Data
• Mean
• Dispersion Matrix
• GEM
• S/S
• Geo. Interp.
Search Area ID
Window Area
Ancillary Data
Attitude Ephemeris

Figure 99. Configuration 7--Funcational Data Flow.

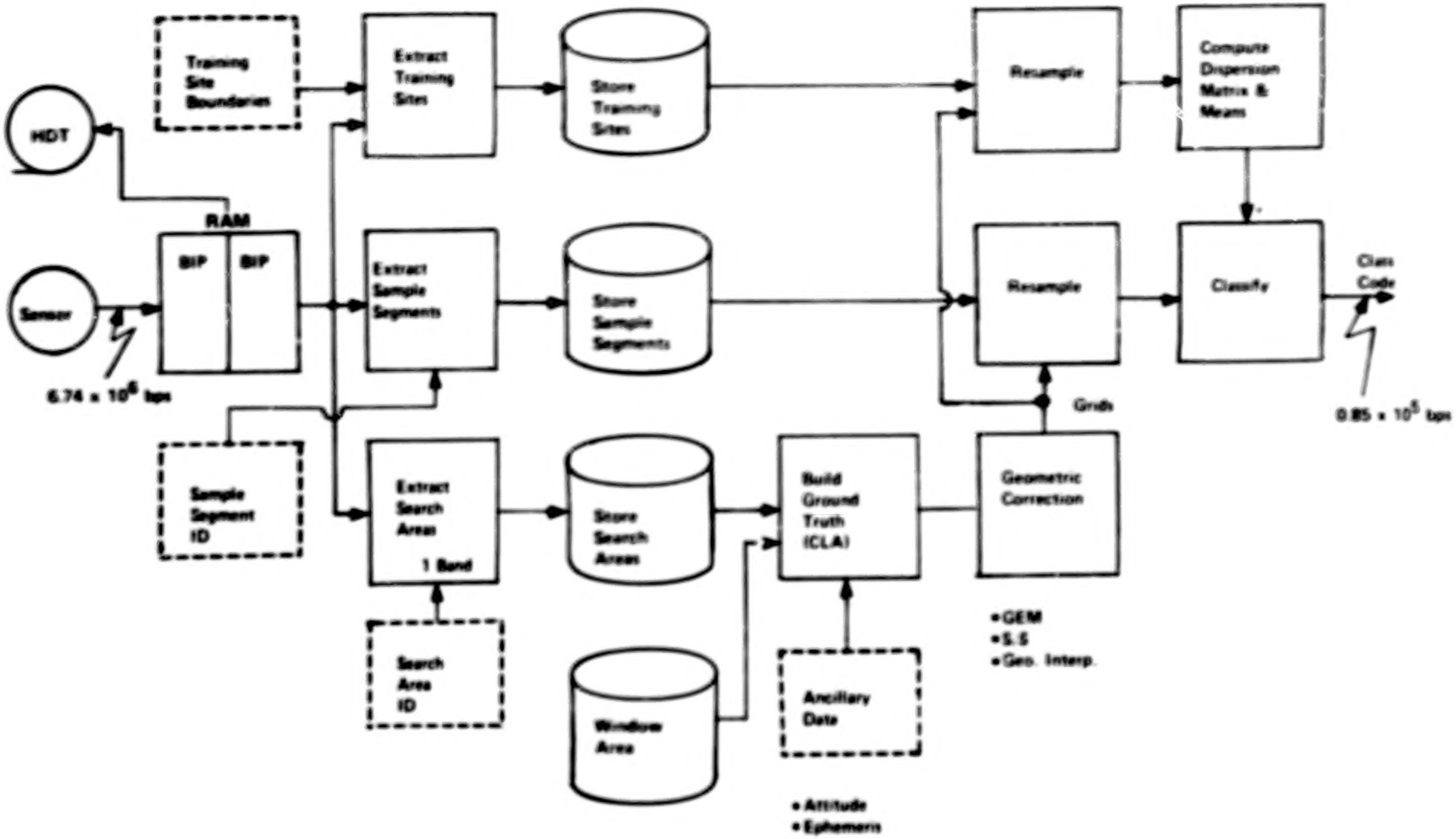
Training Site Boundaries
Extract Training Sites
Store Training Sites
HDT
RAM
BIP
BIP
Sensor
6.74 x 10^6 bps
Extract Sample Segments
Store Sample Segments
Sample Segment ID
Extract Search Areas
1 Band
Store Search Areas
Search Area ID
Window Area
Build Ground Truth (CLA)
Ancillary Data
• Attitude
• Ephemeris
Geometric Correction
• GEM
• S.S
• Geo. Interp.
Grids
Resample
Resample
Compute Dispersion Matrix & Means
Classify
Class Code
0.85 x 10^5 bps

Figure 100. Configuration 8--Functional Data Flow.

within a scene (19.5×10^6 bits or 39×10^6 bits when double buffered) must be stored on-board if the striping correction is required.

As with configurations 2 and 4, computing the classification statistics on the ground introduces a temporal delay relative to classification of test sites resulting in low classification accuracy for configurations 6 and 7. Again, classification statistics become available. Having to store these sample segments results in tape (or disk) storage requirements that are identical to configurations 2 and 4; however, the temporary RAM buffer requirements are greatly reduced (30K bits as compared with 486K bits).

Configuration 8 computes the classification statistics on-board resulting in a high classification accuracy. The 19.5×10^6 bits of tape/disk storage allows all segments within a scene (3 assumed) to be stored while the data is monitored for striping (the striping correction functions are not shown in Figure 100 for purposes of clarity). If the striping correction is not required, this storage requirement could be reduced to any amount sufficient for creating the resampling grids. If a recursive method were implemented for computing the resampling grids capable of extrapolating ahead, the 19.5×10^6 bits of storage could be reduced. Now the only required storage would be an amount large enough to account for the temporal delay required while the classification statistics are being generated. At most this would be equivalent to two sample segments or 13×10^6 bits. A comparison of configurations 5 and 8 indicates that accomplishing radiometric correction within the sensor electronics saves 213K of RAM. Would this saving justify the added sensor complexity?

These three configurations (6, 7, and 8) illustrate that while functions can be removed from the data processing system and incorporated into the sensor electronic design, other system considerations may be the dominant factors in the overall design. Any data correction requiring the total scene contents to be viewed (such as striping correction) or the computation of auxiliary data necessary for accomplishing various functions (i.e., computation of resampling grids and classification statistics) may necessitate either large amounts of on-board storage or excessive interaction with the ground to achieve acceptable geometric and classification accuracy.

The advantages and disadvantages of configurations 6, 7, and 8 are identical to configurations 2, 4, and 5 with the following exceptions:

a. Advantages -- The reformatting, radiometric coefficient computation, and radiometric correction functions are not required (by the data processing hardware) resulting in less on-board storage and a lower processing load.

b. Disadvantages -- A more complex sensor system is required.

SECTION 4

CONCLUSIONS AND RECOMMENDATIONS

The primary purpose of this study has been to investigate the factors relating to on-board multispectral classification. The functions currently implemented in ground-based image processing systems for current earth observation sensors were defined and described in detail. These functions included: data reformatting, radiometric calibration, radiometric correction, geometric correction, and resampling. Conceptual extensions of these functions to an on-board multispectral classification system plus two additional functions--classification statistics generation and classification--were formulated and analyzed.

Eight separate on-board configurations, each with a different mix of functions allocated between space and ground, were defined and analyzed. The advantages and disadvantages of each configuration were outlined while considering the following factors: data compaction, turnaround time, on-board processing requirements, on-board storage requirements, geometric accuracy, classification accuracy, on-board complexity, and amount of ancillary data required.

As a result of this conceptual analysis, the on-board configuration recommended for additional study includes the following functions:

a. Radiometric calibration and correction of the image data

b. Data reformatting compatible with on-board data registration and resampling, preferably in a BIP format

c. Registration of the image data to a reference scene to an accuracy of ± 1 pixel.

It is not recommended that an unsupervised mission involving the generation of the classification statistics or the classification of image data be accomplished by the on-board system at the present time. Technology does exist capable of accomplishing the classification function on-board. However, a procedure for generating the classification statistics on-board that does not require large amounts of on-board data storage, or significant interaction between the ground and the on-board system has not been established. It is recommended, therefore, that a study be initiated to define the ground-space interaction necessary to accomplish the on-board classification of image data.

These recommendations are primarily based on extensive experience with LACIE. LACIE has shown that the selection of training fields (from which the classification statistics are generated) has been a major consumer of analyst time in the classification process. The result has been poor system throughput (i.e., pixels classified per day). In addition, the classification accuracy has been low due to the variability of training field statistics as a function of atmospheric and sun-angle effects, soil conditions, soil type, etc. Success of any on-board classification technique would be, at best, limited to the vicinity of local areas near the training sites and coincident in time unless account is taken of the systematic variations imposed on the signatures by the conditions of measurement.

The configuration analysis has also illustrated that, although functions can be removed from the data processing system and incorporated into the sensor electronic design, other system considerations may be the dominant factors in the overall design. Any data correction requiring either the analysis of the total scene contents or the computation of auxiliary data necessary for accomplishing various functions (i.e., computation of resampling grids prior to resampling, computation of classification statistics prior to classification), may necessitate either large amounts of on-board storage or significant interaction with the ground to achieve acceptable geometric and classification accuracy.

This study has assumed (based on the present NASA Research Experimenter Environment) that only 10 percent of the data collected by current earth observation sensors would actually be processed. Selecting the data to be processed requires on-board data editing. The data editing functions would include the screening of the data to select only those data with an acceptable amount of cloud cover (less than 50 percent) and sample segment extraction. The criteria used for extracting sample segments could be percentage of cloud cover, time, geographic location, and other unspecified parameters. These data editing functions could be implemented on-board to significantly reduce the present downlinked data load. When combined with the radiometric correction, reformatting, and registration functions, the data would be in a form directly compatible with the classification function.

BLANK PAGE

Appendix A

TM AND MSS DATA REFORMATTING STUDY

A.1 TM SENSOR DATA FLOW

The MSS sensor currently used in Landsat-1, -2, and -C, and the TM sensor planned for Landsat-D are both electromechanical scanners. Typically, mechanical motion causes the scene to be sampled in the cross-track direction by a detector or array of detectors while satellite motion provides the orthogonal scan component.

The overall signal flow pattern of each of these sensors or, equivalently, the number of A/D converters and the detector sampling sequence establish the data format to be processed.

The signal data flow for the TM is shown in Figure 101. The signals from 100 data channels are first buffered. From the buffer, the signal goes to the track and hold circuits where the odd detectors and then the even detectors from all bands are sampled simultaneously to eliminate the small staircase (time delay) effect that occurs with sequential sampling (as with MSS). The 100 data channels are comprised of 16 channels from each of six visible bands plus four channels from the IR band. One analog multiplexer per band then multiplexes all detector channels in a band and sends the resultant signal to an A/D converter. The A/D converter digitizes the analog signals into 8-bit words. The signals then go to a serial-to-parallel register and onto the digital multiplexer. Two additional channels provide for synchronization and S/C telemetry data with a resulting data rate of 83.268 Mbps.

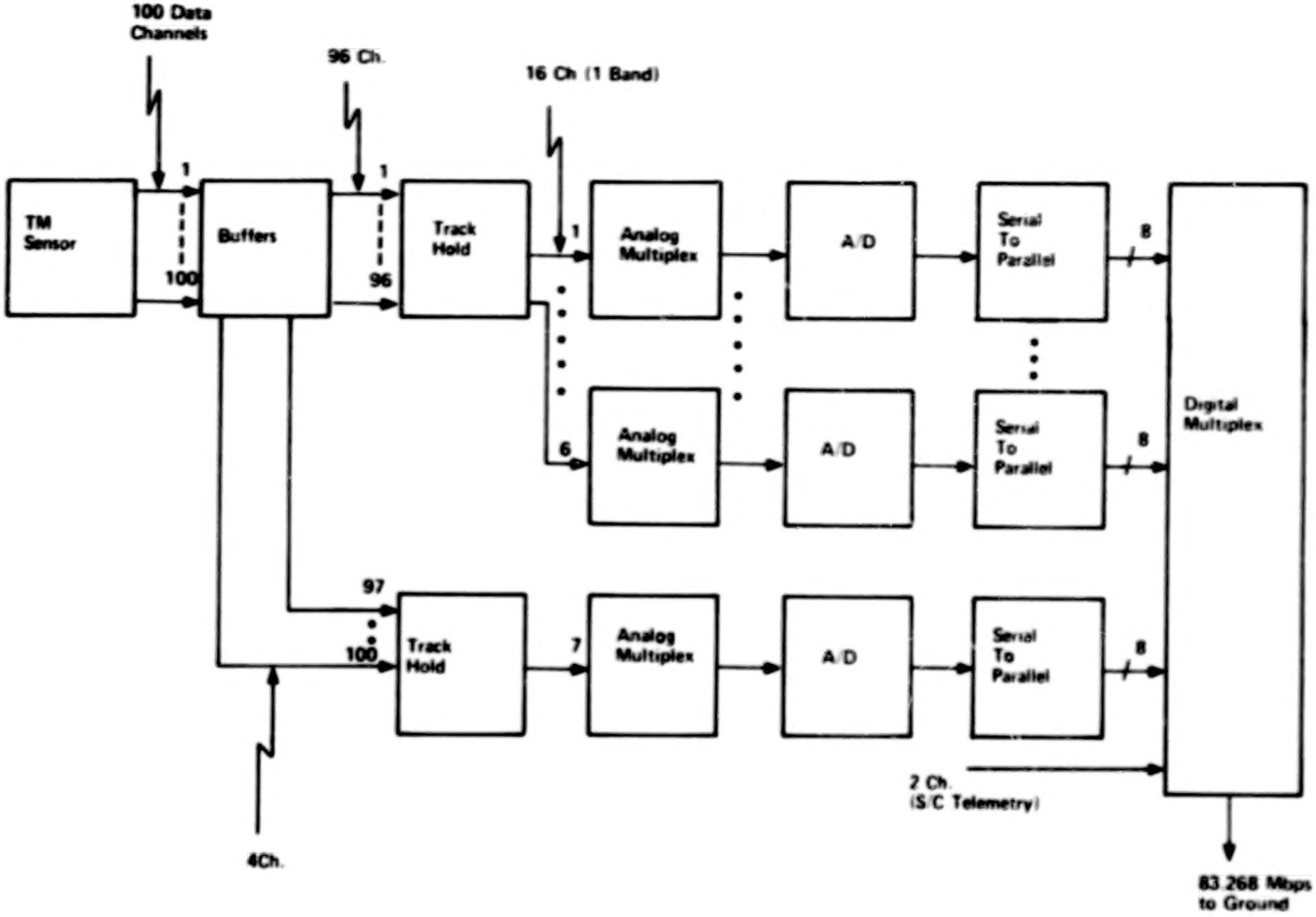
100 Data Channels
96 Ch.
16 Ch (1 Band)
TM Sensor
1
100
Buffers
1
96
Track Hold
1
6
Analog Multiplex
Analog Multiplex
A/D
A/D
Serial To Parallel
Serial To Parallel
8
8
Digital Multiplex
97
100
Track Hold
7
Analog Multiplex
A/D
Serial To Parallel
8
4Ch.
2 Ch. (S/C Telemetry)
83.268 Mbps to Ground

Figure 101. TM Sensor Data Flow.

A.2 MSS SENSOR DATA FLOW

The signal data flow for the MSS is shown in Figure 102. The signals from 26 data channels are buffered for input to track and hold circuits. One analog multiplexer sequentially samples all 26 data channels. The 26 data channels consist of six channels from each of four visible bands plus two channels from the IR band. The two IR detectors (band 8) are alternately sampled and multiplexed into the 25th output channel.

A.3 MSS SAMPLING SEQUENCE

The detector sampling sequence and spatial relationships for the visible MSS bands of Landsats -1, -2, and -C are shown in Figure 103. The light pipe array dimensions, physical arrangement, and sampling sequence are directly related to mirror velocity and spacecraft motion.

Each MSS detector is sampled once every 9.958 microseconds. The cross-track image velocity is nominally 5.612 meters per microsecond. After 9.958 msec the 79- x 79-meter image has moved 56 meters. Therefore, the effective IFOV of a detector in the cross-track direction must be considered to be 56 meters x 79 meters (at nadir).

After completing two sampling intervals (2 pixels), an elapsed time of 19.916 μsec, plus one sequential sample time of 0.3983 μsec (9.958/25), detector A of band 5 is sampled. In 20.314 μsec the image on the ground has moved 114 meters. To achieve spatial registration of band 4 and band 5 of detector A, the bands must be spaced by 35 meters equivalent ground distance. Following the same procedure, the spacing of band 6 and band 7 can be derived. The results are shown in Table 27. This spatial misregistration is currently corrected (for ground processing) by inserting the appropriate number of dummy pixels prior to outputting the data to tape. When processing the data onboard, the data from the different bands must be properly accessed to account for this shift.

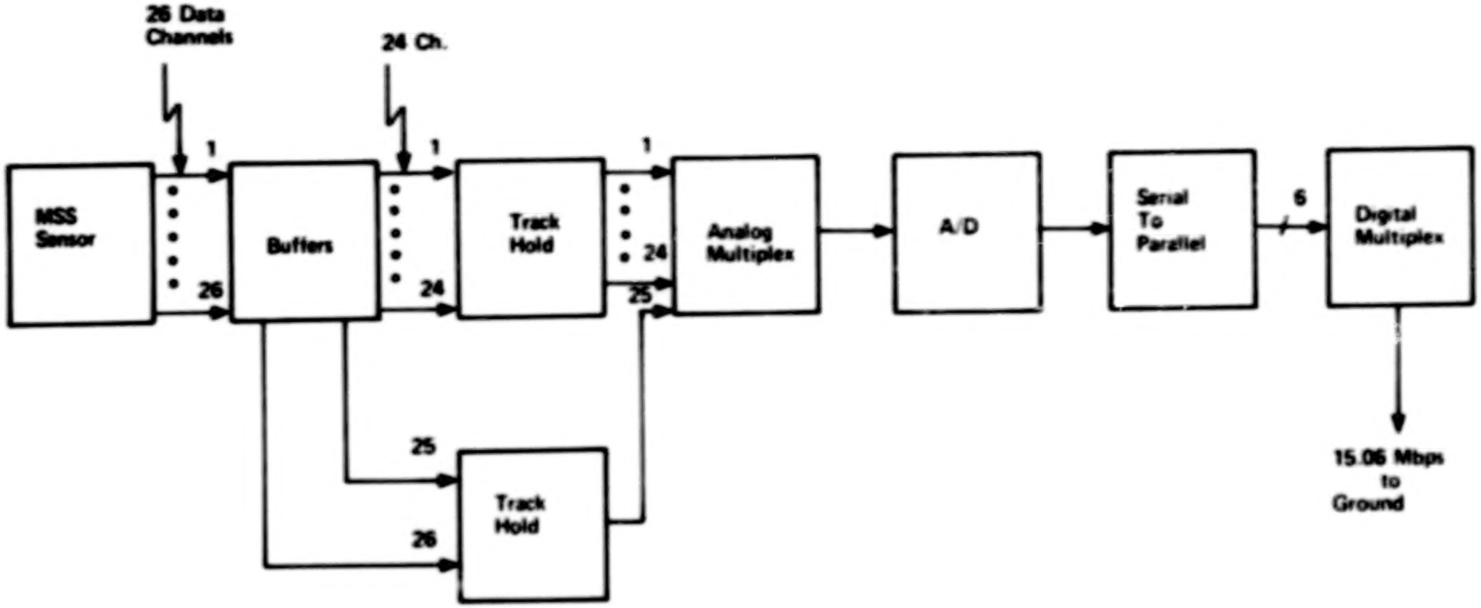
26 Data Channels
24 Ch.
MSS Sensor
1
26
Buffers
1
24
Track Hold
1
24
25
Analog Multiplex
A/D
Serial To Parallel
6
Digital Multiplex
15.06 Mbps to Ground
25
26
Track Hold

Figure 102. MSS Sensor Data Flow.

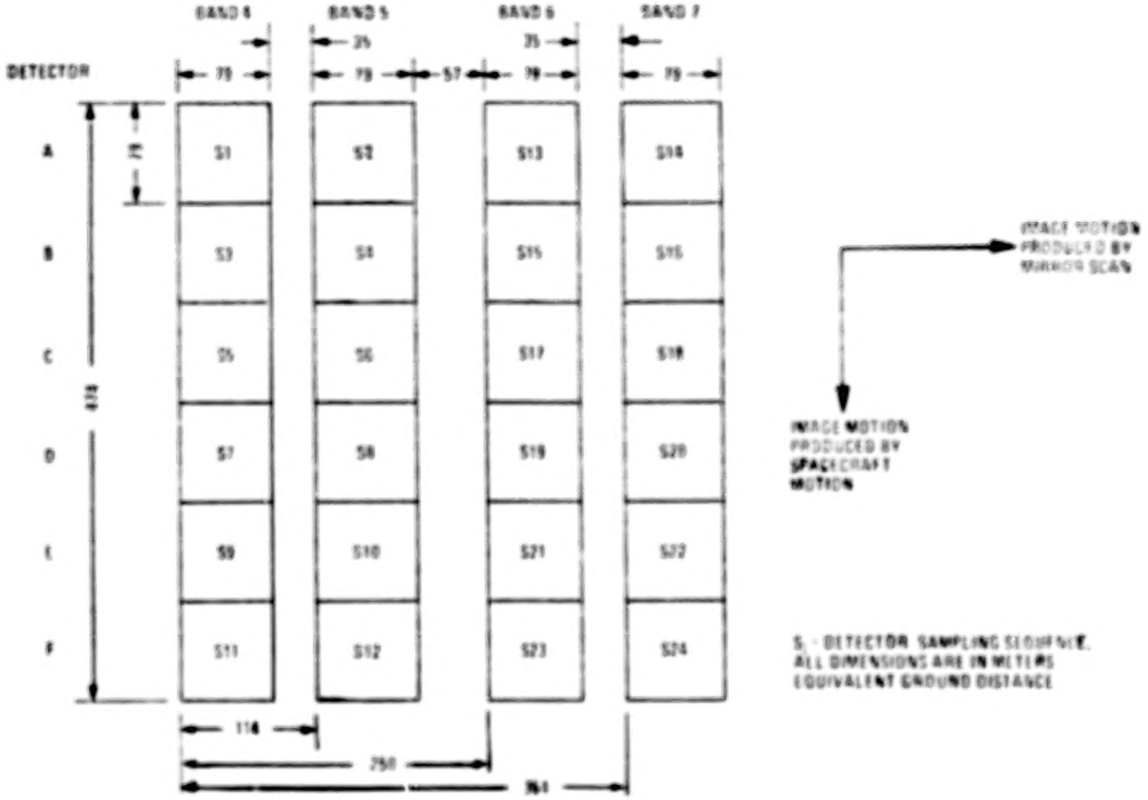
BAND 4
BAND 5
BAND 6
BAND 7
DETECTOR
35
35
79
79
57
79
79
A
B
C
D
E
F
79
474
S1
S2
S13
S14
S3
S4
S15
S16
S5
S6
S17
S18
S7
S8
S19
S20
S9
S10
S21
S22
S11
S12
S23
S24
114
250
361
IMAGE MOTION PRODUCED BY MIRROR SCAN
IMAGE MOTION PRODUCED BY SPACECRAFT MOTION
S_i - DETECTOR SAMPLING SEQUENCE.
ALL DIMENSIONS ARE IN METERS
EQUIVALENT GROUND DISTANCE

Figure 103. Landsat-1, -2 and -C Light Pipe Array and Detector Sampling Sequence.

Table 27. Numerical Values for Light Pipe Array and Detector Sampling Sequence

No. of Complete Sampling Sequences	No. of Completed Samples In Next Sequence	Elapsed Time In Microseconds	Cross-Track Image Motion In Meters	Image Position Det. X Band n
0	0	0	0	Det A Band 4
2	1	20.314	114	Det A Band 5
4	12	44.612	250	Det A Band 6
6	13	64.926	364	Det A Band 7

Average Image Velocity = 5.612m/μsec

A.4 TM SAMPLING SEQUENCE

The detector sampling sequence and spatial relationships for the TM bands is shown in Figure 104. The combination of orbital velocity, scan mirror, and scan line corrector motions cause the scene below the satellite to be projected back and forth across the detector arrays in a rectilinear scan pattern as compared with the unidirectional scan of the MSS (see Figure 105). Alternate detectors in each TM band are separated by 2.5 pixels in the scan direction. The odd-numbered detectors are sampled at one instant in time and the even-numbered ones are sampled at a time equivalent to one half a pixel later. On a forward scan, a line on the ground parallel to the satellite track direction would be sampled by the odd-numbered detectors and then 2.5 sample times later by the even-numbered detectors, resulting in a two-minor frame (pixel) separation of the data. On the reverse scan, the corresponding

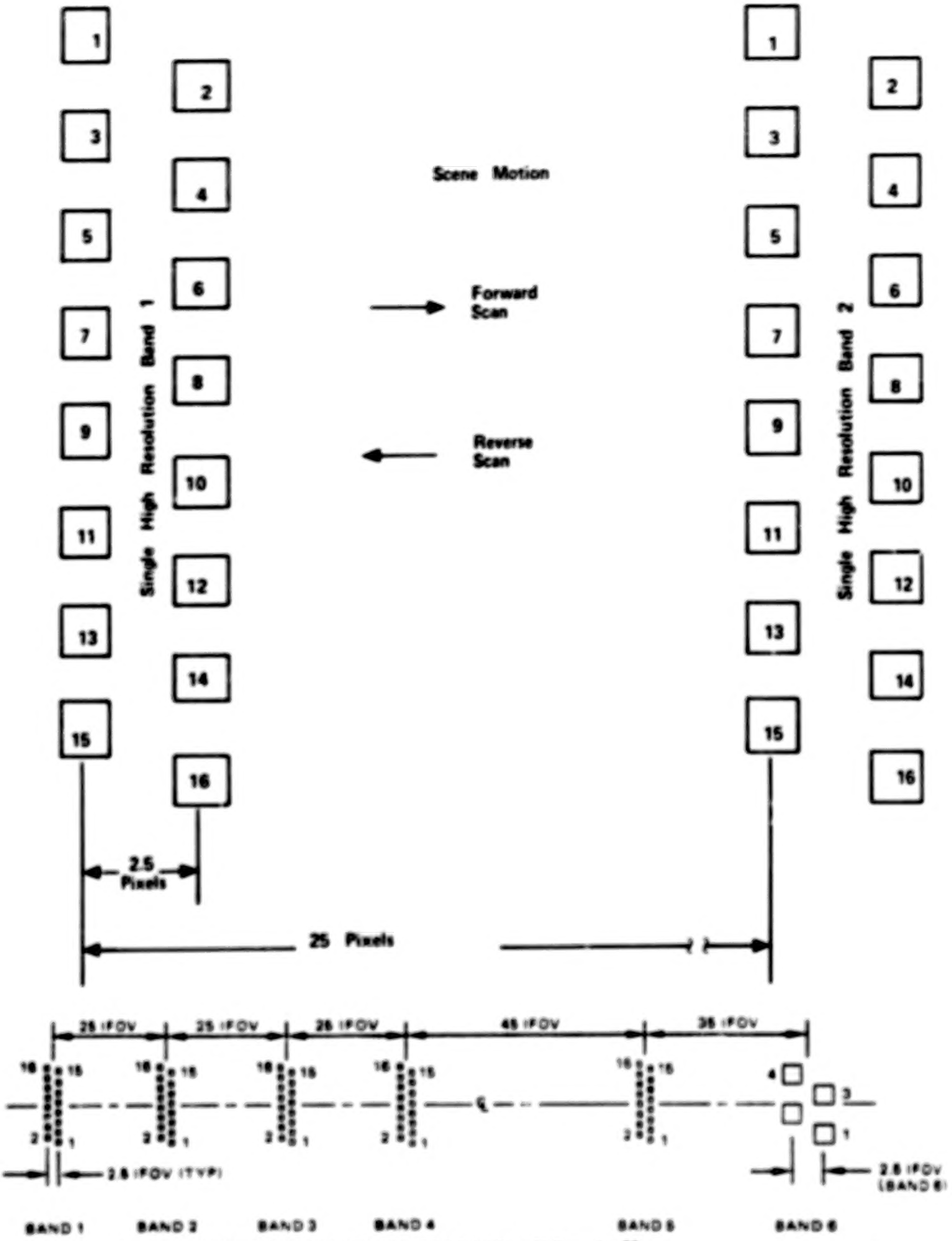
1
2
3
4
5
6
7
8
9
10
11
12
13
14
15
16
Single High Resolution Band 1
Scene Motion
Forward Scan
Reverse Scan
Single High Resolution Band 2
2.5 Pixels
25 Pixels
25 IFOV
25 IFOV
25 IFOV
45 IFOV
35 IFOV
16
15
2
1
℄
4
3
1
2.5 IFOV (TYP)
2.5 IFOV (BAND 6)
BAND 1
BAND 2
BAND 3
BAND 4
BAND 5
BAND 6
TM SENSORS SPATIAL RELATIONSHIPS 1.0 IFOV = 42.5 μrad = 30m
N
W
E
S

Figure 104. Detector Sampling Sequence and Spatial Relationship.

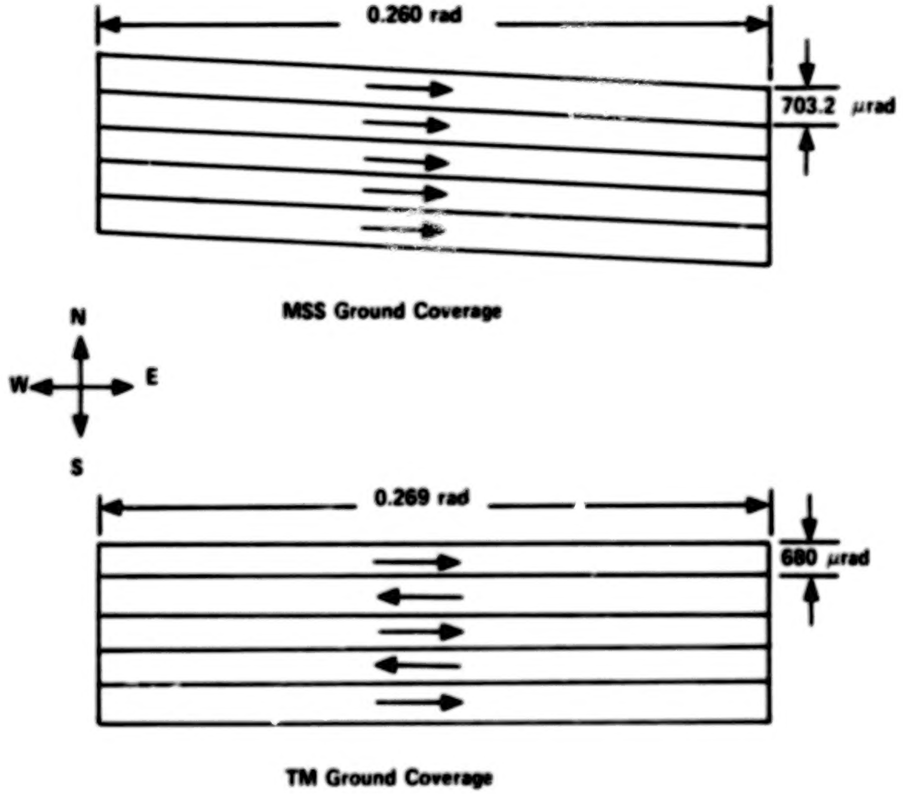
0.260 rad
703.2 μrad
MSS Ground Coverage
N
W
E
S
0.269 rad
680 μrad
TM Ground Coverage

Figure 105. Comparison of MSS and TM Ground Coverage Successive Signs.

detector outputs would be three minor frames (pixels) apart. Adjacent bands are separated by 25 pixels. This 25-pixel separation must be accounted for to gain spatial registration of pixels prior to classification.

A.5 MULTIPLEXED DATA FORMATS

Figures 106 and 107 present the current minor frame data formats for the multiplexed data stream for the MSS and TM, respectively.

The data format for the MSS consists of a 150-word minor frame encompassing six successive samples (pixels) of each of the channels in bands 1 to 4 (144 words) and two successive samples of each of the channels in band 5 (four words). A minor frame synchronization code word, MFSC, and its complement, $\overline{\text{MFSC}}$, are inserted into the remaining two-word locations. Note that each of the sensors in bands 1 to 4 is sampled three times as often as each of the band 5 sensors.

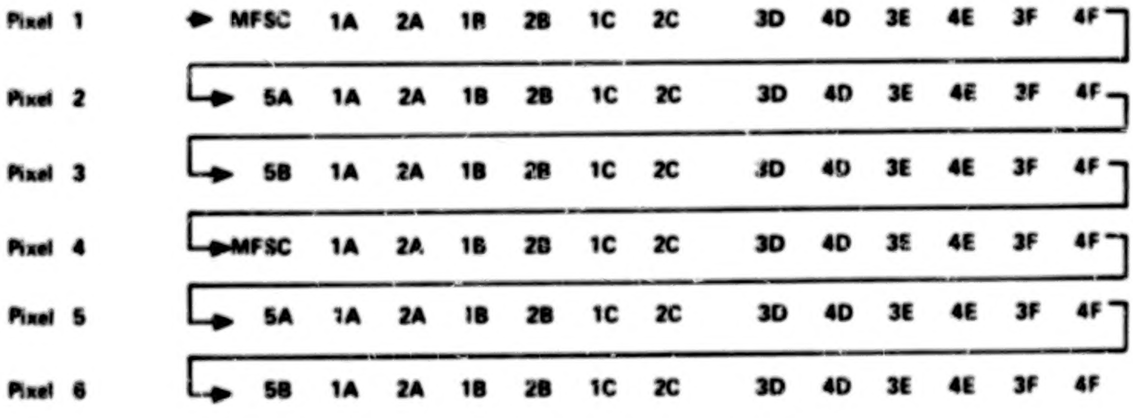
Pixel 1 MFSC 1A 2A 1B 2B 1C 2C 3D 4D 3E 4E 3F 4F
Pixel 2 5A 1A 2A 1B 2B 1C 2C 3D 4D 3E 4E 3F 4F
Pixel 3 5B 1A 2A 1B 2B 1C 2C 3D 4D 3E 4E 3F 4F
Pixel 4 MFSC 1A 2A 1B 2B 1C 2C 3D 4D 3E 4E 3F 4F
Pixel 5 5A 1A 2A 1B 2B 1C 2C 3D 4D 3E 4E 3F 4F
Pixel 6 5B 1A 2A 1B 2B 1C 2C 3D 4D 3E 4E 3F 4F

Note. Sensors within a Band are Designated A to F

Figure 106. MSS Multiplexed Data Format, 150-word Minor Frame.

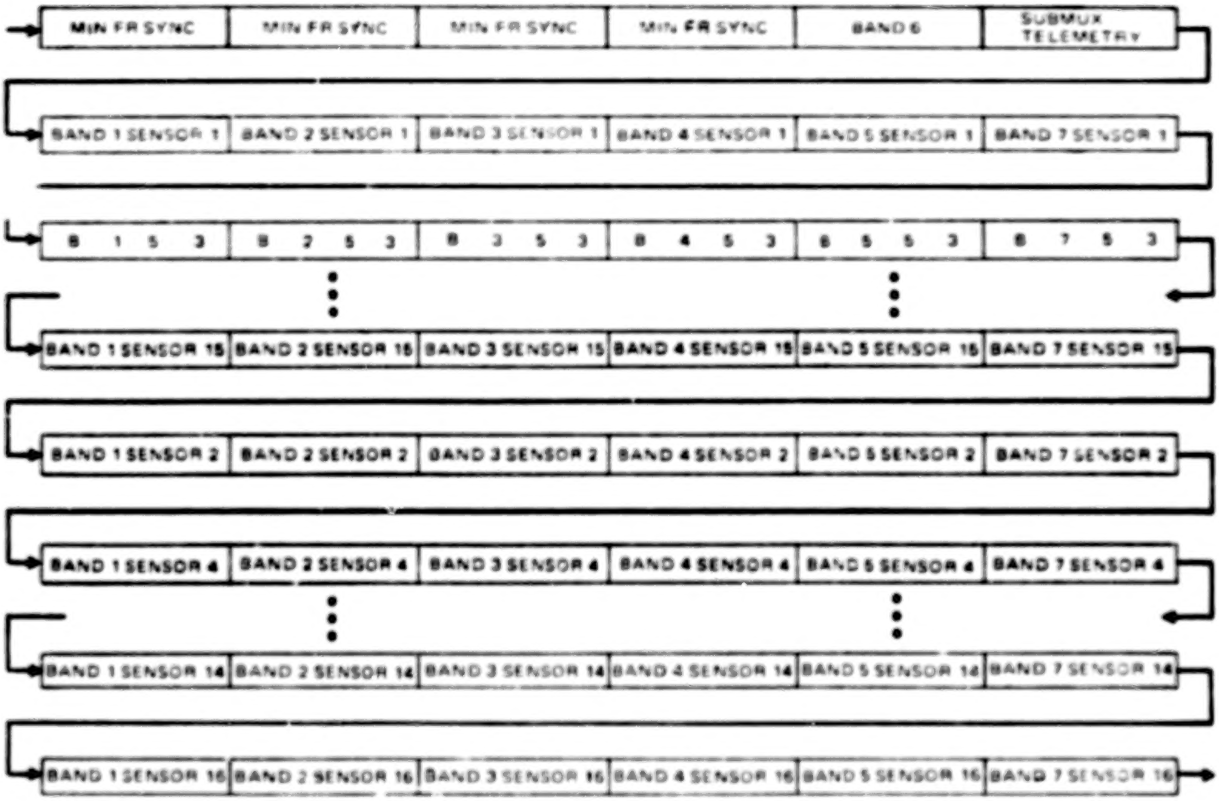
MIN FR SYNC
MIN FR SYNC
MIN FR SYNC
MIN FR SYNC
BAND 6
SUBMUX TELEMETRY
BAND 1 SENSOR 1
BAND 2 SENSOR 1
BAND 3 SENSOR 1
BAND 4 SENSOR 1
BAND 5 SENSOR 1
BAND 7 SENSOR 1
B 1 S 3
B 2 S 3
B 3 S 3
B 4 S 3
B 5 S 3
B 7 S 3
BAND 1 SENSOR 15
BAND 2 SENSOR 15
BAND 3 SENSOR 15
BAND 4 SENSOR 15
BAND 5 SENSOR 15
BAND 7 SENSOR 15
BAND 1 SENSOR 2
BAND 2 SENSOR 2
BAND 3 SENSOR 2
BAND 4 SENSOR 2
BAND 5 SENSOR 2
BAND 7 SENSOR 2
BAND 1 SENSOR 4
BAND 2 SENSOR 4
BAND 3 SENSOR 4
BAND 4 SENSOR 4
BAND 5 SENSOR 4
BAND 7 SENSOR 4
BAND 1 SENSOR 14
BAND 2 SENSOR 14
BAND 3 SENSOR 14
BAND 4 SENSOR 14
BAND 5 SENSOR 14
BAND 7 SENSOR 14
BAND 1 SENSOR 16
BAND 2 SENSOR 16
BAND 3 SENSOR 16
BAND 4 SENSOR 16
BAND 5 SENSOR 16
BAND 7 SENSOR 16

Figure 107. Thematic Mapper Multiplexed Data Format - 102-Word Minor Frame.

The data format of the TM consists of a 102-word minor frame encompassing a single sample (pixel) of each of the channels in bands 1, 2, 3, 4, 5, and 7, each having 16 detectors, and a single sample of one of the band 6 (IR) channels. A single word of Flight Segment Telemetry, including all TM telemetry, is transmitted each minor frame along with four minor frame sync words.

The data flow format emanating from a sensor is therefore dependent on the multiplexer configuration and the sampling strategy. Achieving spatial registration of pixels depends on the light pipe array configuration and the sampling strategy.

A.6 ON-BOARD DATA REFORMATTING

Generally, this resultant data format is the outcome of design trade-offs for the sensor only and do not consider functional requirements downstream from the sensor. For example, radiometric correction is accomplished on a line-by-line basis, thus a band interleaved by line (BIL) format would be best. Often, the final product is a film recording which requires that the data be spectrally separated or in a band sequential (BSQ) format. Classification, however, is accomplished on a vector consisting of spatially registered pixels from all bands or in a band interleaved by pixel (BIP) format.

Scanning sensors, such as the TM and MSS sensors, by their very nature generate information in a BIP format or a pixel at a time from all bands. However, this sensor-produced BIP format is not the proper format for classification. Consider the functional data flow of Figure 108 for MSS data. Here the MSS sensor data is BIP to BIL reformatted, radiometrically corrected, reformatted BIL to BIP, spatially registered, and classified.

Figure 109 indicates the data format as sampled from the MSS. There are 24 samples plus sync from the first block of data. This represents the four visible bands for six lines. The second block of data contains 24 samples

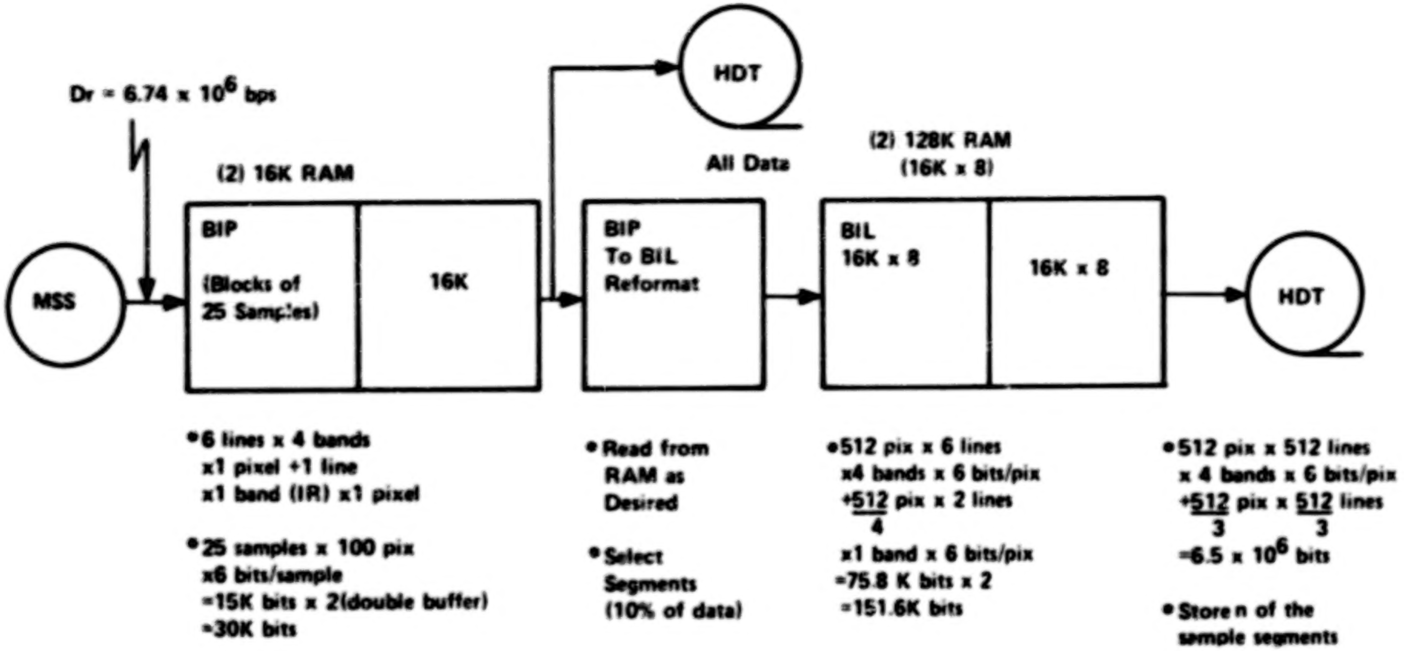
Dr = 6.74 x 10^6 bps
MSS
(2) 16K RAM
BIP
(Blocks of
25 Samples)
16K
HDT
All Data
BIP
To BIL
Reformat
(2) 128K RAM
(16K x 8)
BIL
16K x 8
16K x 8
HDT
•6 lines x 4 bands
x1 pixel +1 line
x1 band (IR) x1 pixel
•25 samples x 100 pix
x6 bits/sample
=15K bits x 2(double buffer)
=30K bits
•Read from
RAM as
Desired
•Select
Segments
(10% of data)
•512 pix x 6 lines
x4 bands x 6 bits/pix
+512/4 pix x 2 lines
x1 band x 6 bits/pix
=75.8 K bits x 2
=151.6K bits
•512 pix x 512 lines
x 4 bands x 6 bits/pix
+512/3 pix x 512/3 lines
=6.5 x 10^6 bits
•Store n of the
sample segments

Figure 108. MSS Data Flow (Sheet 1 of 2).

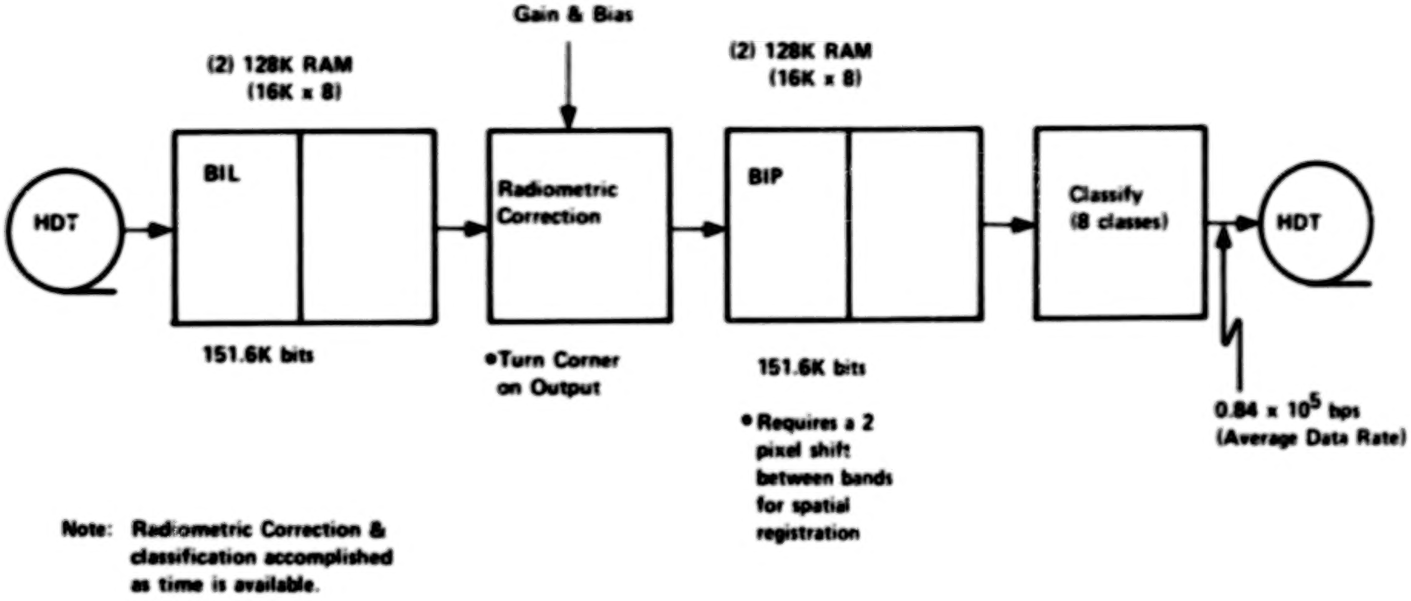
Gain & Bias
(2) 128K RAM (16K x 8)
(2) 128K RAM (16K x 8)
HDT
BIL
Radiometric Correction
BIP
Classify (8 classes)
HDT
151.6K bits
•Turn Corner on Output
151.6K bits
•Requires a 2 pixel shift between bands for spatial registration
0.84 x 10⁵ bps (Average Data Rate)
Note: Radiometric Correction & classification accomplished as time is available.

Figure 108. MSS Data Flow (Sheet 2 of 2).

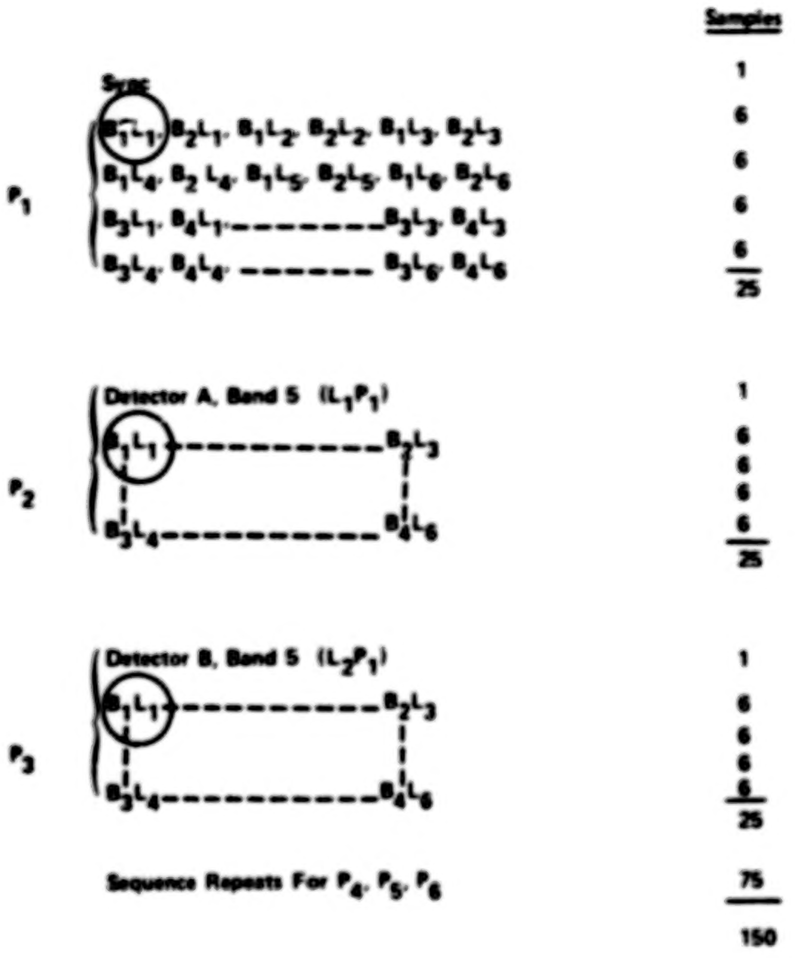
Samples
Sync
P1
B1L1, B2L1, B1L2, B2L2, B1L3, B2L3
B1L4, B2 L4, B1L5, B2L5, B1L6, B2L6
B3L1, B4L1 -------- B3L3, B4L3
B3L4, B4L4 ------- B3L6, B4L6
1
6
6
6
6
25
P2
Detector A, Band 5 (L1P1)
B1L1 ----------- B2L3
B3L4 ------------ B4L6
1
6
6
6
6
25
P3
Detector B, Band 5 (L2P1)
B1L1 ----------- B2L3
B3L4 ------------ B4L6
1
6
6
6
6
25
Sequence Repeats For P4, P5, P6
75
150

Figure 109. MSS Sensor Output Format.

plus detector A of the IR band (band 5). Detector A of band 5 is sampled every 75 samples. The third block of data will contain a sample from detector B of band 5 with detector B being sampled every 75 samples. The circled samples illustrate how the data is accessed in going from the BIP to the BIL format.

As shown in Figure 108 all sensor data is stored on tape with selected 512 x 512 segments reformatted BIP to BIL and stored on a second tape. The BIL output is shown in Figure 110. The six line sweeps of 512 pixels per sweep are stored on tape to queue the sample segment of 512 lines. The BIL data is read from tape and radiometrically corrected six lines at a time.

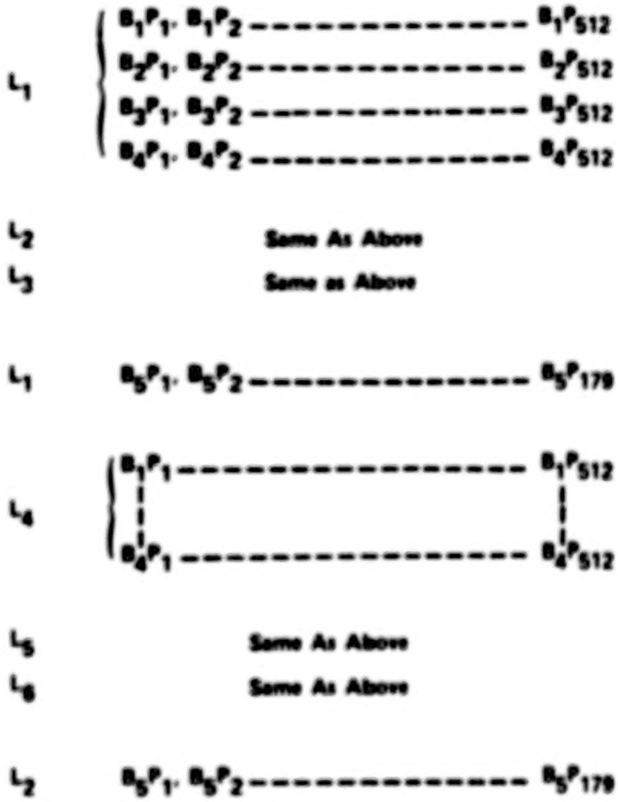
L1
B1P1, B1P2 ---- B1P512
B2P1, B2P2 ---- B2P512
B3P1, B3P2 ---- B3P512
B4P1, B4P2 ---- B4P512
L2
Same As Above
L3
Same as Above
L1
B5P1, B5P2 ---- B5P179
L4
B1P1 ---- B1P512
B4P1 ---- B4P512
L5
Same As Above
L6
Same As Above
L2
B5P1, B5P2 ---- B5P179

Figure 110. MSS BIL Reformatted Output.

Radiometric correction applies the same gain and bias to each pixel of a line. The gain and bias terms are different for each line. Spatial registration of the data is achieved by shifting each pixel to the proper storage location following radiometric correction. The data is then read from storage, classified, and output to tape for latter transmission to ground. The BIP input to classification is shown in Figure 111.

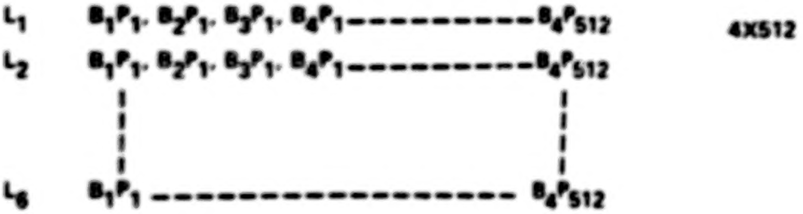

L_1
$B_1P_1, B_2P_1, B_3P_1, B_4P_1$
B_4P_{512}
4X512
L_2
$B_1P_1, B_2P_1, B_3P_1, B_4P_1$
B_4P_{512}
L_6
B_1P_1
B_4P_{512}

Figure 111. MSS BIP Input to Classification.

Note that this approach assumes the gain and bias for radiometric correction has been computed and is available. If the radiometric calibration coefficients have to be computed on-board, additional storage must be provided while the calibration data is being processed.

How might the data be handled given the radiometric correction function was accomplished within the sensor? Figure 112 illustrates this process. The data would be input to buffer the same as before. In this case, however, it is not necessary to reformat the data to BIL but to go directly to BIP format compatible with classification. Figure 113 illustrates how the data would be accessed for classification. The different pixels are accessed to account for the spatial registration between bands. Band 1 is offset from band 2 by two pixels, from band 3 by four pixels, and from band 4 by six pixels.

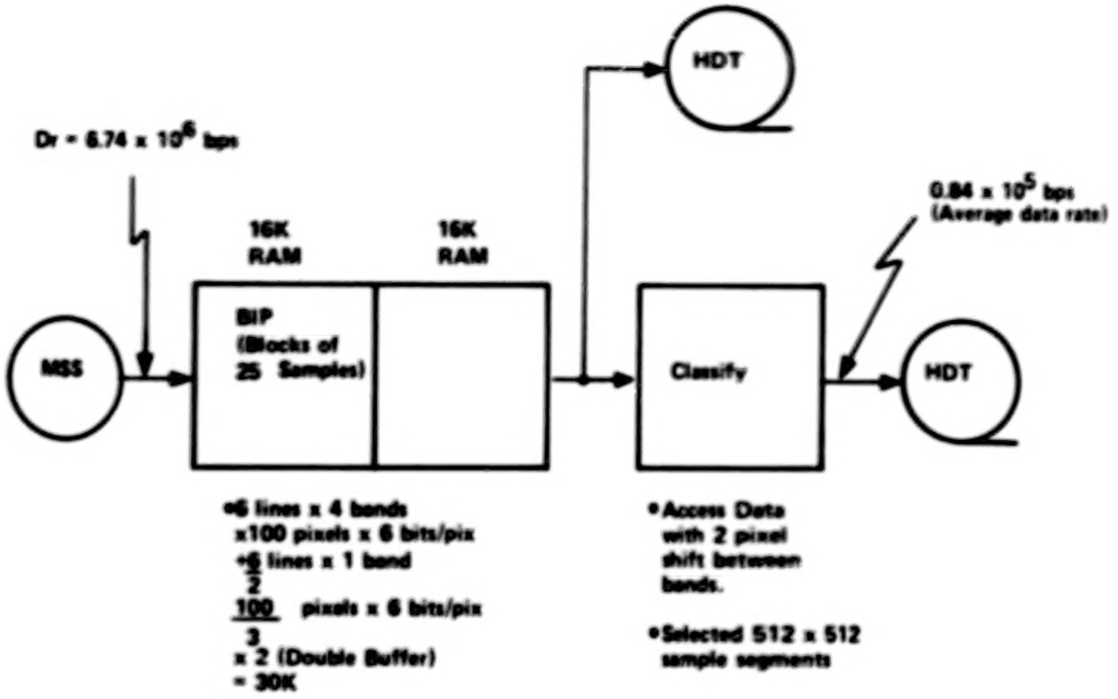
Dr = 6.74 x 10^6 bps
16K RAM
16K RAM
BIP (Blocks of 25 Samples)
MSS
HDT
Classify
HDT
0.84 x 10^5 bps (Average data rate)
•6 lines x 4 bands x100 pixels x 6 bits/pix
+6/2 lines x 1 band
100/3 pixels x 6 bits/pix
x 2 (Double Buffer)
= 30K
•Access Data with 2 pixel shift between bands.
•Selected 512 x 512 sample segments

Figure 112. MSS Data Flow for Sensor Radiometrically Corrected Data.

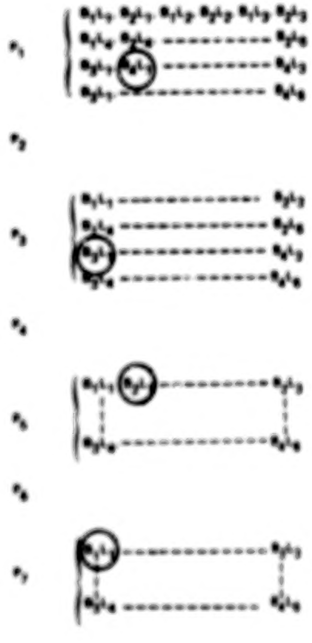

Figure 113. MSS Sensor Output Format.

Note that the total amount of RAM has been greatly reduced plus the intermediate tape drive has been eliminated.

Figure 114 illustrates the data functional flow for the TM sensor. Here there are 97 samples plus four synchronization and one telemetry sample from a block of data. This represents the six visible bands for 16 lines plus one IR sample for one line. Note that compared with the MSS the input data rate for the TM is an order of magnitude larger ($\approx 7.3 \times 10^6$ compared to 6.74×10^6 bps) and the BIL storage more than five times as large (795K bits compared to 152K bits). This shows that the data must be processed faster with larger amounts of on-board storage required. As future sensors are developed having even greater numbers of detectors, these data rates and storage requirements will get even larger.

If, however, sensors can be designed to output radiometrically corrected data, the on-board data storage requirements would be reduced and therefore the cost and complexity as well.

BLANK PAGE

BLANK PAGE

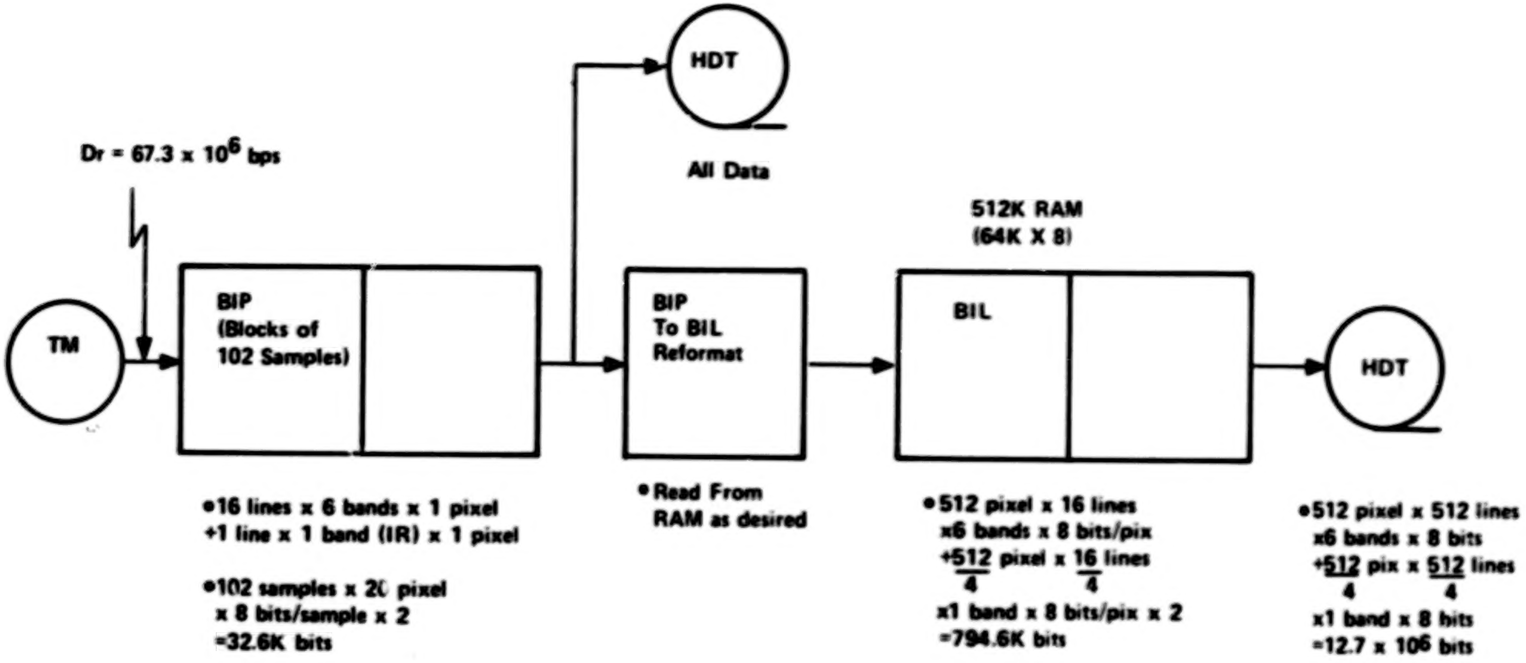
Dr = 67.3 x 10^6 bps
TM
BIP
(Blocks of
102 Samples)
HDT
All Data
BIP
To BIL
Reformat
512K RAM
(64K X 8)
BIL
HDT
•16 lines x 6 bands x 1 pixel
+1 line x 1 band (IR) x 1 pixel
•102 samples x 20 pixel
x 8 bits/sample x 2
=32.6K bits
•Read From
RAM as desired
•512 pixel x 16 lines
x6 bands x 8 bits/pix
+512/4 pixel x 16/4 lines
x1 band x 8 bits/pix x 2
=794.6K bits
•512 pixel x 512 lines
x6 bands x 8 bits
+512/4 pix x 512/4 lines
x1 band x 8 bits
=12.7 x 10^6 bits

Figure 114. TM Data Flow (Sheet 1 of 2).

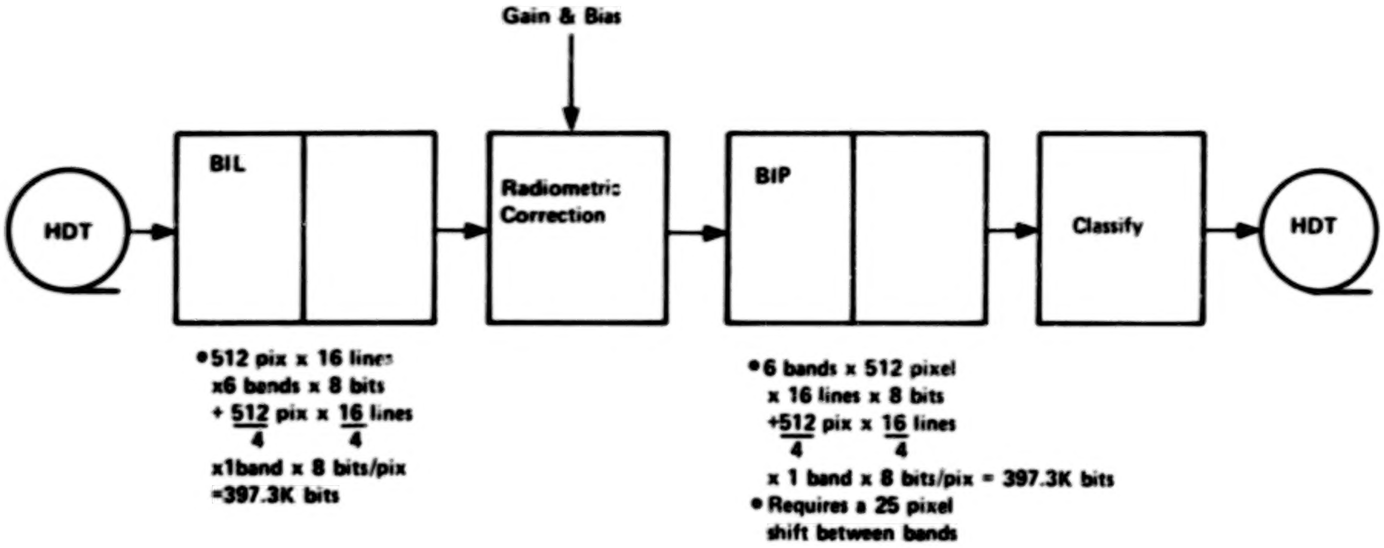
Gain & Bias
HDT
BIL
Radiometric Correction
BIP
Classify
HDT
•512 pix x 16 lines x6 bands x 8 bits + 512/4 pix x 16/4 lines x1band x 8 bits/pix =397.3K bits
•6 bands x 512 pixel x 16 lines x 8 bits +512/4 pix x 16/4 lines x 1 band x 8 bits/pix = 397.3K bits
• Requires a 25 pixel shift between bands

Figure 114. TM Data Flow (Sheet 2 of 2).

Appendix B
ERROR ANALYSIS

B.1 INTRODUCTION

This error analysis relates the expected geometric position accuracy to the following error sources.

a. Attitude

b. Ephemeris

c. Alignment

d. Mirror scan nonlinearities

e. Timing

f. Internal sensor.

The assumption that error effects are linear functions of error sources has been made, along with the further assumption that the effect of rate errors is the average integrated effect over the period of time it takes to sense a scene. Error sources of a given type (for example, attitude) are assumed to be normally distributed and possibly correlated; it is assumed that there is no correlation among errors of different types (for example, attitude and ephemeris).

Since the error sources are normally distributed with zero mean, the geometric position errors will also be normally distributed around the true position. The conventional characterization of these errors is the error ellipse (the curve of constant probability) which contains a certain amount of the total probability. In the present error analysis, the covariance matrix of the geometric position errors are diagonalized. The square roots of the eigenvalues are then the principal semi-axes of a standard error ellipse, and the eigenvectors (which of necessity are orthogonal) are in the directions of these axes. Error ellipses for any desired level of probability P can by found by multiplying the lengths of the principal axes by the quantity k given by $P = 1 - e^{-k^2}/2$. In particular,

k	P
1	0.40
2	0.86
3	0.99

P	k
0.90	2.15
0.95	2.45
0.999	3.72

B.2 ERROR TRANSFORMATIONS

This section relates, in matrix form, the ΔX and ΔY position errors to each of the major error sources. ΔX and ΔY are the geometric position errors along track and along scan as shown in equation (32).

Attitude

$$\begin{bmatrix}\Delta X\\ \Delta Y\end{bmatrix} = \begin{bmatrix} 0 & H & -Y \\ \frac{H^2+Y^2}{H} & 0 & 0\end{bmatrix}\begin{bmatrix}\phi\\ \theta\\ \psi\end{bmatrix} \qquad (32)$$

where H is the nominal altitude, and ϕ, θ, ψ are the roll, pitch, and yaw errors.

Ephemeris

$$\begin{bmatrix} \Delta X \\ \Delta Y \end{bmatrix} = \begin{bmatrix} 1 & 0 & 0 \\ 0 & 1 & -\frac{Y}{H} \end{bmatrix} \begin{bmatrix} AT \\ CT \\ \Delta H \end{bmatrix} \tag{33}$$

where AT, CT, and ΔH are the along-track, cross-track and altitude (radial) errors as shown in equation (33).

Mirror Scan

$$\begin{bmatrix} \Delta H \\ \Delta Y \end{bmatrix} = \begin{bmatrix} 0 \\ \frac{H^2+Y^2}{H} \end{bmatrix} \Delta\alpha \tag{34}$$

where $\Delta\alpha$ is the departure from linearity (as an angle) of the mirror scan, as shown in equation (34).

Timing

$$\begin{bmatrix} \Delta X \\ \Delta Y \end{bmatrix} = \begin{bmatrix} V \\ 0 \end{bmatrix} \Delta T \tag{35}$$

where ΔT is the timing error as shown in equation (35).

The total error is then as shown in equation (36).

$$\begin{pmatrix}\Delta X\\ \Delta Y\end{pmatrix}=\begin{pmatrix}0 & H & -Y\\ \frac{H^2+Y^2}{H} & 0 & 0\end{pmatrix}\left\{\begin{pmatrix}\phi\\ \theta\\ \psi\end{pmatrix}+\begin{pmatrix}\widehat{\dot{\phi}}\\ \widehat{\dot{\theta}}\\ \widehat{\dot{\psi}}\end{pmatrix}\right\}+$$

$$+\begin{pmatrix}1 & 0 & 0\\ 0 & 1 & -\frac{Y}{H}\end{pmatrix}\left\{\begin{pmatrix}AT\\ CT\\ \Delta H\end{pmatrix}+\begin{pmatrix}\widehat{\dot{AT}}\\ \widehat{\dot{CT}}\\ \widehat{\dot{\Delta H}}\end{pmatrix}\right\}+$$

$$+\begin{pmatrix}0\\ \frac{H^2+Y^2}{H}\end{pmatrix}\Delta\alpha+\begin{pmatrix}V\\ 0\end{pmatrix}\Delta T \qquad (36)$$

where the symbol $\widehat{\dot{}}$ denotes the average integrated effect of the corresponding rate error.

Denote the four matrices of equation 33 by A_1, A_2, A_3, and A_4, respectively, (in their order in the equation). Then the covariance matrix of the geometric position errors is given by equation (37).

$$\begin{pmatrix}\sigma_{\Delta X}^2 & \sigma_{\Delta X\Delta Y}\\ \sigma_{\Delta Y\Delta X} & \sigma_{\Delta Y}^2\end{pmatrix}=A_1[\mathrm{Cov(altitude)}+\mathrm{Cov\ (altitude\ rate)}]A_1^T+$$

$$+A_2[\mathrm{Cov\ (ephemeris)}+\mathrm{Cov(ephemeris\ rate)}]A_2^T+$$

$$+A_3\ \mathrm{var(mirror)}A_3^T+A_4\ \mathrm{var(time)}A_4^T, \qquad (37)$$

where cov(•) denotes covariance matrix and var (•) denotes variance of the scalar quantity. The covariance matrices have the form of equation (38).

$$\begin{pmatrix} \sigma_{11} & \rho_{12}\sqrt{\sigma_{11}\sigma_{22}} & \rho_{13}\sqrt{\sigma_{11}\sigma_{33}} \\ \rho_{21}\sqrt{\sigma_{22}\sigma_{11}} & \sigma_{22} & \rho_{23}\sqrt{\sigma_{22}\sigma_{33}} \\ \rho_{31}\sqrt{\sigma_{33}\sigma_{11}} & \rho_{32}\sqrt{\sigma_{33}\sigma_{22}} & \rho_{33} \end{pmatrix} \tag{38}$$

with $\rho_{ij} = \rho_{ji}$. In the case of uncorrelated errors, of course, $\rho_{ij} = 0$.

B.3 APL ERROR SIMULATION

An APL simulation called PROG1 was written to compute and display the principal axes of the error ellipses as given by the formulas of subsection B.2. The simulation, for which a listing is provided, computes the error ellipses at an equally spaced 5 x 5 grid of error grid points (shown in Figure 115). The components of the error grid points (shown in Table 28) are the X and Y coordinates (in meters) of the grid which covers 90 percent of a 185 Km x 185 Km square, the nominal size of a Landsat scene. The user enters values of the error parameters, namely, mirror scan error (in radians), timing error (in seconds), spacecraft velocity error (in meters/sec), roll, pitch, and yaw errors (in degrees) and their corresponding rate errors, and ephemeris errors (in meters) and their corresponding rate errors. The function prints out 1.645 x the square root of the eigenvalues and the eigenvectors for each of the 25 grid points in the same pattern as the grid. The factor 1.645 is the 90 percent point of a one-dimensional normal distribution and was used instead of the k value 2.15 in the simulation PROG1 to conform with NASA usage, which specifies permissible geometric errors in the X (along track) and Y (along scan) directions independently. Nominal values for altitude H and spacecraft velocity V were taken to be 705, 300 meters, and 7500 meters/sec., respectively, the design values for Landsat-D. Values of the error parameters were varied from design values to determine the geometric accuracy achievable without GCPs. It should

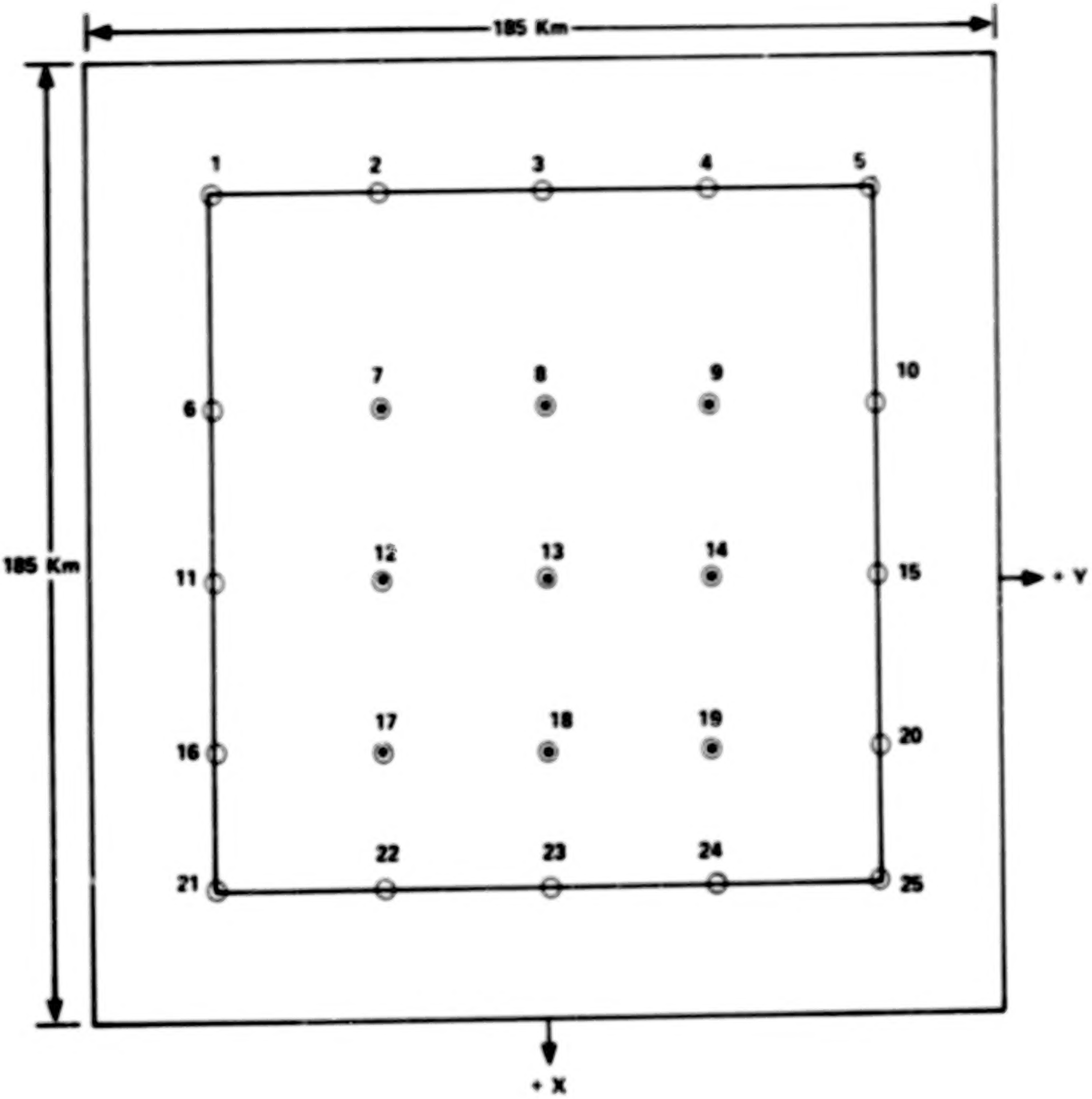
185 Km
185 Km
1
2
3
4
5
6
7
8
9
10
11
12
13
14
15
16
17
18
19
20
21
22
23
24
25
+ Y
+ X

Figure 115. Error Grid Points.

Table 28. Coordinates of Error Grid Points.

PT NO	X	Y
	METERS	
1	-87884	-87884
2	-87884	-43942
3	-87884	0
4	-87884	43942
5	-87884	87884
6	-43942	-87884
7	-43942	-43942
8	-43942	0
9	-43942	43942
10	-43942	87884
11	0	-87884
12	0	-43942
13	0	0
14	0	43942
15	0	87884
16	43942	-87884
17	43942	-43942
18	43942	0
19	43942	43942
20	43942	87884
21	87884	-87884
22	87884	-43942
23	87884	0
24	87884	43942
25	87884	87884

be noted that, while the magnitudes of the principal error sources can be inferred from (1) measurements of existing sensors, (2) design values for sensors under development, or (3) desired geometric accuracy, the magnitude of the correlation coefficients are difficult to measure and are usually not specified as design parameters. Therefore, in view of the lack of either design or emperical values for the correlation coefficients, they were set equal to zero in the sums discussed in subsection B.4. However, to get an idea of the effect of correlation on geometric accuracy, a series of sums was made using the error source values of Sums 1, 2, and 3 (see Table 3G) and attitude and ephemeris correlation coefficients $\rho_{ij} = 0.3$ and another series using the error source values of Run 3 and ρ_{ij} ranging from 0.5 to 0.9. In general, correlation had little effect on the magnitude of the principal semiaxes of the error ellipses. The ellipses exhibited very little rotation at the edges of the error grid, but showed rotation approaching 45° near the center of the grid. But the principal semiaxes in all cases are nearly equal, so the rotation has no significant effect on the estimates of attainable geometric accuracy reported in subsection B.4.

If meaningful values of the correlation coefficients become available in the future, additional runs with PROG1 can be made to determine their effect on geometric accuracy.

B.4 SUMMARY OF RESULTS

A series of runs was made with PROG 1, after a set of initial runs whose purpose it was to validate the simulation. In the initial runs, one error source at a time was given a nonzero value and the resulting geometric position errors compared with analytical results of previous studies made for Landsats -1, -2, and -3. The subsequent runs are summarized in Table 29, which shows the maximum error in the X and Y directions over the error grid. The results cited can be interpreted to be the geometric error in the X and Y directions that 90 percent of the pixels in a given Landsat scene (185 x 185 Km) would have.

The various runs differed in the values assigned to the various error sources. These values are summarized in Table 30, which in conjunction with Table 29, gives a concise summary of the results of the simulation. Note that the results of Table 29 are given in terms of equivalent Landsat-D TM pixels, which are approximately 30m on a side.

Run 1 uses the original nominal design parameters for Landsat-D. Subsequent to conversations with NASA personnel indicated that, because of residual alignment errors, the actual attitude error might be larger than the 0 .01° target value, and Run 2 includes an alignment error as part of the attitude errors. This run shows that unless the alignment errors are removed or compensated for, the geometric accuracy would be unacceptable. Run 3 uses the improved ephemeris accuracy which will be achievable when GPS (Global Position System) is operational. A series of runs, 4a through 4f, were made to determine what attitude error would be permissible in the absence of all other error sources in order to achieve a one-pixel geometric accuracy. That value 0 .00148°, was used in Run 5 with design values for the S/C error sources and GPS ephemeris accuracy. That run showed that one pixel in the Y direction (along scan) is almost attainable without GCPs, but that the accuracy in the X direction (along track) is only five pixels, due to the effect of S/C velocity errors.

Table 29. Maximum Error Over 90 Percent Grid.

Run No	ΔX		ΔY	
	Max Value (m)	Equiv. Pixels	Max Value (m)	Equiv. Pixels
1	256.67	8.56	208.36	6.95
2	1619.59	54.00	1624.91	54.16
3	250.93	8.36	206.64	6.89
4a	20.41	0.68	20.56	0.69
4c	28.57	0.95	28.79	0.96
4f	30.20	1.01	30.43	1.01
5	149.11	4.97	36.60	1.22

CONTENTS

Section Page

1 SUMMARY 1 1/B4

2 INTRODUCTION 2 1/B5

2.1 Background 2 1/B5

2.2 Scope 8 1/B11

3 DIGITAL IMAGE PROCESSING OF EARTH OBSERVATION SENSOR DATA 10 1/B13

3.1 General Overview 10 1/B13

3.2 MSS and TM Functional Description 11 1/B14

3.2.1 Data Reformatting 15 1/C4

3.2.2 Radiometric Calibration 23 1/C12

3.2.3 Radiometric Correction 42 1/E3

3.2.4 Geometric Correction/Temporal Registration 43 1/E4

3.2.5 Resampling for Scanner Sensors 88 2/A12

3.3 Return Beam Vidicon (RBV) 99 2/B11

3.3.1 RBV Functional Overview 100 2/B12

3.3.2 Radiometric Calibration and Correction 104 2/C3

3.3.3 Geometric Correction 110 2/C9

3.3.4 Resampling for RBV 119 2/D4

3.4 Heat Capacity Mapper Mission (HCMM) 120 2/D5

3.4.1 Heat Capacity Mapper (HCM) Functional Description 121 2/D6

3.4.2 HCM Phase I Processing 123 2/D8

3.4.3 Radiometric Calibration Processing. . . 124 2/D9

3.4.4 Radiometric Correction 128 2/D13

3.4.5 Geometric Correction 133 2/E4

Section Page

3.4.6 Resampling for HCM 140 **2/E11**

3.5 Analysis of Geometric Correction/Temporal Registration Errors 141 **2/E12**

3.5.1 Landsat-D TM and MSS Error Analysis . . 143 **2/E14**

3.5.2 Input and Internal Errors 145 **2/F3**

3.6 Classification 158 **2/G5**

3.6.1 Introduction 158 **2/G5**

3.6.2 LACIE Overview 163 **2/G10**

3.6.3 Classification Approaches 167 **3/A3**

3.6.4 Baseline Classification Process 171 **3/A7**

3.6.5 On-Board Classification Configuration Analysis 176 **3/A13**

4 CONCLUSIONS AND RECOMMENDATIONS 209 **3/E2**

Appendix A TM AND MSS DATA REFORMATTING STUDY 213 **3/E6**

Appendix B ERROR ANALYSIS 233 **3/G5**

Appendix C EFFECT OF DATA STRIPING ON CLASSIFICATION ACCURACY 249 **4/A10**

Appendix D EFFECT OF LANDSAT ORBITAL CHARACTERISTICS ON ON-BOARD CLASSIFICATION 278 **4/E1**

Table 30. Error Source Values for the Simulation.

Run No.	ERROR SOURCE									
	Mirror Scan (rad)	Timing (sec)	S/C Velocity (m/sec)	ρ_{ij}	Attitude (degree)			Ephemeris (m)		
					Roll	Pitch	Yaw	Along Track	Cross Track	Radial
1	$1\text{x}10^{-5}$	$1\text{x}10^{-3}$	7.5	0	0.01	0.01	0.01	34.3	19	16.1
2	$1\text{x}10^{-5}$	$1\text{x}10^{-3}$	7.5	0	0.079	0.079	0.079	34.3	19	16.1
3	$1\text{x}10^{-5}$	$1\text{x}10^{-3}$	7.5	0	0.01	0.01	0.01	10	10	10
4a	0	0	0	0	0.001	0.001	0.001	0	0	0
4c	0	0	0	0	0.0014	0.0014	0.0014	0	0	0
4f	0	0	0	0	0.00148	0.00148	0.00148	0	0	0
5	$1\text{x}10^{-5}$	$1\text{x}10^{-3}$	7.5	0	0.00148	0.00148	0.00148	10	10	10

The listing from Run 5 is appended as Exhibit 1 to give the detailed results and to show the arrangement of the computer printout. The listing of the APL program is also appended as Exhibit 2.

```
      PROG1

ENTER MIRROR SCAN ERROR (IN RADIANS):
⎕:
      1E¯5

ENTER TIMING ERROR (IN SECONDS):
⎕:
      1E¯3

ENTER SPACECRAFT VELOCITY ERROR (IN METERS/SEC)
⎕:
      7.5

ARE THE RHOS ASSOCIATED WITH ATTITUDE ERROR ZERO? (YES OR NO)
YES

ENTER THE FOLLOWING AS ASSOCIATED WITH ATTITUDE ERROR (IN DEGREES)
      ROLL        PITCH       YAW
⎕:
      .00148      .00148      .00148

ARE THE RHOS ASSOCIATED WITH EPHEMERIS ERROR ZERO? (YES OR NO)
YES

ENTER THE FOLLOWING AS ASSOCIATED WITH EPHEMERIS ERROR (IN METERS)
      ALONG-TRACK   CROSS-TRACK   RADIAL
⎕:
         10             10            10

ARE ATTITUDE RATE ERRORS ZERO? (YES OR NO)
YES

ARE EPHEMERIS RATE ERRORS ZERO? (YES OR NO)
YES

 FINAL ERROR MATRIX AFTER MULTIPLICATION BY 1.645:

          Y      ¯87884              ¯43942               0                  43942                87884

      X


¯87884      149.11    36.60     149.08    36.23     149.07    36.10     149.08    36.23     149.11    36.60
              1.00      .00       1.00      .00       1.00      .00       1.00      .00       1.00      .00
               .00     1.00        .00     1.00        .00     1.00        .00     1.00        .00     1.00


¯43942       80.99    36.60      80.97    36.23      80.93    36.10      80.93    36.23      80.99    36.60
              1.00      .00       1.00      .00       1.00      .00       1.00      .00       1.00      .00
               .00     1.00        .00     1.00        .00     1.00        .00     1.00        .00     1.00


     0       36.54    36.60      36.30    36.23      36.25    36.10      36.30    36.23      36.54    36.60
              1.00      .00       1.00      .00       1.00      .00       1.00      .00       1.00      .00
               .00     1.00        .00     1.00        .00     1.00        .00     1.00        .00     1.00


 43942       80.99    36.60      80.93    36.23      80.93    36.10      80.93    36.23      80.99    36.60
              1.00      .00       1.00      .00       1.00      .00       1.00      .00       1.00      .00
               .00     1.00        .00     1.00        .00     1.00        .00     1.00        .00     1.00


 87884      149.11    36.60     149.08    36.23     149.07    36.10     149.08    36.23     149.11    36.60
              1.00      .00       1.00      .00       1.00      .00       1.00      .00       1.00      .00
               .00     1.00        .00     1.00        .00     1.00        .00     1.00        .00     1.00


      )SAVE ERRAS
  14.58.44 06/27/78
      )OFF
050  14.58.49 06/27/78 CTJ
CONNECTED     0.05.03  TO DATE     0.33.00
CPU TIME      0.00.01  TO DATE     0.00.05
```

MICROFILMED FROM
BEST AVAILABLE COPY

Exhibit 1

```
     ∇ PROG1
[1]   ⍝  PROGRAMMER:  CL JONES
[2]    I← 1 2 3
[3]    I← 1 2
[4]    GRID← 15 10 ρ0
[5]    F←¯47444
[6]    A←¯87884
[7]    '     '
[8]    '     '
[9]    H←705300
[10]   V←7500
[11] SAMEY:'ENTER MIRROR SCAN ERROR (IN RADIANS):'
[12]   VARMIR←⎕
[13]   VARMIR←VARMIR*2
[14]   '     '
[15]   'ENTER TIMING ERROR (IN SECONDS):'
[16]   VARTIME←⎕
[17]   VARTIME←VARTIME*2
[18]   '     '
[19]   'ENTER SPACECRAFT VELOCITY ERROR (IN METERS/SEC)'
[20]   VARVEL←⎕
[21]   VARVEL←VARVEL*2
[22]   '      '
[23]   E←'ENTER THE FOLLOWING AS ASSOCIATED WITH '
[24]   F←'ATTITUDE ERROR'
[25]   G←'EPHEMERIS ERROR (IN METERS)'
[26]   J←'ATTITUDE RATE ERROR'
[27]   K←'EPHEMERIS RATE ERROR'
[28]   L←'       ROLL    PITCH  YAW  RHO12  RHO13  RHO23 '
[29]   M←'      ALONG-TRACK   CROSS-TRACK   RADIAL   RHO12   RHO13   RHO23'
[30]   N←' (IN DEGREES)'
[31]   'ARE THE RHOS ASSOCIATED WITH ATTITUDE ERROR ZERO? (YES OR NO)'
[32]   REPLY←⍞
[33]   '   '
[34]   →RHOA×⍳(ρREPLY)=3
[35]   '  '
[36]   E,F,N
[37]   L
[38]   S1←⎕
[39]   RAD←(○1)÷180
[40]   S1←(S1×RAD)
[41]   '     '
[42] CONT1:'ARE THE RHOS ASSOCIATED WITH EPHEMERIS ERROR ZERO? (YES OR NO)'
[43]   REPLY←⍞
[44]   '   '
[45]   →RHOE×⍳(ρREPLY)=3
[46]   '    '
[47]   E,G
[48]   M
[49]   S3←⎕
[50]   '   '
[51] CONT2:'ARE ATTITUDE RATE ERRORS ZERO? (YES OR NO)'
[52]   REPLY←⍞
[53]   →ARE×⍳(ρREPLY)=3
[54]   '    '
[55]   E,J,N
```

Exhibit 2 (Page 1 of 3)

```
[56]  L
[57]  S2←⎕
[58]  '     '
[59] CONT3:'ARE EPHEMERIS RATE ERRORS ZERO? (YES OR NO)'
[60]  REPLY←⍞
[61]  →ERE×⍳(⍴REPLY)=3
[62]  '     '
[63]  E,K
[64]  M
[65]  S4←⎕
[66]  '     '
[67]  →CONT4
[68] RHOA:E,F,N
[69]  '        ROLL         PITCH       YAW'
[70]  S1←⎕,0,0,0
[71]  RAD←(○1)÷180
[72]  S1←S1×RAD
[73]  '     '
[74]  →CONT1
[75] RHOE:E,G
[76]  '        ALONG-TRACK   CROSS-TRACK   RADIAL'
[77]  S3←⎕,0,0,0
[78]  '     '
[79]  →CONT2
[80] ARE:S2← 0 0 0 0 0 0
[81]  '     '
[82]  →CONT3
[83] ERE:S4← 0 0 0 0 0 0
[84]  '     '
[85] CONT4:C2A←COV S3
[86]  C2B←COV S4
[87]  C2←C2A+C2B
[88]  C1A←COV S1
[89]  C1B←COV S2
[90]  C1←C1A+C1B
[91] LOOP:SUBTERM1←((H⋆2)+Y⋆2)÷H
[92]  TERM1←-SUBTERM1
[93]  SUBTERM2←Y÷H
[94]  TERM2←-SUBTERM2
[95]  TERM3←X÷V
[96]  Y1←-Y
[97]  A1← 2 3 ⍴0,H,Y1,TERM1,0,0
[98]  A2← 2 3 ⍴1,0,0,0,1,TERM2
[99]  A3← 2 1 ⍴0,SUBTERM1
[100] A4← 2 1 ⍴V,0
[101] A5← 2 1 ⍴TERM3,0
[102] COVGP5←(A5+.×⍉A5)×VARVEL
[103] COVGP4←(A4+.×⍉A4)×VARTIME
[104] COVGP3←(A3+.×⍉A3)×VARMIR
[105] COVGP2←A2+.×C2+.×⍉A2
[106] COVGP1←A1+.×C1+.×⍉A1
[107] COVGP←COVGP1+COVGP2+COVGP3+COVGP4+COVGP5
[108] QCOVGP←1 QLI COVGP
[109] ROOT←(SQRT QCOVGP[1;])×1.645
[110] KROOT← 3 2 ⍴ROOT,QCOVGP[2;],QCOVGP[3;]
```

Exhibit 2 (Page 2 of 3)

```
[111] GRID[I;I̲]←KROOT[1 2 3 ; 1 2]
[112] Y←Y+43942
[113] I̲←I̲+2
[114] →START×⍳Y>87884
[115] →LOOP
[116]START:X←X+43942
[117] Y←¯87884
[118] I←I+3
[119] I̲← 1 2
[120] →END×⍳X>87884
[121] →LOOP
[122]END:' FINAL ERROR MATRIX AFTER MULTIPLICATION BY 1.645: '
[123] '   '
[124] '    '
[125] VX← ¯87884 ¯43942 0 43942 87884
[126] CX← 1 0 0 0 0 0 1 0 0 0 0 0 1 0 0 0 0 0 1 0 0 0 0 0 1 0 0 0 0 0 \ 6 0 ⍕ 5 1 ⍴VX
[127] CGRID← 1 1 1 0 0 0 1 1 1 0 0 0 1 1 1 0 0 0 1 1 1 0 0 0 1 1 1 0 0 0 \(20⍴ 12 2 9 2)⍕GRID
[128] '           Y       ¯87884               ¯43942                 0                 43942
[129] '   '
[130] '     X'
[131] '    '
[132] '    '
[133] CX,'                                  ',CGRID
    ∇
```

Exhibit 2 (Page 3 of 3)

Appendix C

EFFECT OF DATA STRIPING ON CLASSIFICATION ACCURACY

C.1 INTRODUCTION AND SUMMARY

The first of a planned series of experiments to determine the effect of data striping on classification was carried out at the Earth Resources Laboratory (ERL), Houston on the ERMAN II system installed there. The results of this experiment will be of importance in deciding whether on-board classification computations are feasible or not. If it turns out that striping has a significant effect on the classification process, destriping would have to be included in the on-board computations which would increase their complexity and the time necessary to carry them out.

For the first experiment, a Landsat-2 scene including an area of Hand County, SD, for which extensive ground truth is available, was chosen. The scene exhibits a very marked degree of striping on photographic images prepared from the data. Two additional versions of the scene were prepared, one by applying the standard NASA calibrations, the other by applying an IBM-developed destriping algorithm involving mean and standard deviation equalization. The NASA-calibrated scene exhibits considerably less striping than the uncalibrated scene, although close inspection shows that striping is still present, while the scene subjected to the IBM destriping algorithm is almost free of visible striping.

The three scenes were classified by the Bayes classifier facility of the ERMAN II system using the same training fields in all three cases. The results of the three classifications were very close to one another, indicating that the presence of striping has very little effect on the outcome of maximum likelihood multispectral classification. However, this conclusion is strictly valid only for this particular scene classified, and before it can be stated with confidence that classification can be carried out on-board without additional calibration or destriping computations, further experiments will have to be performed. These are described in the concluding section.

C.2 CLASSIFICATION OF LANDSAT DATA

The most widely used model for the classification of data from the multispectral scanners on the Landsat series of satellites and other similar sensors assumes that the vectors of intensity values from a material on the surface of the earth are samples from a multivariate normal distribution. In the case of presently available Landsat 1 and 2 data there are four spectral bands (bands 4, 5, 6, and 7 in Landsat terminology), so the assumed normal distributions are four dimensional. To classify Landsat data, ground truth must be available which usually takes the form of maps or aerial photographs on which homogenous areas of known composition are identified. The classification then proceeds in the following manner:

a. Identification of regions (fields) in the image data corresponding to ground truth areas

b. Computation of the field mean vectors and covariance matrices which characterize the assumed normal distributions

c. Examination of the computed statistics to determine their suitability for classification

d. Classification of the area of interest by a maximum likelihood classifier, that is the assignment of each vector of intensities to that normal distribution from which it had the highest probability of being drawn

e. Generation of classification maps and other summaries of the process and interpretation of the results

C.3 CLASSIFICATION OF THE LANDSAT SCENES

The area chosen for this field experiment is contained in Landsat scene 2183-16433, and represents an approximately 5- x 6-nautical mile rectangle in Hand County, SD (Test Site No. 35 (LACIE 1986)). Extensive ground truth is available in terms of an aerial photograph of the region, an overlay delineating 275 fields varying from a few acres to several hundred acres, and a complete inventory of the composition (in this case agricultural crops) of each of the 275 fields. The test site is composed of approximately 8 percent corn, 6.5 percent oats, 4.2 percent spring wheat, and 81.2 percent pasture and grasses.

Three tapes in LARS MIST format were created, the first from the uncalibrated NASA data, the second from data which had been subjected to the standard NASA calibration, and the third from data which had been subjected to IBM's mean and standard deviation equalization algorithm.

Once the region containing the LACIE site was found in the original image, a 512 x 512 print composite 12-channel image containing the site was formed for further ERMAN-II processing. Channels 1-4 contain the uncalibrated data, channels 5-8 the NASA calibrated data, and channels 9-12 the IBM destriped data. With the aid of the ground truth aerial photograph overlay, 14 test fields were delineated for which statistics were computed. The fields and their statistics are given in the form of ERMAN-II reports in the Appendix. After comparison of the field statistics (corn with corn, oats with oats, etc.), fields CORN 54, CORN 80, and CORN 110 in the class CORN; fields OATS 38 and OATS 192 in the class OATS; fields P76, P91, P105, and P131 into the class PSTR, and fields SW2^6 and SW263 into the class SPRWHT.

The LACIE site (identified as the field GRDTRTH in the field definition report) was classified by the Bayes' classifier with a priori values of 8 percent, 7 percent, 81 percent and 4 percent for the four classes corn, oats, pasture/grasses and spring wheat, respectively. Classification of the uncalibrated data was accomplished by requesting that channels 1-4 be used in the classifications, of the NASA calibrated data by requesting channels 5-9 and of the IBM destriped data by requesting channels 9-12. The results are shown in Table 31.

The results in Table 31 are for the case in which each pixel is assigned to one of the four classes. The Bayes classifier has a thresholding option under which a pixel is not assigned to any class if the value of the quadratic form in the likelihood function exceeds a user-assigned percentile of the chi-square distribution. Table 32 shows the results of setting a 1 percent threshold (a typical value) in the case of the image NASACAL. The differences are not great, the principal effect of the threshold appears to be that approximately 3 percent of the pixels previously assigned to the pasture/grasses class are now unassigned.

Two conclusions can be drawn from the results presented:

a. The classification of the three images are fairly close to ground truth, with the exception of spring wheat, which is clearly underclassified.

b. The differences among the classifications of the three images are quite small.

These conclusions are further analyzed in the next section.

C.4 ANALYSIS OF THE RESULTS

The areal proportion estimates of corn and pasture/grasses are acceptably close to the ground truth values, the estimates of oats somewhat less so. However, the areal proportion of spring wheat is only 40 percent of the ground truth value. Clearly, wheat pixels were assigned to other classes,

Table 31. Proportion Estimates Obtained From Classification of the Three Images.

Image	Areal Proportion Estimates			
	Corn	Oats	Pasture/Grasses	Spring Wheat
Ground Truth	8.06	6.47	81.23	4.24
UNCAL	9.29	8.30	80.76	1.64
NASACAL	9.51	9.41	79.58	1.52
MSEQCAL	9.35	8.70	80.52	1.42

Table 32. Proportion Estimates for Image NASACAL Under Two Threshold Settings.

Image	Areal Proportion Estimates				
	Corn	Oats	Pasture/Grasses	Spring Wheat	Unassigned
Ground Truth	8.06	6.47	81.23	4.24	-
o% Threshold	9.51	9.41	79.56	1.52	-
1% Threshold	9.24	9.22	77.11	1.51	2.92

probably oats. There are several explanations possible for this outcome, among which are:

a. Inadequate training fields. Only two small (< 50 acre) fields were used to derive class statistics. Additional might have altered the class statistics.

b. The multivariate normal distribution is an inadequate model for classification of wheat. This has been demonstrated in a study by Misra and Wheeler, who have proposed an alternate model. The question of the absolute accuracy of the classification will not be pursued further, since for the purposes of this experiment, the differences in classification results among the images is what is important.

As Table 31 shows, the classification results for the three images are quite close to one another, which indicates that the presence of striping has no effect on classification. To determine the reason for this uniformity of the classifications, the data was examined from several points of view. In the first place, the means and standard deviations in a given field were compared in corresponding bands (1-5-9, 2-6-10, 3-7-11, and 4-8-12). Take OATS 38 as an example. It is obvious that the means of Channels 1-4 are almost identical with the respective means of channels 9-12, but that the respective means of channels 5-8 are completely different from those two sets. One reason for this is that the NASA-calibrated data has a different intensity range (0-~180) than the uncalibrated and IBM destriped data (0-63). In the NASA process, the uncalibrated data is first decompressed to give a range of 0-127 and then subjected to a linear transformation to give a range of (0-~180). The decompression is accomplished by a table look-up procedure, while the linear transformation is sensor-dependent as well as time-dependent with the result that, from a practical standpoint, the compressed, unscaled calibrated data cannot be recovered from the decompressed, scaled calibrated data. However, the hypothesis that the means in channels 5-8 would be the same as the means in channels 1-4 or 9-12 were it not for decompression and scale was tested in the following way.

First, the decompression tables of references were fitted with quadratic polynomials for channels 5 and 7 (corresponding to spectral bands 4 and 6), and another for channel 6 (corresponding to spectral band 5). Spectral band 7, and therefore channel 8, is not decompressed. The coefficients (ℓ, m, n) of the quadratics are, respectively, (0.5104, 0.5793, 0.0235) and (1.2459, 0.5696, 0.0233). The coefficients for the linear transformation (a_k, b_k) were taken to be the average values over six detectors for a randomly selected frame in a previous striping study. The overall transformation is shown in equations (39) and (40):

$$I_{OUT} = a_k(\ell + mI_{in} + nI^2_{in}) + b_k \tag{39}$$

and accordingly

$$E(I_{OUT}) = a_k(1 + mE(I_{in}) + nE(I^2_{in})) + b_k \tag{40}$$

Next, it was assumed that the intensity values I_{in} in a given channel were normally distributed with mean μ and standard deviation σ. Then $y = I^2_{in}$ has the probability distribution function as shown in equation (41):

$$g(y) = \exp\,[-(\mu^2 + y)/2\sigma^2]\ \cosh\,(\mu\sqrt{y}/\sigma^2)/\sigma\sqrt{2\Pi y} \tag{41}$$

Equation (42) follows:

$$E(I_{in}{}^2) = E(y) = \int_0^\infty y g(y)dy = \mu^2 + \sigma^2 = E^2(I_{in}) + D^2(I_{in}) \tag{42}$$

If equation (42) is substituted into equation (40), the result is the channel mean formula for channels 5-9 in terms of the means and standard deviations of channels 1-4. Equation (43) results:

$$E(I_{OUT}) = a_k[\ell + mE(I_{in}) + n(E^2(I_{in}) + D^2(I_{in})] + b_k \tag{43}$$

Calculations based on (5) were carried out for fields OATS38 and CORN54 using the average values of a_k and b_k as shown in Table 33.

The results shown in Table 34 indicate that the computed field statistics in channels 5-9 are consistent with the field statistics which would have been obtained from applying 36 to the field statistics for channels 1-4.

It appears that, for this scene, calibration and IBM destriping do not significantly alter field statistics. Therefore, classification results for the three images should be close, as they are, The hypothesis of the invariance of field statistics should be tested on other scenes and by applying quantitative measures of the similarity of distributions (divergence, Bhattacharyya distance) available in the ERMAN II system.

The image data itself was also examined to gain further insight into the reason the presence of striping seems to have little effect on classification results. Because the NASA-calibrated image has a different intensity range from the other two images, as explained above, the usual methods of comparing images--image differences, two-dimensional histograms--cannot be applied. Therefore only the uncalibrated (striped) image and the IBM-destriped image could be compared.

As a first step, a difference image |UNCAL-MSEQCAL| was formed and displayed. The displayed difference image exhibited a striping pattern very clearly. Unfortunately, owing to the substandard performance of the hard copier at ERL, readable copies of the display could not be made. One-dimensional (channel) histograms were computed for channels corresponding to spectral bands 4, 5, and 7, (see Exhibits) for UNCAL and MSEQCAL. The histograms show distinctly similar intensity distributions in corresponding channels. Finally, two-dimensional histograms for channel corresponding to spectral bands 4 and 5 were computed. Again, qualitatively speaking, the two images are statistically similar in the sense that a pixel having a given intensity in one image has a high probability of having the same in-

Table 33. Average (Over Six Sensors) Gain a_k and b_k.

Band	a_k	b_k
4	1.2122	-1.5199
5	1.2057	-1.5219
6	1.2352	-1.7110
7	1.0878	+0.1522

Table 34. Channel Means As Computed in ERMAN II and from Equation 40.

a) Oats 38

Channel 1-4 Mean	Mean Computed from (5)	Channel 5-9 Mean
22.95	30.27	29.75
30.13	46.29	44.75
37.33	66.11	63.75
29.56	32.31	31.39

b) Corn 54

Channel 1-4 Mean	Mean Computed from (5)	Channel 5-9 Mean
17.65	20.41	19.27
18.71	22.71	21.94
28.27	47.62	42.29
21.27	23.29	22.12

tensity in the other image. Thus the IBM destriping algorithm, while it modifies intensity values, does not skew the overall image intensity statistics.

Examination of the image data made more plausible the classification result. However, the classification result itself was obtained from a single scene. More scenes of various types will have to be classified in order to either corroborate or refute its conclusion that striping does not affect classification.

C.5 SUGGESTED FURTHER EXPERIMENTS

Experience has shown that in order to determine the effect of a particular factor (resampling, striping, correction method) on classification, about 15 different scenes should be classified to ensure statistically significant results. This is usually an impractically large number. Nevertheless, additional scenes should be classified to test the validity of the conclusion of the present memo that striping does not affect classification results significantly.

The first sequence of experiments should be conducted with synthetic data sets. The SERID program at Johnson Space Center is designed for this purpose. With synthetic data the experimenter has control over the size and form factors of the fields, as well as the numbers and statistics of the classes represented. Striping can be added in controlled amounts by, in effect, reversing the IBM destriping algorithm. The first experiment could use an existing synthetic data set (generated under Contract NAS1-23585) to which striping would be added until a level is reached at which perceptible differences between the striped and unstriped data occur. Synthetic data sets at this level of striping can then be generated to determine the statistical significance of secondary factors such as field distribution and class statistics.

With confidence that striping effects on classification are well understood, a second sequence of experiments using natural data should be undertaken. It is not realistic to expect that natural data sets which have both the proper variety of classes and the level of striping can be found. It is most probable that scenes with adequate ground truth will be selected, to which a desired level of striping will be added synthetically.

If the results of a small number of experiments support the conclusions of the present memo, it will not be necessary, practically speaking, to conduct additional classifications. If, however, the results are inconclusive or contradictory, a review of the situation to plan an economical series of experiments can be made.

Exhibits 3 through 7 illustrate the ERMAN output as viewed on the CRT display. Exhibit 3 indicates the location, on the input tape, of the data to be classified. Exhibit 4 represents the computed mean and standard deviation for each class and training field for each input channel. Exhibit 5 provides the location (in pixel and line) of each training field. Exhibits 6 and 7 illustrate the histograms for selected input channels.

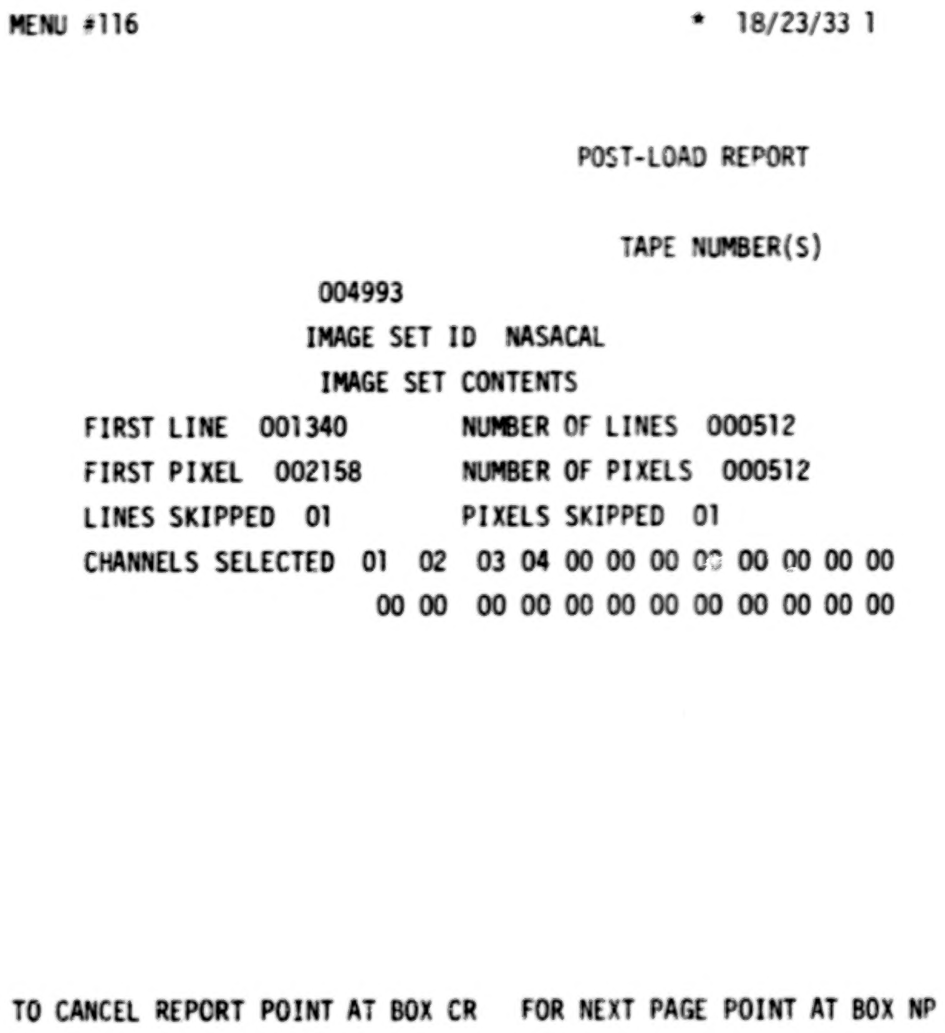

```
MENU #116                                          *  18/23/33 1


                                               POST-LOAD REPORT


                                                  TAPE NUMBER(S)
                              004993
                             IMAGE SET ID  NASACAL
                              IMAGE SET CONTENTS
     FIRST LINE  001340        NUMBER OF LINES  000512
     FIRST PIXEL  002158       NUMBER OF PIXELS  000512
     LINES SKIPPED  01         PIXELS SKIPPED  01
     CHANNELS SELECTED  01  02  03 04 00 00 00 00 00 00 00 00
                        00 00  00 00 00 00 00 00 00 00 00 00








TO CANCEL REPORT POINT AT BOX CR   FOR NEXT PAGE POINT AT BOX NP
```

Exhibit 3

```
PR   01.MEANSTD  .0003                    *  14/52/10  1                  PAGE 01 OF 04
                                MEAN AND STANDARD DEVIATION REPORT
                                  FOR CLASSES AND TRAINING FIELDS
                                    AND ALL AVAILABLE CHANNELS

             FIELD CORN80         FIELD OATS38         FIELD CORN54         FIELD P91
CHANNEL        (   104)             (    61)             (    51)             (   317)
NUMBER       CLASS CORN           CLASS OATS           CLASS CORN           CLASS PSTR
             MEAN    ST DEV       MEAN    ST DEV       MEAN    ST DEV       MEAN  ST DEV

    1        17.89     1.03       22.95     1.61       17.65     1.40       19.21     1.47
    2        18.00     1.13       30.13     3.24       18.71     1.64       21.16     2.33
    3        28.95     1.97       37.33     2.18       28.37     2.09       34.40     2.22
    4        21.29     2.04       29.56     1.72       21.27     1.63       28.60     2.63
    5        19.26     1.34       29.25     2.88       19.27     1.37       22.03     2.19
    6        20.75     1.61       44.75     7.04       21.94     2.45       26.05     4.10
    7        42.88     4.12       63.79     3.79       42.29     3.12       55.95     4.01
    8        22.19     2.23       31.39     2.00       22.12     1.88       30.25     2.85
    9        17.41     0.89       23.38     1.54       17.37     0.89       19.13     1.45
   10        18.00     1.13       30.15     3.28       18.67     1.57       21.00     2.30
   11        28.79     1.94       37.89     1.60       28.51     1.45       34.72     1.78
   12        21.26     1.99       29.56     1.86       21.27     1.63       28.56     2.57
```

Exhibit 4

```
PR01.MEANSTD  .0003                    *  14/52/33  1                PAGE 02 OF 04
                              MEAN AND STANDARD DEVIATION REPORT
                               FOR CLASSES AND TRAINING FIELDS
                                  AND ALL AVAILABLE CHANNELS

           FIELD CORN110          FIELD P105         FIELD SW236         FIELD P131
CHANNEL     (     961)             (    558)          (     45)           (    421)
NUMBER     CLASS CORN             CLASS PSTR         CLASS SPRWHT        CLASS PSTR
           MEAN   ST DEV          MEAN    ST DEV     MEAN    ST DEV      MEAN   ST DEV


   1       18.01      1.21        20.26      1.15    19.09     1.41      22.21      1.57
   2       18.26      2.00        22.87      1.40    22.96     1.04      27.33      2.40
   3       28.86      2.94        33.28      2.13    31.18     1.74      34.12      1.77
   4       20.70      3.12        25.88      2.18    23.93     1.32      25.50      1.37
   5       19.54      1.73        23.88      1.39    21.91     1.62      27.69      2.17
   6       21.26      3.19        29.12      2.74    29.27     1.99      38.57      4.82
   7       42.07      5.93        53.03      3.53    48.11     2.57      55.98      2.12
   8       21.44      3.52        27.28      2.33    25.29     1.24      26.88      1.37
   9       17.54      1.11        20.38      0.87    19.11     1.05      22.57      1.31
  10       18.26      2.00        22.77      1.41    22.87     1.12      27.31      2.36
  11       28.47      2.73        33.39      1.60    31.27     1.14      34.74      1.01
  12       20.70      3.13        25.87      2.17    23.82     1.23      25.48      1.35
```

Exhibit 4 (cont.)

```
PR  .01.MEANSTD  .0003                        *  14/53/08  1                  PAGE 03 OF 04
                                  MEAN AND STANDARD DEVIATION REPORT
                                    FOR CLASSES AND TRAINING FIELDS
                                       AND ALL AVAILABLE CHANNELS

            FIELD OATS274          FIELD CORN 211         FIELD OATS192          FIELD SW263
CHANNEL     (        54)           (        46)           (        56)           (        47)
NUMBER      CLASS OATS             CLASS CORN             CLASS OATS             CLASS SPRWHT
            MEAN   ST DEV          MEAN    ST DEV         MEAN    ST DEV         MEAN    ST DEV


     1      22.47      1.05        19.11      1.43        24.05      2.68        19.87      1.12
     2      28.06      1.81        21.04      2.28        32.16      4.41        23.06      0.82
     3      34.54      1.80        28.98      2.06        38.87      4.42        32.66      1.75
     4      25.43      1.61        20.78      1.87        32.05      4.01        25.47      1.47
     5      28.24      1.76        21.70      2.18        31.89      4.41        23.62      1.41
     6      40.02      3.67        25.87      4.53        49.91     10.09        29.53      1.58
     7      56.35      3.40        42.80      3.75        69.07      9.53        51.94      2.83
     8      26.83      1.76        21.43      2.16        34.12      4.22        26.70      1.52
     9      22.83      0.93        18.96      1.35        24.68      2.20        20.11      0.98
    10      27.91      1.89        21.02      2.29        32.16      4.41        23.09      0.98
    11      34.83      1.58        28.78      1.72        39.79      3.65        32.91      1.32
    12      25.56      1.50        20.70      1.87        32.05      3.95        25.19      1.45
```

Exhibit 4 (Cont.)

```
PR   .01MEANSTD  .0003                    *  14/53/26  1                  PAGE 04 OF 04
                                   MEAN AND STANDARD DEVIATION REPORT
                                     FOR CLASSES AND TRAINING FIELDS
                                       AND ALL AVAILABLE CHANNELS

               FIELD OATS226        FIELD P76
    CHANNEL      (      67)           (  526)
    NUMBER     CLASS OATS           CLASS PSTR
               MEAN   ST DEV        MEAN   ST DEV


       1       25.91     2.66       19.93     1.28
       2       35.16     4.86       21.97     1.51
       3       40.78     3.37       34.63     1.91
       4       33.19     2.61       27.84     1.73
       5       35.34     4.50       23.22     1.61
       6       57.37    11.26       27.41     2.58
       7       74.24     7.70       56.14     2.82
       8       35.37     2.90       29.41     1.87
       9       26.48     2.33       19.92     1.06
      10       36.13     4.74       21.82     1.45
      11       41.70     2.86       34.79     1.26
      12       33.25     2.54       27.84     1.71
```

Exhibit 4 (Cont.)

```
PR   .01.FLDDEF   .0001                * 14/42/02  1                        PAGE 01 OF 02
                                   FIELD DEFINITION REPORT

  FIELD    T  S          1ST   2ND   3RD   4TH   5TH   6TH   7TH   8TH   9TH  10TH
   ID      Y  Y        VERTX VERTX VERTX VERTX VERTX VERTX VERTX VERTX VERTX VERTX
           P  M

GRDIRTH    P  A  LINE   1560  1533  1633  1656      0     0     0     0     0      0
                 PIXL   2460  2296  2258  2424      0     0     0     0     0      0

CORN 80    T  C  LINE   1573  1571  1578  1581      0     0     0     0     0      0
                 PIXL   2456  2444  2442  2453      0     0     0     0     0      0

OATS38     T  O  LINE   1545  1543  1553  1553      0     0     0     0     0      0
                 PIXL   2306  2300  2297  2302      0     0     0     0     0      0

CORN54     T  C  LINE   1565  1563  1566  1569      0     0     0     0     0      0
                 PIXL   2342  2331  2329  2339      0     0     0     0     0      0

P91        T  P  LINE   1577  1586  1585  1589  1588  1575        0     0     0      0
                 PIXL   2423  2421  2410  2405  2392  2398        0     0     0      0

CORN110    T  C  LINE   1584  1583  1588  1590  1593  1593        0     0     0      0
                 PIXL   2348  2339  2338  2341  2341  2348        0     0     0      0

P105       T  P  LINE   1590  1587  1605  1610      0     0     0     0     0      0
                 PIXL   2390  2364  2356  2383      0     0     0     0     0      0

SW236      T  W  LINE   1595  1595  1599  1599  1603  1604        0     0     0      0
                 PIXL   2347  2342  2341  2342  2341  2343        0     0     0      0

P131       T  P  LINE   1599  1607  1608  1600      0     0     0     0     0      0
                 PIXL   2318  2308  2311  2314      0     0     0     0     0      0

OATS247    T  O  LINE   1624  1626  1623  1621      0     0     0     0     0      0
                 PIXL   2378  2393  2394  2379      0     0     0     0     0      0

CORN211    T  C  LINE   1618  1628  1629  1620      0     0     0     0     0      0
                 PIXL   2426  2423  2426  2429      0     0     0     0     0      0
```

Exhibit 5

```
PR   .01.FLDDEF   .0001                 *  14/42/33  1                     PAGE 02 OF 02
                                   FIELD DEFINITION REPORT

  FIELD    T S        1ST   2ND   3RD   4TH   5TH   6TH   7TH   8TH   9TH  10TH
           Y Y       VERTX VERTX VERTX VERTX VERTX VERTX VERTX VERTX VERTX VERTX
           P M

OATS192    T O  LINE     1631  1638  1637  1638      0     0     0     0     0      0
                PIXL     2425  2523  2417  2418      0     0     0     0     0      0

SW263      T W  LINE     1629  1633  1634  1632      0     0     0     0     0      0
                PIXL     2288  2288  2300  2302      0     0     0     0     0      0

OATS226    T O  LINE     1625  1627  1623  1628      0     0     0     0     0      0
                PIXL     2407  2418  2421  2489      0     0     0     0     0      0

P76        T P  LINE     1553  1573  1577  1557      0     0     0     0     0      0
                PIXL     2488  2401  2424  2432      0     0     0     0     0      0

W270       W W  LINE     1647  1649  1646  1644      0     0     0     0     0      0
                PIXL     2354  2367  2368  2356      0     0     0     0     0      0

W204       W W  LINE     1656  1655  1651  1652      0     0     0     0     0      0
                PIXL     2423  2413  2414  2423      0     0     0     0     0      0
```

Exhitit 5 (Cont.)

PR .04.HSTOGRAM.0019 * 14/06/38 1 PAGE 01 OF 01

HISTOGRAMS FOR FIELDS AND/OR CLASSES

GRDTRTH (17226)

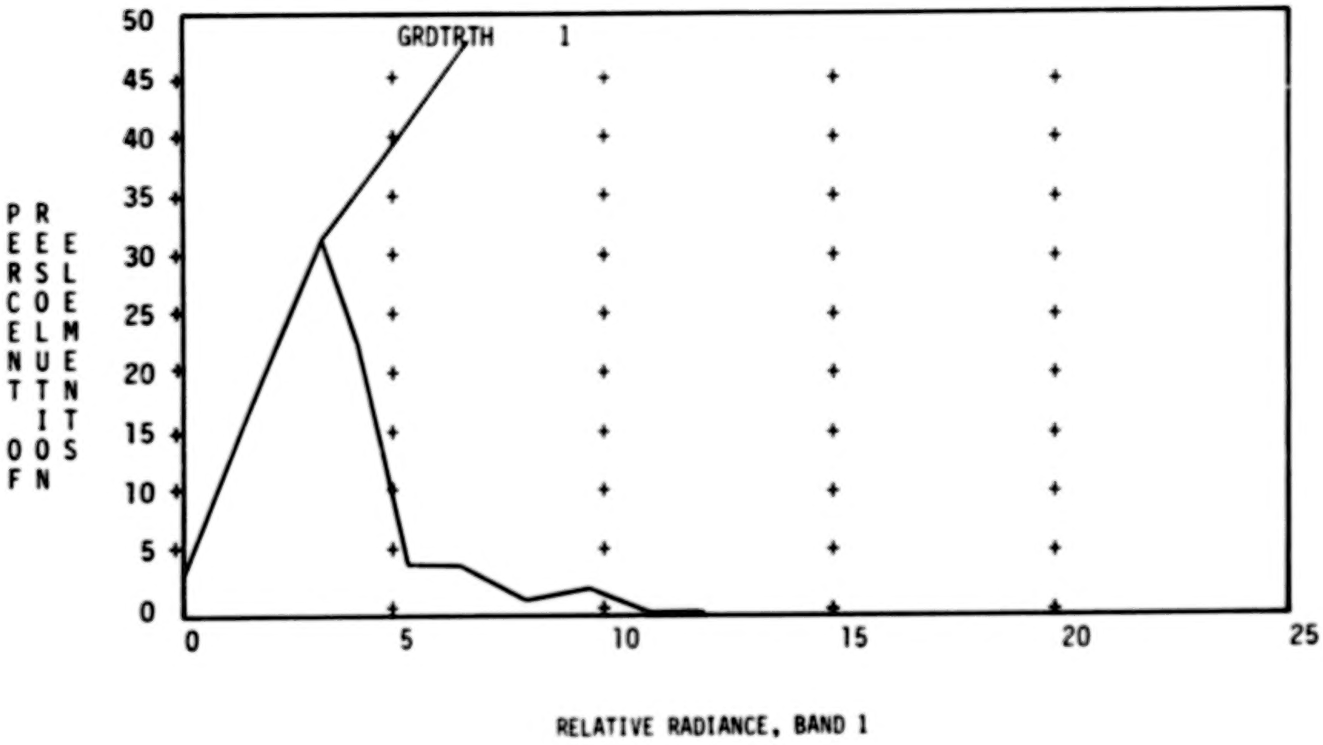

Exhibit 6

268

PR .04.HSTOGRAM.0021 * 14/18/00 1 PAGE 01 OF 01

HISTOGRAMS FOR FIELDS AND/OR CLASSES

GRDTRTH (17226)

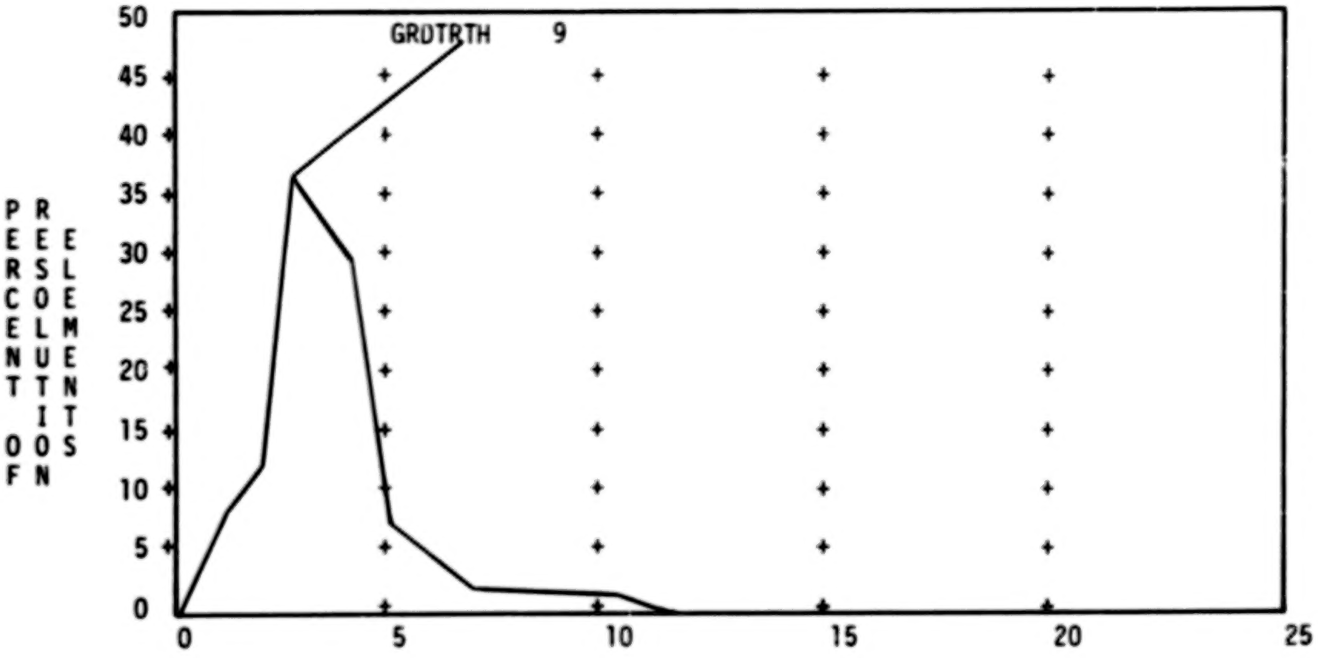

RELATIVE RADIANCE, BAND 9

Exhibit 6 (Cont.)

PR .04.HSTOGRAM.0022 * 14/23/05 1 PAGE 01 OF 01

HISTOGRAMS FOR FIELDS AND/OR CLASSES

GRDTRTH (17226)

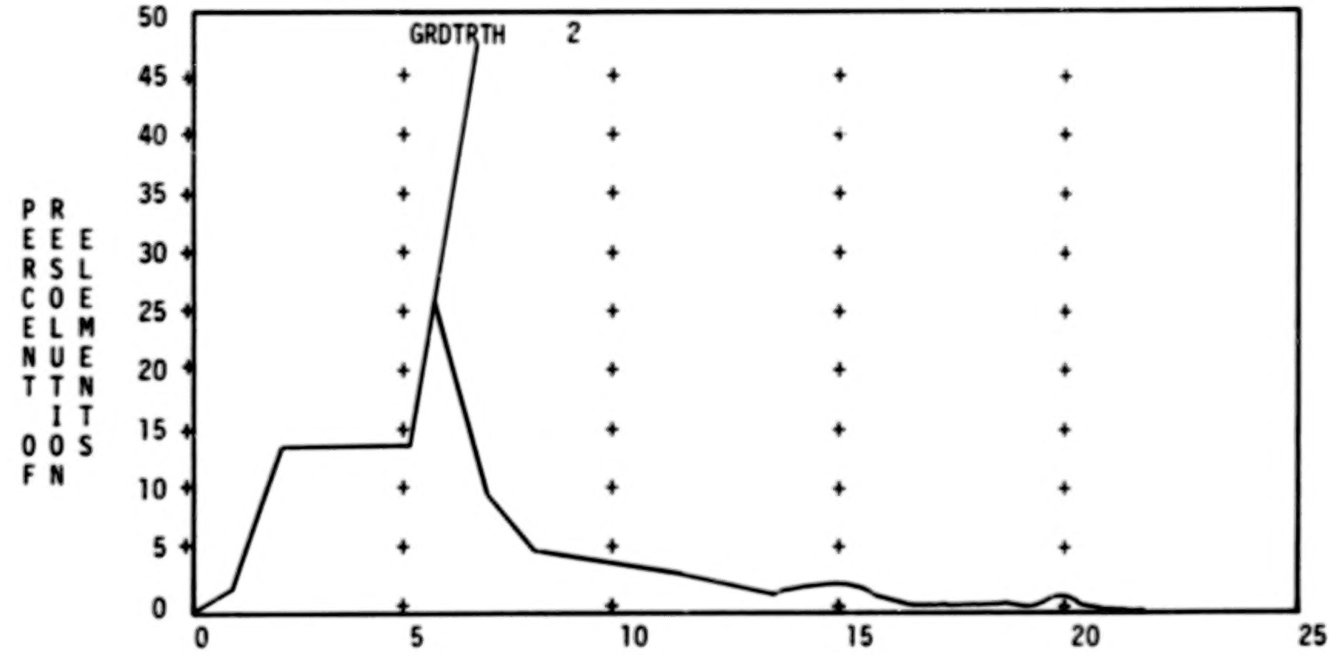

RELATIVE RADIANCE, BAND 2

Exhibit 6 (Cont.)

270

PR .04.HSTOGRAM.0024 * 14/28/43 1 PAGE 01 OF 01

HISTOGRAMS FOR FIELDS AND/OR CLASSES

GRDTRTH (17226)

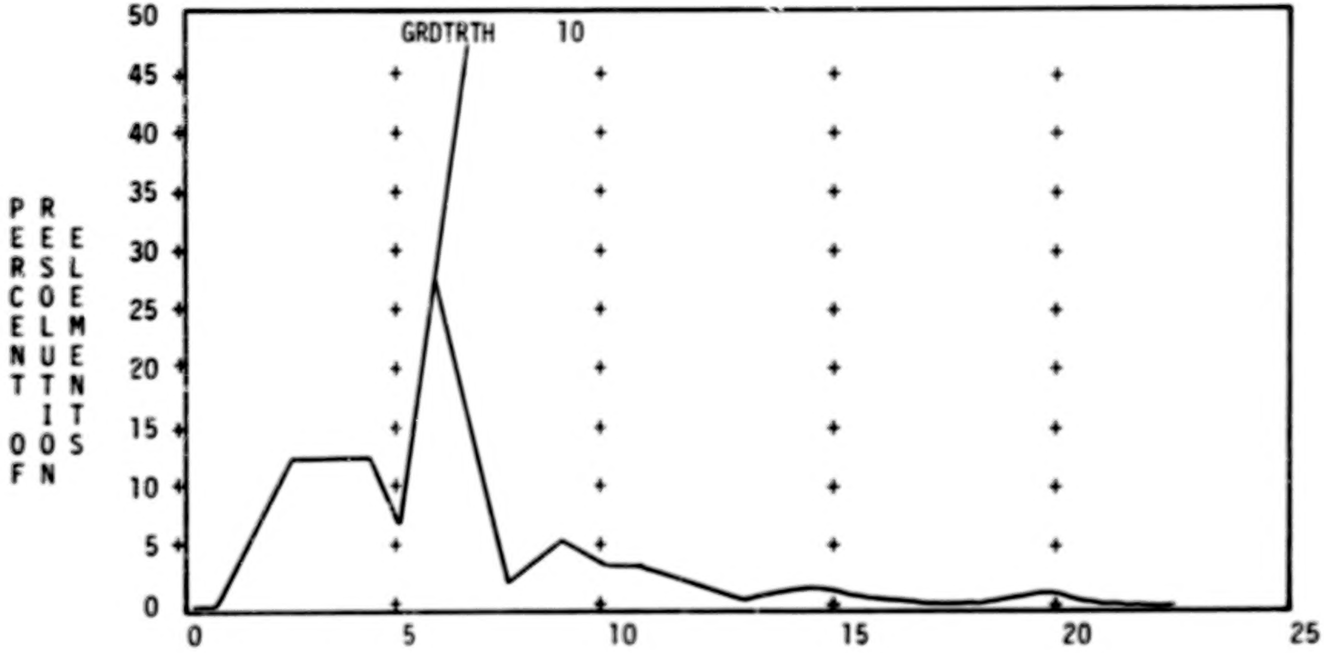

RELATIVE RANDIANCE, BAND 10

Exhibit 6 (Cont.)

HISTOGRAMS FOR FIELDS AND/OR CLASSES

GRDTRTH (17226)

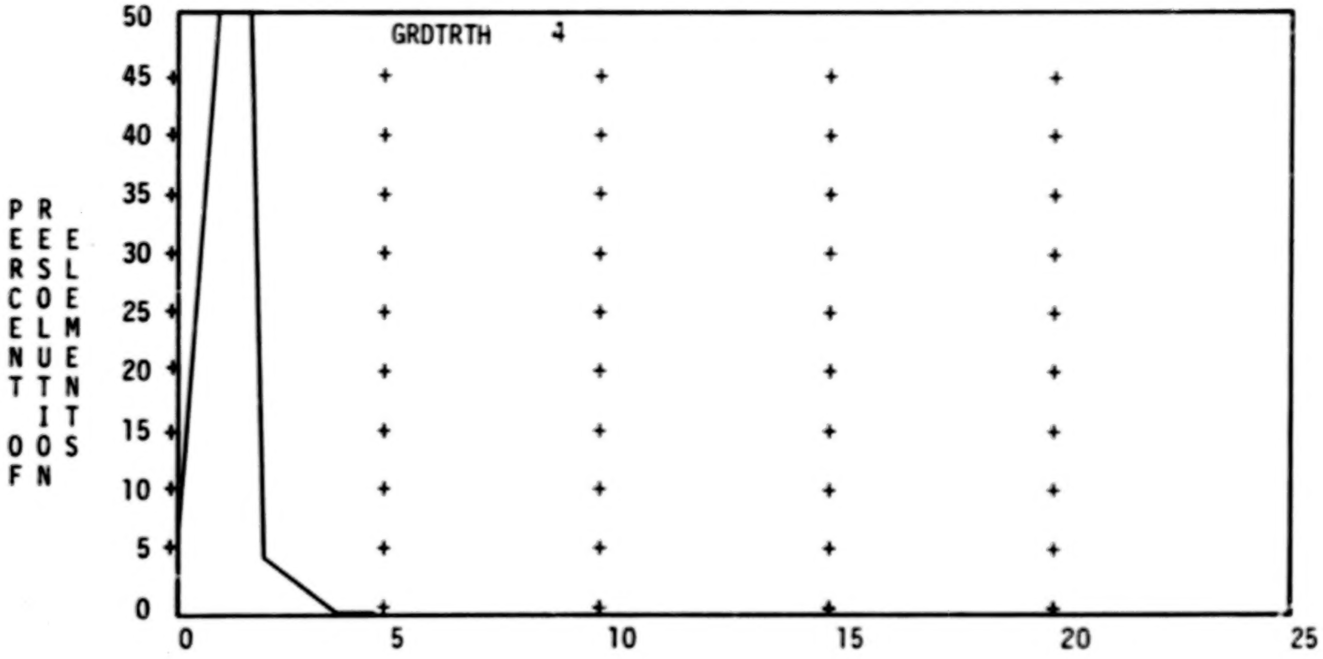

RELATIVE RANDIANCE, BAND 4

Exhibit 6 (Cont.)

271

272

PR .04.HSTOGRAM.0027 * 14/40/02 1 PAGE 01 OF 01

HISTOGRAMS FOR FIELDS AND/OR CLASSES

GRDTRTH (17226)

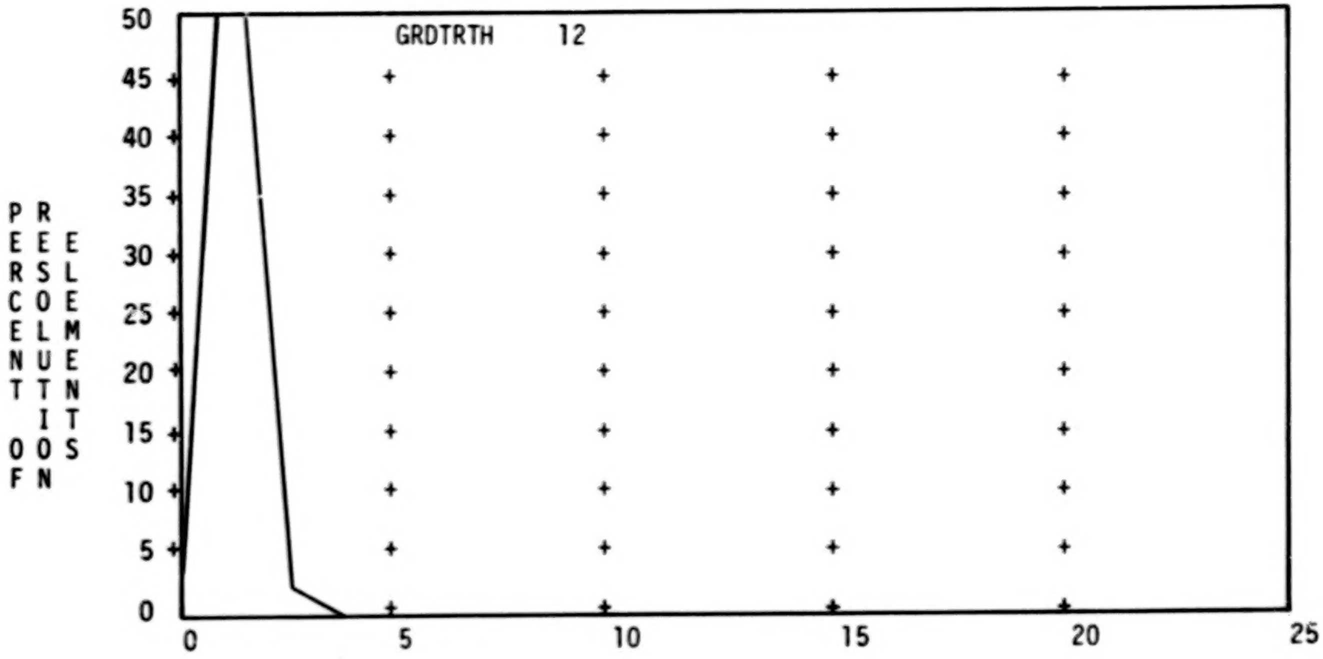

RELATIVE RADIANCE, BAND 12

Exhibit 6 (Cont.)

```
PR  .02.TWODHIST.0006                    *  10/59/17 1                         PAGE 01 OF 01
                                   HISTOGRAM FOR FIELD OR CLASS GRDTRTH
                  TOTAL POINTS = 17226          KMAX = 13382     X VALUE = 382.343
```

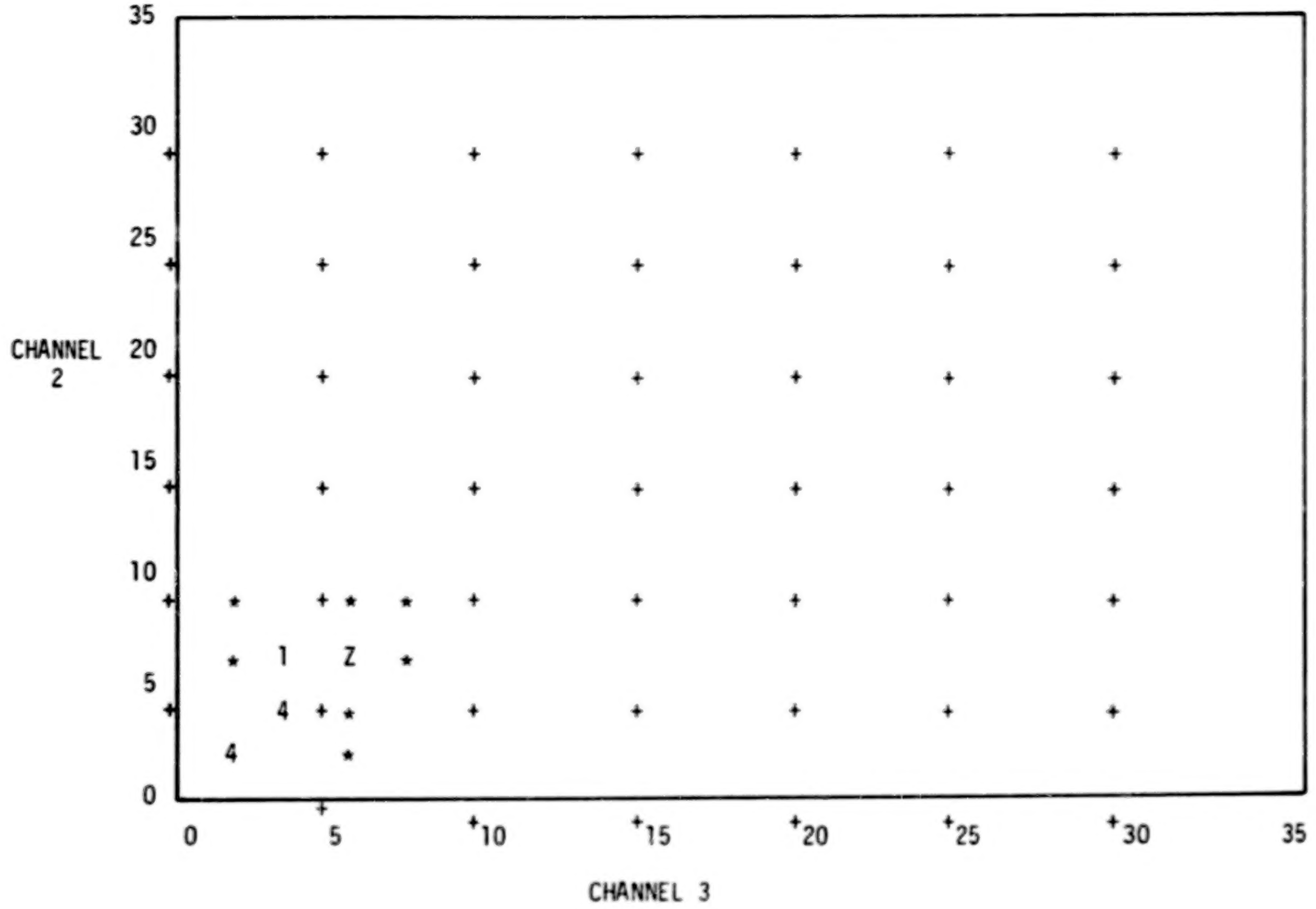

Exhibit 7

```
PR  .02.TWODHIST.0005                * 11/06/03  1                PAGE 01 OF 01

                         HISTOGRAM FOR FIELD OR CLASS GRDIRTH

        TOTAL POINTS = 17226          KMAX = 13482       X VALUE = 385.200
```

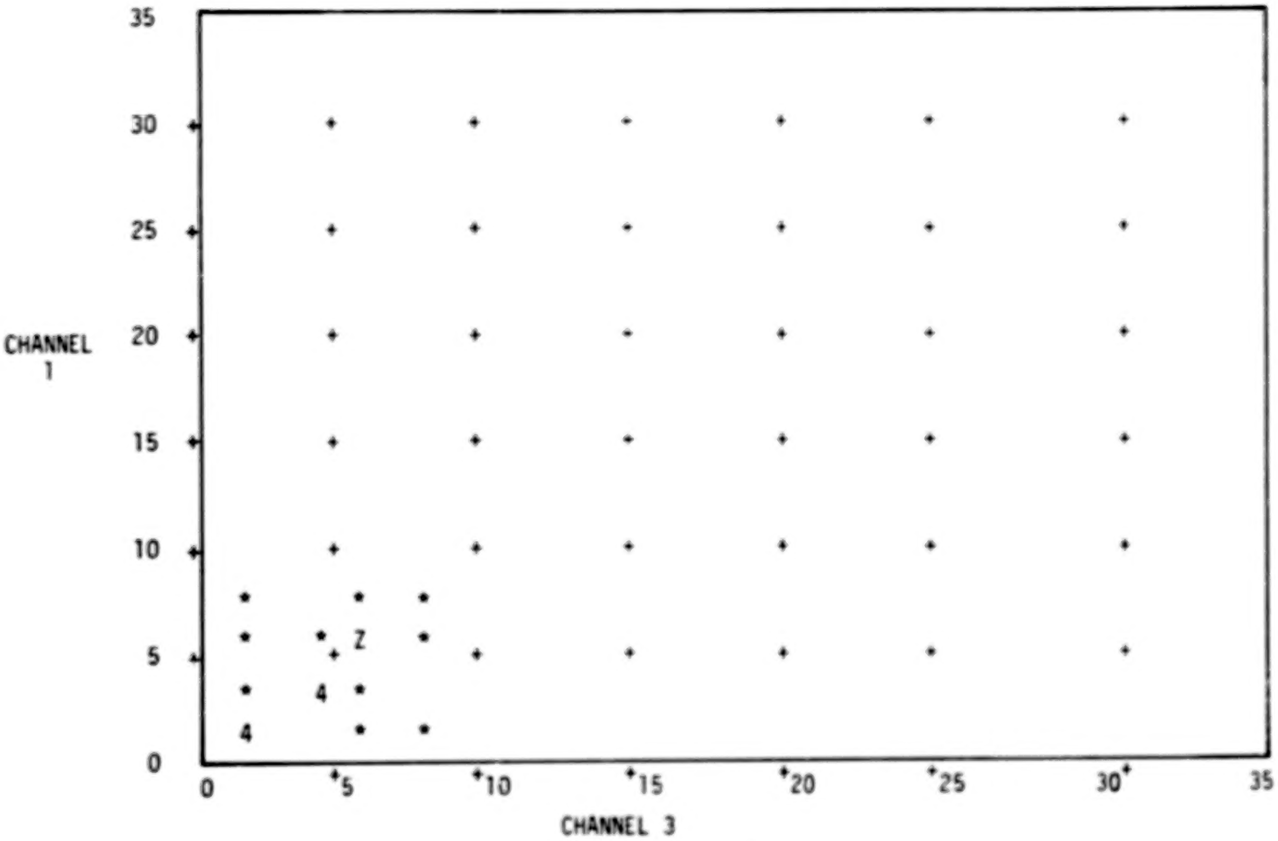

Exhibit 7 (Cont.)

```
PR   .02.TWODHIST.0010                 •  11/34/28  1                    PAGE 01 OF 01

                          HISTOGRAM FOR FIELD OR CLASS GRDTRTH

            TOTAL POINTS - 17226          KMAX = 7845       X VALUE = 224.143
```

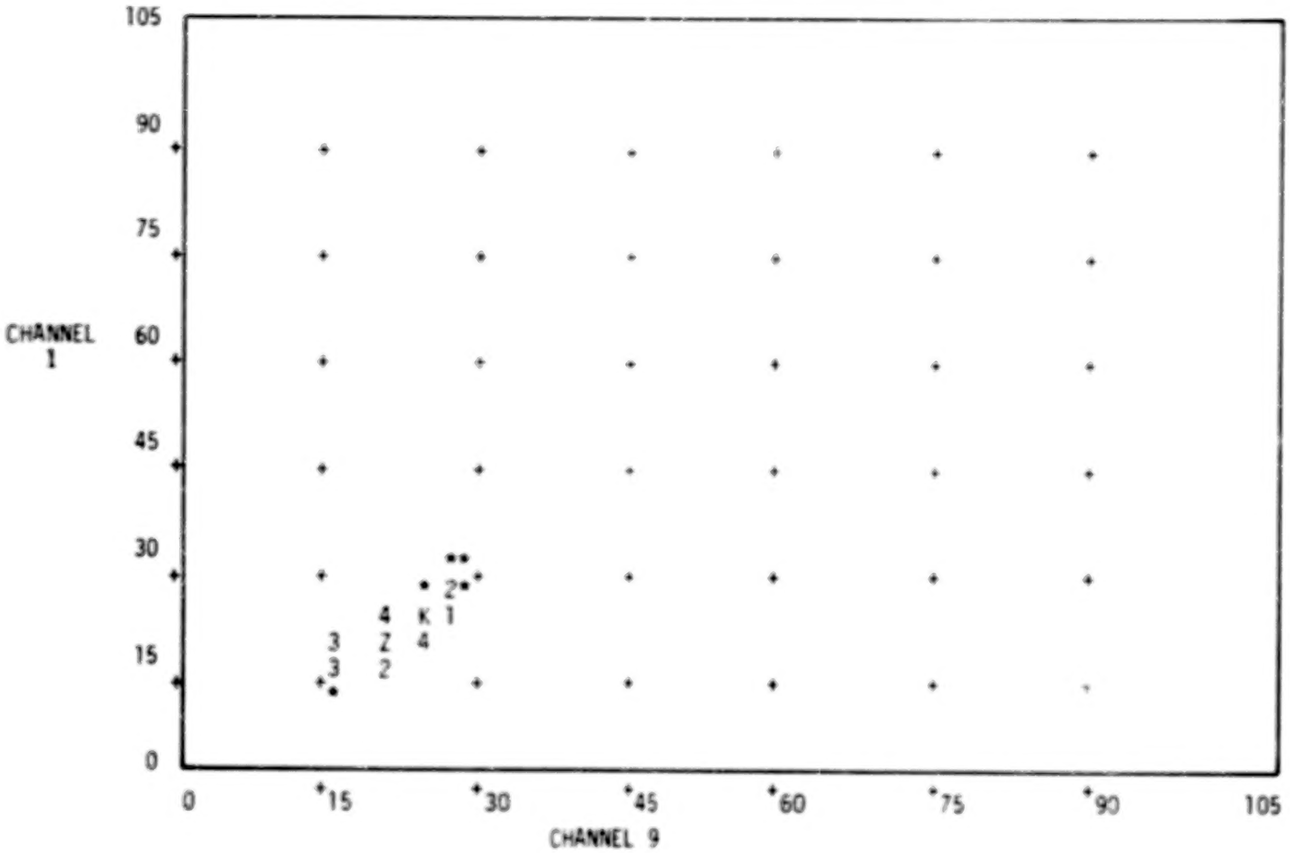

Exhibit 7 (Cont.)

```
PR   .02.TWODHIST.0013              *  12/47/03  1                   PAGE 01 OF 01

                          HISTOGRAM FOR FIELD OR CLASS GRDTRTH

              TOTAL POINTS = 17226         KMAX = 7442       X VALUE = 212.629
```

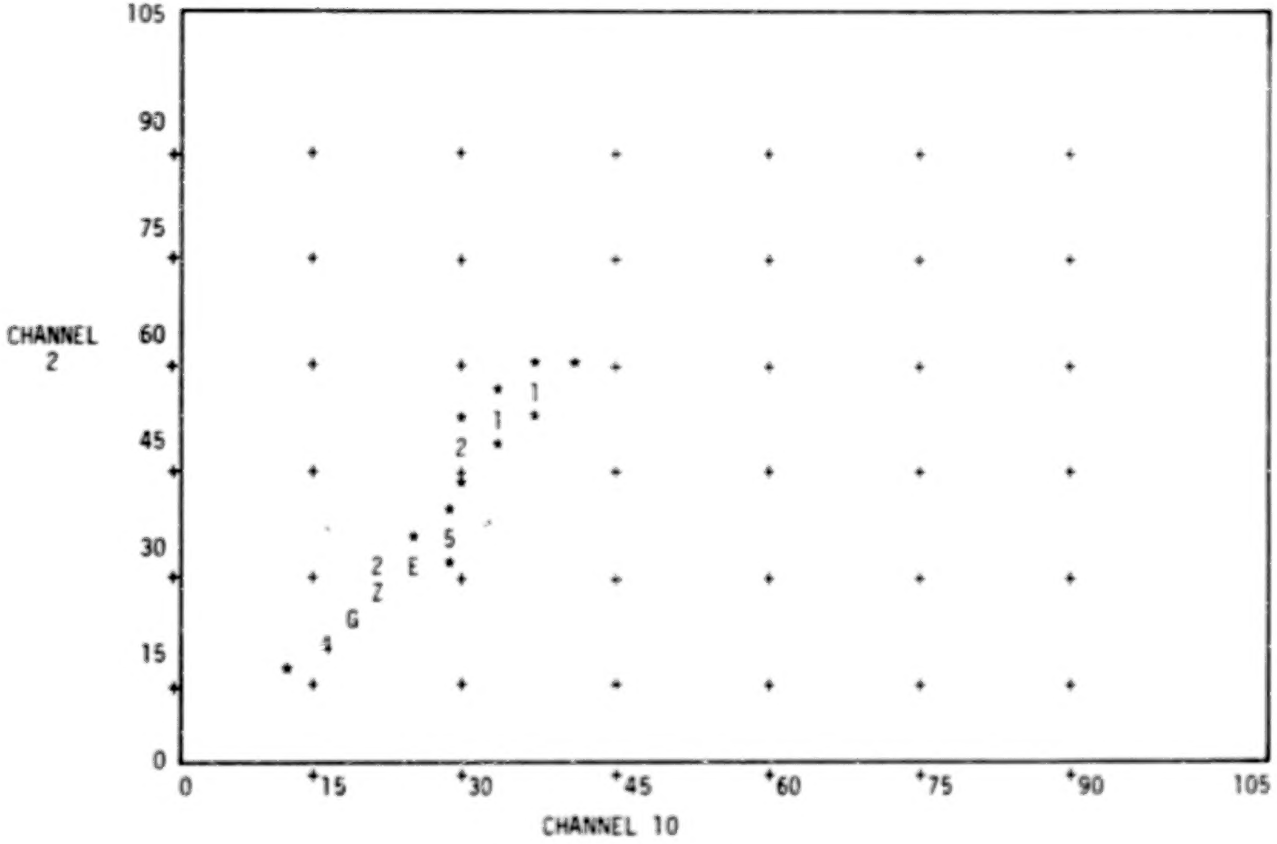

Exhibit 7 (Cont.)

```
PR  .02.TWODHIST.0002                    *  09/53/21 1                    PAGE 01 OF 01

                              HISTOGRAM FOR FIELD OR CLASS GRDTRTH

          TOTAL POINTS = 17226           KMAX = 13427       X VALUE = 383.628
```

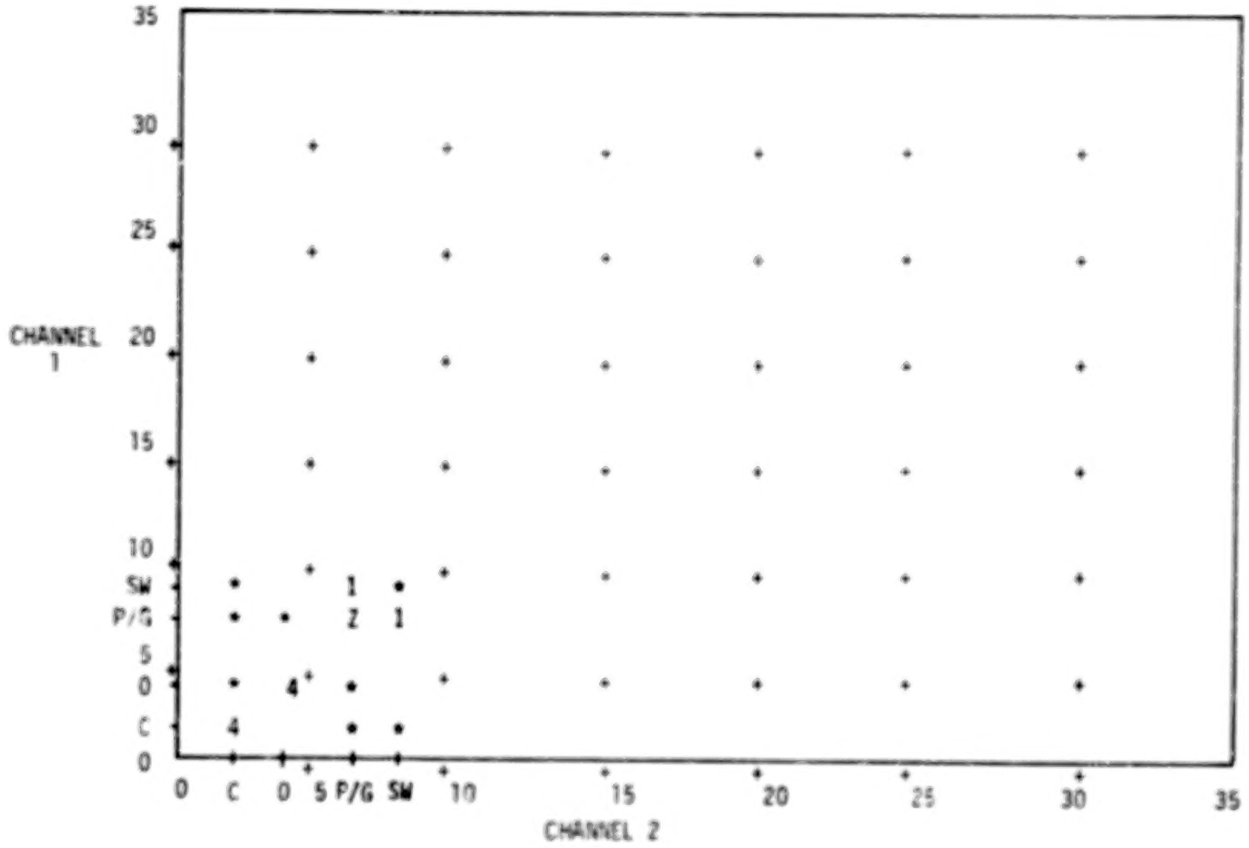

Exhibit 7 (Cont.)

Appendix D
EFFECT OF LANDSAT ORBITAL CHARACTERISTICS ON ON-BOARD CLASSIFICATION

D.1 INTRODUCTION

Subsection 3.6.2.1 discussed supervised on-board data classification. As described, there are two approaches possible for training the classifier:

a. Collect a data sample and compute from the data sample the necessary classification statistics (mean and covariance matrix) in the on-board processing system

b. Transmit the raw image data to the ground, compute the classification statistics on the ground, and transmit the statistics back to the on-board processing system for use in maximum likelihood classifier.

The orbital characteristics of the spacecraft will affect the second approach in that a time delay is introduced to the on-board processor equivalent to the time taken at the ground by an operator to compute the classification statistics plus the time to downlink raw data from the spacecraft to the ground and subsequently to uplink the computed statistics. This time delay can affect the selection of an on-board configuration in the following manner:

a. If the time required to: (a) downlink raw data, (b) compute the statistics, and (c) uplink the statistics exceeds the spacecraft in-view time, the sample segments to be classified must be stored on-board until the spacecraft again comes into view. This could be one orbit later or 1 day later.

b. If adequate on-board storage cannot be provided, the same sample segment will not be again viewed until 18 days have elapsed for Landsat-1, -2, or -C (16 days for Landsat-D). This 18- (or 16-) day delay can significantly affect classification accuracy. The above considerations, as well as others, will be discussed in this Appendix.

D.2 LANDSAT SERIES ORBITAL COVERAGE

Systematic, repetitive, global earth coverage under nearly constant observing conditions is required for maximum utility of the multispectral images collected by Landsat. All Landsat satellites have been (or will be for Landsat-D) launched into circular sun-synchronous orbits with a nominal 9:30 a.m. descending node (equatorial crossing). The orbital characteristics for the Landsat series satellites are given in Table 35. Landsat-D has certain orbital characteristics that differ from those of Landsats-1, -2 and -C. These characteristics, which include the time and distance between adjacent swaths will affect the data flow for an on-board processing system.

Table 35. Landsat Series Orbit Parameters.

Mission Parameter	Landsat 1, 2, C	Landsat D
Orbital Altitude (km)	917	705
Inclination (Degrees)	99	98.2
Period (Minutes)	103	98.88
Orbits/Day	14	14.56
Separation/Orbit at Equator (km)	2878	2778
Time Between Adj. Swaths (Deg.)	1	7
Distance Between Adj. Gr. TKs (km)	159	170
Coverage Cycle Duration (Days)	18	16

The Landsat-D orbit provides coverage of the earth in a 16-day repetitive cycle. The satellite follows a circular, sun-synchronous, near polar orbit with a 98.2 degrees inclination at an altitude of approximately 705 km. The descending (north to south) tracks occur in daylight, nominally passing the equator at 9:30 a.m. mean sun time, and the ascending tracks occur at night.

The satellite makes 14.56 revolutions per day, each 98.88 minutes in duration. Figure 116 shows typical ground coverage patterns across the U.S. The orbital characteristics cause the coverage swath to be advanced to the west at the equator by 24.72 degrees every revolution. Figure 117 depicts the orbit track progression. Track number 16, which occurs at the beginning of day 2, will be 10.82 degrees west of track number 1. Track number 103 will appear adjacent to track number 1, 1.55 degrees to the west at the equator approximately 7 days later. A complete cycle consists of 233 revolutions, during which exactly 16 days have passed and the satellite again passes over the starting location. Orbit tracks are evenly spaced as shown in Figure 117.

The Landsat-D orbit has been designed so that each of the swaths during a 16-day coverage cycle exactly overlay or repeat the corresponding swath of every previous cycle. Also, the centers of each of the images are assumed to be evenly spaced and aligned along the in-track direction as shown in Figure 118.

The orbit provides for a 7 percent sidelap (east-west overlap) of the coverage pattern at the equator, as shown in Figure 119. The overlap in the north-south direction will be between 2 and 5 percent. Figure 119 illustrates a typical overlap of 3.5 percent, which allows 225 frames per revolution.

The image sidelap between adjacent swaths is a function of latitude, as shown in Figure 120. At latitudes above 57.3 degrees, the sidelap is more than 50 percent meaning that complete coverage at a given location is achieved by more than one swath in a given cycle. This duplicate coverage is separated

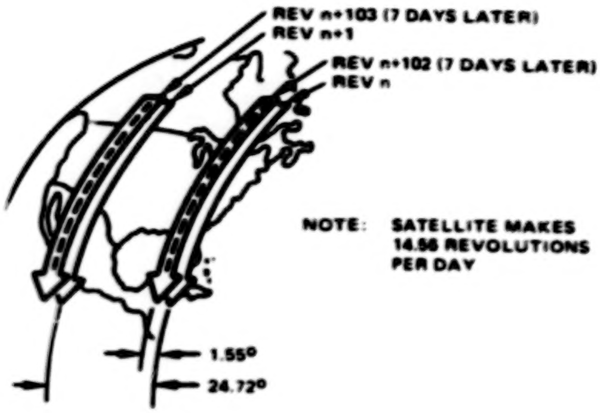
REV n+103 (7 DAYS LATER)
REV n+1
REV n+102 (7 DAYS LATER)
REV n
NOTE: SATELLITE MAKES 14.56 REVOLUTIONS PER DAY
1.55°
24.72°

Figure 116. Ground Coverage Pattern.

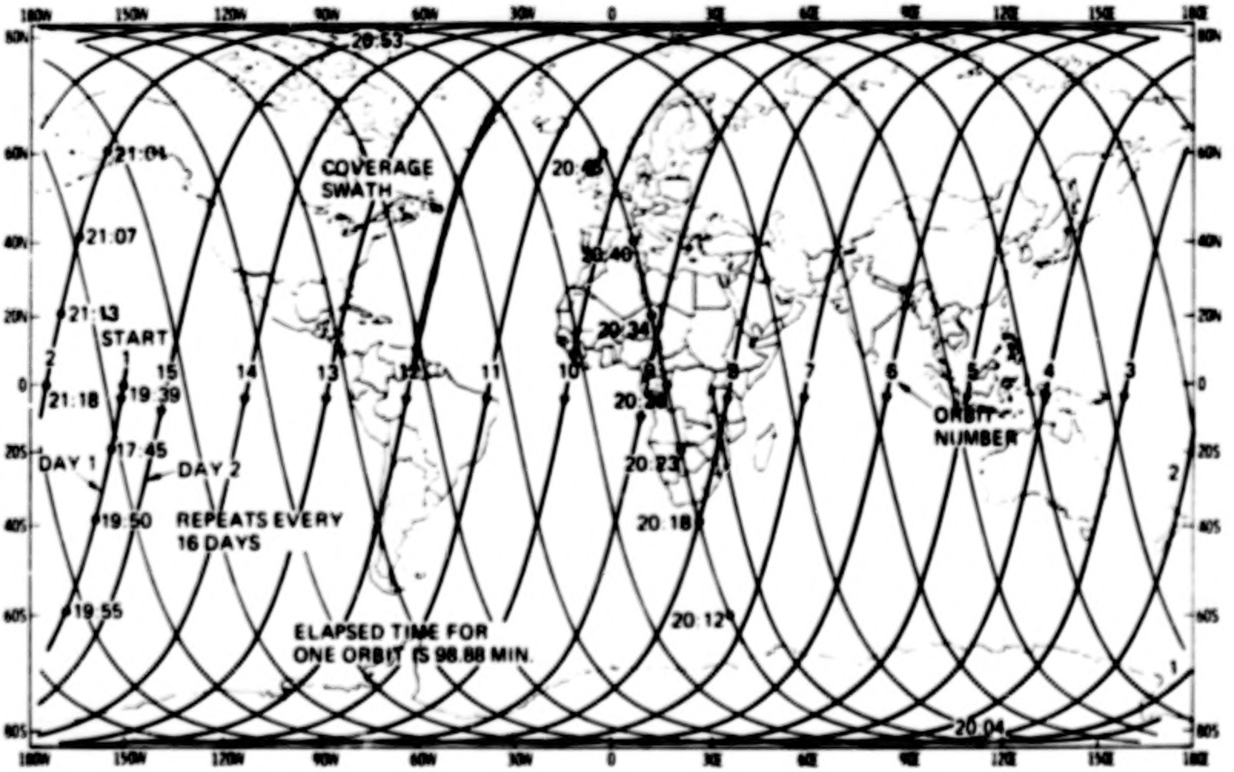
180W
150W
120W
90W
60W
30W
0
30E
60E
90E
120E
150E
180E
80N
60N
40N
20N
0
20S
40S
60S
80S
20:53
21:04
21:07
21:13
START
21:18
19:39
17:45
DAY 1
DAY 2
19:50
19:55
REPEATS EVERY 16 DAYS
COVERAGE SWATH
20:45
20:40
20:34
20:29
20:23
20:18
20:12
20:04
ELAPSED TIME FOR ONE ORBIT IS 98.88 MIN.
ORBIT NUMBER
1
2
3
4
5
6
7
8
9
10
11
12
13
14
15

Figure 117. Typical Landsat-D Ground Trace and GMT.

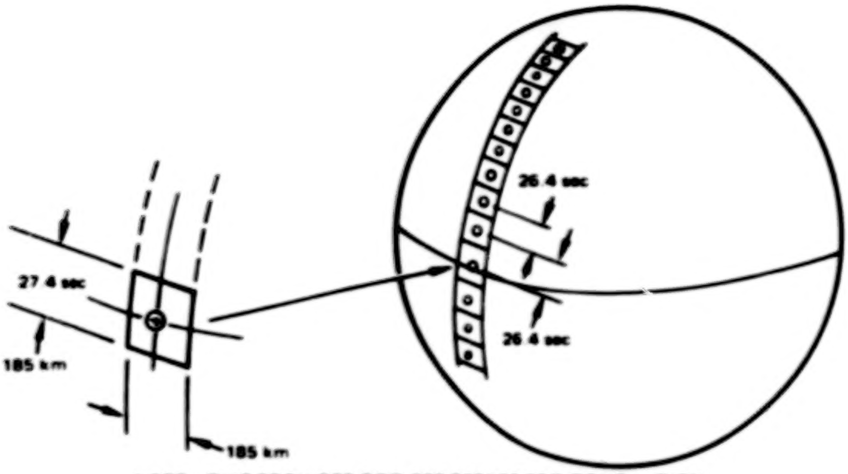
27.4 sec
185 km
185 km
26.4 sec
26.4 sec

NOTE: THIS PROVIDES FOR 225 SCENES PER REVOLUTION IF 3.5% OVERLAP OF FRAMES

Figure 118. In-Track Picture Scheduling.

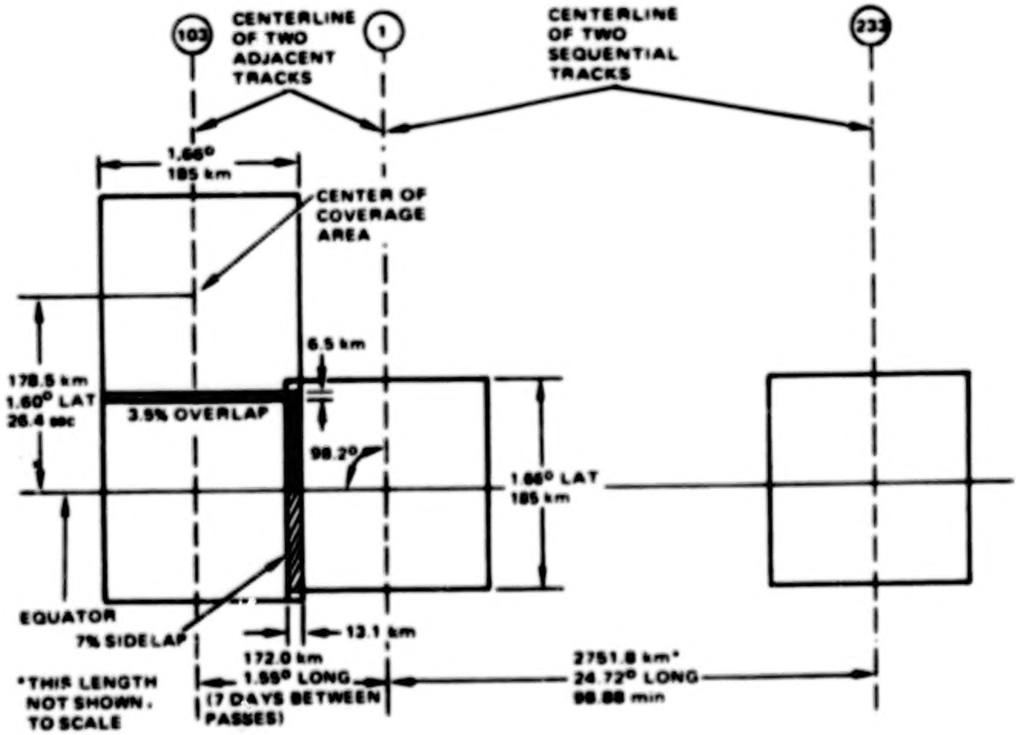
103
CENTERLINE OF TWO ADJACENT TRACKS
1
CENTERLINE OF TWO SEQUENTIAL TRACKS
233
1.66°
185 km
CENTER OF COVERAGE AREA
6.5 km
178.5 km
1.60° LAT
26.4 sec
3.5% OVERLAP
98.2°
1.66° LAT
185 km
EQUATOR
7% SIDELAP
13.1 km
172.0 km
1.55° LONG
(7 DAYS BETWEEN PASSES)
2751.8 km*
24.72° LONG
98.88 min
*THIS LENGTH NOT SHOWN, TO SCALE

Figure 119. Imagery Along-Track Overlap/Sidelap at Equator.

in time, however, by 7 days. Coverage redundancy due to imagery sidelap is given in Table 36 as a function of latitude.

The Landsats-1, -2 and -C orbit provides coverage of the earth in an 18-day repetitive cycle (9 days with two satellites). The satellite follows a circular, sun-synchronous, near-polar orbit with 99 degrees inclination at an altitude of approximately 917 km. Every equatorial crossing of the sunlit face of the earth occurs at approximately 9:30 a.m. local time.

The satellite makes 14 revolutions per day, each 103 minutes in duration. Figure 121 shows typical ground coverage patterns across the U.S. The orbital characteristics cause the coverage swath to be advanced to the west at the

Table 36. Coverage Redundancy Due to Imagery Sidelap.

Latitude, deg	Image Sidelap, percent	Redundancy Factor*	Minimum Number of Days between Coverage
0 to 57.0	7.0 to 50.0	1	16
57.3 to 69.0	50.0 to 66.7	2	7
68.9 to 74.4	66.7 to 75.0	3	2
74.3 to 77.6	75.0 to 80.0	4	2
77.5 to 79.7	80.0 to 83.3	5	2
79.6 to 81.8	**	**	**

*Number of adjoining ground tracks that provide coverage for a given location.

**Image overlap cannot realistically be split into sidelap and in-track overlap. Redundancy factor is > 5.

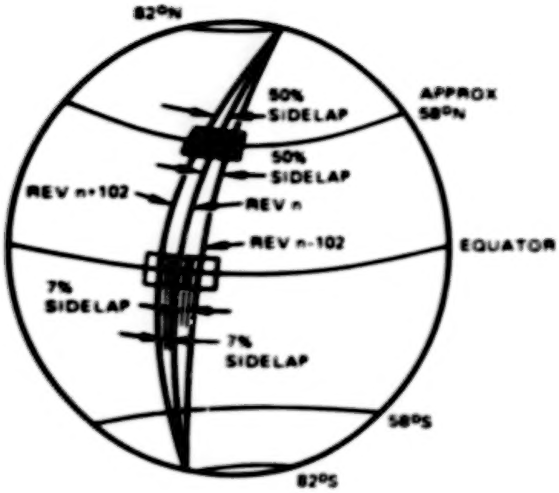
82°N
50%
SIDELAP
APPROX
58°N
50%
SIDELAP
REV n+102
REV n
REV n-102
EQUATOR
7%
SIDELAP
7%
SIDELAP
58°S
82°S

Figure 120. Landsat Sidelapping Coverage.

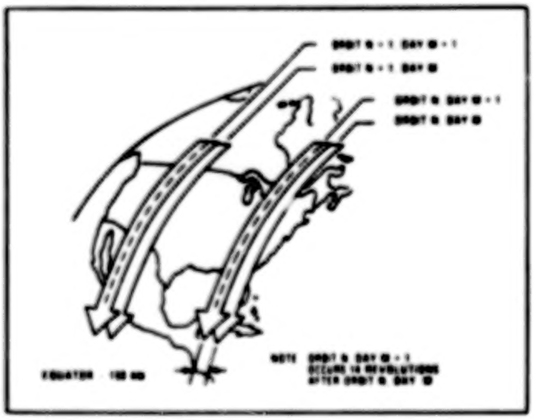
ORBIT N + 1 DAY M + 1
ORBIT N + 1 DAY M
ORBIT N DAY M + 1
ORBIT N DAY M
EQUATOR
NOTE ORBIT N DAY M + 1
OCCURS 14 REVOLUTIONS
AFTER ORBIT N DAY M

Figure 121. Ground Coverage Pattern.

equator by 25.75 degrees every revolution. Figure 122 illustrates this orbit track progression. Track number 15, the first pass of day 2, will appear adjacent to track 1 the first pass of day 1, 1.43 degrees to the west at the equator corresponding to 159 km. A complete cycle consists of 251 revolutions, during which exactly 18 days have passed and providing complete global coverage between 81 degrees north and 81 degrees south latitude.

The coverage pattern provides 14 percent sidelap at the equator as shown in Figure 123. Table 37 indicates the increase in sidelap of the swaths as higher latitudes are reached. As shown in Figure 124, at latitudes above 54 degrees, the sidelap is more than 50 percent, providing complete duplicate coverage on sequential days.

D.3 EFFECT OF ORBITAL PARAMETERS ON ON-BOARD CLASSIFICATION

How then do the orbital parameters affect the various on-board processing configurations?

For those configurations requiring minimum on-board storage and computing, the classification statistics on the ground, the following sequence would be incurred. The sample segment image data are transmitted to the ground in realtime. The operator selects training sites from the sample segments and computes the classification statistics. These classification statistics will be uplinked to the spacecraft, stored on-board, and used to classify the sample segment the next time the segment comes into view of the sensor. If the sample segment is above a given latitude (see Figures 120 and 123) and within the overlapped area the classification delay for Landsats-1, -2 and -C would be 1 day, for Landsat-D, 7 days. If the sample segment is not within the overlap region, the classification delay would be 16 days of Landsats-1, -2, and -C and 18 days for Landsat-D. LACIE has shown that delays in excess of 1 day between computing classification statistics and using same for classification will reduce classification accuracy.

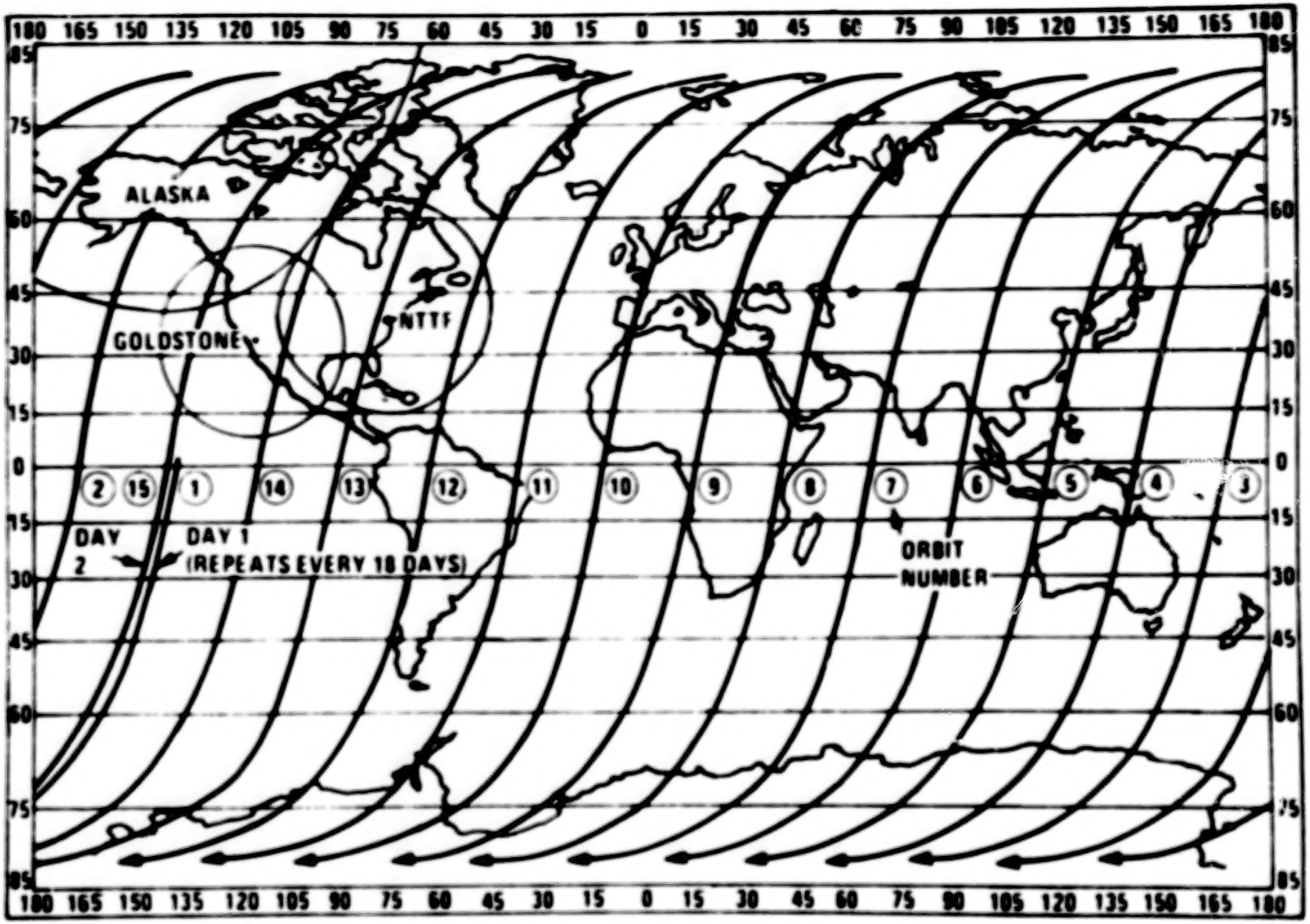
180 165 150 135 120 105 90 75 60 45 30 15 0 15 30 45 60 75 90 105 120 135 150 165 180
85
75
60
45
30
15
0
15
30
45
60
75
85
ALASKA
GOLDSTONE
NTTF
② ⑮ ① ⑭ ⑬ ⑫ ⑪ ⑩ ⑨ ⑧ ⑦ ⑥ ⑤ ④ ③
DAY 2
DAY 1 (REPEATS EVERY 18 DAYS)
ORBIT NUMBER

Figure 122. Daily Ground Trace (Daylight Passes Only) for Landsats -1, -2, and -C.

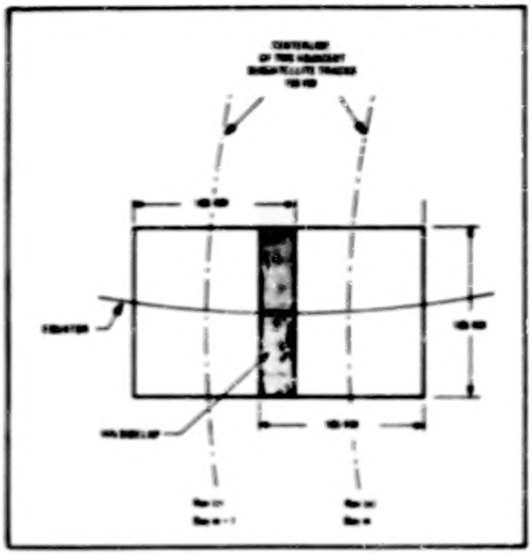

Figure 123. Imagery Sidelap at the Equator.

Table 37. Coverage Redundancy Due To Imagery Sidelap.

Latitude (Deg)	Image Sidelap (%)	Redundancy Factor*	Min. Coverage Requirement
0 - 56	14 - 50	1	Every day
56 - 67	50 - 67	2	Every 2nd day
67 - 72	67 - 75	3	Every 3rd day
72 - 74	75 - 80	4	Every 4th day
74 - 76	80 - 85	5	Every 5th day
76 - 82	> 85	6	Every 6th day

*Number of adjoining ground tracks which provide coverage for a given location.

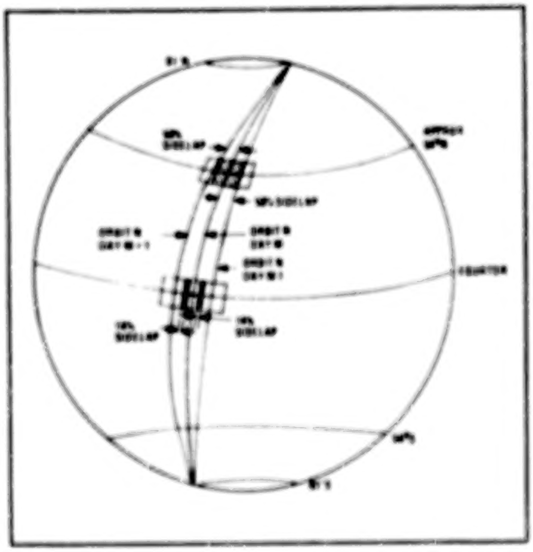

Figure 124. Landsat Sidelapping Coverage.

MICROFILMED FROM
BEST AVAILABLE COPY

If the classification statistics could be computed rapidly and uplinked to the spacecraft while still in line-of-sight of a receiving station, this delay could be reduced and classification accuracy improved.

Figure 125 illustrates the line-of-sight tracking regions for Goddard Space Flight Center (GSFC), Goldstone, and Fairbanks, Alaska. Assuming that the North to South region of interest over the continental U.S. extends 2778 kilometers, there would be 15 scenes (each 185 kilometers) of image data with each scene representing approximately 27 seconds time for each satellite pass. The total time the region of interest is in sight by GSFC would be 6.75 minutes (15 x 27 ÷ 60). As noted in the figure, the line-of-sight region extends beyond the region encompassed by the continental U.S. The 6.75 minutes could therefore be extended, however, storage of the data would have to be provided on-board during the time data evaluation is occurring on the ground.

Thus, there would only be the 6.75 minutes available to transmit the image data to the ground, select the training sites, compute the training site statistics, and transmit the data back to the on-board system. This time can be extended by using the TDRSS (Tracking Data Relay Satellite) to relay information to GSFC when line-of-sight transmission is not available. Figure 126 illustrates the TDRSS coverage zones and Figure 125 the extended visibility limits. This implies large amounts of on-board data storage to allow classification to occur on-board in realtime (i.e., training site data and test site data taken at the same time). Otherwise, the data to be classified could be as much as 18 days different in true time.

If the requirement is to have no time delay between image data used for computing the statistics and the classification, on-board storage of the segment must be provided equivalent to the time latency required to compute the statistics on the ground.

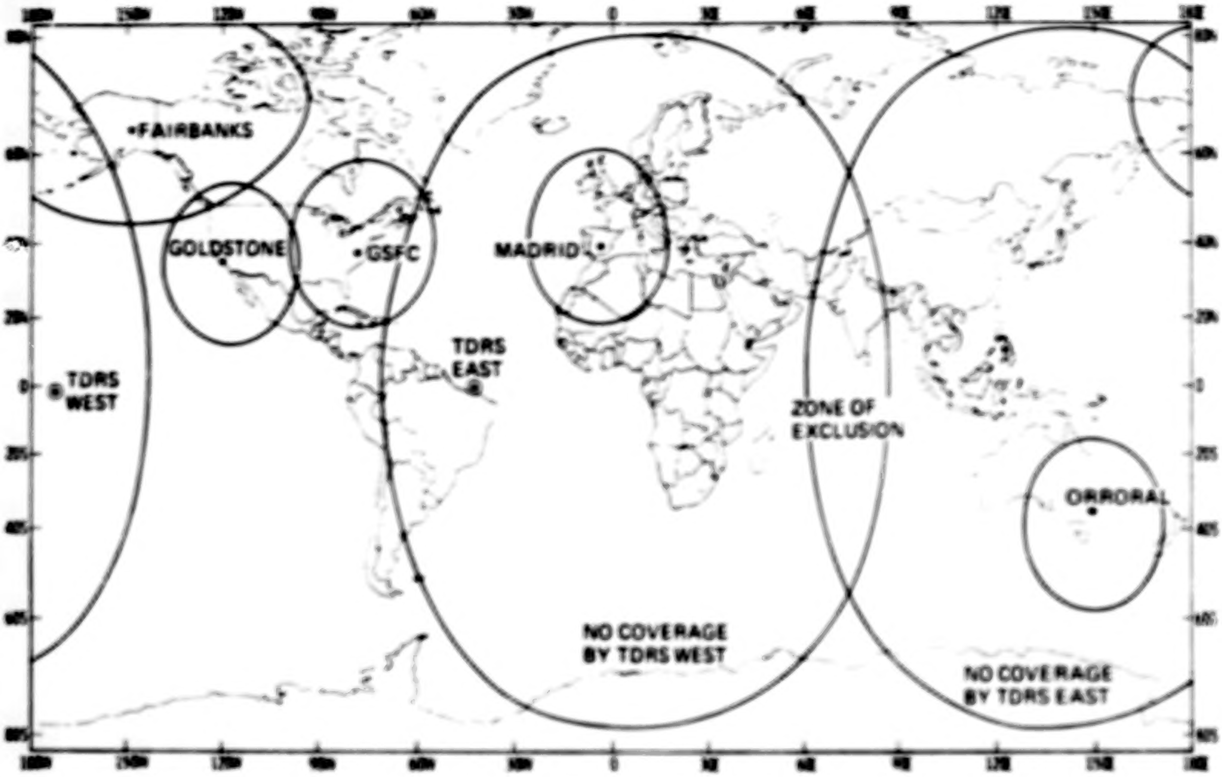
FAIRBANKS
GOLDSTONE
GSFC
MADRID
TDRS EAST
TDRS WEST
ZONE OF EXCLUSION
ORRORAL
NO COVERAGE BY TDRS WEST
NO COVERAGE BY TDRS EAST
180W
150W
120W
90W
60W
30W
0
30E
60E
90E
120E
150E
180E
80N
60N
40N
20N
0
20S
40S
60S
80S

Figure 125. TDRSS/GSTDN Visibility Limits.

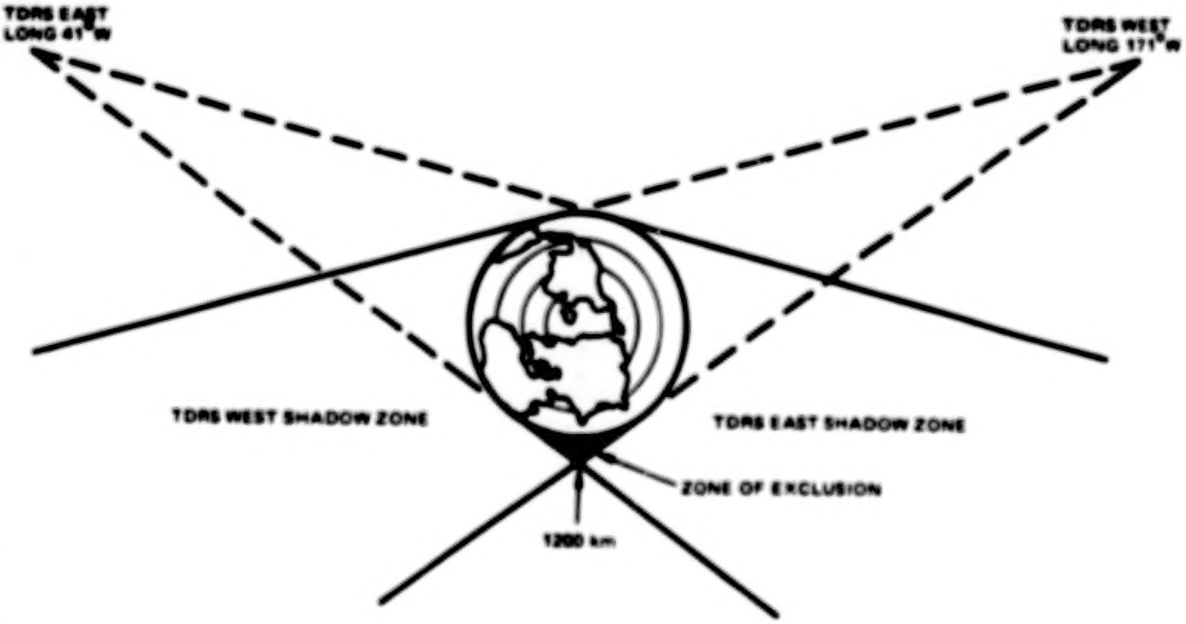
TDRS EAST LONG 41°W
TDRS WEST LONG 171°W
TDRS WEST SHADOW ZONE
TDRS EAST SHADOW ZONE
ZONE OF EXCLUSION
1200 km

Figure 126. TDRSS Coverage Zones.

The trade-off imposed by the orbital parameters, then, is expected classification accuracy vs. on-board storage.

Another approach to classification with training involves adjacent swath coverage. If the same swath width could be viewed on successive orbits of the spacecraft, the classification statistics could be computed on the first pass and the sample segments classified on the second pass. This would minimize on-board storage and only incur a time delay (relative to classification accuracy) of one orbit.

The MSS and TM scanning sensors, in the ideal case (no errors), provide a mirror scan that is symmetric about nadir. As noted in Figures 116 and 121, successive orbits of the spacecraft are separated by more than 24 degrees. Providing this much offset from nadir of subsequent orbits would impose severe conditions on either the spacecraft attitude control system or the sensor system, in particular the sensor mirror scanning assembly.

Figures 116 and 121 also indicate that adjacent swaths are separated by 1 day (1.43 degrees) for Landsat and 7 days (1.55 degrees) for Landsat-D. These offsets would be reasonable, although still imposing changes on the current Landsat mirror assembly or ACS. In the case of Landsat-D, however, there is a 7-day delay that would occur between computing the classification statistics and using the classification statistics.

This trade-off imposes a change in the present operational sequence vs. classification accuracy.

REFERENCES

1. Bernstein, R.,
   Digital Image Processing of Earth Observation Sensor Data,
   IBM Journal of Research and Development, Vol. 20/No. 1/ January 1976.

2. Proceedings of Plenary Session: The Lacie Symposium, NASA TM-79906, 1978.

3. Landsat Data Users Handbook, Document No. 71SD4249, Goddard Space Flight Center, April 1977.

4. IBM Earth Resources Management Symposium, Houston TX, January 27-29, 1976.

5. Generation and Physical Characteristics of the Landsat-1 and -2 MSS Computer Compatible Tapes, Report X-563-75-223, Greenbelt, MD, November 1975, Goddard Space Flight Center.

1. Report No. NASA CR-3134	2. Government Accession No.	3. Recipient's Catalog No.

4. Title and Subtitle On-Board Multispectral Classification Study	5. Report Date December 1979 6. Performing Organization Code
7. Author(s) D. Ewalt	8. Performing Organization Report No. 10. Work Unit No.
9. Performing Organization Name and Address International Business Machines, Inc. 18100 Frederick Pike Gaithersburg, Maryland 20760	11. Contract or Grant No. NAS1-15119 13. Type of Report and Period Covered Contractor Report
12. Sponsoring Agency Name and Address National Aeronautics and Space Administration Washington, DC 20546	14. Army Project No.

15. Supplementary Notes

Langley Technical Monitor: Harry F. Benz
Topical Report

16. Abstract

This study investigated the factors relating to on-board multispectral classification. The study was conducted in two parts. Part 1 reviews, in detail, those functions implemented in ground-based processing systems for current earth observation sensors. The sensors reviewed were the Multispectral Scanner (MSS), Thematic Mapper (TM), Return Bean Vidicon (RBV), and Heat Capacity Mapper (HCM). Part 2 of the study reviews the concept of classification and conceptually extends the ground-based image processing functions to an on-board system capable of multispectral classification.

Eight different on-board configurations, each with varying amounts of ground-spacecraft interaction, were evaluated. Each configuration was evaluated in terms of turnaround time, on-board processing and storage requirements, geometric and classification accuracy, on-board complexity, and ancillary data required from the ground.

17. Key Words (Suggested by Author(s)) Multispectral classification Image processing On-board processing	18. Distribution Statement Unclassified - Unlimited Subject Category 60

19. Security Classif. (of this report) Unclassified	20. Security Classif. (of this page) Unclassified	21. No. of Pages 305	22. Price* $11.75

*For sale by the National Technical Information Service, Springfield, Virginia 22161

NASA-Langley, 1979

292

END

June 15, 1981